Nano hetero-structures for improving performances of superconductors under high fields

Yasmine Kalboussi

université PARIS-SACLAY

Nano hetero-structures for improving performances of superconductors under high fields

Nano hétéro-structures pour l' amélioration des performances de supraconducteurs sous champs intenses

Thèse de doctorat de l'université Paris-Saclay

École doctorale n° 576, particules, hadrons, énergie et noyau : Instrumentation, imagerie, cosmos et simulation (PHENIICS)
Spécialité de doctorat : Sciences des Matériaux
Graduate School : Physique
Référent : Faculté des sciences d'Orsay

Thèse préparée au **Département des Accélérateurs, de la Cryogénie et du Magnétisme** (Université Paris-Saclay, CEA), sous la direction de **Claire ANTOINE**, Directrice de recherche, et le co-encadrement de **Thomas PROSLIER**, Chargé de recherche

Thèse soutenue à Paris-Saclay, le 10 mars 2023, par

Yasmine KALBOUSSI

Composition du Jury

Membres du jury avec voix délibérative

Mohamed BELHAJ Directeur de recherche, ONERA, Université de Toulouse III	Président
Nathanaelle SCHNEIDER Chargée de recherche (HDR), Institut Polytechnique de Paris	Rapporteur & Examinatrice
Anne-Marie VALENTE FELICIANO Chargée de recherche (HDR), Thomas Jefferson National Accelerator Facility	Rapporteur & Examinatrice
Sergio CALATRONI Directeur de recherche, CERN	Examinateur
Jens KNOBLOCH Professeur, Institute Science & Technology of Accelerating Systems, Universität Siegen	Examinateur

THESE DE DOCTORAT

NNT : 2023UPASP029

université PARIS-SACLAY

ÉCOLE DOCTORALE
Particules, hadrons, énergie et noyau : instrumentation, imagerie, cosmos et simulation (PHENIICS)

Titre : Nano hétéro-structures pour l'amélioration des performances de supraconduteurs sous champs intenses

Mots clés : Supraconductivité, ALD (déposition par couche atomique), Cavités radiofréquence, Films minces

Résumé : Depuis environ cinq décennies, les résonateurs en niobium massif ont été les meilleures cavités radiofréquences disponibles pour les accélérateurs. Grâce aux énormes efforts de recherche fournis par la communauté SRF, les cavités en niobium offrent aujourd'hui des performances exceptionnelles et fiables avec des gradients accélérateur allant jusqu'à 40 MV/m. Néanmoins, les cavités en niobium connaissent encore des limitations de performances lorsqu'elles sont exposées à des champs élevés qui sont essentiellement dus aux tourbillons de courant qui apparaissent dans les supraconducteurs lorsqu'un champ magnétique est appliqué. Ces tourbillons commencent à dissiper de l'énergie et à créer de la chaleur dès qu'ils sont mis en mouvement par le champ radiofréquence. De plus, leurs interactions avec les oxydes natifs et les défauts du matériau dégradent considérablement les performances supraconductrices.

Ce travail vise à explorer une nouvelle voie technologique pour améliorer les performances des cavités SRF en fonctionnalisant leur surface interne avec des revêtements en couches minces. En raison de sa forme complexe, le revêtement d'une cavité SRF nécessite un contrôle fin des propriétés chimiques et structurelles du film et une uniformité d'épaisseur jusqu'à l'échelle nanométrique. Le dépôt par couche atomique (ALD) est une technique de dépôt particulierement adaptée pour répondre à ces exigences. Ce projet est une approche synergique entre la synthèse, la caractérisation et les tests de performance sur cavités recouvertes par ALD de couches minces les plus efficaces pour traiter certains des phénomènes les plus limitants au fonctionnement des cavités RF et pour explorer de nouvelles voies technologiques pour améliorer leurs performances.

Title : Nano hetero-structures for improving performances of superconductors under high fields

Keywords : Superconductivity, ALD (Atomic Layer Deposition), Radiofrequency cavities, Thin films

Abstract : For approximately five decades, bulk niobium resonators have been the best RF accelerating cavities available for accelerators. Thanks to the huge research efforts made by the SRF community, niobium cavities provide today reliably exceptional performances with accelerating gradient up to 40 MV/m. Nonetheless, niobium cavities still witness performance limitations when exposed to high fields which are essentially due to current vortices that appear in the superconductors when a magnetic field is applied. These vortices start dissipating energy and creating heat as soon as they are set to motion by the RF field. Moreover, their interactions with native oxides and the material defects drastically demeans superconducting performances.

This work aims at exploring a new technological pathway to enhance the performances of SRF cavities through functionalizing their inner surface with thin film coatings. Due to its complex shape, coating an SRF cavity demands a finetuning of the film's chemical and structural properties and a thickness uniformity down to the nanometric scale. To our knowledge, atomic layer deposition is a very well suited deposition technique to fulfill these requirements. This Project is a synergistic approach between synthesis, characterization and performance tests of the most effective ALD deposited thin films to address some of the most detrimental phenomena to RF cavities operation and to explore new technological routes to boost their performances.

Contents

Introduction **1**

1 Accelerating Radio-Frequency cavities **3**
1.1 Introduction . . . 3
1.2 Birth of resonant cavities . . . 3
1.2.1 Origin of particle acceleration . . . 3
1.2.2 The direct-voltage acceleration . . . 4
1.2.3 The shift from DC to RF acceleration . . . 5
1.3 Key parameters in RF cavities design . . . 9
1.4 Superconducting RF cavities for particle acceleration . . . 10

2 Superconducting RF cavities **12**
2.1 The discovery of superconductivity . . . 12
2.1.1 Conduction in normal metals . . . 12
2.1.2 What happens to the resistance at very low temperatures ? . . . 12
2.1.3 The phenomenon of superconductivity . . . 13
2.1.4 Perfect diamagnetism . . . 14
2.2 Overview of the superconducting theories . . . 15
2.2.1 The two-fluid model of Gorter and Casimir -1934 . . . 15
2.2.2 The London equations -1935 . . . 16
2.2.3 The BCS theory - Bardeen Cooper Schrieffer - 1956 . . . 16
2.2.4 Superconductor classification according to the Ginzburg-Landau theory . . . 18
2.3 Superconductivity in the radio-frequency domain . . . 20
2.3.1 Surface resistance . . . 20
2.3.2 The radio-frequency critical field . . . 21
2.3.3 Niobium - the material of choice for SRF cavities . . . 22

3 Breaking the frontiers of bulk niobium SRF technology **24**
3.1 Introduction . . . 24
3.2 The long march of bulk niobium cavities . . . 24
3.2.1 The hydrogen Q-disease . . . 25
3.2.2 Multipacting . . . 25
3.2.3 Thermal breakdown . . . 25
3.2.4 Field emission . . . 26
3.2.5 High field Q-slope - HFQS . . . 27
3.3 Breaking the frontiers of bulk niobium . . . 27

3.3.1 Thin film on copper . . . 28
3.3.2 Doped bulk niobium cavities . . . 28
3.3.3 The multilayer theory . . . 28

4 Atomic layer deposition for SRF cavities 30
4.1 Introduction . . . 30
4.2 Overview . . . 30
4.3 Basics . . . 32
4.4 Example: the ALD deposition of niobium nitride . . . 33
4.4.1 ALD temperature dependence . . . 34
4.4.2 ALD Precursors . . . 35
4.4.3 Nucleation and substrate effect . . . 36
4.5 ALD deposition systems at CEA-Saclay . . . 37
4.5.1 Research-scale ALD system . . . 37
4.5.2 ALD system for cavity coating . . . 42
4.6 Characterization methods . . . 44
4.6.1 Thickness measurement and structural analysis . . . 44
4.6.2 Chemical composition analysis . . . 46
4.6.3 Superconducting measurements . . . 47
4.6.4 Optical and morphological analysis . . . 47

5 Protection and enhancement of niobium superconductivity 48
5.1 Introduction . . . 48
5.2 Niobium-Oxygen system . . . 49
5.3 Metal-oxide interface . . . 50
5.4 Magnetic impurities in Niobium oxides . . . 51
5.5 Replacing niobium native oxides with an ALD-deposited protective layer . . . 52
5.6 Deposition and characterization of the different oxides layers . . . 53
5.6.1 Deposition parameters . . . 53
5.6.2 X-ray reflectivity measurements . . . 53
5.6.3 X-ray photoelectron analysis . . . 54
5.6.4 Thermal stability of niobium native oxides . . . 55
5.6.5 TEM analysis . . . 60
5.7 Test on 1.3 GHz cavity geometry . . . 61
5.8 Al_2O_3 coating of 1.3 GHz niobium cavities . . . 62
5.8.1 The cavity preparation . . . 62
5.8.2 RF tests of the Al_2O_3 coated niobium cavities . . . 63
5.8.3 Low field RF behaviour . . . 65
5.9 Summary . . . 67

6 Multipacting mitigation in RF cavities 68
6.1 Introduction . . . 68
6.1.1 Multipacting . . . 68
6.1.2 Titanium nitride coating for multipacting mitigation . . . 70
6.2 Experimental conditions . . . 70
6.3 Preliminary results . . . 71

6.3.1 First SEY measurements . . . 71
6.3.2 Multipacting simulation on 1.3 GHz cavity geometry . . . 72
6.3.3 First RF test of 1.3 GHz cavity coated with 5 nm of TiN . . . 73
6.4 Minimum thickness of TiN for multipacting mitigation in SRF cavities 75
6.4.1 Secondary emission yield measurements . . . 75
6.4.2 TiN film thickness and growth . . . 78
6.5 XPS analysis on TiN films . . . 79
6.5.1 Sub-nanometer film thickness estimation . . . 79
6.5.2 Chemical composition of TiN films . . . 82
6.6 Electron bombardment of thin TiN films and its effect on the SEY . . 83
6.6.1 40 cycles TiN film . . . 83
6.6.2 50 cycles TiN film . . . 84
6.7 Test on 1.3 Ghz cavity . . . 87
6.7.1 Thermal stability on niobium . . . 87
6.7.2 RF test on 1.3 Ghz Niobium cavity . . . 88
6.8 Summary . . . 89

7 ALD-deposited multilayer to improve the superconducting performances of RF cavities 90
7.1 Introduction . . . 90
7.2 State of the art . . . 91
7.3 Choice of the multilayer structure . . . 92
7.3.1 Choice of the superconductor . . . 92
7.3.2 Choice of the insulator . . . 93
7.3.3 Choice of the film thickness . . . 93
7.4 ALD-deposition of the multilayer structure . . . 94
7.4.1 ALD-deposition parameters . . . 94
7.4.2 X-ray reflectivity measurements . . . 94
7.4.3 NbTiN films chemical composition . . . 96
7.5 NbTiN film superconducting properties . . . 101
7.5.1 NbTiN films resistivity . . . 101
7.5.2 NbTiN films critical temperature . . . 101
7.5.3 NbTiN film structural analysis . . . 103
7.6 Enhancing NbTiN films superconducting properties . . . 106
7.6.1 Testing the vacuum annealing on NbTiN-AlN bilayers . . . 106
7.6.2 Effect of the vacuum annealing on the crystalline structure of NbTiN films . . . 109
7.6.3 Thermal stability of the NbTiN-AlN bilayer on niobium substrates . . . 111
7.6.4 SEM analysis . . . 113
7.7 Optimizing the thermal treatment on niobium substrate . . . 114
7.7.1 Comparison of the NbTiN crystalline structure on niobium and sapphire substrates . . . 117
7.7.2 Comparison of the NbTiN critical temperature measured on niobium and sapphire substrates . . . 119
7.8 Conclusion . . . 123

8 Towards high-performance multilayer-coated niobium cavities 124
8.1 Introdcution . . . 124
8.2 Critical field enhancement on Niobium sample . . . 124
8.2.1 Preparation of the ellipsoid sample . . . 124
8.2.2 Critical temperature measurement . . . 126
8.2.3 Hysteresis loop analysis . . . 127
8.3 High pressure rinsing test . . . 129
8.4 Nitrogen diffusion at the interface between the multilayer and bulk niobium . . . 132
8.5 Topography and roughness considerations of the NbTiN films . . . 134
8.6 NbTiN-AlN uniformity test on 1.3 GHz cavity geometry . . . 137
8.6.1 Experiment preparation . . . 137
8.6.2 Optimizing the deposition parameters on the 1.3 GHz cavity . 138
8.7 Testing the NbTiN-ALN layer on 1.3 GHz Niobium cavity . . . 141
8.7.1 Cavity Preparation . . . 141
8.7.2 RF test results . . . 143
8.8 Perspectives . . . 145

9 New route for doping SRF cavities using atomic layer deposition 146
9.1 Introduction . . . 146
9.2 Conventional approach for N-doping . . . 147
9.3 ALD-approach . . . 148
9.4 Preliminary results on Nb coupons . . . 149
9.4.1 Niobium nitride . . . 150
9.4.2 Titanium nitride . . . 152
9.4.3 Zirconium nitride . . . 154
9.4.4 Aluminium nitride . . . 156
9.5 Test on SRF cavity . . . 157
9.6 Perspectives . . . 159

Conclusions and perspectives 160

Acknowledgments 161

Introduction

For approximately five decades, bulk niobium resonators have been the backbone of superconducting particle accelerators. Thanks to the huge research efforts made by the SRF community, niobium cavities provide today reliably exceptional performances with accelerating gradient up to 40 MV/m. Nonetheless, niobium cavities still witness performance limitations when exposed to high fields which are essentially due to vortices that appear in the superconductors when a magnetic field above the first critical field is applied. These vortices start dissipating energy and creating heat as soon as they are set to motion by the RF field. Moreover, the interactions of the fields with native oxides and the surface defects drastically demeans superconducting performances.

This work aims at exploring a new technological pathway to enhance the performances of SRF cavities through functionalizing their inner surface with thin film coatings. Due to its complex shape, coating an SRF cavity demands a fine-tuning of the film's chemical and structural properties and a thickness uniformity down to the nanometric scale. Accordingly, atomic layer deposition technique is chosen to fulfill these requirements.

This project is a synergistic approach between synthesis, characterization and performance tests of the most effective ALD deposited thin films to address some of the most detrimental phenomena to RF cavities operation and to explore new technological routes to boost their performances.

During this research project, we studied four different experimental routes to boost RF cavities performances:

1. Replacing the Niobium native oxides with a more thermally stable oxide layer deposited by ALD.

2. Suppressing multipacting using a ultra thin film of titanium nitride deposited by ALD.

3. Testing the multilayer approach as suggested by Gurevich [1] to screen the magnetic field inside the RF cavity.

4. Exploring a new Niobium cavity doping approach using ALD-deposited thin films as a dopant source.

This dissertation is organized as follows: Chapters 1, 2 and 3 introduce the basics of superconducting radio-frequency cavities and presents some of the most promising research routes to break the frontiers of bulk niobium cavities. Then, in chapter 4 we introduce the principle of atomic layer deposition and describe the ALD system

used in this project. Followed by chapter 5, where we study the thermal stability of niobium native oxides and test ALD-deposited oxides layers to protect and enhance niobium superconductivity. Chapter 6 is dedicated to multipacting mitigation in SRF cavities through the deposition of sub-nanometric titanium nitride films. Chapters 7 and 8 are dedicated to testing the multilayer approach [1]. A bilayer of NbTiN-AlN on niobium is optimised with critical temperature of 16 K. This approach is tested for the first time in a 1.3 GHz niobium cavity. Finally, chapter 9 presents a new route to doping niobium cavities using atomic layer deposition thin films as a dopant source. A synthesis of the results, conclusions and perspectives are provided in the last chapter.

Chapter 1

Accelerating Radio-Frequency cavities

1.1 Introduction

Ever since the 1920s, several devices have been designed to accelerate particles, constantly with the aim of achieving higher particle energies. Throughout this long journey, several technical limitations have been encountered and scientists have had to adapt their accelerating cavity design and make technical choices in order to overcome these difficulties. Throughout this chapter, we will give an overview of some of the most significant advances in accelerating cavities. We will also introduce their key design parameters. A more extensive description of the early developments in accelerators design can be found in [2].

1.2 Birth of resonant cavities

1.2.1 Origin of particle acceleration

Particle accelerators are based on the simple application of the **Lorentz force**: When a charged particle of a velocity $\vec{v}$ and a charge q crosses a volume containing a magnetic field $\vec{B}$ and an electric field $\vec{E}$, the Lorentz force acted upon the particle is:

$$\vec{F} = q(\vec{v} \times \vec{B}) + \vec{E} \tag{1.1}$$

$\vec{F}$ is the combination of the electric force and the magnetic force. As the particle moves from a point r_1 to a point r_2 , its energy changes by the amount of ΔE where:

$$\Delta E = \int_{r_1}^{r_2} \vec{F}\, \vec{dr} = q \int_{r_1}^{r_2} (\vec{v} \times \vec{B} + \vec{E})\, \vec{dr} \tag{1.2}$$

Since the motion path $\vec{dr}$ is always parallel to the velocity vector $\vec{v}$, the entity $(\vec{v} \times \vec{B}).\vec{dr}$ is equal to zero and the magnetic field $\vec{B}$ does not add any contribution to the energy of the particle. Acceleration requires an increase in the particle energy and therefore, it can only result from the use of electric field $\vec{E}$. The gain in the

particle's energy is then equal to:

$$\Delta E = \int_{r_1}^{r_2} \vec{F}\,\vec{dr} = qU \tag{1.3}$$

where U is the voltage seen by the particle.

Although the magnetic field does not change the energy of the particle, it can change its trajectory. Accelerator physics is mainly governed by these two aspects: the acceleration and the deviation of charged particles. Particles are accelerated using electric fields and deviated or focused using magnetic fields.

1.2.2 The direct-voltage acceleration

The most basic particle accelerator used a voltage generator to create a potential difference between two electrodes. In order to avoid collisions with gas molecules, a relatively good vacuum is needed.

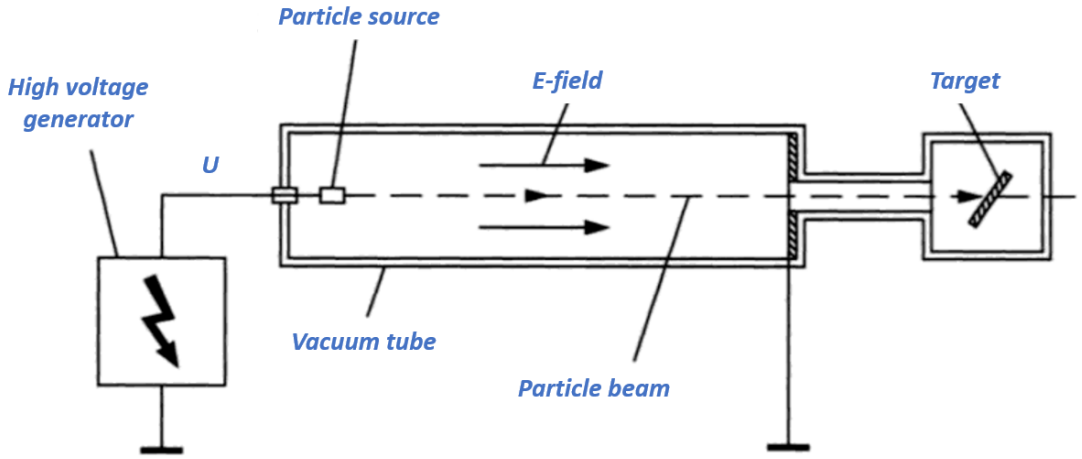

Figure 1.1: Illustration of the direct-voltage accelerator (figure after [2])

If we use a direct voltage generator, a positive charge will form on one electrode and a negative charge on the other and in between will lie a uniform electric field. As explained previously, a charged particle traveling through this electric field will see its energy increase by an amount ΔE =qU where q is the particle charge and U is the potential difference between the two electrodes. This simple yet efficient principle is commonly used in technologies such as screens and oscilloscopes. However, the energies achievable by this mean are directly proportional to the voltage applied between the two electrodes which is fundamentally limited by "**Corona discharge**":

If one continuously increases the voltage difference between two electrodes, one will come to a point where the field strength close to the electrodes will accelerate ions and electrons in this region to considerable energies. These ions and electrons will collide with residual gas molecules creating many more ions, which in turns will be accelerated and so on. This generates an avalanche of charge carriers creating a conductive path in the gap, which will give rise to a spark discharge and the break-down of the high voltage [2]. This phenomenon can lead to disastrous consequences and can even cause the destruction of the equipment.

In practice, due to Corona discharge and vacuum physics, electrostatic generators are incompatible with generating high accelerations. Another inherent limit of DC accelerators are their massive size: to reach few MV of potential, Van de Graaff built a generator using a 18 meter long electrodes which was quite complicated to handle [3]. To suppress dielectric breakdown, he filled the generator and accelerator sections with a SF_6 which is a gas with a high dielectric constant. Due to these limitations, accelerator scientists had to come up with an ingenious trick and a more practical design of accelerators.

1.2.3 The shift from DC to RF acceleration

To circumvent the practical limitations of DC accelerators, scientists came up with the simple yet brilliant idea of replacing one large DC accelerator with many smaller ones in series: This lead spontaneously to AC acceleration.

In 1925, Gustav Ising, first designed, a linear accelerator using several high frequency changing voltages in series to accelerate progressively a particle beam [4]. Three years later, the design was improved by Rolf Wideroe for his PhD thesis [5], and was built to successfully accelerate Na and K ions to 50 KV using a 1-MHz - 25 KV oscillator. Let us focus on Wideroe design illustrated in figure 1.2:

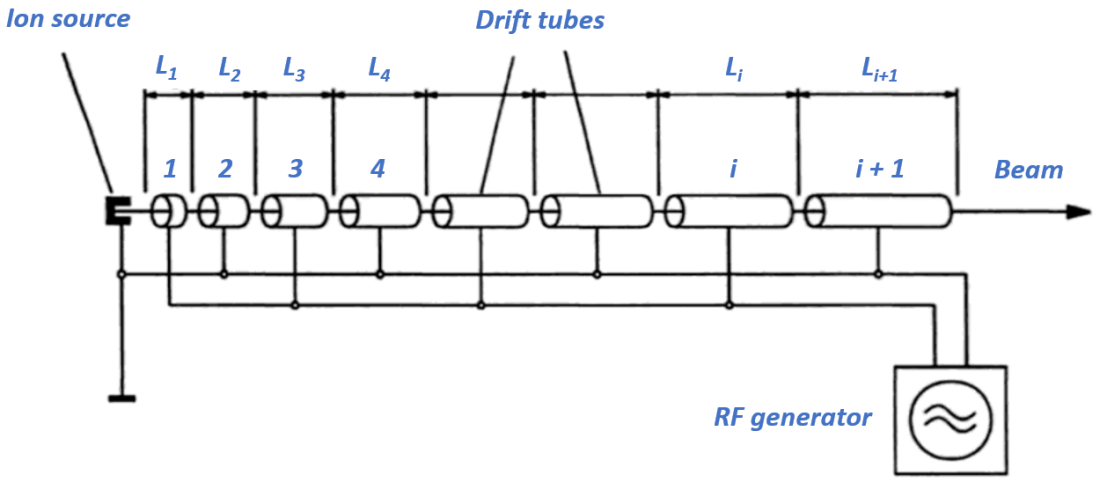

Figure 1.2: Illustration of Wideroe accelerator (figure after [2])

The accelerator consists in a sequence of drift tubes, which are connected alternatively to the poles of an RF generator. The drift tubes were separated by a gap in which lies a longitudinal oscillating electric field. The drift tubes acted like a Faraday cage protecting the beam from external fields so that the particles can only be accelerated across the gaps. The key aspect of this accelerator is that the length of the tubes must increase with the particle velocity so that the time of flight of the particle inside each drift tube is always equal to half of the RF period. This condition ensures that each time the particles are about to cross the gap, they only experience an electric field in the direction that pushes them further in the accelerator. Their kinetic energy is therefore increased by ΔE =qU.

One could wonder about the choice of the radio-frequency domain in particular. To see why, let us consider the transit time Δt for a particle to go through a drift tube of length L. To ensure synchronous acceleration which means that the particle only sees an accelerating electric fields when it reaches the gap, Δt must be equal to half of a period T.

$$\Delta t = \frac{T}{2} \tag{1.4}$$

If we assume that the particle velocity is equal to the speed of light c, we derive that:

$$\Delta t = \frac{L}{c} = \frac{1}{2f} \tag{1.5}$$

which means that:

$$f = \frac{c}{2L} \tag{1.6}$$

For a drift tube of 10 cm length, we would need an operating frequency of 1.5 GHz. Radio-frequencies are chosen to keep the lengths of the acceleration structures reasonable. However, one must not forget that the problem with such high frequency structures is that it radiates RF energy at a rate of:

$$P = \omega_{rf} C V_{rf}^2 \tag{1.7}$$

with ω_{rf} is the frequency, C is the capacitance of the gap and V_{rf} is the RF voltage [6].

An easy solution to eliminate RF power losses would be to add an inductive load to the structure. So that, instead of dissipating power through radiation, it would be stored in the form of a magnetic field making up a resonant LC circuit. Thus, if the capacitor is charged initially, it will discharge through the inductance, giving rise to alternating current flow that will create an oscillating electric field between the plates. In such LC resonant circuits, electromagnetic energy could be stored perpetually, as the electric and magnetic fields would maintain themselves according to Maxwell's law.

Let us suppose we have a simple capacitor which consists in two parallel circular plates separated with a gap (as it can be seen in figure 1.3[1]) and try to transform it into a LC circuit resonating at an frequency $\omega_{rf} = \frac{1}{\sqrt{LC}}$ in the RF range. We can do that by simply connecting the parallel plate capacitor to an inductive load such as a coil of an inductance L. To increase the resonant frequency of this system and bring it to the RF range, we can lower the inductance L by lowering the number of turns in the coil. However, we will get eventually to the last turn, and we will have just a piece of wire connecting the top and the bottom plates of the capacitor. At this point, we can continue raising the frequency by lowering the capacitance, but we can also continue decreasing the inductance L by using several inductance in parallel. So, we can continue adding other single loops connecting the two plates of the capacitor until eventually make the transition to a completely closed resonant cavity. This is nothing more than the "**pillbox cavity**" geometry that is used to accelerate particles. Evidently, we need to make openings in the sides to allow the particle beam to go through the cavity.

[1]inspired from the cavity resonator lecture of Richard Feynman,Volume 2.

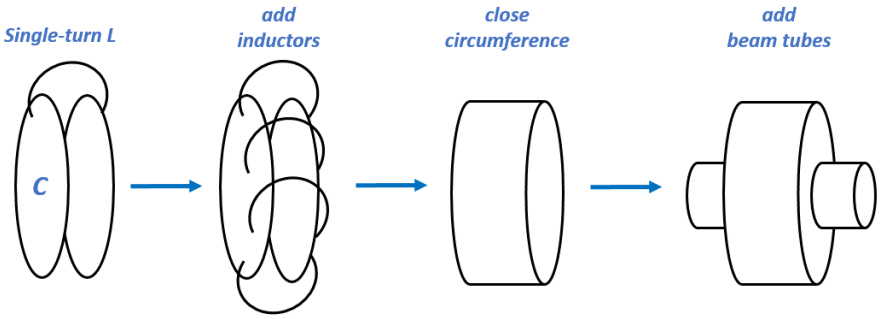

Figure 1.3: Illustration explaining the transformation of an LC circuit into a resonant cavity

In a resonant cavity, several possible geometrical arrangement for the electric and magnetic fields - called modes- coexists. The only requirement is that the fields comply to the Maxwell equations. For particle acceleration, it is obvious that the most convenient mode is the one where the electric field is longitudinal along the particle beam axis and the magnetic field is parallel to the cavity walls. This mode is called the transverse magnetic mode TM_{010} and it is represented in figure 1.4. For a pillbox cavity, the resonant frequency of the TM_{010} mode is equal to:

$$\omega_{010} = \frac{2.405c}{r} \tag{1.8}$$

where r is the radius of the cavity.

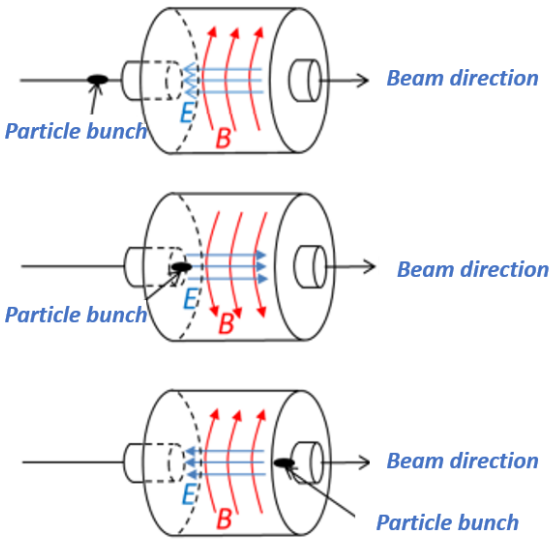

Figure 1.4: Illustration of the transverse magnetic mode TM_{010} in a pillbox cavity after [7]

The other excited modes are called higher order modes (HOMs). They are undesirable since they can deflect the particle beam and can cause power dissipation. In

practice, higher order modes are damped using specially designed couplers. The RF energy generated through an external circuit is coupled to the cavity by the mean of an input antenna. The RF energy should be inevitably matched to resonant frequency of the cavity, which is determined by its shape and size. We have mentioned previously that electromagnetic energy could be stored perpetually. This is not exactly right because of the resistance of the cavity material. Currents flowing through the material walls will dissipate energy through **Joule effect**. As a consequence, The cavity is better represented through an RLC resonant circuit as represented in figure 1.5.

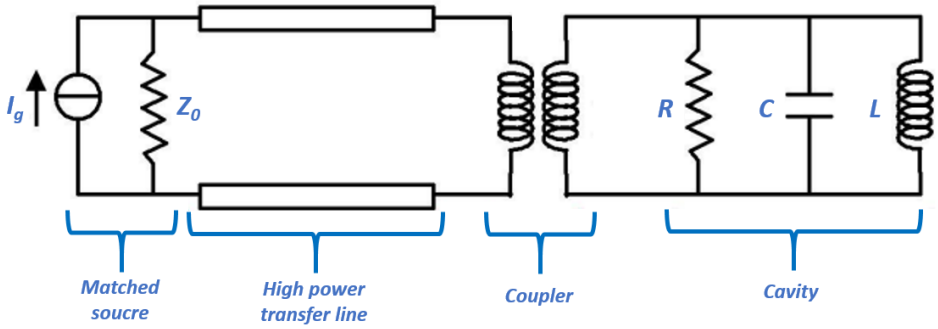

Figure 1.5: Illustration of the electrical circuit of a resonant cavity connected to the high power transfer line using a coupler

1.3 Key parameters in RF cavities design

Resonant cavities come in different sizes and shapes depending on the type of particles that needs to be accelerated and their desired velocity. Cavities are therefore classified based on a parameter called $\beta = v/c$:

- Low β cavities ($\beta \sim 0.001$ - 0.2) are used for heavy ions accelerators (such as "Grand Accélérateur National d'Ions Lourds " GANIL in France or "Japan Atomic Energy Research Institute" JAERI in Japan)
- Medium β cavities ($\beta \sim 0.2$ - 0.7) are used for to accelerate heavy ions at higher energy and protons (for example, "Spallation Neutron Source" SNS in USA and "European Spallation Source" ESS in Sweden).
- High β cavities ($\beta \sim 0.7$ - 1) are used to accelerate electrons, positrons and heavier particles once they reach relativistic velocities such as ("Large Hadron Collider" LHC in Switzerland and "European X-Ray Free-Electron Laser" XFEL in Germany) .

In the following sections, we will focus mainly on high β elliptical cavities which are the typical cavities used for R&D nowadays. Modern elliptical cavities are basically pillbox cavities whose edges are rounded to inhibit multipacting [8]. A schematic of a single cell elliptical cavity is present in figure 1.6. The electric field $\vec{E}$ is maximum along the beam axis and the magnetic field $\vec{B}$ is maximum in the equatorial region.

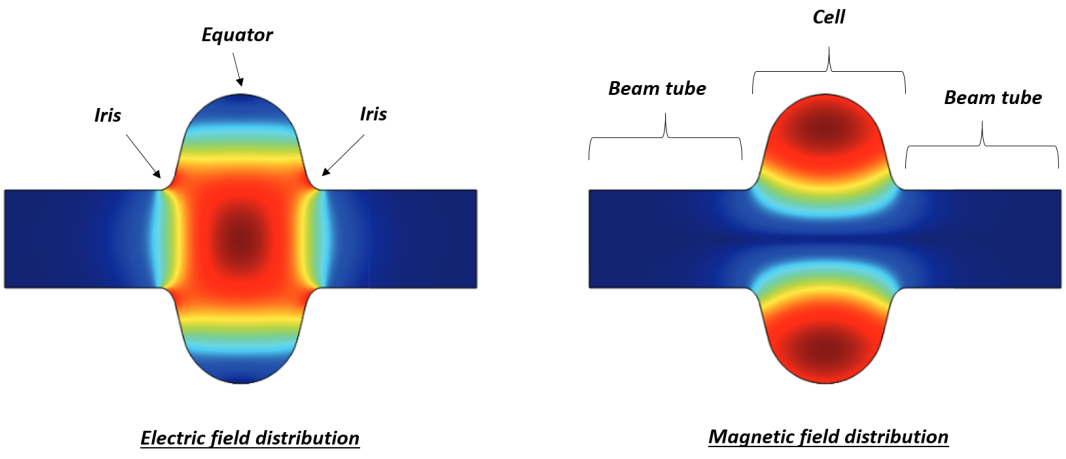

Figure 1.6: The electric and magnetic field distribution in an elliptical single cell 1.3 GHz cavity. The dark red regions represents the highest fields density whereas the dark blue region indicates the lowest (figure after [9])

A key parameter for a resonant cavity is the accelerating field E_{acc} with:

$$E_{acc} = \frac{V_{acc}}{d} \tag{1.9}$$

where V_{acc} is the accelerating voltage the particle sees when crossing the cavity and d is the cavity length.

To assess the performance of a resonant cavity, we measure its quality factor Q. The quality factor of a resonator reflects the number of oscillations a resonator will go through before losing a significant amount of its stored energy.

In an accelerator cavity, energy can be fed to the particle beam travelling along the axis, it can be reflected through coupling probes, or it can be converted to heat by resistive losses in the cavity walls. If we only take into account the dissipation in the cavity walls, we would consider the unloaded Q_0 which is equal to:

$$Q_0 = \frac{\omega U}{P_d} \tag{1.10}$$

where ω is the resonant frequency, U is the energy stored in the cavity and P_d is the power dissipated. Since the time-averaged electric energy is energy is equal to the magnetic energy energy for a volume of a cavity V. The total energy stored in a cavity is equal to:

$$U = \frac{1}{2}\mu_0 \int_V |H|^2 \, dv = \frac{1}{2}\epsilon_0 \int_V |E|^2 \, dv \tag{1.11}$$

The dissipated power can be expressed as:

$$P_d = \frac{1}{2} R_s \int_s |H|^2 \, ds \tag{1.12}$$

Where the integration is done over the internal cavity surface S, assuming that the surface resistance R_s is invariable all over the cavity walls. Q_0 is then equal to:

$$Q_0 = \frac{\omega \mu_0 \int_V |H|^2 \, dv}{R_s \int_s |H|^2 \, ds} = \frac{G}{R_s} \tag{1.13}$$

where G is a geometrical constant.

Based on the expression of the Q_0, it seems straightforward that a resonant cavity performances are closely related to its surface resistance. The lower the surface resistance of the cavity walls is, the higher the quality factor is and the better the cavity will perform.

1.4 Superconducting RF cavities for particle acceleration

Reducing the surface resistance of the cavity walls is crucial to guarantee to insure that most of the energy is communicated to the beam rather than lost by Joules effect. Cavities were typically manufactured out of copper, as it is highly conductive, easy to machine and relatively cheap. However, for accelerators that require continuous operation, the power losses through Joule effect in the copper cavity walls become prohibitive and their use become severely power-consuming [10]. In addition to that, the surface temperature becomes very high causing vacuum degradation and metal fatigue. To avoid melting the cavity, it is necessary to cool the

cavities and to keep the average injected power low which limits copper cavities to gradients near 1 MV/m in continuous operation [11]. Here, superconductivity comes to the rescue. As it will be seen in the following chapter, the RF surface resistance of a superconductor is not 0 but it is 5 to 6 order of magnitude lower than that of copper which results in quality factors of the order of 10^{10}. Even after accounting for the cryogenic power needed to cool superconducting cavities at few kelvins, the net gain varies from a factor of two to few hundreds depending on the application. This is mainly the fundamental advantage of superconducting cavities over normal conducting ones. In the following chapter, we will go through the discovery of superconductivity and introduce its basic principles in the radio-frequency domain.

Chapter 2

Superconducting RF cavities

2.1 The discovery of superconductivity

Superconductivity is at the heart of accelerator technology. While superconducting magnets provide the high magnetic fields needed to deflect and focus the particle beam, SRF cavities provide the high voltage required for their acceleration. In this chapter, we will introduce the basic principle of superconductivity and go through some of the most important milestones of our understanding of this phenomena.

2.1.1 Conduction in normal metals

According to the well-established Drude formalism, conduction electrons in a metal flow randomly in the crystalline lattice formed by the positively charged ions. These ions are tightly linked to their lattice positions. Nonetheless, they undergo some vibrations at quantized frequencies called **phonon**. In the absence of an electrical field, electrons get scattered by these ions randomly, so they do not drift in any particular direction. However, once an electrical field is applied to the material, all electrons start to move in the same direction opposite to the field creating a net current flow. As they continue to get scattered by phonons, electrons face resistance in their movement, which results in an energy loss in the form of heat (called Joule effect). Impurities present in the lattice are also a source of scattering for the electrons and add a supplementary contribution to the resistivity of the material. Since the dominant part of resistance comes from scattering with phonons, which are strongly dependent of the temperature, physicists got very curious about the behavior of this conduction at very low temperatures[12].

2.1.2 What happens to the resistance at very low temperatures ?

This question led scientists to try to reach lower and lower temperatures and even before succeeding in achieving such temperatures, there were already some predictions made about the subject.

James Dewar suggested that resistance should become zero when one reaches zero kelvin as the lattice will freeze and phonons would completely vanish. At

the contrary, Kelvin imagined that the resistance will decrease to a minimum and increase again approaching the absolute zero as electrons will freeze. Matthiessen predicted that the resistance would decrease when one lowers the temperature and remains constant at a finite value.

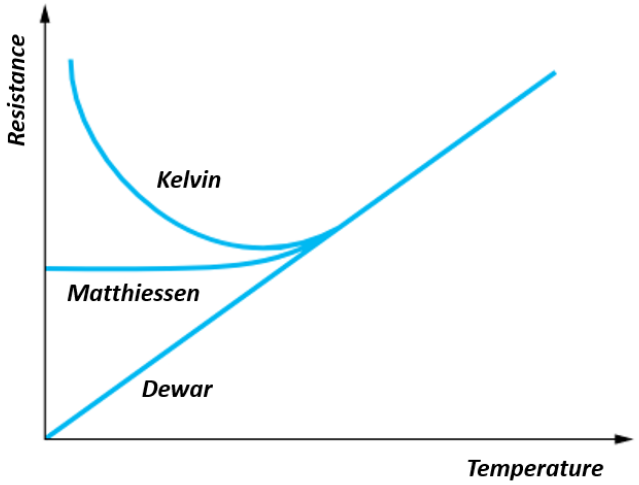

Figure 2.1: Predictions made by Kelvin, Matthiessen and Dewar about the behaviour of resistance in metals at low temperatures (figure after[13])

According to Matthiessen conjecture, which turned out to be the most accurate, resistance at low temperature consist in two components: A first component caused by the phonon scattering which tends to decrease when lowering the temperature and a second component which is due to scattering with impurities and which is temperature-independent:

$$R = R_{phonon}(T) + R_{impurities} \tag{2.1}$$

2.1.3 The phenomenon of superconductivity

When Dewar managed to liquefy hydrogen and to measure the resistivity of pure silver and gold down to 16 K, he found out that their resistivity decreased down to a finite value and remained constant. He believed that this is due to the impurities still present in the materials.

These results motivated Kamerlingh Onnes, in 1911, to study the resistivity of mercury, which unlike gold and silver, can be obtained in ultra-high purity by the means of multiple distillations. Once he succeeded in liquefying helium, Kamerlingh measured the resistance of ultra-high purity mercury when decreasing its temperature and observed a sudden disappearance of resistance below 4.2 K (as it can be seen in figure 2.2). He recognized that below 4.2 K, mercury transitioned into a new state that he called **superconducting state**.

Soon after that, Onnes also found out that superconductivity gets destroyed when exposed to a magnetic field. As a matter of fact, a magnetic field in excess to a specific value forces a superconductor back into its normal state. There exists

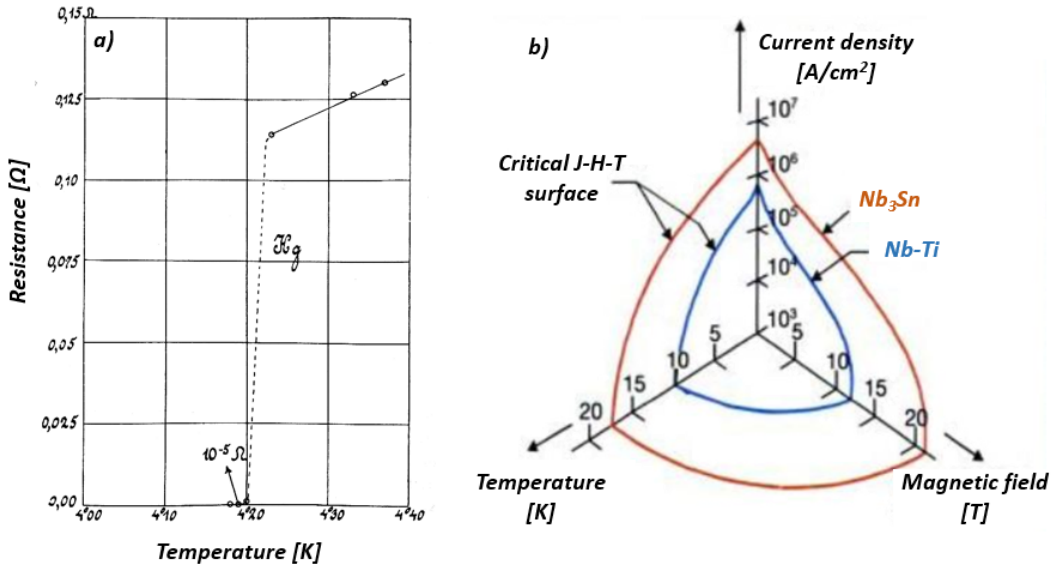

Figure 2.2: a) The first observation of superconductivity in pure mercury by Kamerlingh Onnes in 1911. b) The superconducting critical surface: the magnetic field, the temperature and the current density must be below the critical surface in order to maintain superconductivity

a region of temperatures, magnetic fields and current densities within which the material is superconducting (see figure 2.2). We call **critical temperature $\mathbf{T_c}$** and **critical field $\mathbf{H_c}$** respectively the highest temperature and the highest magnetic field a material can withstand before turning back into its normal state. They are related through:

$$H_c = H_0[1 - (\frac{T}{T_c})^{2}] \tag{2.2}$$

During the following years, several metals were found to be superconductors like lead, tin, aluminum, zinc and niobium. Unexpectedly, the best-known conductors like copper, gold or silver were found to be non-superconducting. Soon, other compounds such as NbTi, NbTiN and Nb_3Sn were found to be superconducting at even higher temperatures.

2.1.4 Perfect diamagnetism

Perfect conductivity was thought to be the only peculiarity of a superconductor, up to 1933, when Meissner and Ochsenfeld discovered another exceptional hallmark of superconductivity. They found out that a magnetic field is not frozen inside a superconductor upon the transition but rather expelled from it. This observation went against all expectations, as it was believed that a superconductor, being a perfect conductor, would obey to the Maxwell law (which dictates that the magnetic flux variation in time is null). In other words, the magnetic flux should remain constant and trapped inside the material when we cool it down for T $< T_c$.

Surprisingly, this was not the case. A superconductor changes its magnetic

behavior from being weakly paramagnetic above T_c to being a perfect diamagnet when $T < T_c$ (as illustrated in figure 2.3). This observation is referred to as the **Meissner-Ochsenfeld effect**. This effect can be interpreted in terms of screening currents flowing across the surface of a superconductor in a way to create a magnetic field equal and opposite to the external field.

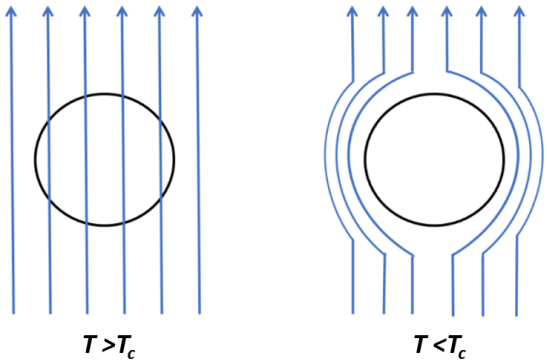

Figure 2.3: The Meissner-Ochsenfeld effect: Below T_c, the superconductor expels the magnetic flux from its body.

The fact that the magnetic flux inside a superconductor is zero even when exposed to a certain magnetic field indicates that a magnetization is induced in the superconductor which cancels out the magnetic flux. This means that a superconductor has a magnetic susceptibility of -1.

As we mentioned earlier, the screening currents flow along the surface of a superconductor to prevent flux entry without experiencing any resistance. The zero resistance was investigated using currents flow in superconducting rings. These currents flew persistently without any Joule heating and showed a characteristic decay time higher than 10^5 years.

Historically, Meissner and Ochsenfeld work paved the way to a correct theoretical understanding of superconductivity. In the following sections, we will concisely introduce some of the theoretical aspects of superconductivity. A much deeper description can be found in [12, 14].

2.2 Overview of the superconducting theories

2.2.1 The two-fluid model of Gorter and Casimir -1934

The first intuitive explanation of the superconductivity theory came with the "Two-fluid model" of Gorter and Casimir in 1934. They predicted that electrons in a superconductor below T_c are divided into two interpenetrating electronic fluids: a fraction of electrons were assumed to remain "normal" and therefore continue to get scattered by phonons and impurities whereas the other fraction of electrons "condensed" into a superconducting aggregate. This aggregate behaves as a macro-

scopically coherent system. At T=0 K , all electrons are superconducting whereas at T $> T_c$, all electrons are normal and the condensate disappears.

Gorter and Casimir theory, although incomplete, showed a good agreement to the experiments and provided a useful description of the superconducting state. The density of superconducting electrons n_s is temperature dependant and can be expressed as:

$$n_s = n_0[1 - (\frac{T}{T_c})^4] \tag{2.3}$$

where n_0 is the superconducting electron density at T=0 K.

2.2.2 The London equations -1935

In 1935, The two german brothers, Fritz and Heinz London, succeeded in giving the first phenomenological explanation of superconductivity. Starting from a two-fluid model, they adapted the well-known Maxwell equations to the field exclusion and the infinite conductivity of a superconductor. They concluded that the magnetic field does not abruptly vanish at the surface of a superconductor but rather decreases exponentially into the bulk with a characteristic depth called the London penetration depth λ_L. The penetration depth λ_L in most pure metals is of the order of 10 to 100 nm. The magnetic flux at a distance x inside the superconductor follows:

$$B(x) = B_0 \exp(-\frac{x}{\lambda_L}) \tag{2.4}$$

with

$$\lambda_L = [\frac{m}{\mu_0 n_s e^2}]^{\frac{1}{2}} \tag{2.5}$$

where m is the mass of the electron, e is its charge and μ_0 is the vacuum magnetic permeability.

Following this theory, Fritz London expanded his work on superconductivity and postulated that it has a quantum origin. He even made the remarkable prediction that a magnetic flux inside a superconducting cylinder will be quantified in units of h/e where h is the plank constant and e the charge of an electron.

Several years later, the flux quantification was proven experimentally but it was found that the elementary flux quantum Φ_0 is equal to h/2e rather than h/e. The factor 2e is of great significance, as it is the total electronic charge involved in superconductivity. This fact became evident to understand thanks to the BCS theory [12].

The period of the early 1950's culminated with the elaboration of the Ginzburg-Landau theory. Based on the previous work of Landau on the second-order phase transition, the two theoretician expended the London theory by introducing a complex order parameter Ψ with $|\Psi|^2$ describes locally the fraction of superconducting electrons. This theory will be discussed further in a subsequent section.

2.2.3 The BCS theory - Bardeen Cooper Schrieffer - 1956

For decades, a fundamental understanding of superconductivity eluded the physicists, until the advent of the microscopic theory of superconductivity by Barden,

Cooper and Schrieffer in 1957.

The BCS Theory assumed that an effective attractive interaction between electrons with equal and opposite momenta and spins enables them to form pairs. Consequently, the supercurrent is not carried out by single electrons like the normal current is, but rather by a pair of electrons called a "**cooper pair**" with a charge 2e. This cooper pair formation was assumed to result from a phonon-mediated lattice-electron interaction. One can envision this interaction by imagining an electron travelling through the crystalline lattice of a superconductor. Because of his negative charge, the electron will attract positive ions which will deform the lattice. This deformation, which is much slower than the electron movement, will create a net positive potential area that will attract another electron. Through this mechanism, the two electrons form a cooper pair whose size is ξ or what we refer to as **the coherence length**. The size of a cooper pair is large compered to the lattice spacing and for very regular crystalline lattices, ξ can be as great at 10^{-4} cm [14].

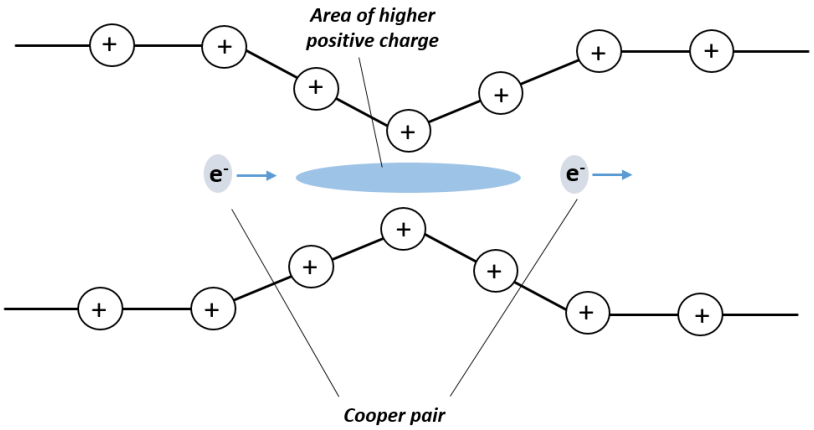

Figure 2.4: The formation of a cooper pair through a lattice-electron interaction

Once the cooper pairs are formed, since they form a boson (because their total spin is integer), many of these pairs can co-exist coherently and they form a unique ground state with a lower energy than the Fermi level. It is important to recall that the cooper pair interaction can be easily broken by thermal activation. This gives rise to one of the most important ideas in superconductivity theory which is the superconducting energy gap Δ. It represents the energy needed to bring back a superconducting electron to the normal state. It is typically in the order of 10^{-4} eV and can be expressed at T=0 K as:

$$\Delta(0) = 1.764 k_B T_c \tag{2.6}$$

with k_B is the Boltzmann constant.

The energy gap is maximum at T= 0 K and becomes zero when T reaches the critical temperature T_c.

The number of cooper pairs is also temperature dependent. Only at T= 0 K that all electrons from the conduction band form Cooper pairs. For T $>$ 0 K, Cooper

pairs dissociate by thermal activation and the density of superconducting electrons n_s decreases exponentially with the temperature.

2.2.4 Superconductor classification according to the Ginzburg-Landau theory

The transition from normal to superconducting state can occur only when the new state is energetically favorable. The thermodynamic entity of interest here is the so-called Gibbs Free energy G. Let us consider a material at its superconducting state with no applied magnetic field. The material would have a certain Gibbs free energy $G_{sup}(H = 0)$. Now, how does a magnetic field affect the energy balance ?

A magnetic field has an energy density of $\mu_0/(2H^2)$ and as a result of the Meissner effect, the magnetic field needs to be expelled from the superconductor which adds a positive energy of $\mu_0/(2H^2)$ over a distance equal to the penetration depth λ_L. Hence, the free energy per unit of volume is equal to:

$$G_{sup}(H) = G_{sup}(H = 0) + \frac{\mu_0}{2H^2} \tag{2.7}$$

Which means that the material stays in the superconducting state as long as $G_{sup}(H) < G_{normal}$. In this sense, we can express the thermodynamic critical field H_c, the field for which $G_{sup}(H_c) = G_{normal}$.

Let us consider the case of a very thin film of a given superconductor, where the thickness is lower than λ_L. Because of the fact of that the magnetic field does not have enough room to drop to zero, the magnetic flux that needs to be expelled from the superconductor is lower than what it would have been in a thicker film. In that sense, we can imagine that the critical field H_c of a very thin film of superconductors can be enhanced compared to the bulk and it can appear energetically favorable for a thick film to subdivide itself into thin normal and superconducting areas [15].

However, this subdivision requires the creation of superconducting-normal boundaries. At these boundaries, the density of cooper pairs n_c rises progressively over the coherence length ξ. This means that the creation of a boundary requires to spend a cooper-pair condensation energy over a length ξ but results in a gain of magnetic energy over a thickness λ_L.

Within the framework of their theory, Ginzburg and Landau introduced a parameter $\kappa_{GL} = \lambda_L/\xi$ that defines two types of superconductors:

- For superconductors whose $\kappa_{GL} < \frac{1}{\sqrt{2}}$, such Hg, Pb and Zn, creating normal-superconducting interfaces is not energetically favorable and as a results, they maintain their Meissner state until they reach the H_c where all the material is forced back to its normal state. These superconductors are called type I superconductors.

- For superconductors whose $\kappa_{GL} > \frac{1}{\sqrt{2}}$, such as Nb, NbTi, Nb_3Sn and NbTiN, at a given magnetic field H_{c1} , it becomes energetically favorable to create a mixed state where normal and superconducting regions coexists. They are called type II superconductors. Above a critical field H_{c2}, the material becomes fully normal.

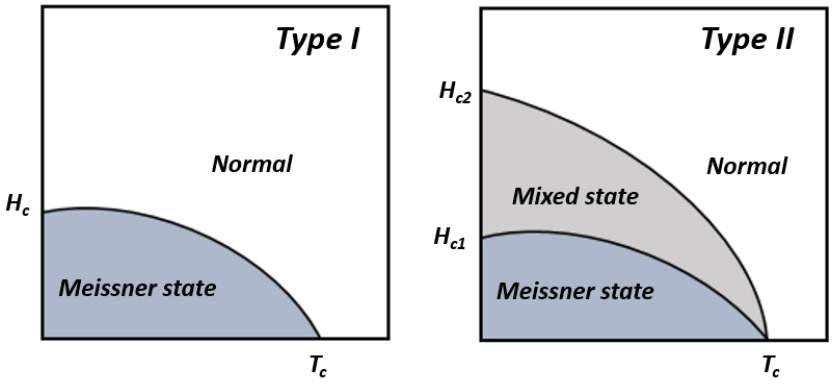

Figure 2.5: The different behaviour of type I and type II superconductors when exposed to a magnetic field

In reality, in a type II superconductor above the first critical field H_{c1}, the magnetic field penetrates the superconductors in the form of flux tubes. These flux tubes are formed by normal cores surrounded by superconducting currents. The nucleation of quantized magnetic flux tubes, also called Abrikosov vortices, enables the material to remain superconducting in high applied magnetic fields up to the upper critical field H_{c2} [16].

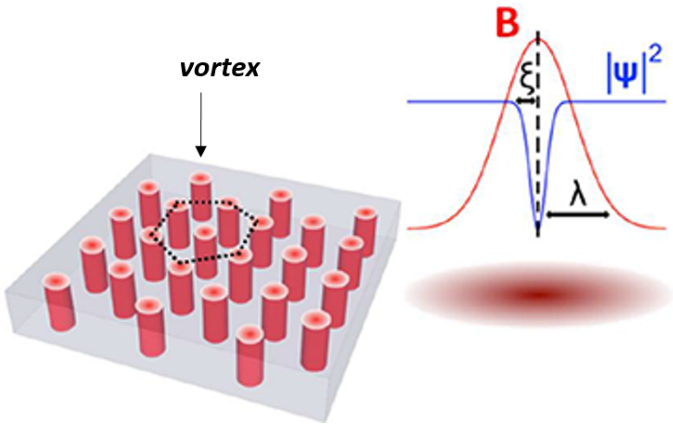

Figure 2.6: Periodic arrangement of vortices in a type-II superconductor in an external applied magnetic field. Each vortex has a normal core, where the superconducting electron density $|\Psi|^2$ (blue line) drops to zero on the scale of ξ while the magnetic field (red line) exponentially decays on the scale of λ (figure after [16])

Vortices repel each other and arranges themselves in a particular lattice arrangement that minimize the energy of the system. Since every vortex contains one elementary flux quantum Φ_0, when increasing the applied magnetic field, the number of vortices increases and they get closer to each other. When the applied field reaches H_{c2}, normal areas overlap and the superconductivity vanishes. According to Ginzburg-Landau theory, the upper critical field is equal to:

$$B_{c2} = \frac{\Phi_0}{2\pi\xi^2} \tag{2.8}$$

It is important to notice that flux lines (normal cores) experience a Lorentz force when a longitudinal currents flows through the superconductor. If set to motion, the flux lines creates a voltage and the resistance reappears. The movement of flux lines can be prevented through the presence of lattice defects via a pinning force [12]. In this sense, the DC resistance remains 0 as long as the pinning force is larger than the Lorentz force. Type II superconductors with strong pinning are well suited for high-field magnets as they allow currents flow in high magnetic fields without any dissipation [15].

2.3 Superconductivity in the radio-frequency domain

Up to now, we have been discussing superconductor's behavior when facing steady magnetic fields. Accelerating cavities are however operated in the radio-frequency range with alternating electric and magnetic fields. The superconductor behavior is quite different. While superconductors exhibit zero DC resistance, they do have small losses in the RF regime, which are critical to the good performances of resonant cavities. In the following sections, we will describe the superconductor behaviour in the RF range.

2.3.1 Surface resistance

As mentioned above, for a temperature above zero kelvin, there still remains a fraction of normal electrons that are not paired and would potentially dissipate energy if set to motion. In the DC regime, superconductors show zero dissipation because the normal electrons are short-circuited by cooper pairs but this no longer holds true in the RF regime.

In the RF regime, the time-varying magnetic field penetrates a thin surface layer and induces a time-varying electric field that causes oscillations of normal electrons as well as cooper pairs. As normal electrons move, they convey a non-zero resistance to the material. This resistance is called surface resistance and can be described by two components:

$$R_s = R_{BCS} + R_{res} \tag{2.9}$$

- R_{BCS} is a temperature and frequency dependent component. Based on the Mattis and Bardeen theory [17] that combined the anomalous skin effect and the two fluid model, R_{BCS} can be expressed as:

$$R_{BCS} = A({\lambda_L}^4, \xi, l, \sqrt{\rho_n})\frac{f^2}{T}\exp\left(-\frac{\Delta}{k_B T}\right) \tag{2.10}$$

  The pre-factor A depends on the superconducting parameters of the material such as the coherence length ξ, the electron mean free path l, the resistivity in the normal state ρ_n and the penetration depth λ_L.

- R_{res} is is not theoretically predicted by the BCS theory but have been observed experimentally. Residual resistance can find its origin in several mechanisms:

– Insufficient shielding of the earth's DC magnetic fields, which results in trapped vortices dissipating under RF.

– Chemical residues left out by chemical treatments. For instances, hydroxile groups in the oxide, sulfur, fluorine and carbon.

– Other reported causes of the residual resistance such as poor quality natives oxides, grain boundaries and interface losses.

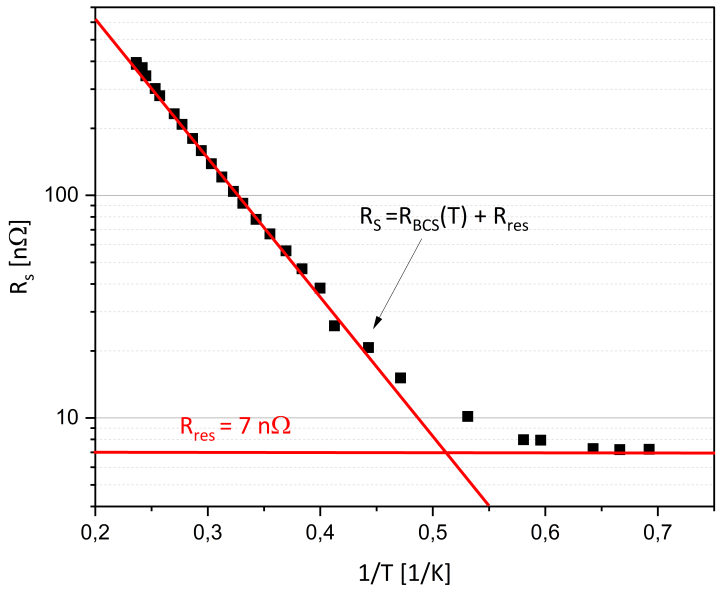

Figure 2.7: The surface resistance of niobium at 1.3 GHz

2.3.2 The radio-frequency critical field

When the field is parallel to the surface as it is the case in RF cavities, it is possible to maintain the superconductor in the Meissner state at higher fields than those predicted (H_c for type I superconductors and H_{c1} for type II superconductors). This metastable limit is called the superheating filed H_{sh} and is assumed to be the effective critical field in RF cavities. This can be explained in terms of delayed flux entry thanks to the Bean-Livingstone surface barrier [18].

Depending on the Ginzburg-Landau parameter, the superheating filed can be approximated by:

$$H_{sh} \sim \frac{0.89}{\kappa_{GL}} H_c \text{ for } \kappa_{GL} << 1 \tag{2.11}$$

$$H_{sh} \sim 1.2 H_c \text{ for } \kappa_{GL} \sim 1 \tag{2.12}$$

$$H_{sh} \sim 0.75 H_c \text{ for } \kappa_{GL} >> 1 \tag{2.13}$$

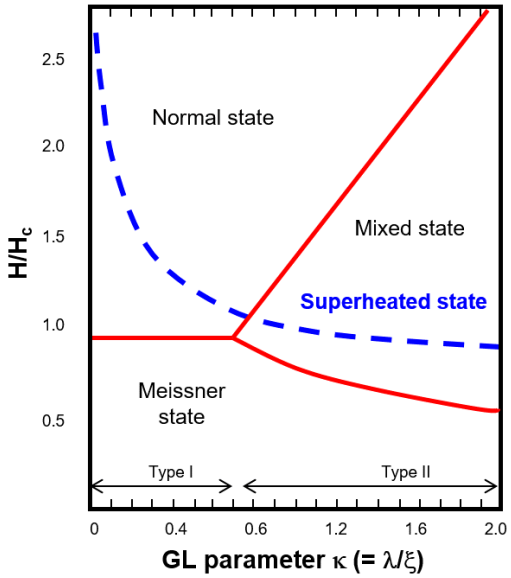

Figure 2.8: The critical field of superconductors according the κ_{GL} parameter (figure after [19])

In contrast to magnets were large upper critical field H_{c2} (10 – 20 T) are needed, SRF cavities are not limited by the upper critical field but rather by the superheating field H_{sh}. As a matter of fact, SRF cavities need to be operated in the Meissner state. Otherwise, vortices would oscillate under RF resulting in substantial energy dissipation. In order to optimize the performances of SRF cavities, several material aspects needs to be considered.

2.3.3 Niobium - the material of choice for SRF cavities

As discussed in chapter 1, the two main figures of merit of RF cavities are their quality factor Q_0 and their maximum accelerating gradient E_{max}. The quality factor of a cavity is inversely proportional to its surface resistance. The lower the surface resistance is, the higher the quality factor would be. In order to have a minimal R_{BCS} resistance (see equation 2.10), we need to maximize the gap Δ and as a result have a high T_c (since T_c is proportional to the gap Δ), we need also to have a low resistivity in the normal state ρ_n , a low mean free path l and a low penetration depth λ_L. In addition to that, we must grant a very low residual resistance R_{res} as it becomes dominant at low temperatures (SRF cavities are typically operated at 2 K).

The other critical requirement for an RF cavity is a high accelerating field E_{acc}. This implies a high RF critical field H_{sh} which is of the order of the thermodynamic critical field H_c. As H_c increases with the critical temperature T_c, optimizing cavities performances require a high T_c, a high H_c and a small κ_{GL} parameter to increase the H_{sh}.

Niobium comes with the best superconducting parameters among pure metals which made it the material of choice for SRF applications since nearly 40 years.

Other superconductors with higher T_c such as NbTiN, Nb_3Sn or MgB_2 have the potential to increase the operation temperature of RF cavities. Unfortunately, they are very sensitive to defects and do not exhibit the high performances one could expect for now. The present results obtained with these materials are not satisfactory because the difficulties inherent to their deposition onto an RF cavity geometry are not yet overcome.

Chapter 3

Breaking the frontiers of bulk niobium SRF technology

3.1 Introduction

Based on the fundamental aspects of superconductivity, the RF electromagnetic field penetrate only a few tens of nanometers in the cavity material. Therefore, coating a high thermal conductivity copper cavity with a thin superconducting layer presented an ingenious solution to combine both the high thermal conductivity of copper necessary to lower the cooling costs and the low RF losses of superconductors. The first SRF cavities were made out of lead (which is a type I superconductor) electroplated on copper. These cavities were very useful for heavy-ions accelerators and the whole understanding of SRF, but they were very soon limited by the critical magnetic field of lead (~ 80 mT). An instinctive step forward was to turn to niobium which benefits from the highest first critical field among all pure metals (~ 180 mT) and the highest T_c (9.25 K). However, the deposition of high-quality niobium on copper turned out to be much more challenging at the time and researchers started using bulk niobium as cavities material.

3.2 The long march of bulk niobium cavities

Regardless of the application, a "good" resonant cavity is a cavity that offers the highest possible accelerating field while maintaining the highest quality factor. For 1.3 GHz elliptical Nb cavities, good performances would be a quality factor of 10^{10} and an accelerating gradient higher than 40 MV/m. Despite the great potential that niobium intrinsically offers, reaching these performances needed tremendous R&D efforts from SRF laboratories all over the world. In the following sections, we will briefly introduce the main practical limitations that niobium technologies faced and the great leaps forwards in the cavity preparation that have brought bulk niobium cavities close to their intrinsic limit. A more detailed analysis can be found in reference [20].

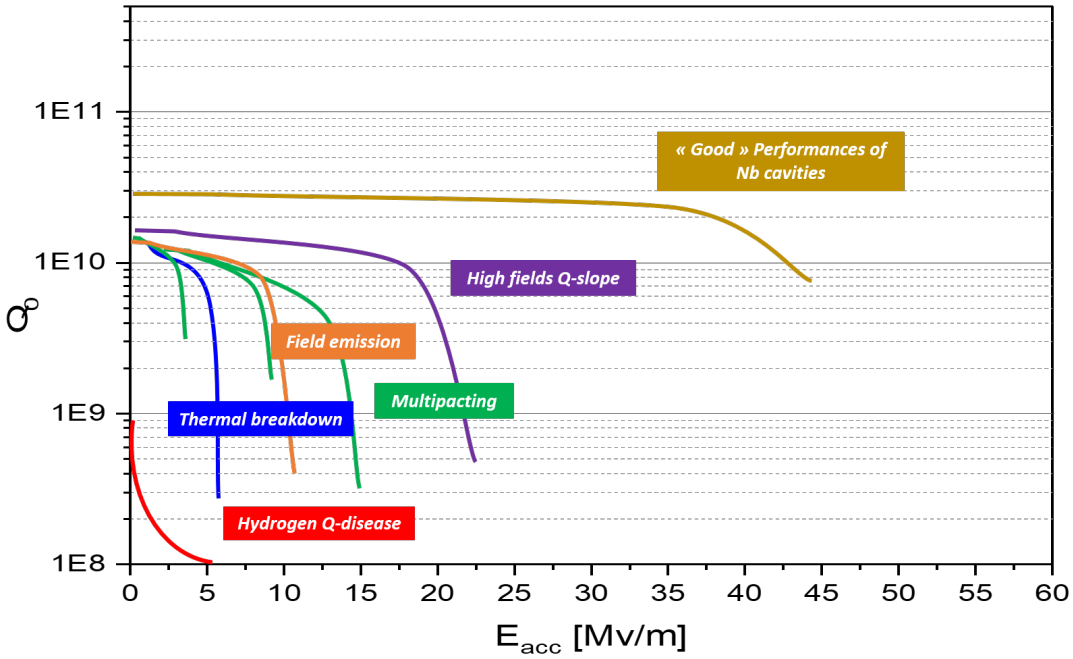

Figure 3.1: Q_0 versus E_{acc} curves illustrating the typical Q-limitations due to various phenomena compared to nowadays standard "good" performances of bulk niobium cavities after [20]

3.2.1 The hydrogen Q-disease

The hydrogen Q-disease is characterized by a sharp drop in the Quality factor of a cavity. It is an anomalous loss mechanism caused by hydrogen dissolved at the surface of niobium. This have been proven to cause the formation of metallic hybrids around 150 K that increases the cavities dissipation by two or three orders of magnitude [21]. It can be inhibited by rapidly cooling the cavity. Annealing at 800°C for 2 hours (or 650°C for 10 hours) in a vacuum better than 10^{-6} Torr can also help recrystallizing niobium and thus suppressing hydrogen trapping sites along with decreasing slightly the hydrogen concentration.

3.2.2 Multipacting

Before 1980, multipacting was the dominant issue for SRF cavities limiting accelerating gradient to few MV/m. It is a resonant electron discharge that raises exponentially the number of electrons inside the cavity. This ends up by degrading very rapidly the quality factor. Thanks to the invention of the curved-wall cavities, multipacting became less critical. Other innovative cures for multipacting can be considered. This matter will be the main object of chapter 6.

3.2.3 Thermal breakdown

Even when multipacting was avoided, accelerating gradient only rose to about 4-6 MV/m due to thermal breakdown of superconductivity [20]. The established model

of thermal breakdown or "quench[1]" specifies that heat originates from high-RF loss regions around defects (also called hot spots). Heat generated can spreads out and bring the temperature of good superconducting regions higher than the critical temperature thus causing the cavity to quench. For this reason, a high thermal conductivity is a crucial for an SRF cavity. The higher the thermal conductivity of the cavity walls is, the better the heat will be evacuated from these dissipating regions and the easier is it to avoid the thermal breakdown. Unfortunately, superconductors are intrinsically bad thermal conductors: this originates from the simple fact that at a temperature below T_c, a large fraction of conduction electrons are paired into cooper pairs and thus can not take part in the heat transfer. This problem has been partially circumvented by using very pure niobium.

As discussed in chapter 1, impurities in the lattice are scattering centers for conduction electrons and thus limit the thermal conductivity of a metal. The purity of a metal have been commonly characterized by its residual resistivity ratio or triple R (RRR), which is expressed as the ratio of the electrical resistivity at 295 K to the resistivity at 0 K. As a rule of the thumb, the thermal conductivity of niobium at 4.2 K is roughly equal to RRR/4 [22]. For SRF standards, a RRR of at least 200 is needed. High purity niobium ingots can be obtained by multiple electron beam melting under vacuum. These ingots are then rolled and transformed into sheets, which are formed to make half-cells and the beam tubes. To finally fabricate a whole cavity, the half-cells and the beam tubes are welded under vacuum using an electron beam. The mastering of the electron beam welding plays also a major role in the manufacturing of niobium cavities. As a matter of fact, niobium is a getter material and can be easily contaminated with light element such as hydrogen, oxygen, carbon and nitrogen when heated under poor vacuum conditions.

Another crucial step in the cavity process is the chemical etching. It consists in removing 100 to 200 µm of the damaged layer. Several surface treatments such as buffered chemical polishing (BCP), electro-polishing (EP) and centrifugal barrel polishing (CBP) have been studied to remove the surface damaged layer (100-150 µm) and improve the surface rugosity.

3.2.4 Field emission

With higher purity niobium cavities, average accelerating gradient E_{acc} reached 10 MV/m. At these gradients, field emission became the major limitation. Field emission is an emission of electrons from a metal surface when subjected to high electric fields. Electrons start to tunnel out of the cavity walls when exposed to high electric fields and get accelerated themselves. This results in X-ray production, heat generation and large RF dissipation. Nonetheless, in cavities where fields are of some MV/m, the field emission observed was several orders of magnitude higher then predicted by Fowler-Nordhiem model [23]. Intensive DC and RF studies have shown that particle contamination is the main cause of this effect. In particular, dust particles whose sharp and fractal geometry results in a local enhancement of the electric field [24]. To avoid contamination, cavities are cleaned and assembled in particulate-free environments called clean rooms. A very important step of the cavity

[1] turn back to the normal state.

preparation process was also added which is the high pressure rinsing (HPR). It has been proven that a 100 bar jet of ultra pure water drastically reduce the number of particulate stuck on the RF surface [25] which pushed further the achievable gradient to around 20 MV/m.

3.2.5 High field Q-slope - HFQS

Above 20-25 MV/m , a new phenomenon called the high field Q-slope (HFQS) became the major "headache" for SRF performances. The origins of the “high field Q-slope” are far from being settled. Nonetheless, the SRF community succeeded in finding an empirical cure for it. Two steps became essential in the preparation recipe niobium cavities: preparing a very smooth RF surface by electro-polishing and baking the cavity at 120°C during 48 hours that have been initially discovered at CEA.

- At the times where the HFQS started to raise concerns in the SRF community, the dominant method of chemical etching used in niobium cavity preparation was buffered chemical polishing BCP. This is mainly due to the fact that BCP can easily implemented by immersing the cavity in an acid mixture bath. However, researchers from KEK proved that electropolishing (EP) is by far more beneficial to cavity performances [26]. A possible explanation is that by using EP which is well known for producing smoother grain boundary steps than BCP, one could avoid the local enhancement of magnetic field at these steps.

- A second key step in avoiding the HFQS is the baking step at 120°C in ultra-high vacuum for 24 to 48 hours. This step has been proven to remove reliably the high field Q-slope. The microscopic origins of these improvements is not fully understood but it have been suggested that the mild baking changes the impurity concentration profile within the first 10 nm of the surface. It is believed that oxygen diffusion prevent the formation of hybrides and hence increases the critical field.

3.3 Breaking the frontiers of bulk niobium

Bulk niobium cavities are the backbone of modern superconducting accelerators. Thanks to several decades of research efforts, they provide today reliably exceptional performances with accelerating gradient up to 40 MV/m. Recent cavities nonetheless seem to reach the material’s ultimate limits which means that it have become crucial to break the bulk Niobium’s monopoly and find new ways to reach even higher performances to meet the next generation of particle accelerators needs. In the following sections, we will introduce briefly the most promising routes for future SRF cavities.

3.3.1 Thin film on copper

Since the superconducting currents are carried out through thickness of typically 10 to 20 λ ($\sim$ 500 nm), we theoretically need only few microns of a superconductor to operate an SRF cavity. This fact motivated Benvenuti at CERN in the 1980s to develop the Nb/Cu technology by sputtering few microns of Nb into a copper cavity. This technology has been successfully implemented in the past in several accelerators such as the "Large Hadron Collider" LHC [27] and "Large Electron-Positron collider" LEP-II with an operating temperature of 4 K. It offers several advantages among which: the lower cost (in particular for large cavities whose frequency is lower than 400 MHz), the reduced sensitivity to the earth's magnetic field and an increased thermal stability thanks to the high thermal conductivity of copper. Recent Nb/Cu cavities at CERN [28] showed improved accelerating gradient up to 20 MV/m and high quality factors (3- 4 10^{10}) which makes them very promising for application in next generation circular colliders such as the "Future Circular Collider" FCC. Nonetheless, limitations due to defects such as inclusions and thermo-currents at the interface between niobium and copper still need to be overcome.

Another promising thin film on copper candidate is the Nb_3Sn. Thanks to its high superconducting temperature (T_c= 18 K), Nb_3Sn have the potential to increase the operating temperature of SRF cavities from 2 to 4 K (which can significantly decrease the operations costs). The proof of principle of this technology is already established on niobium cavities [29] but further research efforts are needed to overcome the gradient limitation observed [30].

3.3.2 Doped bulk niobium cavities

During the last decades, a new approach for improving the SRF cavity performances emerged: It consists in doping bulk niobium cavities with non-magnetic impurities such as N and Ti which resulted in an exceptional enhancement of the Q_0. Soon after its fortuitous discovery in 2013 [31], efforts where focused into the optimization of this process and its eventual application in a superconducting linear collider. Nitrogen doping showed unprecedented values of quality factors but limited to gradients of 25 MV/m. A variation of N doping called N-infusion was recently suggested [32]. This method achieved not only high Q_0 but also high gradients up to 45 MV/m. These approaches along with a novel doping route for enhancing RF cavities performances will be thoroughly discussed in chapter 9.

3.3.3 The multilayer theory

An original approach have been proposed by Alex Gurevich suggesting that coating an SRF cavity with a multilayer of thin superconducting (S) and insulating (I) material (also refereed to as SIS structure) would increase significantly both the quality factor and the accelerating gradient [1]. This structure would allow to take advantage of high T_c superconductors such as NbN, NbTiN and Nb_3Sn without being restricted with their limited H_{c1} (20 mT, 30 mT and 40 mT respectively).

According to Gurevish theory, the superconducting layer (S) whose thickness must be lower than the penetration depth λ_L would bring down the surface magnetic

field to a level that bulk niobium could withstand. In this way, we can artificially increase the critical field of niobium which can therefore remain superconducting at much higher accelerating gradients. The insulating layer (I) plays a key role in protection against vortex penetration avalanche. It will intercept the propagating vortex and restrains the dissipation in the superconducting layer.

The quality factor of the cavity would also benefit from such a structure as high T_c superconductors benefit from a lower BCS resistance. Up to now, encouraging results have been obtained on flat samples and quadrupole resonators using several high T_c superconductors such NbTiN, Nb_3Sn and NbN [33, 34]. However, this approach has never been tested on an accelerating cavity which is mainly due to technological limitations. Due to the complex shape of RF cavities and the stringent requirement in term of thin film homogeneity, we decided to explore the use of atomic layer deposition to synthesize this multilayer. Chapters 7 and 8 of this thesis will be dedicated to testing this approach into a 1.3 GHz niobium cavity.

Chapter 4

Atomic layer deposition for SRF cavities

4.1 Introduction

During the last decades, atomic layer deposition (ALD) have gained in maturity and completely shifted from a pure R&D technology to industrial applications in particular in semiconductors and photovoltaic cell industry. Thanks to its excellent uniformity and its sub-nanometer thickness control, ALD presents an undeniable advantage over all physical vapor deposition techniques. Nonetheless, it remains a niche application in SRF. The use of ALD in SRF technology was pioneered by Proslier et al [35, 36, 37]. Nowadays, more SRF research groups seem to be convinced by its potential and are actively working on implementing it to improve SRF cavity performances.[1] This chapter aims at introducing the principle of atomic layer deposition and describing our ALD systems at CEA-Saclay that i participated actively in their construction, commissioning and maintenance. A more detailed description of ALD and its different applications can be found in [38, 39].

4.2 Overview

Atomic layer deposition was first developed in Finland in the mid-1970s by Dr Tuomo Suntola and his co-workers to meet the needs of thin electroluminescent film production for flat panel displays. Dr Tuomo had the idea of depositing ZnS, layer by layer, starting with the elemental precursor Zn and S in order to have a very precise control of thickness over a large surface [40]. In its early history, this technique was called "Atomic layer Epitaxy" or (ALE) due to the epitaxial growth feature. Then, in the early 2000s, "Atomic layer deposition" took over ALE and was used to refer to the deposition layer by layer of thin films in the thickness range of $1 \sim 100$ nm.

Although physical vapour deposition PVD and chemical vapour deposition CVD techniques are still the most common deposition techniques, the increasing demand in miniaturization and growth control in terms of thickness, uniformity and confor-

[1] More details about these results will be discussed in the following chapters.

mality became very challenging to meet with PVD and CVD. ALD, on the other hand, has the unique capability among other deposition techniques, to coat substrates with complex geometries with a high conformality and a thickness control up to the sub-nanometer scale [39]. It became the technique of choice for microelectronics, nano-patterning and the fabrication of nano-structures such as nanoparticles and nanotubes for biomaterials and photovoltaics. For demonstration purposes, using our research-scale ALD-system, we performed the deposition of 10 nm of molybdenum nitride MoN on a capillary tubes sample with an aspect ratio of 1/20. Using scanning electron microscopy, the film was inspected and it was found to be uniform throughout the structure (see figure 4.1).

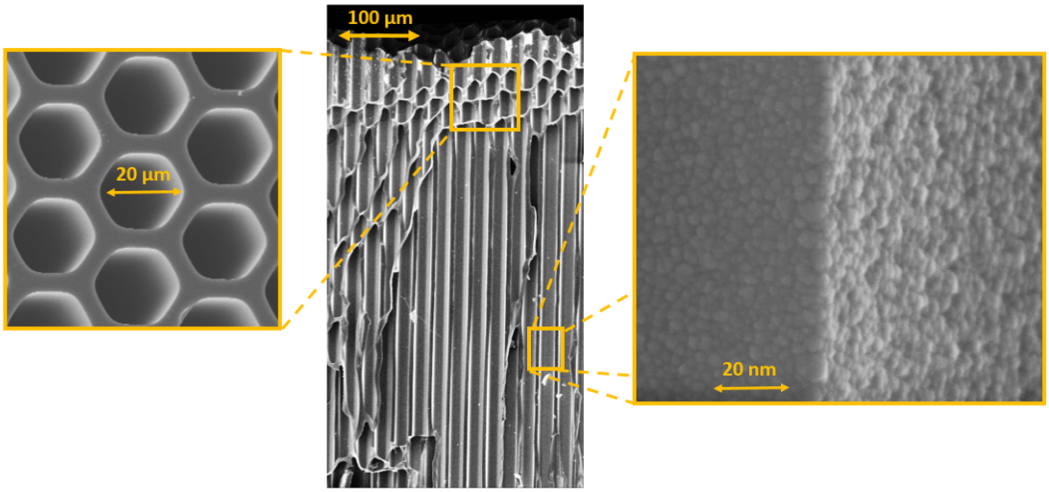

Figure 4.1: Scanning electron microscopy (SEM) image of a section of MoN coated capillary tubes deposited using our research-scale setup

Throughout the years, different variations of ALD have been developed such as plasma-enhanced ALD[2], photo-assisted ALD[3] or spatial ALD[4]. Simultaneously, a wide range of materials has been successfully deposited: ALD is intrinsically best suited for multi-component materials deposition (binary, ternary and quaternary). As a matter of fact, the majority of ALD processes consists in depositing binary compound with metal and non-metal compounds such as oxides (mainly because of the thermodynamic stability of the Metal-Oxygen bond), nitrides, carbides, sulfides, chalcogenides and pnictides. Nevertheless, singles-elements have been also deposited by ALD such as Cu, Ru, Pd, Pt, W and Mo [41]. Figure 4.2 gives an overview of the different alloys that can be grown using ALD.

Most of the ALD processes are based on using inert carrier gas such as nitrogen or argon at about 1 mbar. Deposition temperatures varies from room temperature

[2]Plasma enhanced ALD or PE-ALD uses the high reactivity of the plasma species to reduce the temperature of molecular vaporization without compromising the coating quality.

[3]Photo-assisted ALD uses Ultra-violet (UV) light to initiate and accelerate the surface reactions on the substrate which allows reducing the process temperature. The wavelength, the intensity and the illumination time of the UV light are used to control and tune the surface reaction.

[4]In spatial ALD, the precursor's exposure occurs at different positions using different reaction zones separated by purging areas. To do so, either the substrate or the deposition head moves.

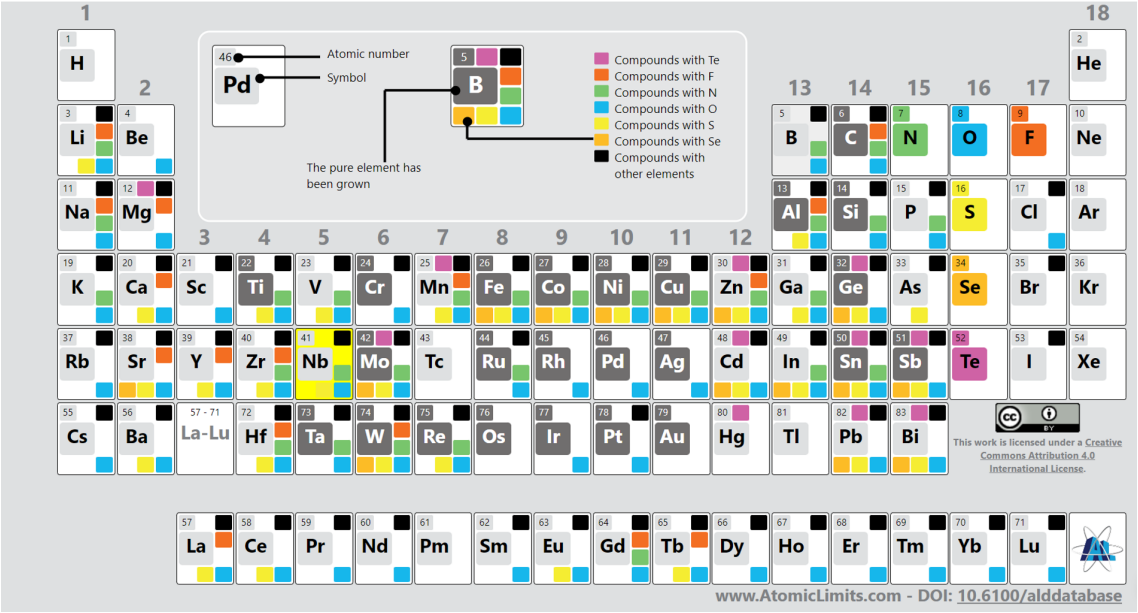

Figure 4.2: An overview of materials grown with ALD (figure after [41])

to over 500°C but the majority of ALD processes are operated between 100°C and 400°C. These relatively low temperatures offer the possibility of working on soft substrates such as organic and biological samples.

4.3 Basics

Atomic layer deposition (ALD) is a vapor phase deposition technique based on sequential, self-saturating gas-surface reactions. Two or more chemical precursors are introduced to the surface separately, one at a time, following a cycle. An ALD cycle is composed typically of four steps:

1. Pulse of precursor 1, enabling the first gas-surface reaction.
2. Purge of precursor 1, enabling the evacuation of the excess of the precursor 1 and the reaction products of the first gas-surface reaction.
3. Pulse of precursor 2, enabling the second gas-surface reaction.
4. Purge of precursor 2, enabling the evacuation of the excess of precursor 2 and the products of the gas-solid reaction.

Therefore, after each pulse, one monolayer of precursor reacts with the surface and after each cycle, a monolayer of about 1 Å of the desired material is grown, which guarantees a film thickness control on atomic level. ALD is a sub-set of CVD (chemical vapor deposition). The key difference is that in ALD, the precursors only react with the reactive sites on the surface and the purging time is optimized to make sure that different precursors never meet in the deposition chamber. Consequently, the film is constrained to follow perfectly the geometry of the surface regardless of its roughness or defects. This grants ALD its exceptional conformality.

4.4 Example: the ALD deposition of niobium nitride

An example of an ALD process of niobium nitride is described in figure 4.3. To deposit niobium nitride, we used $NbCl_5$ and NH_3 as precursors and heated the substrate at 450°C. Initially, the surface is filled with reactive sites, basically O-H terminated sites (figure 4.3 -a). First, we pulse the first precursor $NbCl_5$ (figure 4.3 -b). It will react with these reactive sites forming a first monolayer of $NbCl_x$ molecules on the surface and produces HCl as a by-product (figure 4.3 -c). Then, the system is purged for few seconds to evacuate HCl and any excess of $NbCl_5$ (figure 4.3 -d). NH_3 is then pulsed into the system, which will react with the $NbCl_x$ molecules releasing also HCl. A second purge is performed to remove HCl and any excess of NH_3 (figure 4.3 -e). The new surface is now composed of N-H reactive site that can react with the following $NbCl_5$ pulse.

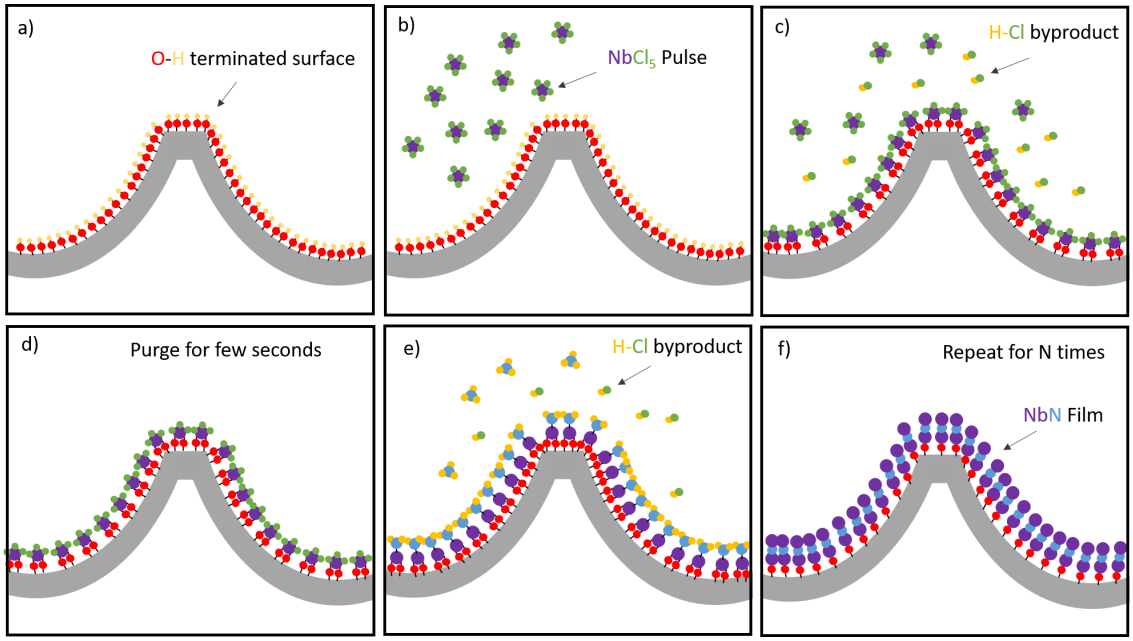

Figure 4.3: Schematic description of a niobium nitride ALD cycle

One major criterion of this technique is that the surface reactions are self-limiting which means that at each pulse, the precursors will react with the surface until there are no more active sites available and will not react with itself. Once all the surface of the substrate is covered, the reaction stops. The reaction of the first precursor provides the active sites for the second precursor and so on until the desired material is obtained. For instance, in the example of NbN , $NbCl_x$ present on the surface provides reactive sites for the NH_3 reaction.

Another Key element in atomic layer deposition is the surface saturation: The pulse time (t-pulse), or in other terms, the amount of injected precursors, have to be sufficient to fill all the surface reactive sites. Usually the growth rate per cycle (GPC) increases when increasing the t-pulse until it becomes independent when the surface reaches saturation. It is straightforward to notice that only irreversible and

saturated reactions automatically lead to the same amount of material adsorbed regardless of the amount of the precursors available [38]. Once t-pulse is long enough to reach surface saturation, any excess of precursor will not increase the GPC provided adequate purge times. T-purges should be long enough to ensure the good evacuation of excess precursors and byproducts. As shown in figure 4.4, usually the GPC increases when increasing the t-pulse until it becomes independent when the surface reaches saturation. On the other hand, lower purge times can give higher GPC because the two precursors coexist in the ALD chamber therefore a CVD component take place.

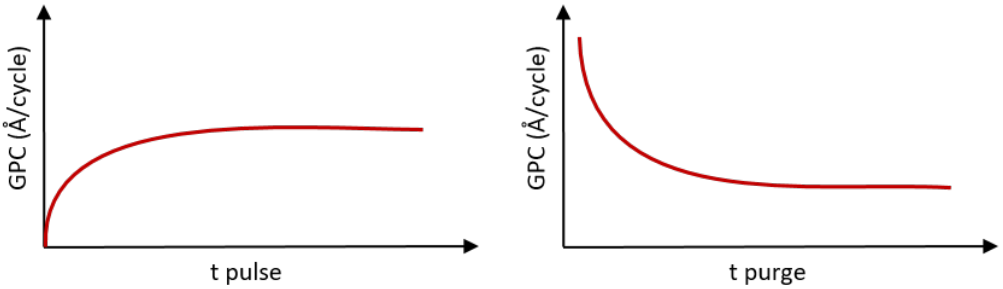

Figure 4.4: The influence of t-pulse and t-purge on the GPC in ALD

4.4.1 ALD temperature dependence

Temperature is a key parameter in the ALD process. We call "ALD window" the temperature range where the growth per cycle (GPC) is constant and is only dependent of the reactive sites density present on the surface and the surface saturation by the precursor's chemical reactions. Outside this temperature window, several physical and chemical phenomena can disturb the ALD behavior and influence the growth rate per cycle (as presented in figure 4.5)

- At lower temperatures, the GPC can either increase due the precursor's condensation or decrease due to a low reactivity of the precursors with the surface sites.
- At higher temperature, the precursors can decompose before reaching the surface leading to a CVD component and an increase of the GPC. In some cases, we can also witness a decrease of the GPC instead, if the deposited film get desorbed or etched.

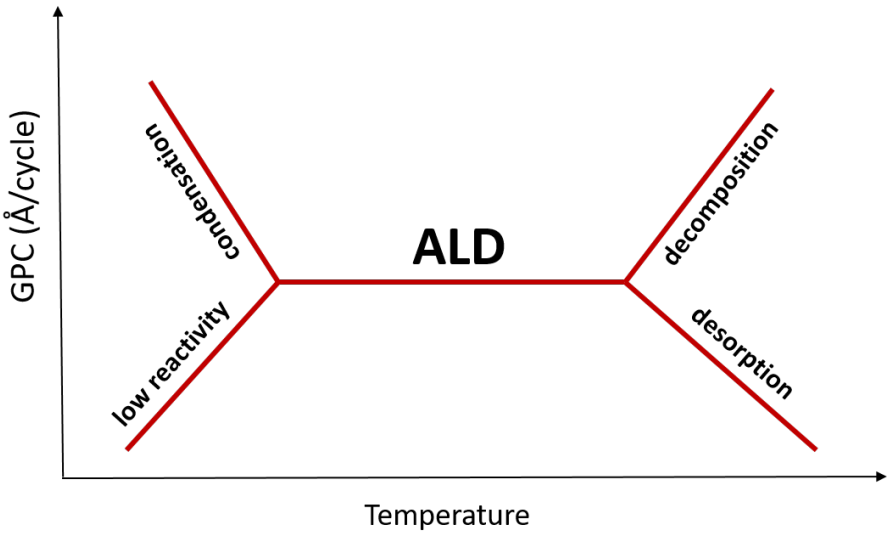

Figure 4.5: Atomic layer deposition temperature window

4.4.2 ALD Precursors

ALD precursors should meet several requirements to ensure a proper ALD growth, they must:

- be gaseous or vaporizable at a temperature lower than the growth temperature [38].
- have a good thermal stability i.e a sufficiently high decomposition temperature to prevent their deterioration neither at the vaporization temperature nor at the ALD growth temperature.
- have a reasonably high vapor pressure in order to allow the saturation of the reactive surface.
- have a high reactivity towards the surface groups in a self-limiting, irreversible manner. Their by-products should be gaseous, inert and should not contaminate the film.
- have a low toxicity, low cost, high purity and preferentially easy to synthesize and to handle.

The list of criteria is long and therefore, not many available precursors can fulfill these requirements. Sometimes, compromises are made regarding the reactivity and corrosiveness of the by-products [38].

In the scope of this thesis, we deposited by ALD several materials, mainly oxides and nitrides using standard ALD recipes, the following tables summarizes the chemical precursors and the ALD recipes we used[5].

[5]Organometalic and chloride precursors were purchased in high purity grade from STREM chemicals,Inc or Sigma-Aldrich Chimie Sarl (depending on the availability), Ammonia was purchased from Air liquide.

Table 4.1: ALD parameters of oxide films

Film	Precursor 1	Precursor 2	Growth temperature	(Pulse 1–Purge 1-Pulse 2-Purge 2)
Al_2O_3	TMA	H_2O	250°C	1 s-15 s-1 s-15 s
Y_2O_3	$Y(MeCp)_3$	H_2O	250°C	1 s-15 s-1 s-15 s
MgO	$Mg(MeCp)_3$	H_2O	250°C	1 s-15 s-1 s-15 s

Table 4.2: ALD parameters for nitride films

Film	Precursor 1	Precursor 2	Growth temperature	(Pulse 1–Purge 1-Pulse 2-Purge 2)
TiN	$TiCl_4$	NH_3	450°C	2.5 s-10 s-0.5 s-10 s
NbN	$NbCl_5$	NH_3	450°C	1 s-10 s-0.5 s-10 s
ZrN	$ZrCl_4$	NH_3	450°C	1 s-10 s-0.5 s-10 s
AlN	$AlCl_3$	NH_3	450°C	1.5 s-15 s-0.5 s-15 s
MoN	$MoCl_5$	NH_3	450°C	1 s-15 s-0.5 s-15 s

4.4.3 Nucleation and substrate effect

The substrate has a great influence on the ALD growth as it determines how the nucleation starts. The substrate can also determine whether the film grows amorphous or crystalline, its grain sizes and in some cases its crystalline orientation. Appropriate adsorption sites are crucial for growth to start. If there are none, no growth occurs. The way the deposited atoms gets arranged on the surface during ALD growth is defined by the growth mode. In ALD, different growth modes are possible:

- we can observe a **two-dimensional growth** where the deposited material settles preferentially in the lowest unfilled material layer until covering completely the substrate.
- We can observe an **island growth** where the material gets deposited preferentially on the ALD-grown material forming islands that grows progressively until they coalesce to form a continuous film.
- We can also observe a **random deposition** where the material gets deposited with an equal probability on all surface sites [39].

The growth rate per cycle (GPC) does not need to be constant during the first cycles or tens of cycles of ALD. As the ALD process alters the chemical composition of the surface through material deposition, the GPC should be expected to vary with the increasing number of cycles. This variation in the beginning of the growth reveals details of the substrate–reactant interaction. ALD processes can be divided into four groups depending on how the GPC varies with the number of ALD cycles as shown in figure 4.6 :

- Linear growth when the GPC is constant since the start of the ALD process.
- Substrate-enhanced growth where the GPC is higher at the beginning of the ALD process than reaches a steady value. This can occur when the number of reactive sites is higher on the substrate than on the ALD-grown film.

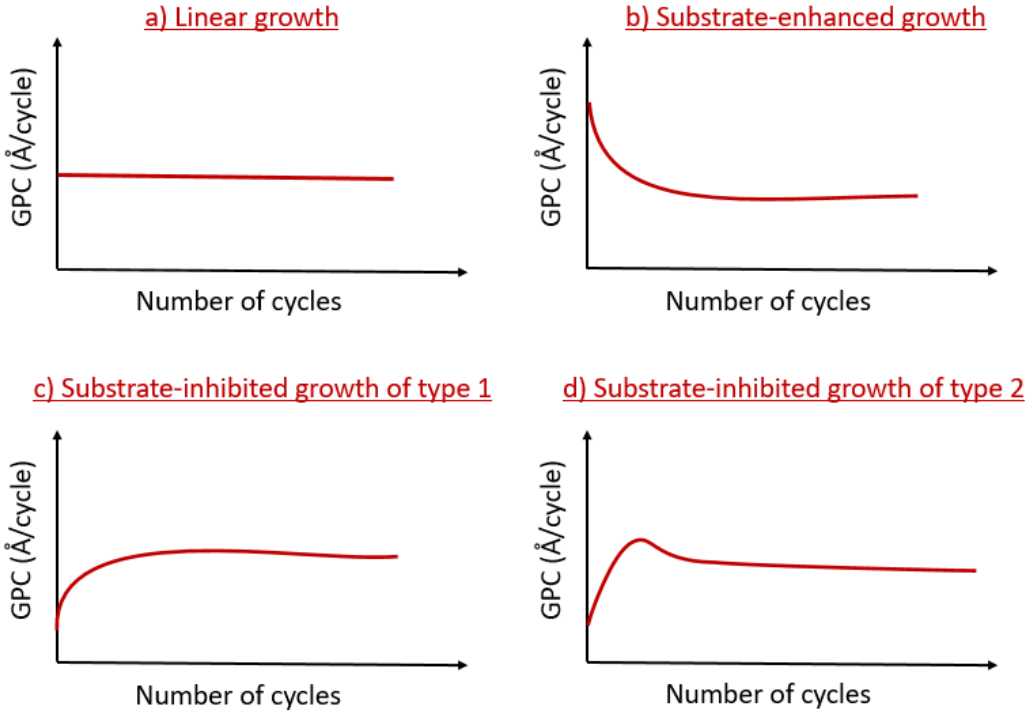

Figure 4.6: Influence of the number of ALD cycles on the GPC (figure after [42])

- Substrate-inhibited growth of type 1 and type 2 when the GPC is lower at the beginning of the ALD process than reaches a steady value. This can occur when the number of reactive sites is lower on the substrate than on the ALD-grown film. In the substrate-inhibited growth of type 2, the GPC can reach a maximum before settling to a lower constant value [42].

Determining a relationship between the behaviour of the GPC during the first cycles and the growth modes would be attractive. However, experimental investigations do not underline the existence of such a relationship except for the substrate-inhibited growth of type 2 which seems to corraspond to an island growth mode [39].

4.5 ALD deposition systems at CEA-Saclay

4.5.1 Research-scale ALD system

Most of ALD films studied in this thesis were deposited using our homemade research-scale thermal ALD reactors . Typically, an ALD reactor is composed of four important elements: a deposition chamber, a heating system, an injection source for precursors and a pumping system. As it can be seen in figure 4.7, to perform the deposition of the previously described ALD recipe of NbN, we would need two precursors injection lines (one for each chemical species). These lines must be connected to the carrier gas source. At each pulse, the corresponding gas-switching valve is opened to allow the precursor to be transported to the deposition chamber.

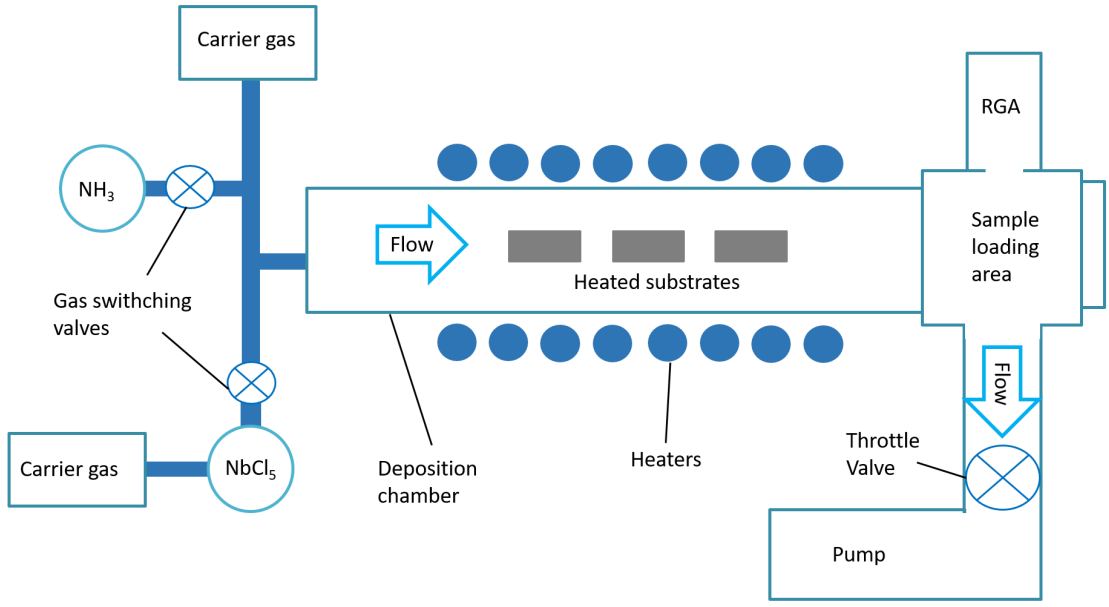

Figure 4.7: Simplified representation of our research-scale atomic layer deposition system

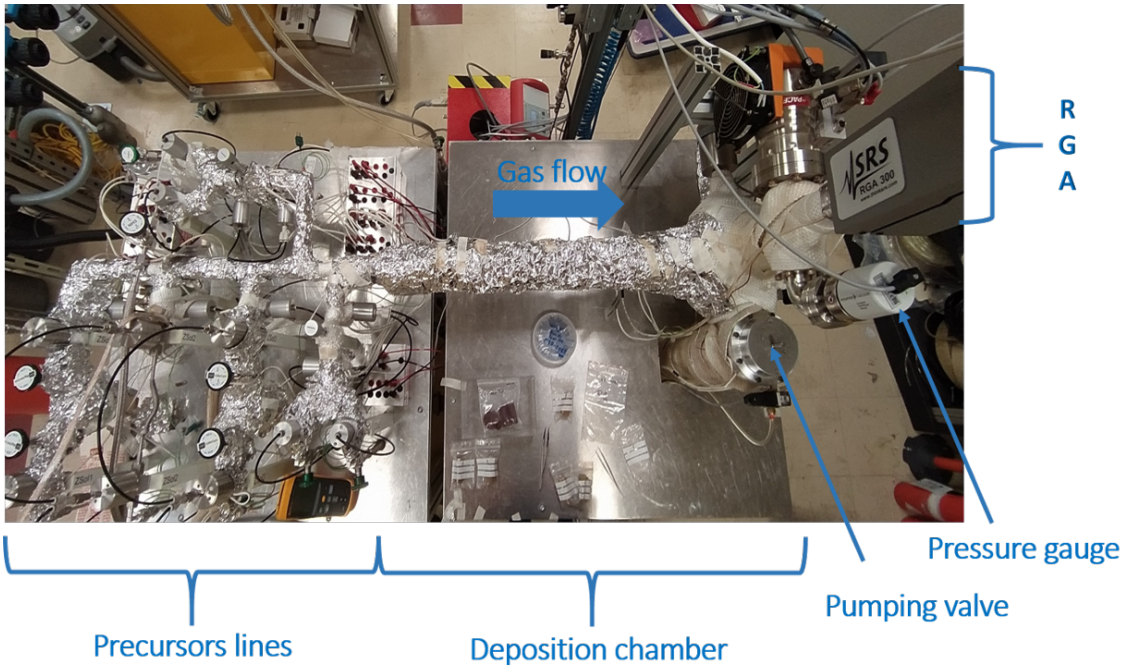

Figure 4.8: Picture of the research-scale ALD system

Transport Gas

A constant flow of ultrahigh-purity nitrogen or argon (UHP, 99.999 %) was used to transport precursors to the substrate. During the growth, we used 50 sccm per channel, so a total of 300 sccm for 6 channels that correspond to a pressure of $\sim$ 1 mbar. The system was equipped with two oil pumps (one connected to the

deposition chamber through a throttle valve, and the second one connected to the precursors lines). An inert gas purifier was also used to further purify the transport gas by limiting the H_2, CO, and CO_2 levels to less than 1 ppb and O_2 and H_2O to less than 1 ppt. The pressure inside the reactor where monitored using two pressure gauges.

The deposition chamber

The deposition chamber is a 75 cm long stainless steel tube with a 5 cm diameter. Samples can be loaded and unloaded into the deposition chamber through a loading door (see figure 4.9). The reactor temperature was maintained between 60°C and 450°C by an external computer-monitored resistive heater system. To control and monitor the temperature along the system, several K-type thermocouples were placed along the length of the flow tube.

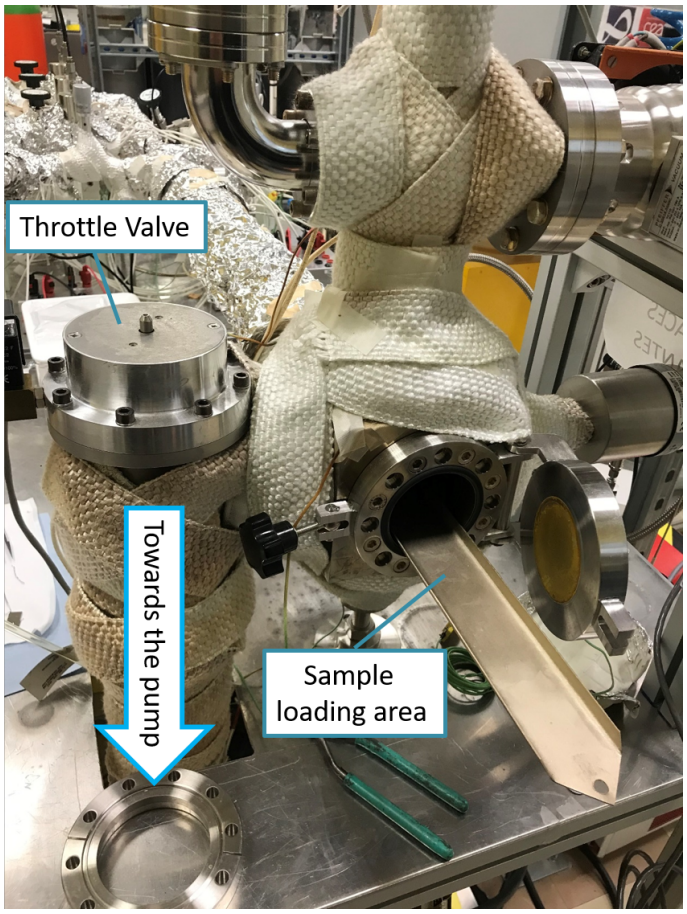

Figure 4.9: Picture of the sample loading area of the research-scale ALD system

Control and monitoring system

The ALD system was fully controlled with a home-made Labview program. The program enables the monitoring of temperature, gas flow and valves states along the system using electronic modules. The program also monitors the ALD recipes

and allows overnight depositions as well as the time evolution of the chamber gas composition via a connection to the Residual Gas analyzer (RGA). (see figure 4.10 and 4.11). As RGA requires a high vacuum environment to properly works, a 30 µm pin hole separate the reaction chamber and the RGA chamber that is pumped with a small turbo and dry pumps. During growth the RGA chamber is $\sim 2.10^{-7}$ mbar. The signal measured on the RGA for different species is therefore not an absolute quantification of the total number of molecules present in the reaction chamber but can rather be used in a comparative and relative manner.

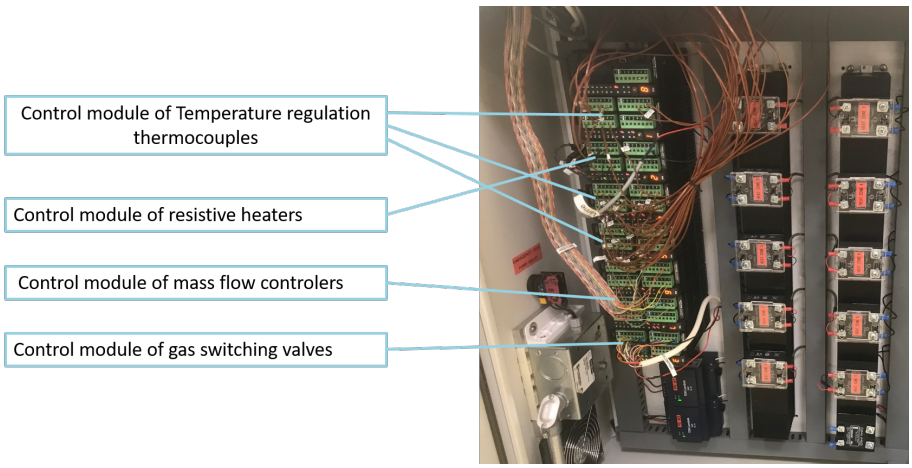

Figure 4.10: Picture of the electronic modules of the research-scale ALD system

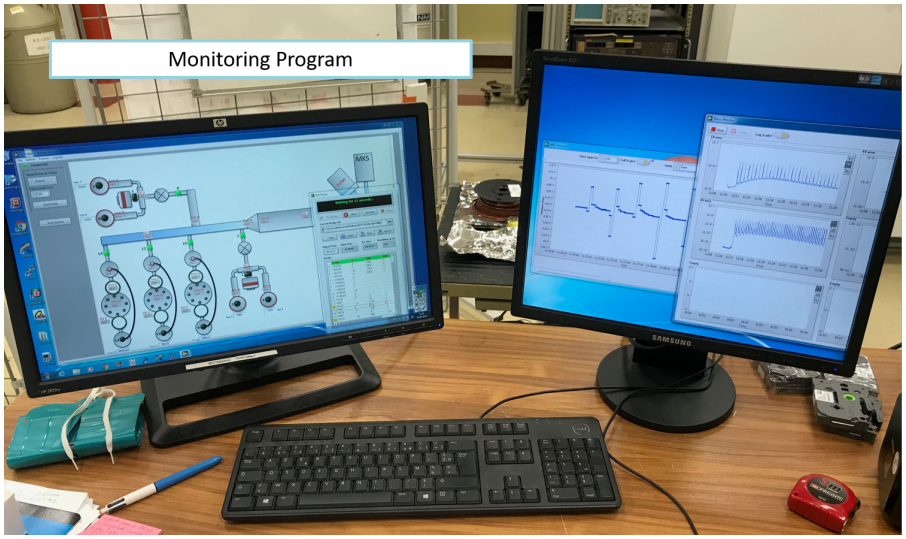

Figure 4.11: Picture of the monitoring program of the research-scale ALD system

Precursor storage and injection

The system has 7 precursors lines (2 gases, 2 liquids, 3 solids). As seen previously, ALD precursors need to be gaseous when pulsed into the deposition chamber. For solid precursors, we used specially designed bubblers to store and inject them. A

bubbler is a metallic container that we initially filled with the solid precursor (see figure 4.12) using our glove box to prevent any contamination or reaction with ambient air. It is then connected to the ALD system through valves and covered with thermocouples, resistive heaters and thermal isolation. During the pulse of a solid precursor, the inert carrier gas is forced to flow through the bubbler in order to optimize the amount of molecule transported to the reaction chamber.

An hour before launching the ALD deposition, we heated the solid precursors such as $NbCl_5$, $ZrCl_4$ and $AlCl_3$ at 110°C to generate enough vapor to be then transported into the system by the carrier gas. Care should be taken to not heat the precursors too high as sintering can occur and reduce the effective surface area and hence the number of gas phase molecules injected in the reactor. Liquid and gaseous precursors have sufficiently high saturation vapour pressure, therefore they were not heated prior to the deposition.

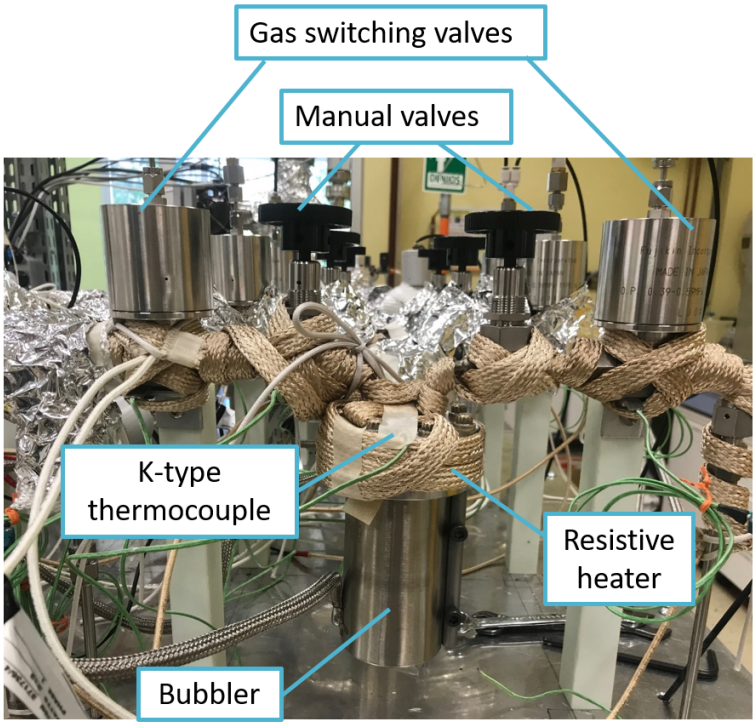

Figure 4.12: Picture of a bubbler connected to the ALD system (the bubbler is partially covered with resistive heaters)

Initial testing of the ALD system consisted in measuring the film thickness and its uniformity on samples located along the chamber. For all the materials studied the GPC were conformed with literature values and uniformity was below 5%.

Cavity coating

Using our research-scale ALD system, we were able to perform successfully cavity coating up to temperatures of 250°C (mainly oxide film coating). The deposition chamber tube was replaced with the cavity itself which was then covered by resistive

heaters and thermal isolation (see figure 4.13). When we tested the deposition of titanium nitride at 450°C using this procedure, we noticed that the cavity external walls were damaged (due to heating/oxidation under ambient atmosphere) (see figure 4.14) which can potentially deteriorate the RF performances of Nb cavities. In order to overcome this hurdle, we constructed a cavity-dedicated ALD system.

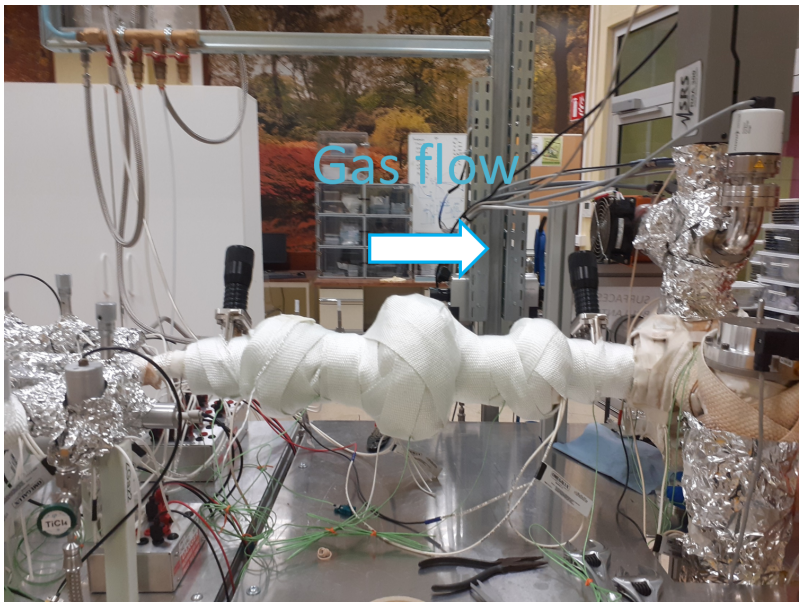

Figure 4.13: Picture of a 1.3 GHz cavity installed onto the ALD system

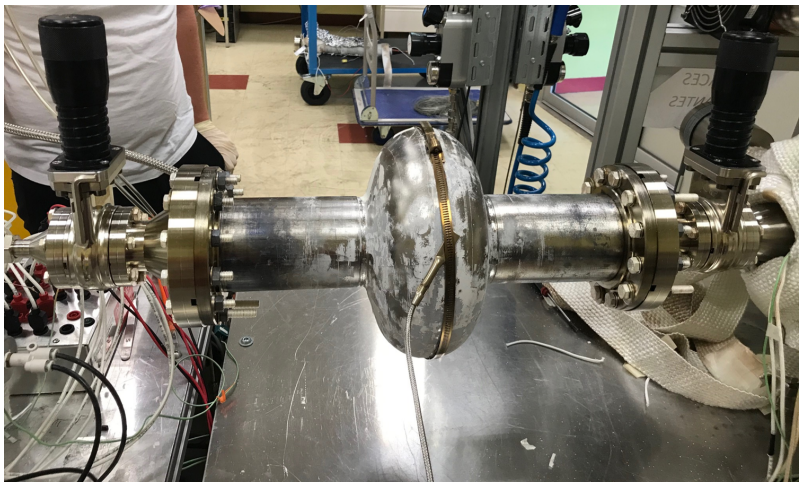

Figure 4.14: Picture of 1.3 GHz niobium cavity damaged by ambient heating to 450°C

4.5.2 ALD system for cavity coating

We build a sophisticated ALD system equipped with custom-made high vacuum oven (as shown in figure 4.15). It enables cavity coating under controlled atmosphere. The oven can reach 650°C under 10^{-6} mbar of vacuum or inert gases and 900°C once filled with 1 bar of N_2. The retort is 110 cm long and has a diameter of 49 cm (

as it can be seen in figure 4.16), which enables coating on a large variety of objects and cavity shapes such as 1.3 GHz and 0.7 GHz cavities (see figure 4.17).

- The systems has 9 precursors lines (2 gases, 2 liquids, 4 solids, 1 Ultra-high temperature)
- Monitoring have been ensured through a custom made Labview program.
- The system is equipped with a residual gas analyser (RGA) to monitor the chemical reaction inside the chamber.

By the end of this research project, the system have been successfully mounted and commissioned and we could use it to coat three 1.3 GHz niobium cavities. Results of these experiments will be discussed throughout the following chapters of this thesis.

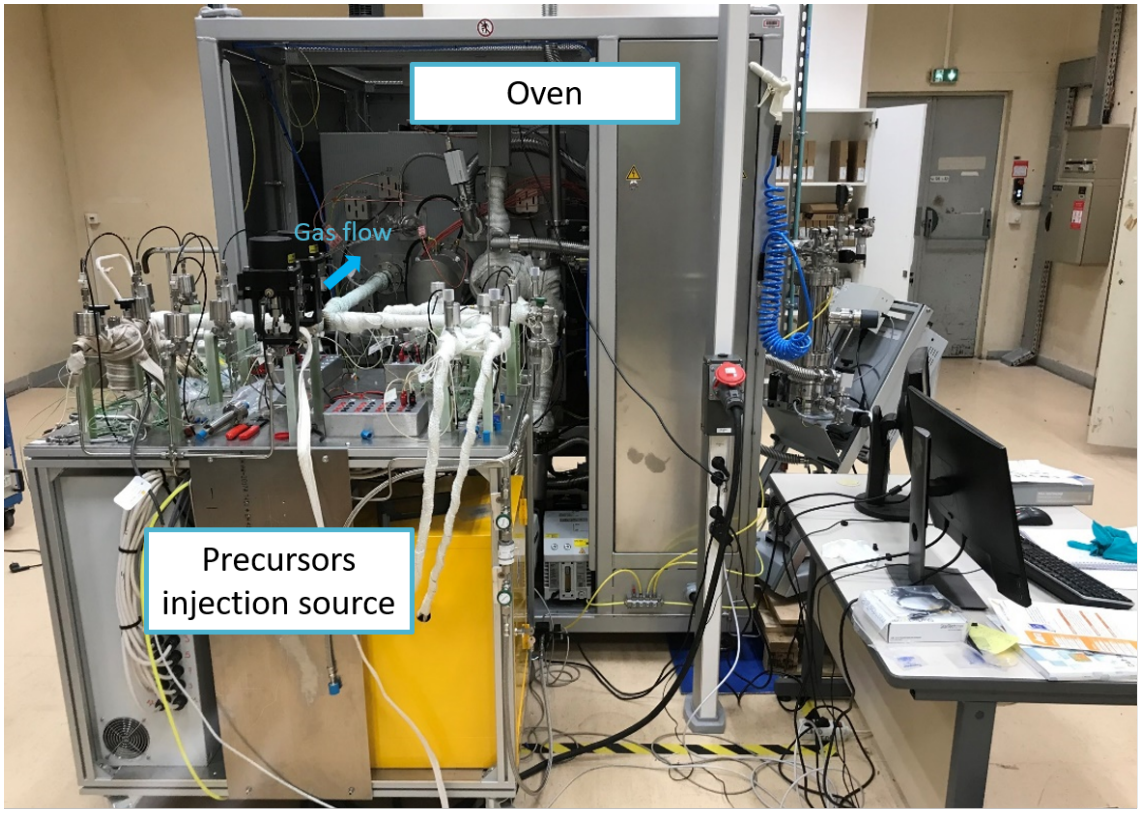

Figure 4.15: Picture of the ALD system for cavity coating

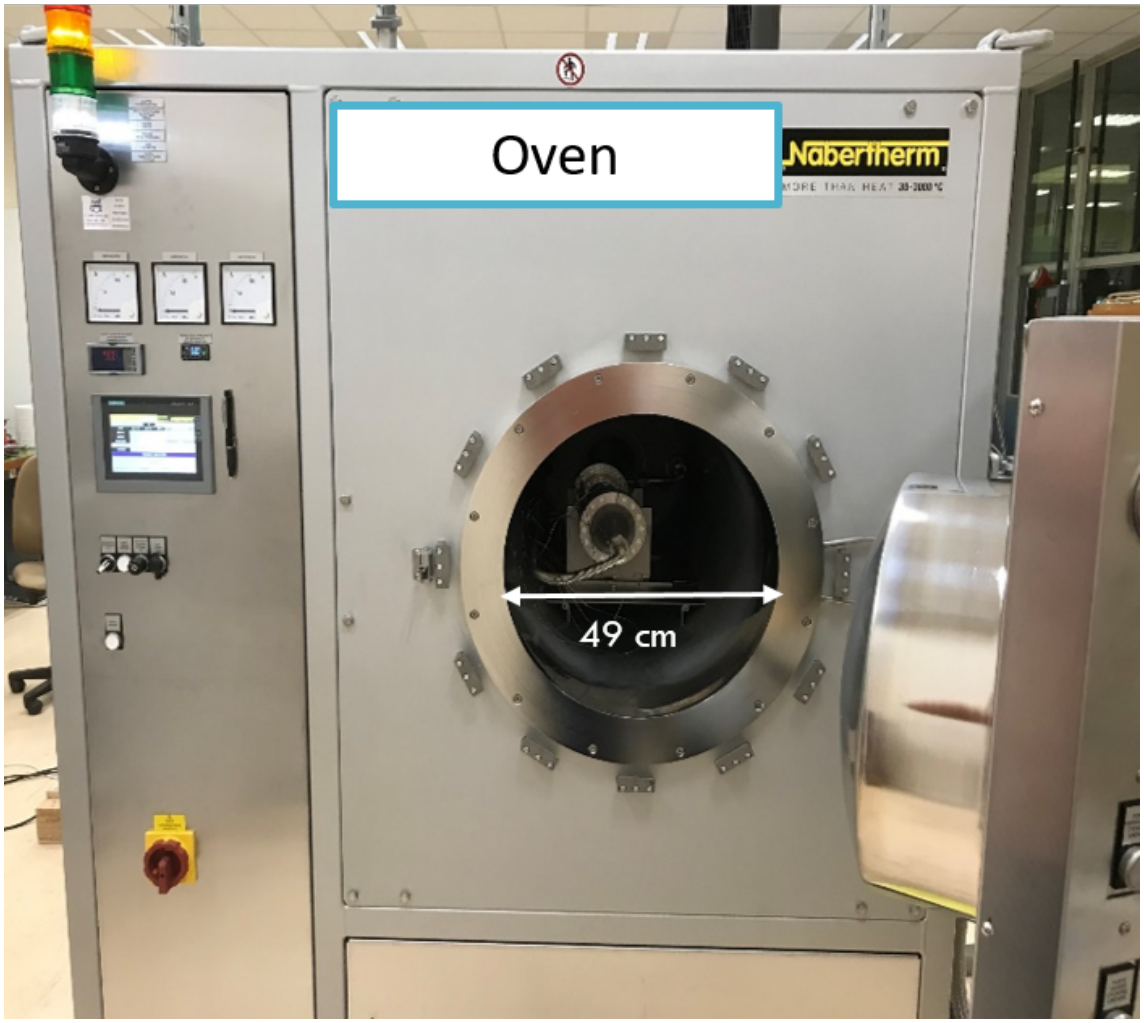

Figure 4.16: Picture of the retort of the oven

4.6 Characterization methods

In order to evaluate the quality of ALD-grown thin films and study their physical properties, several characterization methods have been used. This section will give an succinct overview of some of the different characterization techniques used in this work.

4.6.1 Thickness measurement and structural analysis

X-ray reflectivity

The thickness of the ALD-grown films have been measured using X-ray reflectivity (XRR). X-ray reflectivity is a surface sensitive characterization method used to determine the layer structure of a multi-layer or a single film and evaluate the thickness, density and roughness of the film.

In XRR, an X-ray beam is directed to the sample in an incidence angle close to the critical angle and a detector measures the intensity of the reflected x-rays in the

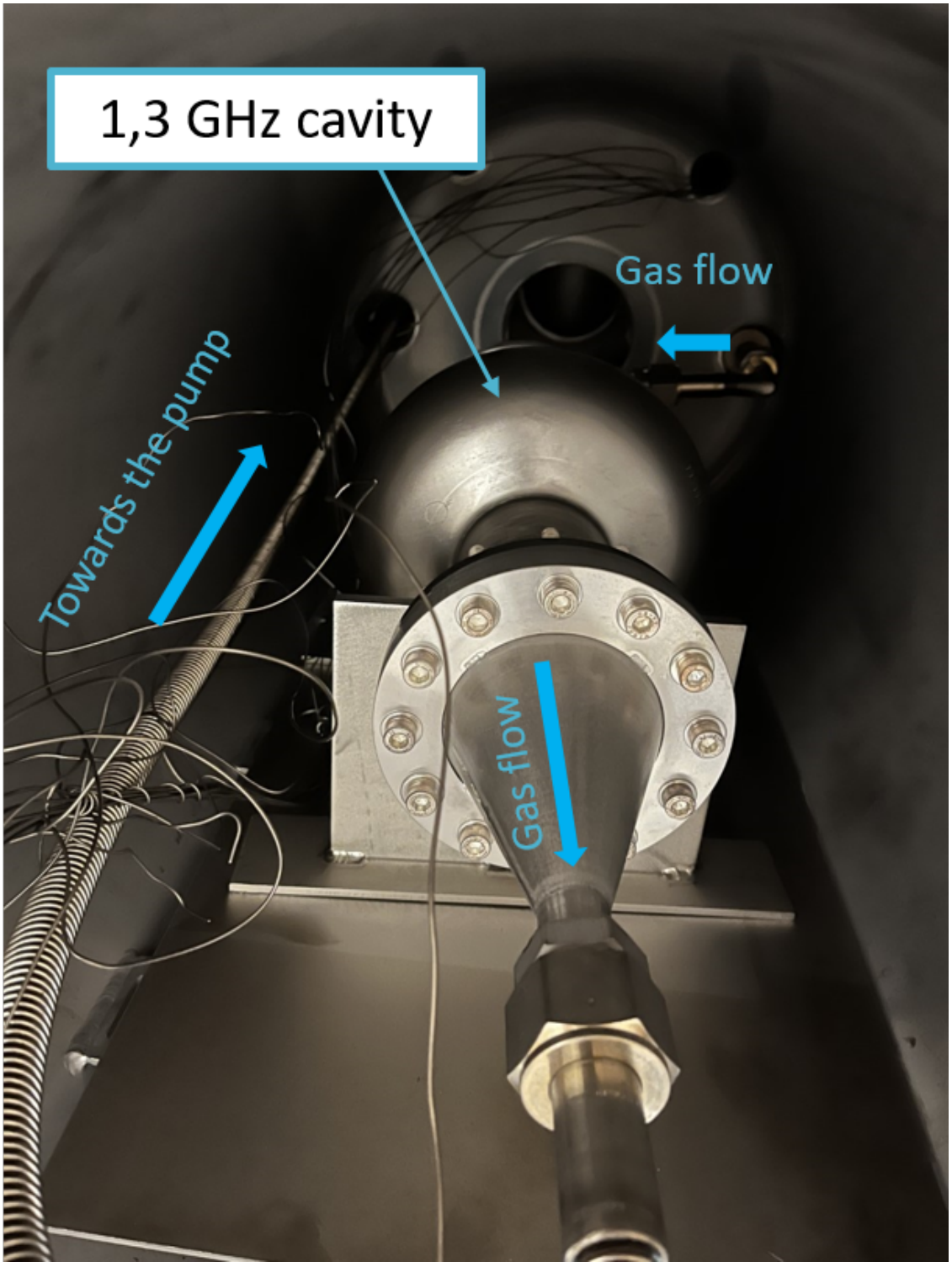

Figure 4.17: Picture of the 1.3 Ghz niobium cavity connected to the ALD system inside the furnace chamber

specular direction. The deviation of the reflected intensity from the Fresnel law due to the fact that the surface is not perfectly smooth and flat are then analyzed and fitted using mathematical models (such as Fourrier transformation and non-linear

least-squares model) to provide information on thickness , density and roughness of the film [43].

In this project, X-ray reflectivity measurements were performed at "Université Paris-Saclay, CNRS/IN2P3, IJCLab, 91405 Orsay, France", " Plateforme de Diffraction des Rayons X, Ecole Polytechnique , 91128 Palaiseau, France" and "Sorbonne Université, Campus Pierre et Marie Curie, 75005 Paris, France" depending on their availability using a 5-circle diffractometer (Rigaku SmartLab) with CuKα radiation from a rotating anode. The curves were then fitted using the "X'pert reflectivity" software to determine the thickness, density and roughness of deposited films.

Grazing incidence X-ray diffraction

X-ray diffraction is a nondestructive characterization technique used for studying the structural properties of materials. It provides information on the crystalline structures, preferred crystal orientations, average grain size and strain of materials. Used in completion with other characterization techniques, it can also help identify the chemical composition of materials.

X-ray diffraction is based on the scattering of the monochromatic x-rays beam by the lattice planes of a material. Whenever the geometry of the incident X-rays satisfies Bragg's law, a phenomenon of constructive interference takes place and a peak of the intensity of the reflected X-rays is recorded. The peak intensities as well as their d-spacing is determined by the arrangement of atoms within the lattice which makes the diffraction pattern obtained with this method a real fingerprint of a given material [44].

X-ray diffraction is most commonly used in "the bragg-brantano geometry". In this configuration, both the X-rays source and the detectors rotate simultaneously around the sample keeping the same angle θ. The peak intensities are recorded and converted into a count rate as a function of θ. However, for the study of thin films, grazing incidence configuration is better suited. As a matter of fact, even if diffraction is not intrinsically a surface selective tool, impinging the samples with a very small incidence angles (typically 0.5°) can significantly reduce the penetration depth of the x-rays and thus provides the opportunity to probe the structure of films near the surface [45]. We manage through this technique to reduce significantly the signal coming from the substrate and we can even tune the thickness of the probed layer by changing the incidence angle of the X-rays. For this research, grazing-incidence X-ray diffraction were performed using the same Rigaku SmartLab diffractometer mentioned earlier.

4.6.2 Chemical composition analysis

In order to study the chemical composition of our ALD-deposited films, we used predominantly X-ray photo-electron spectroscopy (XPS). When needed, complementary techniques were used such as Time-of-Flight Secondary Ion Mass Spectrometry (ToF-SIMS) [46] and Rutherford backscattering spectrometry (RBS) [47].

X-ray photoelectron spectroscopy

X-ray photoelectron spectroscopy is a surface sensitive analytical technique, in which the surface is irradiated by x-rays (energies lower than 6 KeV) and the kinetic energy of the emitted electrons is measured . The photoelectron emitted is the result of the energy transfer of the X-ray to a core level electron. This is expressed in equation 4.1 where BE is the binding energy of the electron, KE is its kinetic energy and Φ_{spec} is the spectrometer work function which is a constant value [48].

$$hv = BE + KE + \Phi_{spec} \tag{4.1}$$

Using the binding energy of the photoelectron peaks, XPS provides information on the elements present at the surface, their chemical environment and their oxidation state. It can be used in line profiling of the elemental composition present at the surface, or in depth profiling if paired with ion-beam etching.

In this project, XPS analysis were performed essentially at "The Instrumental Platform ICCMO, 91400 Orsay, France" and "Service de la Corrosion et du Comportement des Matériaux dans leur Environnement (SCCME), CEA Saclay, 91191 Gif-sur-Yvette, France" depending on their availability using respectively K-alpha and ESCALAB 250Xi spectrometers from Thermo Fisher Scientific both equipped with a monochromatic X-ray Al-Kα source (hv = 1486.6 eV). The data acquired have been fitted using CasaXPS software [49].

4.6.3 Superconducting measurements

- In order to evaluate the quality of the superconducting films, the room temperature resistivity and the critical temperature were measured using a four-point probe home-made setup at CEA.

- Magnetometry measurements were also performed at the "Plateforme Mesures Physiques à Basses Températures, Sorbonne Université, 75005 Paris, France" using a vibrating sample magnetometer (VSM) "Quantum Design PPMS 9T" and a superconducting quantum interference device SQUID (Quantum Design MPMS XL 5T).

4.6.4 Optical and morphological analysis

- Scanning electron microscopy (SEM) have been regularly used to assess the quality of the deposited films and check the presence of defects. To that end, "ZEISS Sigma 300" microscope were used at the "laboratoire de physique des deux infinis IJCLAB, Orsay, France".

- Atomic force microscopy (AFM) were also used in order to measure the film's surface roughness. We used a Bruker diinnova AFM availbale at "Plateform ICMMO, Orsay, France".

Chapter 5

Protection and enhancement of niobium superconductivity

5.1 Introduction

Ever since the emergence of niobium based applications such as superconducting cavities and Josephson junctions in the 1960s, niobium oxides seemed to play a crucial role in their performances. Their growth mechanism and their different properties have been widely studied in order to understand how they affect superconductivity. Niobium is naturally passivated by a native oxide layer of ∼5 nm thickness. Unfortunately, this oxide is known to be defective and to have a poor thermal stability [50]. It has been also considered responsible for lowering SRF cavities performances through introducing some magnetic impurities. Preliminary studies by Proslier et al [35, 51] also showed that replacing the defective native niobium oxide with an ALD-deposited alumina film improved the performances of RF cavities. It both increased the quality factor and the maximum accelerating gradient. These particular results inspired our work. In this project, one of our goals is to functionalize the Nb surface by depositing a multilayer structure.

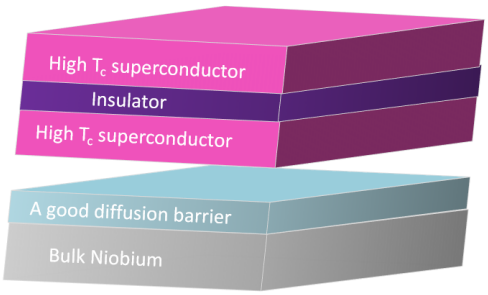

Figure 5.1: An illustration of the multilayer structure on top of the Nb surface protected by a diffusion barrier

This will necessarily involve putting the cavity through several thermal cycles[1] and makes protecting the bulk Nb from potential diffusion a critical step. This chapter will be dedicated to finding an effective diffusion barrier with a high thermal stability to replace niobium native oxides and possibly to be the foundation of the multilayer structure. We will be also investigating whether this layer can improve the cavity performances in the same way suggested by [35]. It is crucial for the diffusion layer to be a good dielectric in order to be transparent for the RF waves and not cause any additional losses. Prior to that, let us recall the basics of the niobium-oxygen system and introduce the three main niobium oxides.

5.2 Niobium-Oxygen system

The complexity of Niobium-Oxygen system comes from the existence of several non-stoichiometric phases some of which are metastable. The niobium-oxygen system have been first established by Elliot [52]. Niobium can be found in four different oxidation states: 0, +II, +IV and +V which are related to the four thermodynamically stable phases of Nb, NbO, NbO_2 and Nb_2O_5 respectively as it is shown in figure 5.2:

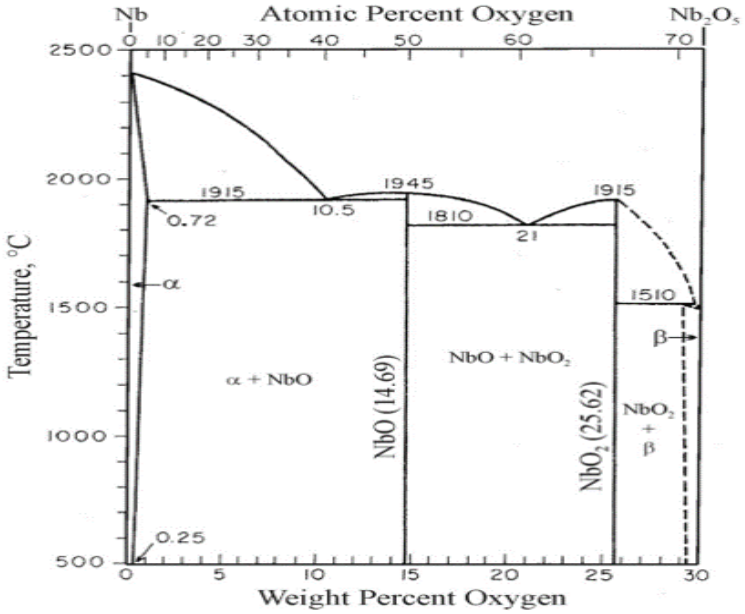

Figure 5.2: Niobium-Oxygen phase diagram (Elliott, 1960)

- Niobium is known to have a great affinity and a high binding energy to oxygen. At a low concentration, oxygen occupies octahedral sites in the Nb lattice and has a solubility of 0.8% at 500°C [53]. Interstitial oxygen have drastic effects on niobium's electrical properties. It increases its resistivity by 4.1 µohm.cm per at% of oxygen and lowers the superconducting temperature of ~ 1 K per at% of oxygen [52].

[1]The deposition process along with other potential heat treatments

- NbO is believed to be the first oxidation step after oxygen adsorption in vacuum [54]. It forms in a very narrow range of oxygen concentration NbO_x with $0.96<x<1.02$ [52] and crystallizes in a face-centered cubic structure with the particularity of having 25% of ordered vacancies in the sub-lattices of Nb and O. It has a typical metallic behavior with a resistivity of $\sim$ 21 µohm.cm at room temperature and becomes superconductive below 1.4 K [55]. In the native oxide, NbO is a very thin interfacial layer of thickness $\leq$ 1 nm [56].

- NbO_2 is the intermediate oxidation step before the formation of the Nb_2O_5. It is known to be a weak Peierls semiconductor with a gap of 0.1 eV [51] and to have a distorted rutile structure [57]. Its thickness is of the order of $\sim$ 1 nm [56, 58].

- Nb_2O_5 is an insulator with a band gap higher than 4 eV [51] and is the most thermodynamically stable among the others niobium oxides. It is polymorphous and its structure is based on NbO_6 octahedra linked to each other by corner or edge sharing. Oxygen vacancies in $Nb_2O_{5-\delta}$ are stable with $0<\delta<0.17$ and induce both increased conductivity and spin magnetic moments due to unpaired electron on the Nb atom. In the native oxide, Nb_2O_5 is the dominant oxide and decomposes above 200°C into NbO_2, NbO and NbO_x.

5.3 Metal-oxide interface

The metal-oxide interface have been extensively studied using several surface characterization techniques such XPS [50, 56], LEED[59], AES [59] and X-ray diffuse scattering [56]. The prevailing belief about niobium-native oxide interface is that it consists of a continuum of gradually increasing oxygen concentration NbO_x from interstitial oxygen ($x<1$) to the metallic NbO layer up to the topmost insulating Nb_2O_5. Since the native oxides properties depends highly on the preparation technique, we focused mainly on electro-polished niobium surfaces, which is proven to be the best preparation technique for niobium SRF cavities.

In order to have a reference of the initial state of the niobium oxides, we performed XPS analysis[2] of an electro-polished cavity grade niobium sheets. The sample where cleaned with deionized water and air-dried in a similar manner to that done on cavities. The 3d core-level XPS spectra was fitted using CasaXPS software [49] using the fitting parameters suggested in the NIST database and shown in table 5.1. It is important to note that the fitting parameters where fixed for all the coated samples in order to compare the evolution of the niobium oxides after the coating.

The XPS spectra of the Nb 3d core level is shown in figure 5.3:

The XPS peak deconvolution showed four main chemical species, which were assigned to Nb_2O_5, NbO_2, NbO and Nb located respectively at 207.4 eV, 206.2 eV,

[2]XPS analysis were performed at "the Laboratory of Innovation in Surface Chemistry and Nanosciences , 91191 Gif sur Yvette, France", "The Instrumental Platform ICCMO, 91400 Orsay, France" and "Service de la Corrosion et du Comportement des Matériaux dans leur Environnement (SCCME), CEA Saclay, 91191 Gif-sur-Yvette, France" depending on their availability. The author would like to recognize the help of Frédéric Miserque, Diana Dragoe and Jocelyne Leroy in acquiring the XPS spectra.

Table 5.1: XPS fitting parameters for the Nb 3d core-level spectra

Component	Line Shape	B.E (eV)	FWHM (eV)
Nb	A(0.38,0.6,10)GL(10)	202.2 ± 0.3	0.5
NbO	GL(30)	203.7 ± 1	2.25
NbO_2	GL(30)	206.2 ± 1	2
Nb_2O_5	GL(30)	207.4 ± 0.4	1

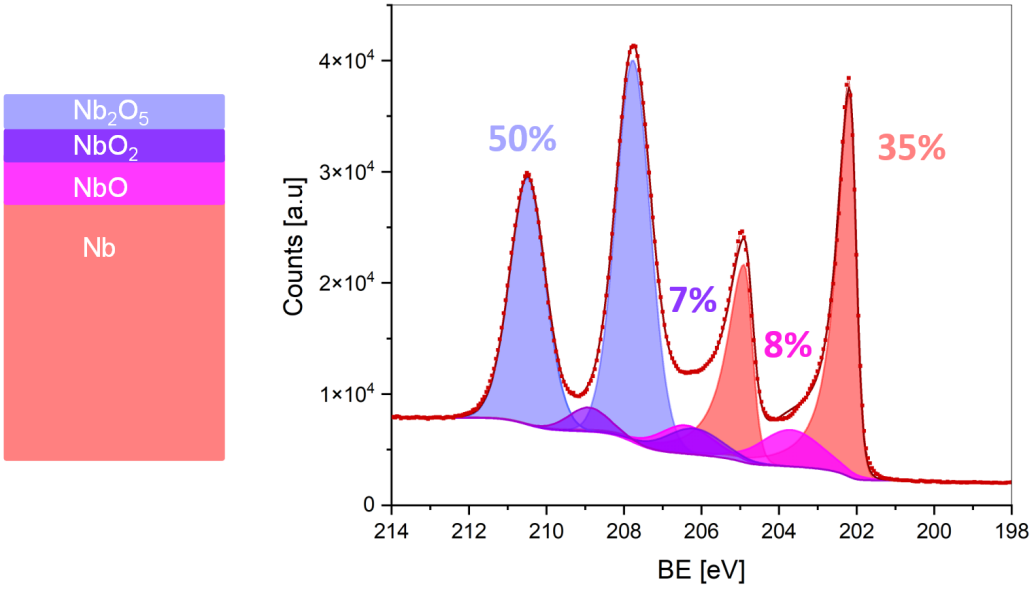

Figure 5.3: XPS spectra of Nb 1d region of a bare niobium EP sample

203.7 eV and 202.2 eV. Nb_2O_5, the highest oxidation state of niobium, constituted 50% of the total XPS signal. The NbO_2 and NbO oxides contributed respectively with 7% and 8% of the signal whereas the Nb metal signal accounted for 35 % of the signal. We can safely conclude that Nb_2O_5 is the predominant oxide specie under ambient conditions which is consistent with results reported in [50, 56].

5.4 Magnetic impurities in Niobium oxides

At the interface of the metal-oxides, the transition from one oxide layer to another is not sharp. Each of the niobium native oxides can stabilize a substantial off-stoichiometry, which results in oxygen vacancies especially in the pentoxide Nb_2O_5. Oxygen vacancies in the Nb_2O_x with ($2<x<2.5$) and in the underneath sub-oxides (NbO_2 and NbO) create Nb4d1 ions that are left with an unpaired electron. These ions can be considered as localized charge and spin carriers. The existence of these magnetic impurities have been confirmed by Cava et al [60] showing that indeed Nb_2O_5 exhibits magnetic moments and this increases with the oxygen vacancies

concentration. A further tunneling spectroscopy study [51] showed that these magnetic impurities can degrade superconductivity by inelastic scattering induced pair-breaking and attributed the improvement of the superconducting performances after the mild baking to a decrease of the magnetic scattering. According to their findings, the baking step, even at low temperatures, causes an irreversible rearrangement of the oxygen in the niobium oxides which results in the reduction of the defective Nb_2O_5 and the growth of a thicker NbO_2 which is non-magnetic by nature.

5.5 Replacing niobium native oxides with an ALD-deposited protective layer

In the quest of getting rid of the problematic effects caused by niobium native oxides, Proslier et al [35, 51] suggested an original approach summarized in figure 5.4. It consisted in ALD-coating the inner surface of the Nb cavity with a thin protective layer of alumina followed by a subsequent annealing at 450°C for 24 hours in UHV. This resulted in the dissolution of the niobium native oxide by oxygen diffusion into the bulk while the Al_2O_3 layer maintained the metal layer protected. A cavity test showed an improvement in both the quality factor and the maximum accelerating gradient.

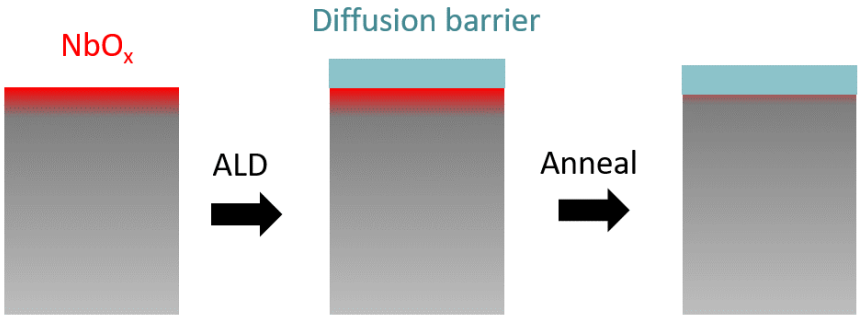

Figure 5.4: The approach suggested by Proslier et al in [35]

In this study, we performed the deposition of three different diffusion layer candidates Al_2O_3, Y_2O_3 and MgO, all known to have a high thermal stability and good insulating properties:

- Magnesium oxide (MgO) is known to be a refractory material with a high thermal stability and high dielectric constant (k$\sim$ 9,8 from [61]). It has been considered as a promising functional layer for several applications such as tunneling barriers for magnetic junctions [62], a passivation layer for photonic devices [63] and a high-k dielectric layer for Si-based electronics [64].
- Yttrium oxide (Y_2O_3) is known to be the most thermodynamically stable compound among all the metal oxides and can withstand temperature up to

2200°C [65] . It has a relatively high dielectric constant in the range of 14-18 [66] and an excellent protective behavior in severe reactive environment [67]. It has been proved effective as a coating layers of crucibles used at high temperature for molten metals [68].

- Aluminum oxide (Al_2O_3) is one of the most versatile of refractory oxides. It has a dielectric constant in the range of 7.5-10.5 and a melting point of 2015°C [69] . It is a widely used insulator in Si-based integrated circuits and in Josephson junctions [70] and as a tunneling barrier for superconducting devices such as single-electron transistors and superconducting quantum interference devices (SQUIDs).

In the following sections, we will present the results from the as-deposited oxides followed with a subsequent annealing in UHV at different temperatures up to 800°C. The goal is to find the best protective layer in terms of thermal stability and reduction of niobium native oxides.

5.6 Deposition and characterization of the different oxides layers

5.6.1 Deposition parameters

We used standard ALD recipes to deposit the oxides layers using organometallic precursors and H_2O (see chapter 4 for more details on ALD). The deposition were performed on clean electro-polished niobium samples. Si-wafer coupons were also used in order to perform subsequent XRR analysis. Prior to the film deposition, the samples were introduced in the reactor, which was then heated up to 250°C. The recipe is launched at least an hour after the chamber have reached the deposition temperature set-point in order to insure a uniform temperature along the deposition chamber. The deposition parameters are summarized in table 5.2. It is necessary to recall that all the ALD recipes where tested several times and optimized on dummy samples in order to make sure that they were reliable.

Table 5.2: Deposition parameters of the different oxides (for further detail see chapter 4)

Film	Precursors (A-B)	(Pulse A–Purge A-Pulse B-Purge B)
Al_2O_3	TMA/H_2O	1 s-15 s-1 s-15 s
Y_2O_3	$Y(MeCp)_3/H_2O$	1 s-15 s-1 s-15 s
MgO	$Mg(MeCp)_3/H_2O$	1 s-15 s-1 s-15 s

5.6.2 X-ray reflectivity measurements

Following the coating step, the samples were taken out of the reactor, stored in clean special boxes and characterized usually few days later. Si samples were measured

using X-ray reflectivity[3] The curves were then fitted using the X'pert reflectivity software to determine the thickness, density and roughness of the oxides films. The growth rate per cycle GPC is then calculated. Table 5.3 summarizes the X-ray reflectivity measurements. As presented in the table above, the X-ray reflectivity

Table 5.3: Summary of XRR measurements on deposited oxide-layers

Film	Number of cycles	Thickness [nm]	GPC (Å/cycles)	Density (g/cm^3)	Roughness (nm)
Al_2O_3	100	9	0.9	3.3	0.6
Y_2O_3	65	7.5	1.15	5.01	0.7
MgO	100	8.5	0.86	3.58	0.3

measurements showed that we managed to deposit dense and smooth oxide layers with reasonable growth rate per cycles. As the XRR is performed on silicon samples only[4] , we will assume for now that the growth dynamics is similar on niobium and that the film has overall the same thickness whether it is deposited on niobium or silicon.

5.6.3 X-ray photoelectron analysis

As a second characterization step, we performed X-ray photoelectron spectroscopy, this time on niobium samples, to evaluate the stoichiometry of the deposited oxides and check whether we have deposited the desired compound. The XPS analysis of the Al_2O_3, MgO and Y_2O_3 are summarized in figures 5.5, 5.6 and 5.7 respectively. First, a survey scan is done in order to check the presence of the desired elements then a high-resolution scan is performed on the elements of interest to examine their chemical state. The different peaks are then fitted with CasaXPS software [49].

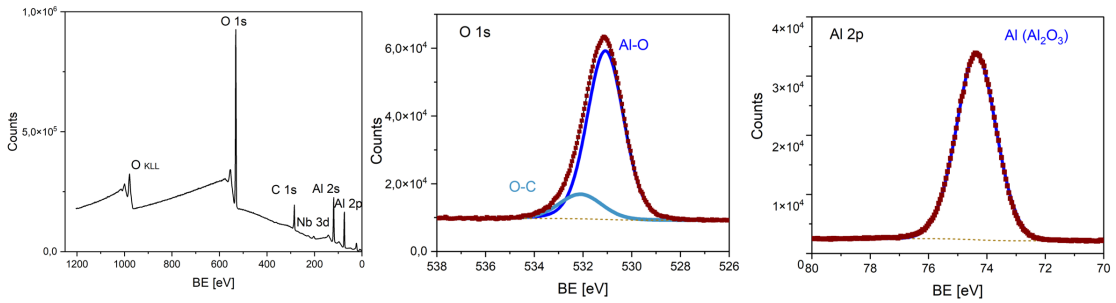

Figure 5.5: XPS analysis of 9 nm thick Al_2O_3 film on niobium substrate

Figure 5.5 shows the peak of Al 2p at 74.3 eV corresponding to aluminum bonded to oxygen in the form of Al_2O_3 oxide. On the O 1s core-level spectrum, we observe the oxygen peak at 530.8 eV assigned to oxygen bonded to aluminum along with a small peak assigned to oxygen bounded to carbon at 532.4 eV.

[3]X-ray reflectivity measurements were performed at "Université Paris-Saclay, CNRS/IN2P3, IJCLab, 91405 Orsay, France", " Plateforme de Diffraction des Rayons X, Ecole Polytechnique , 91128 Palaiseau, France" and "Sorbonne Université, Campus Pierre et Marie Curie, 75005 Paris, France" depending on their availability.

[4]The roughness of niobium samples is too high to be used for X-ray reflectivity.

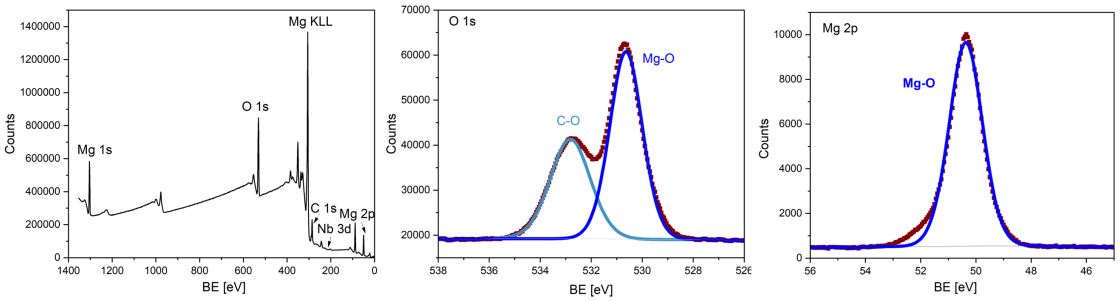

Figure 5.6: XPS analysis of 8.5 nm thick MgO film on niobium substrate

Figure 5.6 shows the Mg-O peak fitted on Mg 2p core-level spectrum at a binding energy of 50.34 eV. On the O 1s core-level spectrum, we can observe two peaks assigned to oxygen-magnesium bond at 530.6 eV and oxygen-carbon bond at 532.8 eV.

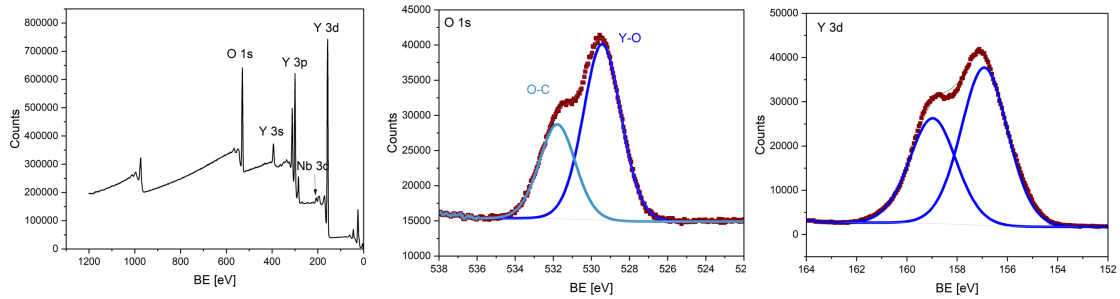

Figure 5.7: XPS analysis of 7.5 nm thick Y_2O_3 film on niobium substrate

Figure 5.7 shows the peaks deconvolution on the Y 3d core-level spectrum showing the 3d 5/2 and 3/2 doublet at a binding energy of 157 eV and separated with 2.05 eV. The oxygen O-1s spectrum shows two main peaks as observed previously on Al_2O_3 and MgO samples: a first peak at 529.6 eV assigned to oxygen bonded to Yttrium and a second peak at 532 eV assigned to oxygen bonded to carbon.

5.6.4 Thermal stability of niobium native oxides

In order to study the evolution of niobium native oxide and test the thermal stability of the different deposited oxides, we performed different thermal treatments in UHV on niobium samples coated with Al_2O_3, MgO or Y_2O_3 thin films. Then, we used XPS to examine the chemical state of niobium and compare its evolution underneath the different protective layers.

Figure 5.8 shows the evolution of the different niobium peaks of a sample coated with Al_2O_3 film with the different thermal treatments whereas figure 5.9 summarizes these measurements. We found it interesting to study thermal treatment at 650°C and 800°C for few hours in vacuum (the pressure is $\sim 10^{-6}$ mbar) because they are already a part of a standard preparation process of Nb cavities.

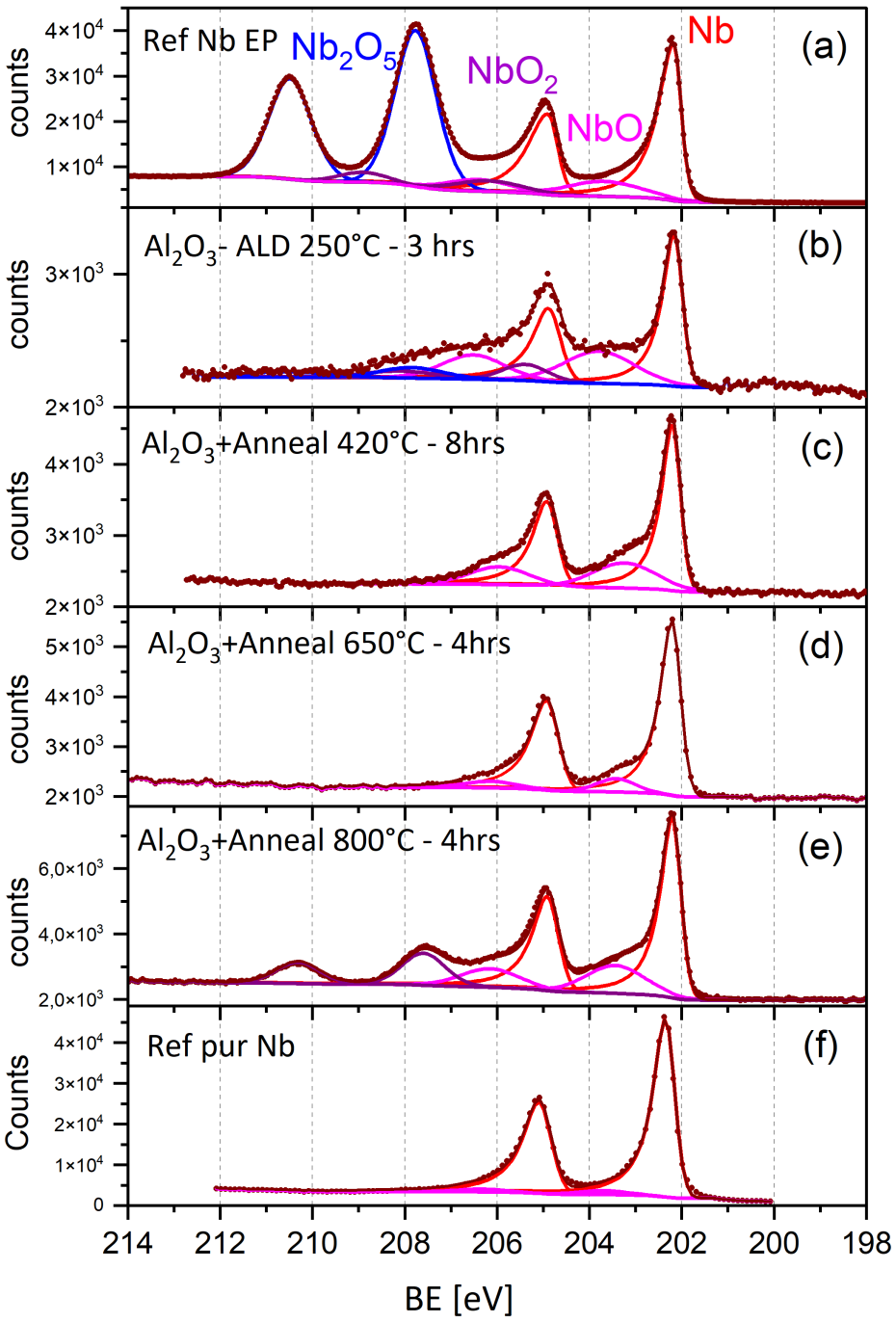

Figure 5.8: XPS spectrum of Nb 3d core level spectra with different thermal treatments

The XPS analysis shows that the ALD-coating at 250°C causes the reduction of 80 % of the Nb_2O_5 into sub-oxides such as NbO and NbO_2. After annealing 420°C during 8 hours, the NbO_2 is transformed mainly into NbO whereas after the annealing 650°C during 4 hours, the Nb 3d core-level spectrum shows only two components of metallic niobium with only 10 % of NbO. This is in perfect agreement

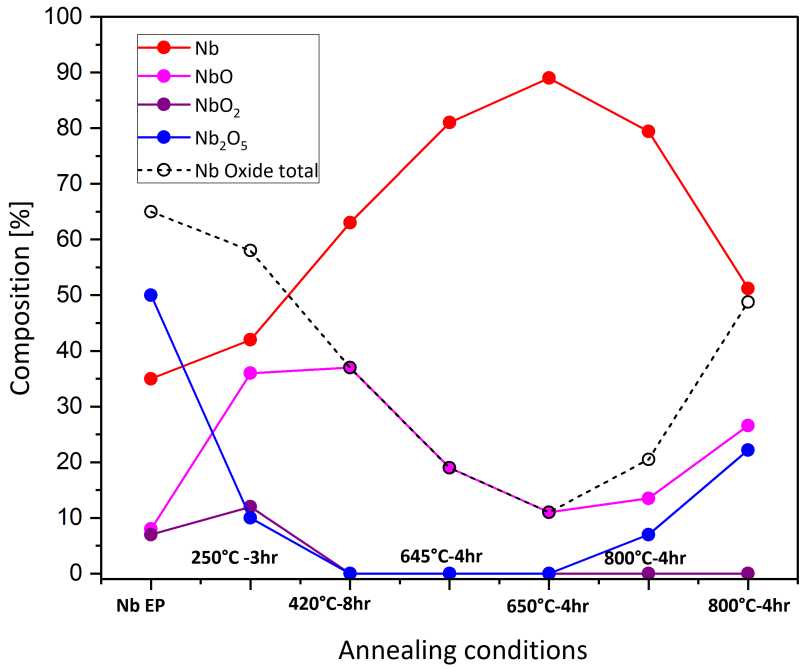

Figure 5.9: Summary of the Nb 3d core level composition of Al_2O_3-coated niobium

with what have been observed in [51]. Surprisingly, annealing at 800°C for 4 hours does not reduce the oxides contribution but rather increase it. The XPS spectrum unveils the re-appearance of Nb_2O_5 peaks and the increase of NbO contribution. We interpret this observation by a possible degradation of the Al_2O_3 at 800°C, which no longer protects efficiently the Nb surface (despite the fact that the Al_2O_3 layer is still present on the surface).

In order to further investigate the origin of this observation, we performed an XPS analysis of 10 nm Al_2O_3 coated niobium sample with an in-situ annealing up to a temperature of 800°C. The evolution of XPS signals is shown fin figure 5.10. We can see that the signal of metallic niobium increases progressively when increasing the chamber temperature to reach saturation around 500°C. Interestingly, we can observe an exponential decrease of oxygen and aluminum above 700°C accompanied with an increase of Nb signal. It seems that above 700°C, the Al_2O_3 layer is depleted from its oxygen either by diffusion to the bulk or through evaporation but most probably through diffusion as Nb is a getter material. This leaves at the surface a thin layer of aluminum that evaporates itself rapidly at this high temperature (aluminum melting temperature is 620°C). This would explain the re-exposition of the Nb surface and hence the re-appearance of the Nb_2O_5 after annealing at 800°C.

The same process is tested on Nb samples coated with Y_2O_3 and MgO films. The results obtained from Y_2O_3 and MgO summarized respectively in figures 5.11 and 5.12:

We observed a similar trend in the evolution of niobium oxides: Nb_2O_5 is reduced

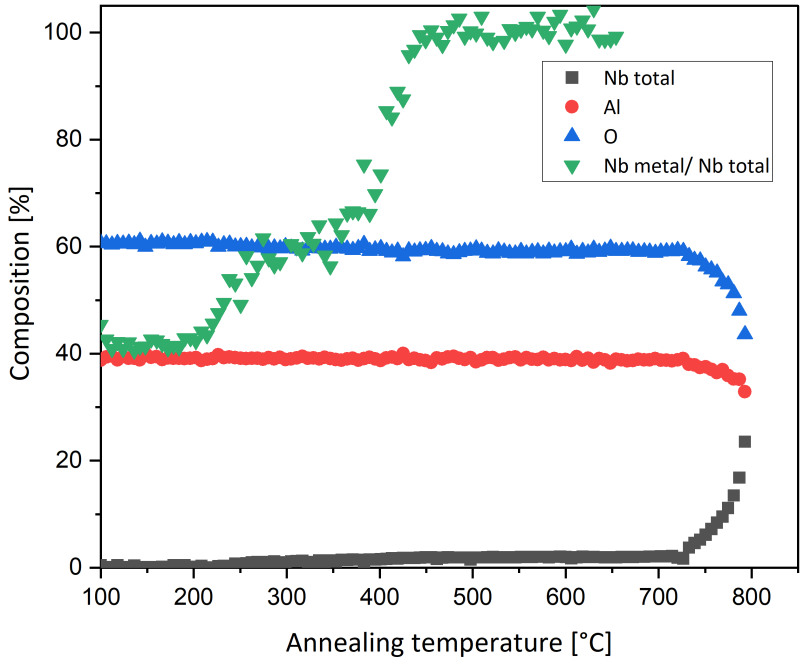

Figure 5.10: XPS analysis of Al_2O_3-coated Nb sample with in-situ annealing

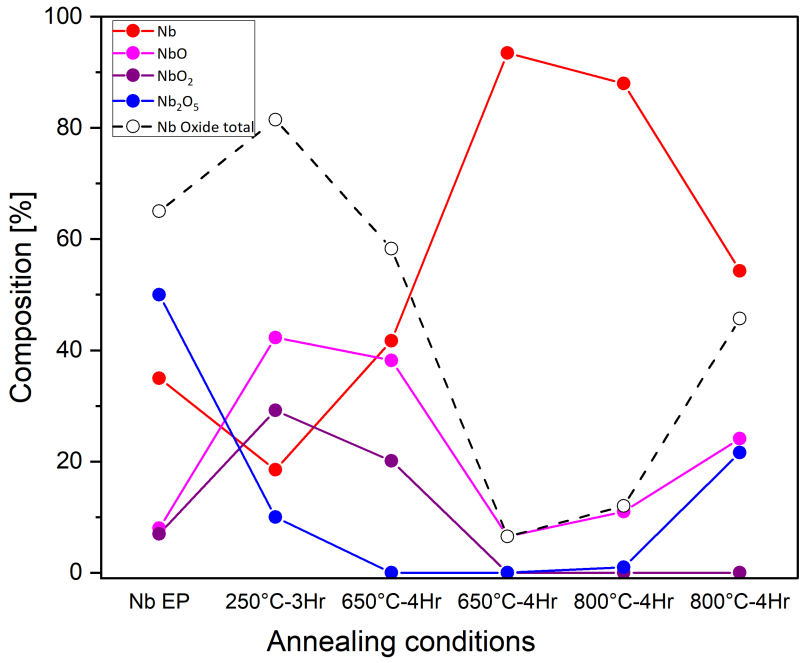

Figure 5.11: Summary of the Nb 3d core level composition of Y_2O_3-coated niobium

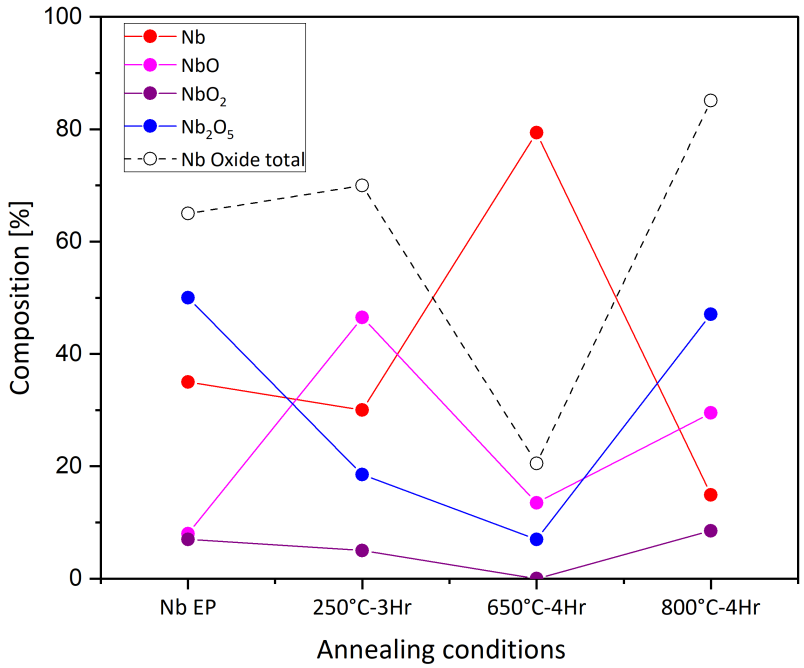

Figure 5.12: Summary of the Nb 3d core level composition of MgO-coated niobium

into NbO_2 and NbO, which are in turns reduced into metallic niobium through the diffusion of oxygen into the bulk. Based on our experiments, we can conclude that there is a minimum of Nb oxidation after ALD-coating followed by a thermal treatment of 650°C-4 hours.

It is important to notice that for the Y_2O_3 coated sample annealed at 800°C-4 hours, we show two different compositions: One sample showed a high oxide content whereas the second one showed a good passivation of the Nb surface. We think that the sample with high oxides content suffered from a great amount of carbon contamination. This results have been previously discussed in S.Bira PhD theses [71][5] . When contamination is avoided, Y_2O_3 can guarantee a good protection for the Nb surface even at temperatures higher than 650°C.

For the MgO coated Nb sample, annealed at 800°C -4 hours, we witnessed a complete re-oxidation of the Nb surface and a no Mg signal was recorded using XPS. We suspect a similar scenario to that observed on Al_2O_3 where the MgO is reduced to Mg, which gets then evaporated (the melting point of Mg is 650°C). If we compare the Nb oxide compositions obtained after the annealing at 650°C-4 hours with the three layers tested, we notice that Al_2O_3 and Y_2O_3 are the most efficient layers among the three oxide tested: The corresponding Nb core-level signal is almost composed of only metallic Nb and shows only 5 % contribution of NbO. These findings are quite interesting and would enable us to test Nb cavities with

[5]Some of the XPS analysis presented in this chapter along with the TEM images are the result of our collaboration with IJCLAB that took place during my first year of my PhD. A part of these data were previously presented by S.Bira in her PhD thesis [71]

almost no native niobium oxides at its surface.

5.6.5 TEM analysis

In order to better study the Niobium-Native oxide-ALD oxides interfaces, we performed STEM-EELS (Scanning Transmission Electron Microscopy-Electron Energy Loss Spectroscopy) analysis on an Al_2O_3-coated niobium samples before and after UHV annealing at 650°C during 4 hours. Focused ion beam (FIB) technique was used to prepare thin cross-section of the samples dedicated to TEM analysis. Figure 5.13 shows two TEM images taken on a niobium sample coated with 100 cycles of Al_2O_3 before and after annealing. Before annealing, we can see the Al_2O_3 film of 10 nm on top of a Nb oxide interface of about 5 nm thickness. It seems that the Al_2O_3 grew thicker on Nb than on silicon wafer (as we previously measured around 9 nm for 100 cycles). This can be due to higher density of reactive sites on niobium and no nucleation delay as compared to Si substrates. After Annealing, the Al_2O_3 maintains its shape whereas the Nb oxide layer at the interface between bulk niobium and Al_2O_3 becomes much lighter and almost invisible.

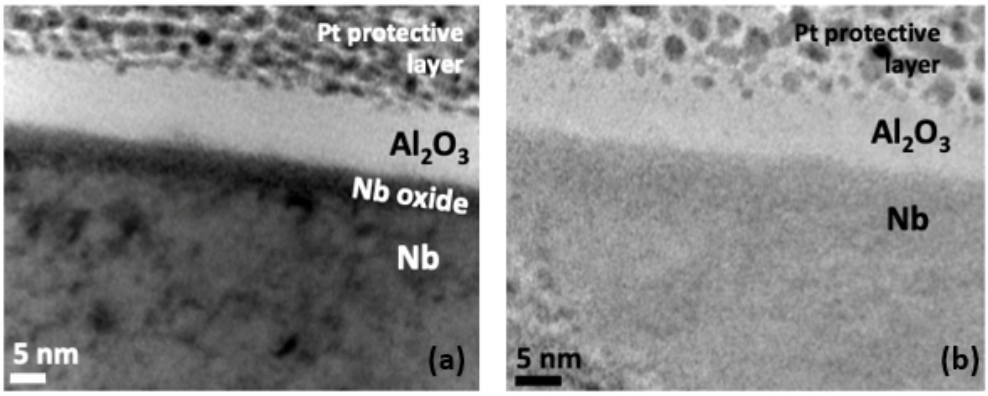

Figure 5.13: Transmission Electron Microscopy bright field images (JANNuS-SCALP facility at IJCLab) of Al_2O_3 films deposited on niobium: (a) as-deposited ,(b) after annealing at 650°C during 4 hours

EELS analysis on the as-deposited sample (see figure 5.14-a) shows that, indeed, there is a 5 nm thick oxide layer separating the Al_2O_3 film and the bulk niobium. After annealing in UHV at 650°C during 4 hours, this oxide layer thickness is reduced to 2 nm as shown in figure 5.14-b. These results are in perfect agreements with our expectations, and based on our previous XPS analysis, this 2 nm oxide interface must correspond to the remaining NbO signal after annealing.

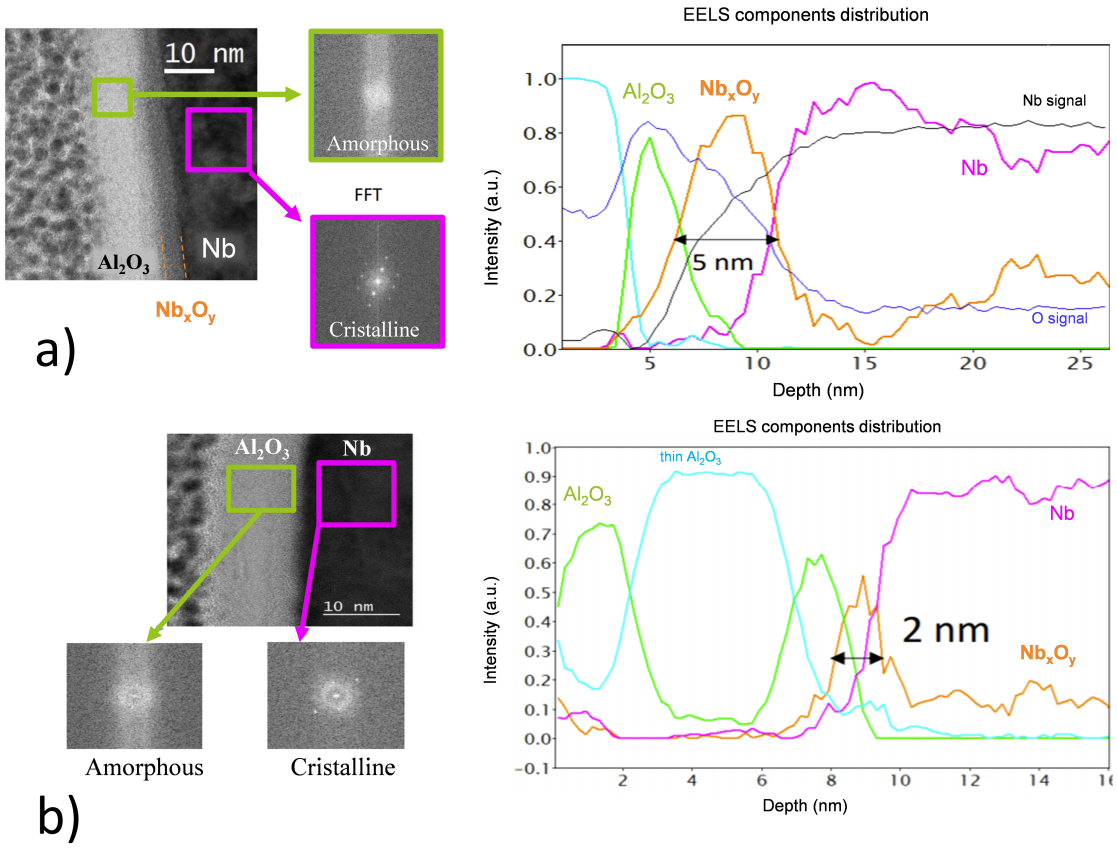

Figure 5.14: EELS analysis of Al_2O_3-coated Nb sample: a) as-deposited. b) after annealing in UHV at 650°C during 4 hours [71]

5.7 Test on 1.3 GHz cavity geometry

Before testing the Al_2O_3 on a niobium cavity, we must make sure that we use appropriate deposition parameter for the 1.3 GHz cavity. To do so, we performed a deposition test of a layer of Al_2O_3 in an Aluminum cavity with the same 1.3 Ghz geometry. In order to measure the respective oxide thickness, we inserted a Si-sample holder that follows closely the shape of the cavity. Figure 5.15 shows the different steps of the experiment preparation in the clean room: First, the sample holder were loaded with 15 clean Si wafer samples. The sample holder were then put inside the Al cavity, which was then sealed and transported to the ALD-lab to be installed onto the research-scale ALD system.

For our deposition recipe, we used the same deposition parameters used for our previous sample coating. The Al cavity was heated at 250°C and then coated with 625 cycles of Al_2O_3. Once the deposition step is achieved, we disconnected the cavity from the ALD system, unsealed the cavity-system flanges in the clean room and retrieved the sample holder with our witness-Si samples. The results of X-ray reflectivity measurements on these samples are summarized in figure 5.16.

As it can be seen on the XRR measurements, the Al_2O_3 film was deposited uniformly along all the samples at different positions in the cavity. We measured a

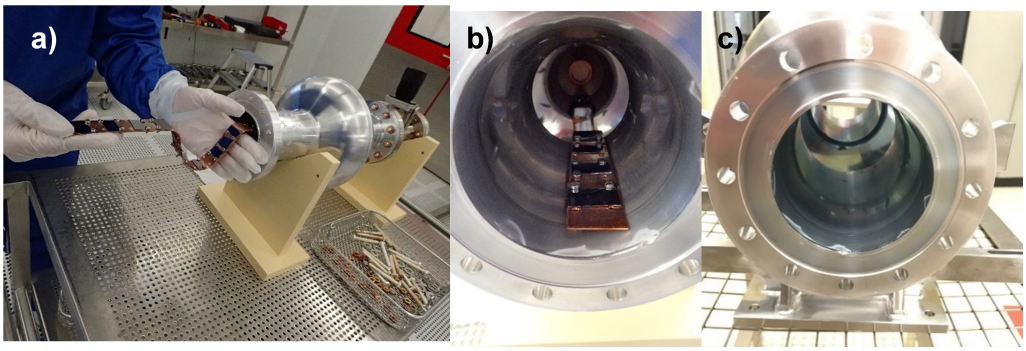

Figure 5.15: a) Pictures of the Aluminium cavity with the sample holder, (b) before the deposition ,(c) the aluminum cavity after the deposition showing a blue shade characteristic of the Al_2O_3 oxide layer

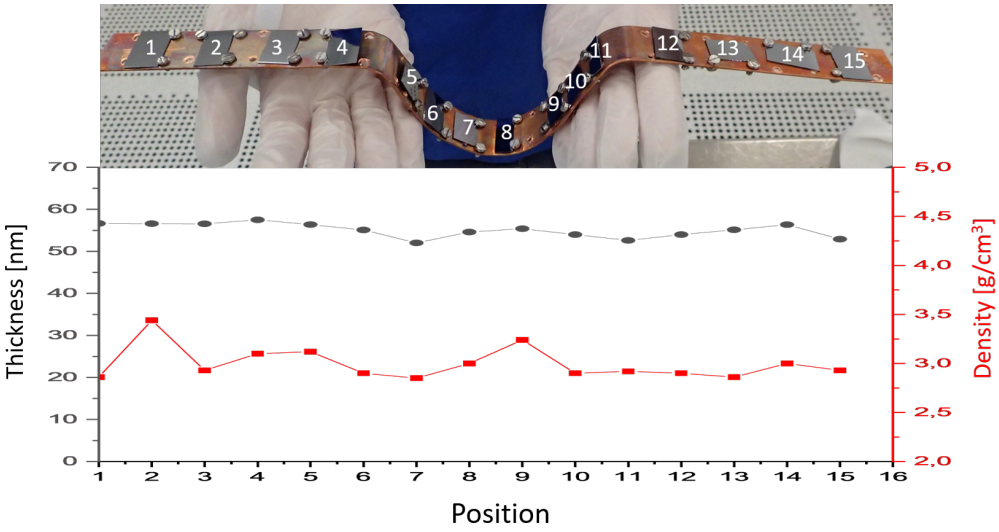

Figure 5.16: XRR measurements on Si-samples placed all over the 1.3 Ghz aluminium cavity

film of $\sim$ 56 nm on all the samples, which is consistent with the GPC of 0.9 Å per cycles measured previously.

5.8 Al_2O_3 coating of 1.3 GHz niobium cavities

5.8.1 The cavity preparation

At this point of our research, we were ready to test our Al_2O_3 layer recipe onto a niobium cavity. During the frame time of my PhD thesis, we were able to perform the experiment twice on the same niobium cavity. Since our cavity-coating ALD system were under construction at that time, we connected the niobium cavity to the research-scale ALD system as showcased in figure 5.17. We performed the deposition of 100 cycles of Al_2O_3 at 250°C using the same deposition parameters used on samples.

After the coating, the Nb cavity were disconnected from the ALD system and

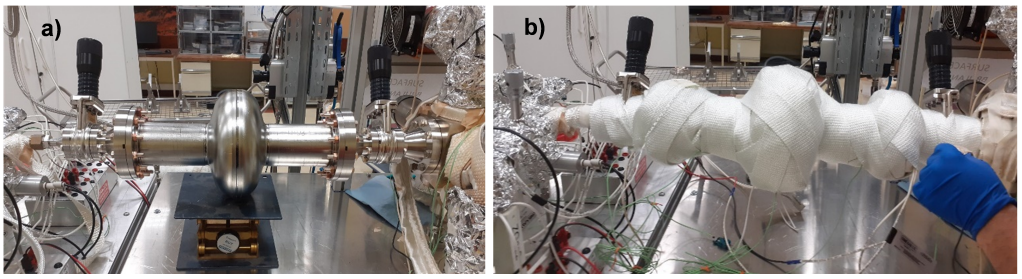

Figure 5.17: Pictures of the Nb cavity connected to the ALD-system (a) naked (b) covered with the heaters and thermal isolation

received an annealing step in UHV at 650°C in the IJClab furnace (the pressure is $\sim 10^{-6}$ mbar). Figure 5.18 shows a picture of the cavity prior to the annealing step in the dedicated titanium box.

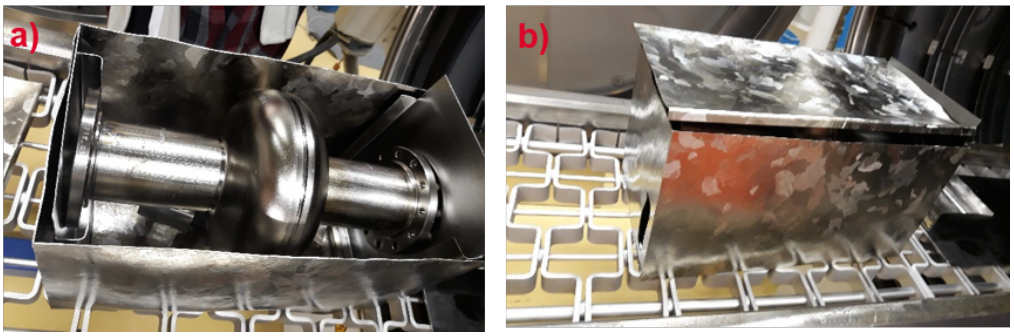

Figure 5.18: Pictures of the Nb cavity inside the Ti box prior to the UHV annealing in the IJClab furnace

5.8.2 RF tests of the Al_2O_3 coated niobium cavities

We tested the Al_2O_3 coated cavity in our vertical-testing facility at CEA. The results of the two RF tests are presented in figures 5.19 and 5.20.

Figure 5.19 shows the evolution of quality factor as a function of the accelerating gradient and the evolution of surface resistance as a function of 1/T after Al_2O_3 coating followed with a thermal treatment. The baseline measurement are plotted in green[6] whereas the performances of the cavity after the Al_2O_3 coating followed by annealing at 650°C during 4 hours are plotted in blue. We can see that the quality factor of the cavity is slightly improved compared to the baseline and this improvements is enhanced when we increase the accelerating gradient until we reach a multipacting barrier at 18 MV/m. The surface resistance of the coated cavity is also slightly lower than the baseline at temperature lower than 2 K. Above 2 K, the coated cavity showed a higher surface resistance.

As a second test, we electro-polished the niobium cavity to remove the Al_2O_3 layer and reset the niobium surface. We then tested the cavity to have a new baseline and performed the same Al_2O_3 coating. However, this time we annealed the cavity

[6]The baseline test was limited to 20 MV/m due to helium leakage.

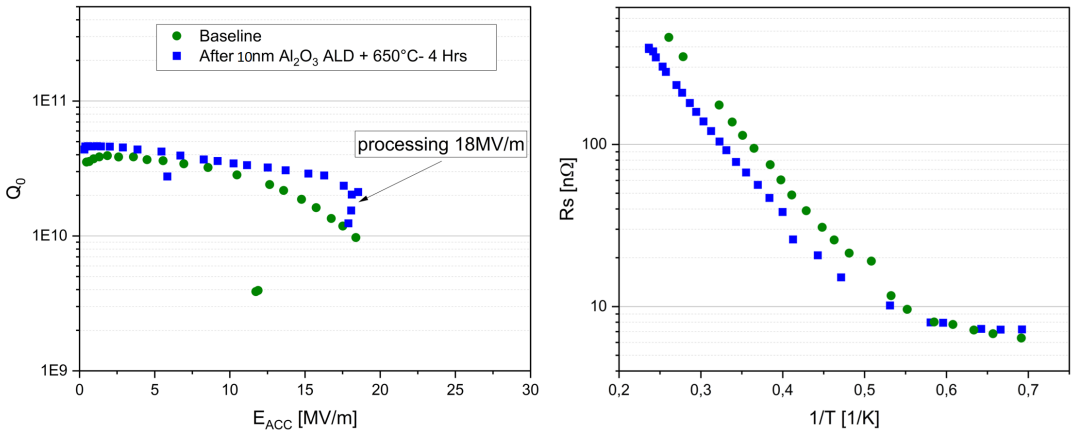

Figure 5.19: Summary of the RF tests done on Al_2O_3 coated Nb cavity after annealing at 650°C during 4 hours in UHV

at 650°C during 10 hours. Figure 5.20 shows the coated cavity performances in blue whereas the second baseline is plotted in green. We observe a greater improvement of the quality factor after coating under low fields: the quality factor gains a factor of 2 after the coating. However, we observed again a multipacting barrier at 18 MV/m. The surface resistance showed this time the same baseline values at T>2.2 K and become lower for T<2.2K. The fact that the Al_2O_3 coated cavity performed better after 10 hours annealing as opposed to the 4 hours annealing can indicate a better dissolution of Niobium oxides. Perhaps, the remaining 2 nm layer of NbO_x (seen by TEM) at the interface between the Al_2O_3 and bulk niobium gets completely dissolved after 10 hours of annealing at 650°C in UHV. As far as the observed multipacting barrier is concerned, we will discuss it in details in the following chapter.

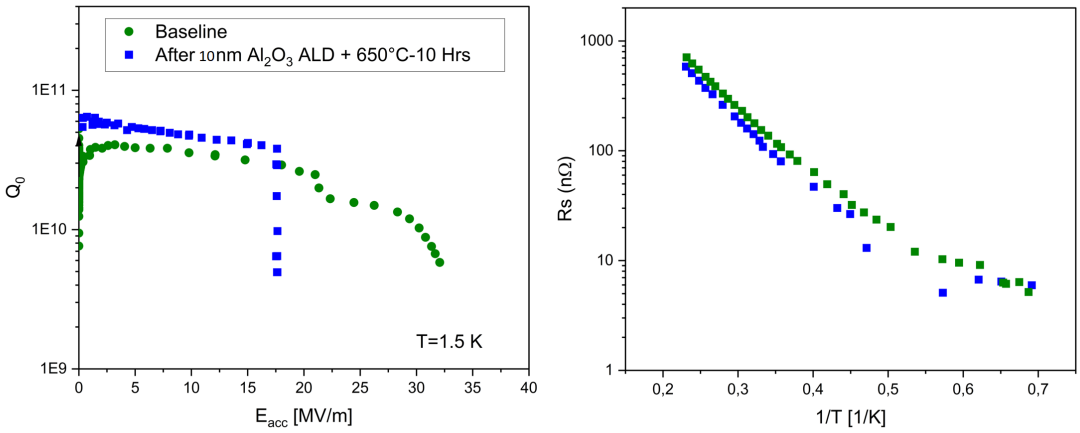

Figure 5.20: Summary of the RF tests done on Al_2O_3 coated Nb cavity after annealing at 650°C during 10 hours in UHV

5.8.3 Low field RF behaviour

The low RF field domain of SRF cavities have been reported [72] to be sensitive to defects in the oxide layer. Such defects, modeled as two level systems (TLS), is an intense research field and their microscopic origin is still under debate. Recent results however seems to point toward hydroxide groups in the oxide [73] as a potential contributor to these TLS. Our surface engineering approach using ALD and post thermal treatments open new possibilities to understand, control and ultimately improve the low field performance, i.e., lowering the defect concentration. The low field quality factor region has been measured following the cavity ring down procedure [22]. A typical dataset is represented in figure 5.21.

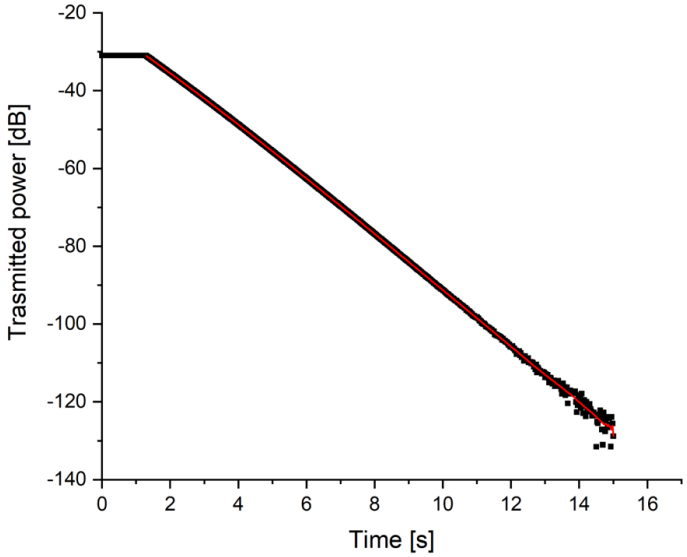

Figure 5.21: 1.3 GHz cavity ring down and the corresponding 20 points averaging in red.

From the cavity parameters geometrical factor R/Q, length L, the transmitted and incident quality factor Q_T and Q_I, and the cavity frequency f_0, we can reconstruct from the P_t vs t curve in figure 5.21 the intrinsic cavity factor vs acceleration field; the power P is converted to electrical field intensity and its time derivative give access to the quality factor via the use of the following formulae:

$$E = \sqrt{R/Q}/L \times \sqrt{Q_T P}/10^5 \tag{5.1}$$

$$\tau_L = -P/\frac{dp}{dt} \tag{5.2}$$

$$Q_L = 2\pi f_0 \tau_L \tag{5.3}$$

$$\frac{1}{Q} = \frac{1}{Q_L} - \frac{1}{Q_T} - \frac{1}{Q_I} \tag{5.4}$$

Following this procedure, we can extract the Q vs E curves at low fields for the two cavities that corresponds to the RF tests at high field represented in figure 5.19 and 5.20. The low field curves are represented in figure 5.22.

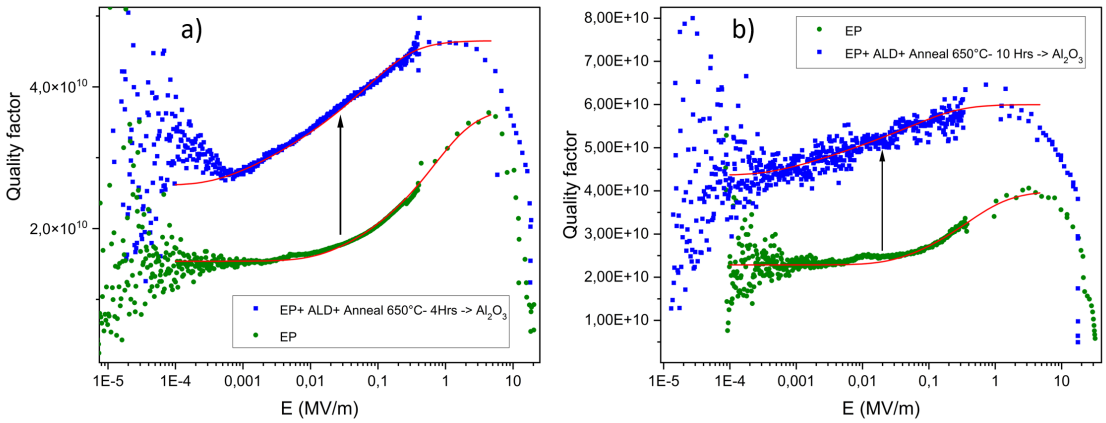

Figure 5.22: Tests Q vs E at 1.5K in the low field regime on a Nb cavity coated with Al_2O_3 (10 nm) and post annealed at 650°C for (a) 4 hours and (b) 10 hours.

The green curves are the baselines and the blue curves represent the RF tests after deposition of 10 nm of Al_2O_3 and post thermal treatments. It is clear that for both tests, the quality factor has been improved by a factor of two at low fields for both cavities. The red lines are fits using the simplified Two Level system (TLS) equation [72]:

$$\frac{1}{Q} = \frac{1}{Q_{QP}} + \frac{F\delta_{TLS}(T)}{(1 + (\frac{E_{acc}}{E_c(T)})^2)^\beta} \tag{5.5}$$

Where E_c is a characteristic electrical field for saturation of the TLS, Q_{QP} is the non-TLS quasiparticle contribution, β is a fitting parameter and F is the filling factor defined as:

$$F = \frac{\int_{V\ \text{dielectric}} \varepsilon_{dielectric} |E(r)|^2\, d^3r}{\int_{V\ vacuum} \varepsilon_{\text{vacuum}} |E(r)|^2\, d^3r} \tag{5.6}$$

For TM_{010} mode, the electrical field distribution in the cavity is not uniform as shown in figure 1.6.

Assuming a 5 nm Nb_2O_5 layer with a dielectric constant $\epsilon \approx 33$, we obtain F $\approx$ 3 10^{-9}, leading to the TLS values for EP cavities in table 5.4. For the 10 nm Al_2O_3 coated and annealed cavities, assuming a a dielectric constant $\epsilon \approx 9$, we obtain a F $\approx$ 1.6 10^{-9}, leading to the δ_{TLS} values listed for the ALD processed cavities.

Table 5.4: Fitting parameters of TLS function at low RF fields

Treatment on 1.3 GHz tesla shape cavity	Fδ_{TLS}	δ_{TLS}	E_c	β
Baseline EP	$(4.14 \pm 0.4)\times10^{-11}$	1.33×10^{-2}	0.028	0.18
ALD of Al_2O_3 10 nm + 650°C for 4 hrs	$(1.6 \pm 0.2)\times10^{-11}$	10^{-2}	0.0013	0.19
Baseline EP	$(1.8\pm 0.04)\times10^{-11}$	0.6×10^{-2}	0.047	0.26
ALD of Al_2O_3 10nm + 650°C for 10 hrs	$(0.75 \pm 0.03)\times10^{-11}$	0.4×10^{-2}	0.001	0.1

We noticed first that the saturation field E_c decrease by a factor of 20 to 50 with the Al_2O_3 and post-annealing step, indicative of a change in the nature of the TLS defects present in the oxide layer. In addition, the dielectric loss tangent δ_{TLS}, appears to consistently decrease after the ALD deposition and post-annealing process that suggest a decrease in the concentration of TLS defects. These two effects combined are responsible for the increased quality factor of both cavities at low fields.

5.9 Summary

Through this chapter, we managed to study the thermal stability of three ALD deposited potential diffusion barrier: Al_2O_3, Y_2O_3 and MgO. We have shown that we can engineer the surface layer of SRF cavities in order to improve the RF performances of SRF cavities at low and higher accelerating fields. In particular, the low field regime is of huge interest to the Qubits community that aims at increasing their lifetime and hence their quality factor at very low field (down to a few photons). The following chapter will be dedicated to understanding the origins of the multipacting barrier observed on the RF tests.

Chapter 6

Multipacting mitigation in RF cavities

6.1 Introduction

As seen in the previous chapter on the RF tests of the Al_2O_3 coated niobium cavities, multipacting is one of the most detrimental phenomena to RF systems performance, in particular in RF cavities. Once it occurs, it causes energy dissipation which makes the quality factor of the cavity decline very sharply and prevent reaching high accelerating gradient. Through this chapter, we will investigate the possibility of suppressing multipacting in RF cavities using an ALD-deposited titanium nitride thin film.

6.1.1 Multipacting

Secondary electron emission (SEE) is a well-known phenomenon of electron-solid interaction where a primary electron of sufficient energy hits a surface, and induces the emission of secondary electrons from the surface. The number of these secondary electrons is called the secondary emission yield (SEY) of the material.

SEE has been considered as accounting for the parasitic multipacting effect in microwave systems. Multipacting in RF cavities, is triggered by some seed electrons present inside the cavity[1] [74]. In high magnetic filed regions (cavity equator), electrons travel in quasi-circular trajectories returning to almost their emission location at about the same RF phase. Depending on the energy they gained from the electrical field component (30 eV-200 eV) [20] and the secondary emission yield of the surface, secondary electrons can be emitted from the surface. These electrons may in turn be accelerated by the RF fields and impact the surface again releasing even more electrons and so on. This process give rise to an uncontrolled electron avalanche or what is referred to more commonly as multipacting. This results in an exponential increase of the number of electrons inside the cavity within few RF cycles. These unwanted electrons consume an important share of the RF energy and end up heating the surface at each impact, leading eventually to a reduced quality

[1] seed electrons can originate from the interaction of the residual gas with the RF power, the electron beam (in operation) or field emission of structural or chemical origines

factor or, in case of severe multipacting, to thermal breakdown of the superconducting cavity[2].

Multipacting is not only inherent to RF cavities, but rather takes place in a wide range of RF devices extending from divertors in tokamaks [76], space satellites [77] to power couplers [78] and antennas [79]. This detrimental effect can cause consequent energy dissipation, window breakage in power coupler, vacuum breakdown and in severe cases, even the destruction of the RF device. Consequently, huge research efforts, in all these fields, are being made into solving this problem. To suppress multipacting inside a resonant device, we basically have two routes: either by optimizing the geometry to get rid of multipacting prone locations or by minimizing the secondary emission yield of the surface.

Historically, the geometry of the RF cavity have been adjusted from the pillbox shape to the elliptic shape to suppress multipacting [80, 81]. In a spherical geometry, the electron trajectories are pushed by the electromagnetic fields to the equatorial region where the electric field is very low. Therefore, secondary electrons generated in this region hardly gain sufficient energy to multiply. This resulted in a significant reduction of multipacting but the problem still occurs in the equator region even in recent elliptical cavities.

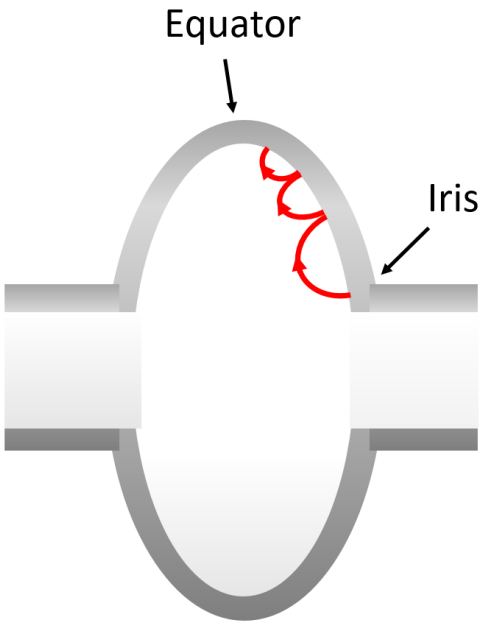

Figure 6.1: Multipacting trajectories in elliptically shaped RF cavities

In the scope of this work, we take on a material approach and rather focus on how to modify the cavity surface in order to reduce its secondary emission yield. This approach have been widely employed to suppress multipacting in other RF

[2]Studies led in 1.5 GHz Niobium cavities of the CEBAF shape showed that multipacting can raise the temperature of the cavity wall up to $\sim$ 100 mK [75]

devices such as power couplers [78, 82, 83, 84]. Coating the RF surface with an intrinsically low SEY material such as titanium nitride [82, 83, 84], chromium oxide [78] and carbon[85] were found to be one of the most effective routes to suppress multipacting.

6.1.2 Titanium nitride coating for multipacting mitigation

Titanium nitride is the most commonly used coating for multipacting suppression due to its low secondary emission yield and its good stability in RF field. It proved its effectiveness in several devices such as the RFQ accelerator in Los Alamos [86] and coupler windows in Fermilab [87] and DESY [78] where the RF surface were coated with $5 \sim 10$ nm nanometers of TiN mainly by sputtering and sublimation techniques. However, coating an RF surface to decrease its SEY must necessarily meet with its other design specifications in particular its surface resistance. For an RF coupler ceramic window, it is crucial for the coating to be conductive in order to evacuate charges. In this case, the coating must have a high conductivity and a low SEY. On the contrary, for a superconducting cavity, a low surface resistance is needed. Any normal conducting coating (like metals) would generate additional losses within the skin depth of electromagnetic wave. In this case, it is better to use a coating with a high resistivity (dielectrics are transparent to RF fields) and a low SEY. A very thin coating, even if poorly conductive, might not increase drastically the surface resistance but can reduce significantly its overall SEY and therefore prevent multipacting.

Another important aspect to take into consideration is the coating quality and whether or not the deposition technique is suitable to perform uniform coverage all over the devices surface, especially when the device have a complex geometry such as RF cavities. For this particular reason, we use atomic layer deposition (ALD) as a deposition technique as it is widely known for its excellent uniformity and atomic-level thickness control. It is important to highlight that, unlike other deposition techniques such as evaporation and sputtering where nanoparticles agglomerate randomly on the surface until they form a continuous film, during an ALD process, the precursors molecules reacts covalently with the substrate through a self-limiting reaction and leaves no more than one monolayer at the surface after each ALD cycle. The film is therefore deposited one monolayer at a time and this stages an outstanding thickness control which will play a key role in our research.

6.2 Experimental conditions

Through this chapter, we mainly present the results of SEY and X-ray photoelectron spectroscopy (XPS) measurement on Si and Nb samples coated with 10 nm thick film of ALD-deposited Al_2O_3 with increasing thickness of titanium nitride film. Both Al_2O_3 and TiN were deposited by thermal ALD in our research-scale ALD reactor (see chapter 4 for more details).

The films thickness and density were measured using X-ray reflectivity on Rigaku Smartlab diffractometer with a rotating anode Cu K alpha X rays. The X-ray curve

was then fitted using X'pert Reflectivity software to extract the density, thickness and roughness of the different layers.

The SEY measurements were performed in UHV facility (typically 10^{-10} mbar), specially designed for SEY characterizations at ONERA [88]. The analyses chamber is equipped with a Kimball Physics ELG-2, Omicron Mgkalpha/Alkalph X-ray source, a SIGMA hemispherical electron energy analyzer and a Focus –FDG150 ion source. The surface conditioning was performed at 500 eV using a high current flood gun. In order to avoid additional conditioning of the surface during the SEY measurement, short electron beam pluses were used (typically ms). The incident electron beam was set normal to the surface.

6.3 Preliminary results

As discussed above, our initial motivation was to understand the origin of multipacting in the Al_2O_3 coated niobium cavity (seen in chapter 5) and suppress it.

6.3.1 First SEY measurements

As a starting point, we performed SEY measurement of a bare niobium sample and an Al_2O_3 coated niobium samples as shown in figure 6.2.

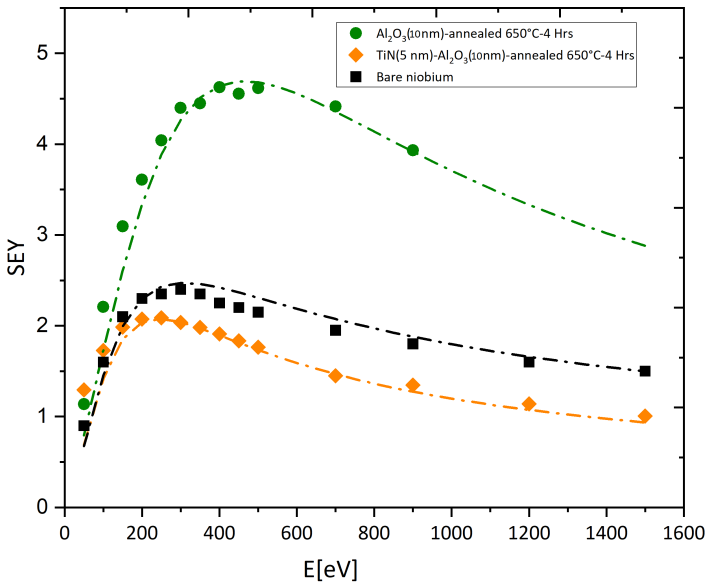

Figure 6.2: SEY measurement of a bare niobium surface, Al_2O_3 coated niobium surface annealed during 4 hours at 650°C and TiN (5 nm) -Al_2O_3 (10 nm) coated niobium sample annealed during 4 hours at 650°C.

The Al_2O_3 coated niobium showed a maximum SEY of 4.5, which is much higher than the maximum SEY of the initial niobium sample of 2.5. At this point, we

coated the Nb-Al_2O_3 (10 nm) sample with a 5 nm film of titanium nitride TiN and the SEY_{max} of the surface drastically decreased from 4.5 to 2.1. This measurement is in a perfect agreement with previous measurement of SEY_{max} of TiN coated surfaces [82, 83, 84].

6.3.2 Multipacting simulation on 1.3 GHz cavity geometry

In order to further investigate the origins of the multipacting barrier observed in the previous Al_2O_3 coated niobium cavity (see section 5.8.2), multipacting simulation were performed using Fishpact [89] as an electron trajectory tracking code. First, we used Superfish [90] code as the field solver to provide the electromagnetic fields map in the single cell elliptical cavity[3]. Then, we used FishPact code that reads the SuperFish solution file and searches for the electron possible trajectories. Because of axial symmetry, simulation were run only on the upper cavity wall, 10 emitting sites were defined along the cavity equator and the electron were considered to be emitted with average axial accelerating gradient varying from 11-21 MV/m in 1 MV/m steps. Phases from 0° to 360° in steps of 1° were varied and multipacting trajectories were counted if they survived up to 10 impacts. Their final energy were recorded at each impact. Then, the SEY curves measured (see figure 6.2) were used to calculate the number of secondary electron emitted as a function of the E_{acc} in the 1.3 GHz geometry.

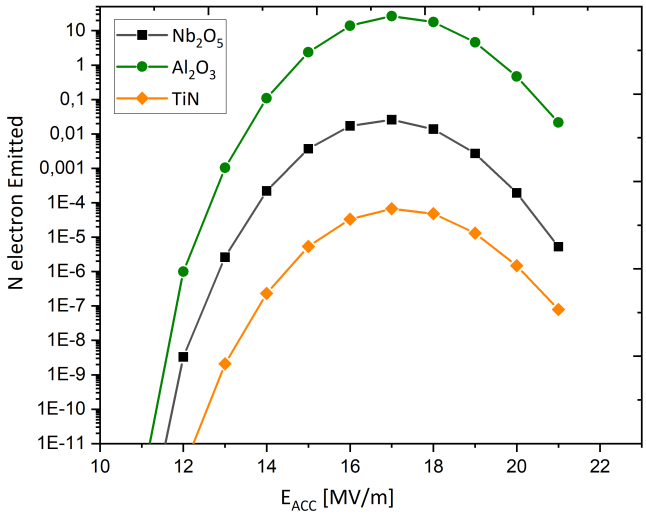

Figure 6.3: Calculated number of secondary electron emitted in a 1.3 GHz niobium cavity as a function of the accelerating field coated with Al_2O_3, TiN or with its native oxide Nb_2O_5

Figure 6.3 shows that there is a maximum in the number of secondary electron emitted in the 1.3 GHz cavity around 17 MV/m which is in good agreement with our previous observation on the multipacting onset of the Al_2O_3 coated cavity (see figures

[3]We acknowledge the help of our CEA colleague Enrico Cenni in performing these simulations.

5.19 and 5.20). The simulation indicates that the high SEY of Al_2O_3 is responsible for the observed multipacting barrier. Moreover, it suggests that coating the cavity inner-walls with a 5 nm TiN film can reduce the multipacting probability by 6 orders of magnitude compared to that in the Al_2O_3-coated cavity. The number of emitted electron can even be reduced compared to a bare niobium cavity.

6.3.3 First RF test of 1.3 GHz cavity coated with 5 nm of TiN

In order to put into test the numerical simulations, we added a 5 nm TiN coating inside of the previously tested Al_2O_3-coated cavity and tested its performance under RF fields.

Figure 6.4 summarizes the performances of the cavity after the TiN coating. We witnessed a strong degradation of the performance of the cavity: The quality factor decreased by more than a factor of 100 in comparison with its previous performances and the surface resistance was more than 100 times higher at 1.4 K. Due to the very low quality factor, we couldn't increase the E_{acc} up to 17 MV/m to see whether the multipacting barrier is still present after the TiN coating.

Given the high surface resistance of the cavity, we suspected that the 5 nm thickness of the TiN was probably not the most suitable choice for SRF cavities. As a matter of fact, TiN has a superconducting temperature of 4.2 K but when deposited as a thin film, it shows a metallic behavior down to sub kelvin temperature. The presence of a normal metal within the RF penetration depth have induced additional losses under RF fields which explains the degradation of the quality factor of the cavity. In light of these findings, we decided to look for the optimal thickness of the TiN coating that can suppress multipacting but at the same time maintain a reasonable quality factor of the coated cavity. In other terms, we are looking for a combination of a low SEY and a highly resistive TiN film.

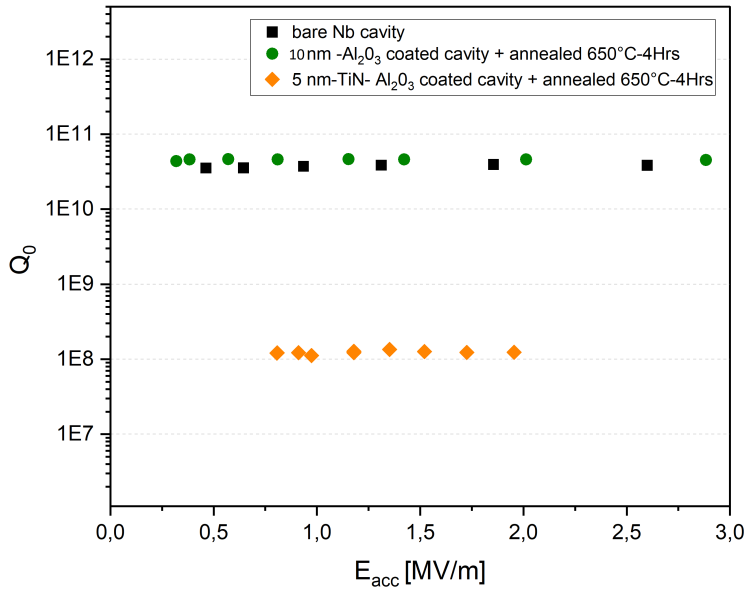

(a) Quality factor as a function of the accelerating gradient at 1.4 K

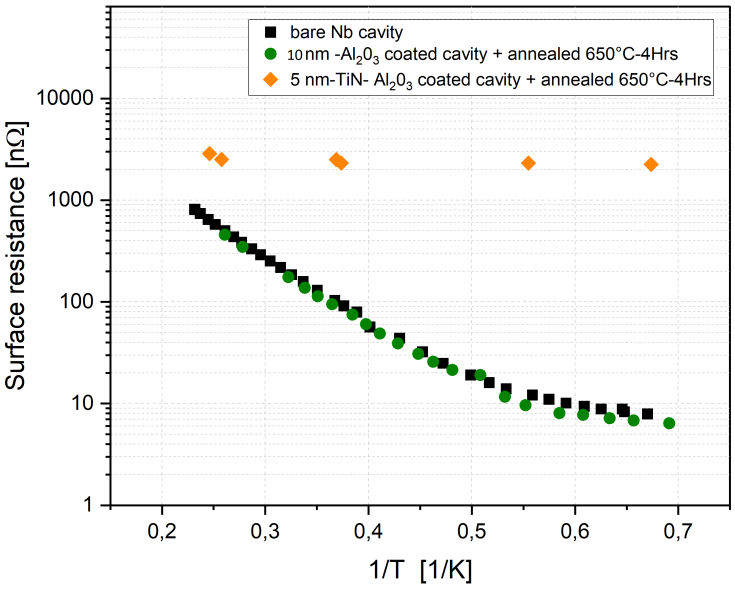

(b) Surface resistance as a function of the temperature at 1 MV/m

Figure 6.4: RF test of the bare niobium cavity (in black), Al_2O_3 coated niobium cavity annealed during 4 hours at 650°C (in green) and TiN (5 nm)-Al_2O_3(10 nm) coated cavity annealed during 4 hours at 650°C (in orange).

6.4 Minimum thickness of TiN for multipacting mitigation in SRF cavities

6.4.1 Secondary emission yield measurements

To establish the minimum thickness of the titanium nitride coating that provides a sufficiently low SEY while granting an insulator behavior under RF, several Al_2O_3-TiN samples were prepared by thermal ALD with different TiN thicknesses. The thickness of the TiN film was controlled by varying the number of ALD cycles N, whereas the thickness of Al_2O_3 film was kept constant for all the samples: 100 cycles of Al_2O_3 was deposited on all the Si substrates.

SEY measurement on the TiN-Al_2O_3 samples as deposited

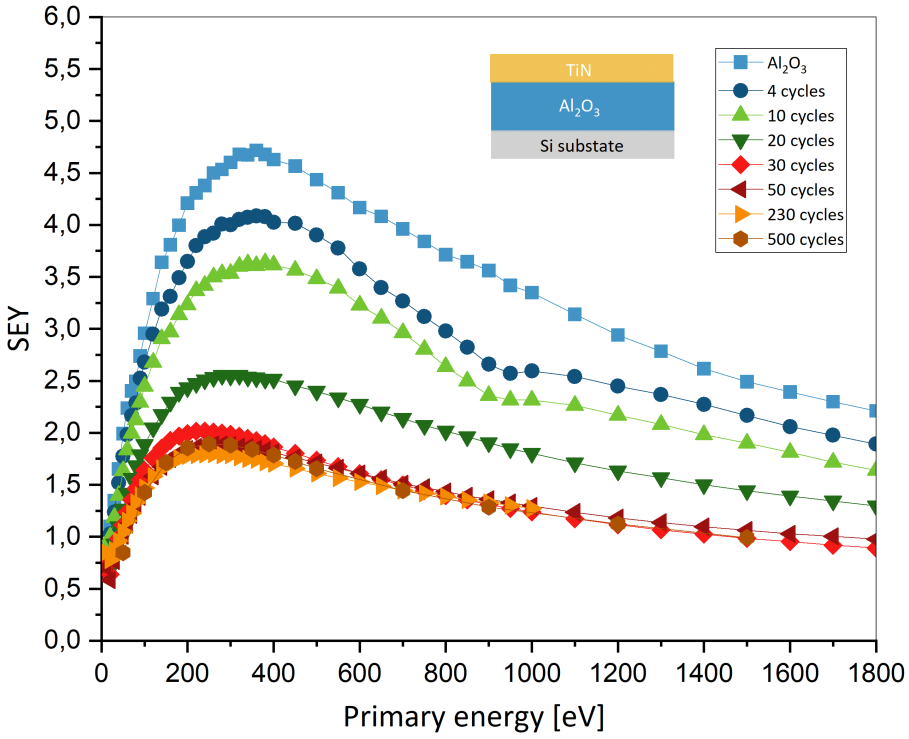

Figure 6.5: SEY measurements on TiN-Al_2O_3 coated Si samples

Figure 6.5 shows the SEY curves measured as a function of primary electron energy, which varies between 0 and 1800 eV.

- All the SEY curves shows a typical first-increase, later-decrease behavior of the SEY coefficient where the SEY first increase with the energy of the primary electrons until it reaches a maximum value of SEY_{max} at energy E_{max} than decreases again when increasing the primary electron energy.

- The SEY of the bare Al_2O_3 film shows a SEY_{max} of 4.65 at around E_{max} = 320 eV which agrees well with literature results [84].
- The SEY of the TiN coated samples progressively decreased when we increased the number of TiN ALD cycles.

SEY measurement on the TiN-Al_2O_3 samples after conditioning with

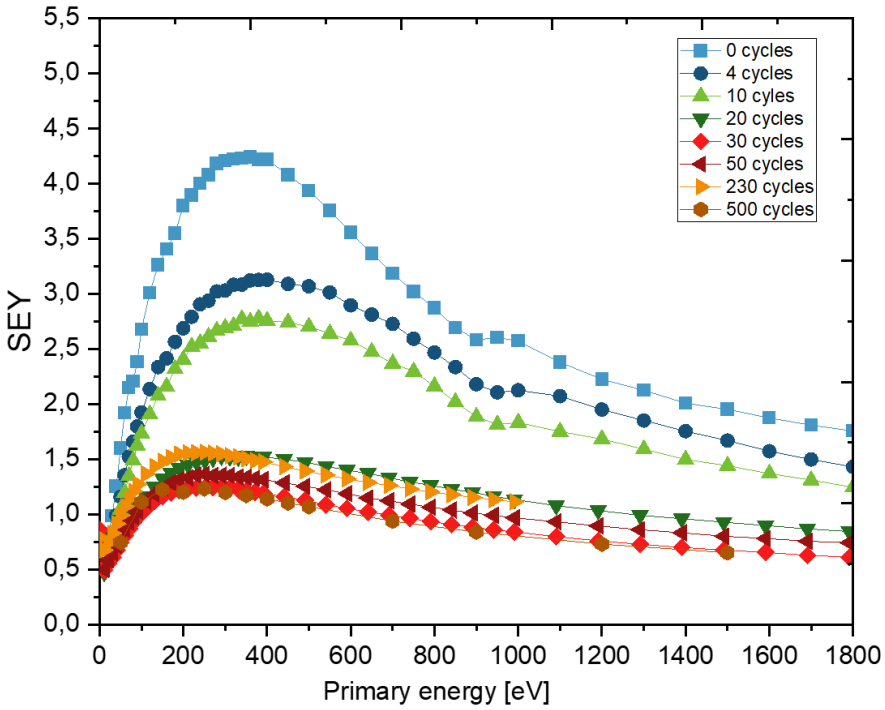

Figure 6.6: SEY measurements on TiN-Al_2O_3 coated Si samples after conditioning with a 400 mC/mm^2 dose

For several RF systems used in particle accelerators, the SEY of the RF exposed surface decreases along the operation time. This effect is refereed to as conditioning and have been accredited to the several surface modifications induced by electron bombardment. To investigate the conditioning effect on the SEY of our ALD-deposited films, we measured the SEY of these samples after they have been conditioned by electron bombardment, with electrons of energy 500 eV and a dose of 400 mC/mm^2.

The SEY curves after conditioning are shown in figure 6.6. The SEY of all the samples decreased compared to their initial value before conditioning as widely reported in literature [85, 91, 92, 93]. For instance, after 400 mC/mm^2 dose of electron bombardment, the SEY of the bare Al_2O_3 films decreases from 4.65 to 4.22. It decreased from 4.02 to 3.12 for the 4 cycles film and reaches an almost constant value of 1.35 starting above 30 cycles of TiN.

Summary of SEY measurements

Figure 6.7 summarizes the maximum values SEY_{max} for TiN coated Al_2O_3 film before and after conditioning for better comparison between the different ALD number of TiN cycles and their corresponding SEY. The 2 point resistance was also measured and plotted as a function of the number of TiN ALD cycles (in blue).

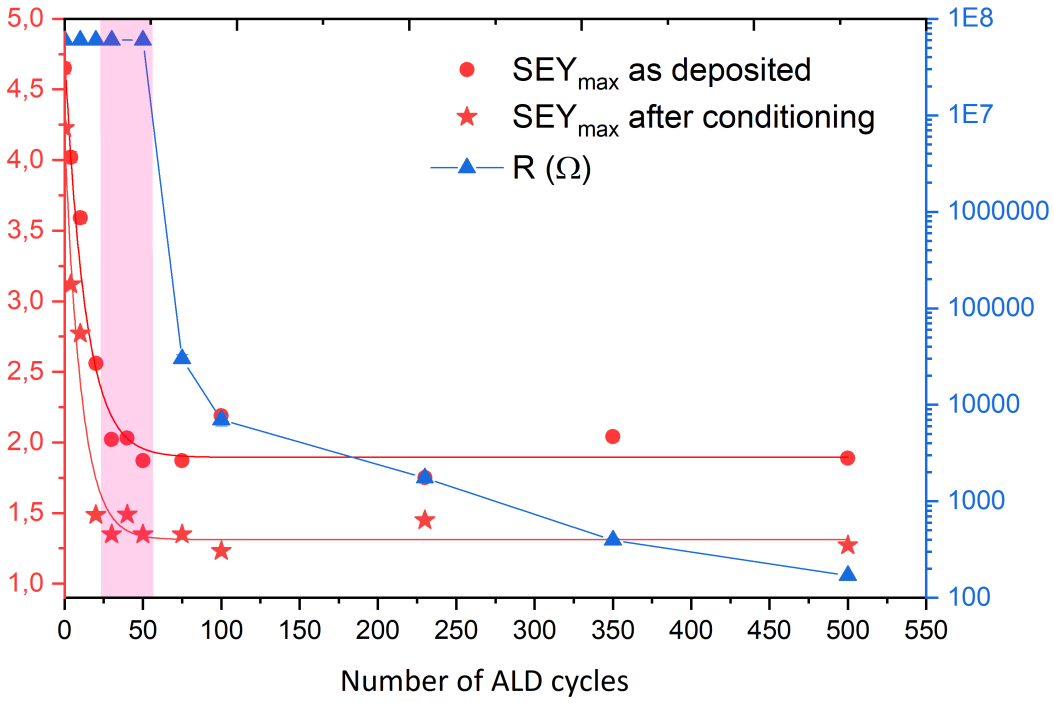

Figure 6.7: Summary of the resistance and SEY_{max} measurements on the TiN-Al_2O_3 coated Si samples as a function of the number of TiN ALD cycles

- The SEY shows a clear exponential dependence of the TiN ALD cycles. Fitting the curve with an exponential decay function $SEY_{max} = SEY_{offset} + A \exp \frac{-(N-N_0)}{t_1}$, we found out that the decay constant $t_1 = 13.09$ of ALD TiN cycles , $SEY_{offset} = 1.89$, $N_0 = 1$ and A=2.67. The same applies for the SEY values after 400mC dose, where the exponential dependence is maintained and gives a $t_1 = 10.09$ of ALD cycles , $SEY_{offset} = 1.31$, $N_0 = 0.08$, and A=2.86.
- The SEY of the Al_2O_3-TiN films showed significantly lower SEY_{max} than that of the Al_2O_3 film:
  - For the N $<$ 50 cycles of TiN, which corresponds to the nucleation regime of ALD processes with partial surface coverage, we notice a significant reduction of the SEY when increasing the number of ALD cycles: the SEY decreases from 4.02 to 1.87 upon increasing the number of ALD cycles from 4 to 50. These results highligthts how sensitive the SEY is with respect to the very surface chemistry. In this regime, the electrons

emitted by the surface originates both from the Al_2O_3 film and the TiN overlayer. The SEY measured is governed by both material properties. The resistance measured on these films showed high values (above 10^8 Ω).

– For N > 50 cycles of TiN, SEY_{max} no longer evolves because it is now dominated by the overlayer of TiN with a thickness d > 2 nm as determined by XRR (see section 6.4.2), in this bulk-like regime, the TiN film is very likely to be continuous. The SEY curves of all TiN films with N> 50 are identical. The TiN films resistance decreased exponentially upon increasing N from 50 to 500 to reach 170 Ω.

Based on these results, we can recognise a window ranging from 20 to 50 cycles (coloured in pink in figure 6.7) where the SEY is interestingly low (∼ 1.9 and decreases to ∼ 1.35 after conditioning) whereas the film has a high resistance which is very appealing for coating our RF cavity.

6.4.2 TiN film thickness and growth

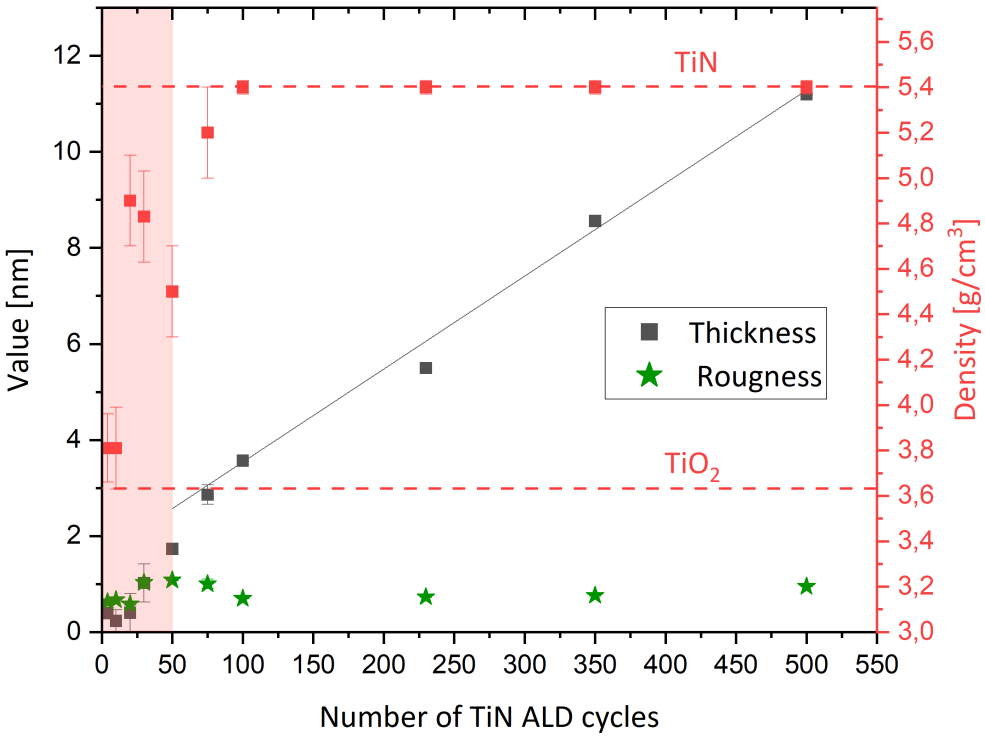

Figure 6.8: X-ray reflectivity measurements on the TiN-Al_2O_3 coated Si samples as a function of the number of TiN ALD cycles

In order to have a full understanding of the growth mechanisms of the ALD-deposited TiN, X-ray reflectivity were used to determine the thickness, density and

roughness of the TiN films. They are plotted as a function of N the number of ALD deposition cycles in figure 6.8.

We notice two growth regimes of the TiN film:

- For N $>$ 50, the film density remains constant and equal to 5,4 g/cm^2, which is consistent with the density of bulk-like TiN film. We observe a linear dependence of the thickness with number of ALD cycles with a GPC equal to 0.019 nm/cycle which agrees well with an ALD growth mechanism and confirms the precise thickness control of the ALD process.

- For N $<$ 50, we notice that the density of the film is intermediate between the density of the bulk TiN and the density of TiO_2 at 3,6 g/cm^2 which indicates a strong presence of titanium oxide in the film chemical composition.

If we look closely at the region from 0 to 50 ALD cycles, it can be seen that the roughness and thickness are very close in value for the films below 50 ALD cycles. This is due to the nucleation phase which is widely referenced for ALD film growth. This can be a sign that the film grows by first forming islands and increasing the number of ALD cycles the islands sizes grow progressively until they coalesce to form a continuous film. In this regime, the roughness value is close to the film thickness, as observed. In addition, it is worth-noting that for such film thicknesses, the measurement errors bars are comparable to the values obtained for 4, 10 and 20 cycles. However, despite the high uncertainties on the thickness values, we can estimate a growth rate per cycle in this region equal to 0.027 nm/cycle, which is about 50 % times higher than the GPC found for films with N $>$ 50. A possible explanation is that for N$<$ 50, the Al_2O_3 film is not yet completely covered. In this case, because Al_2O_3 is richer in -OH reactive sites than TiN, the growing TiN film can show a higher GPC when it grows on Al_2O_3 to that on TiN itself.

Based on the density values of the 30 $\sim$ 50 cycles TiN films, It seemed that these films contain a high concentration of oxygen which can also explain their high resistance as seen in figure 6.7.

At this point, we need to extract a more reliable value of average thickness, or "amount of Ti" deposited for TiN film $<$ 50 cycles. In the following section, XPS will be used to estimate the film thickness and investigate their chemical composition.

6.5 XPS analysis on TiN films

6.5.1 Sub-nanometer film thickness estimation

XPS analysis have been performed on our TiN-Al_2O_3 coated Si samples in order to study the film's chemical composition and estimate the TiN overlayer thickness for the sub-nanometer films i.e films below 50 cycles of ALD where the XRR fits shows large uncertainties. Figure 6.9 shows the Ti-2p and N-1s core level spectra obtained with different number of TiN ALD cycles whereas figure 6.10 summarizes their respective areas.

As it can be seen in figure 6.10, the areas of the Ti 2p and N 1s shows a linear dependence upon increasing the number of ALD cycles from 0 to 40 until it reaches

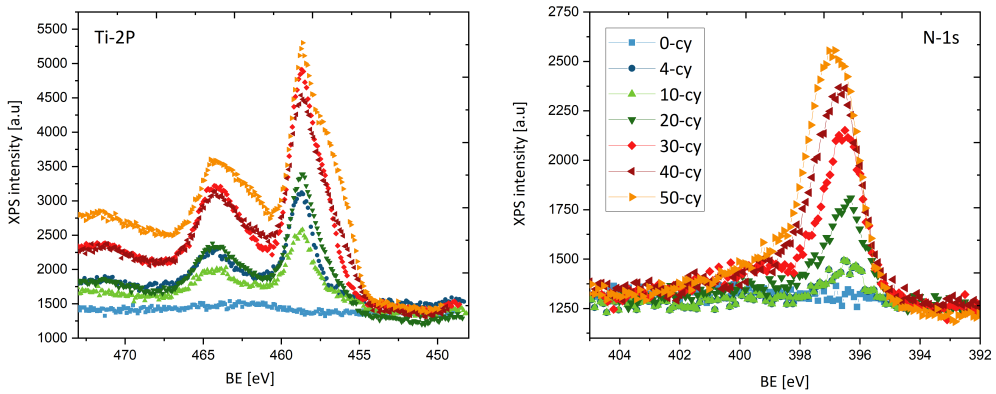

Figure 6.9: The XPS Ti-2p and N-1s core level spectra of the TiN-Al_2O_3 coated Si samples with the number of TiN ALD cycles from 0 to 50

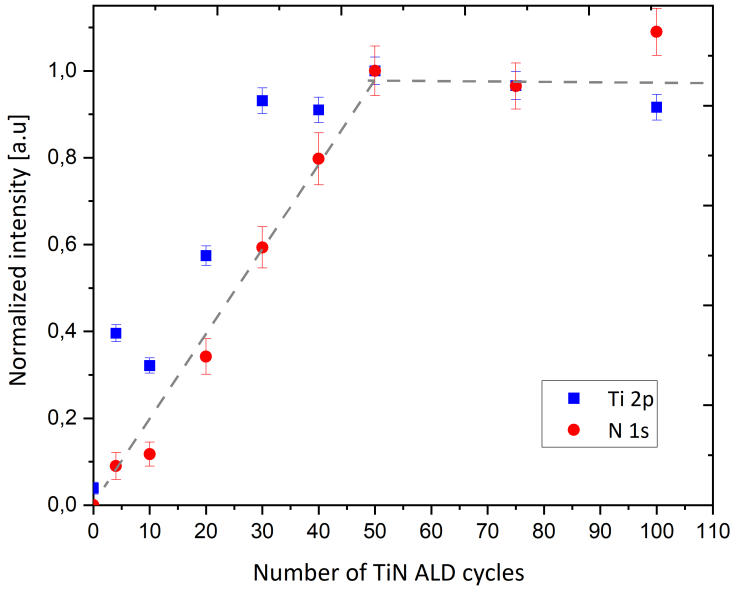

Figure 6.10: The XPS Ti-2p and N-1s intensities of the TiN-Al_2O_3 coated Si samples with the number of TiN ALD cycles from 0 to 100

saturation at 50 cycles. This observation can be explained by the fact that the areas measured are proportional to the amount of Ti and N present on the surface as long as the TiN thickness is lower than the escape depth of photo-electrons. Beyond this characteristic depth of few nanometers, the TiN thickness increases but the area of the Ti-2p and N-1s signals saturates.

Given the fact that the our Ti-2p signal is in fact a combination of pure TiN, titanium oxide TiO_2 and oxynitrides TiO_xN_Y signals (see section 6.5.2) , we can not extract the thickness of TiN but rather an average thickness of deposited Ti and N.

Starting with the TiN thickness of the 50 cycles film measured with XRR with reasonable error bar, we can calculate an estimated thickness of deposited Ti (d_{Ti})

and deposited N (d_N) on the surface using a simple proportionality rule. These estimated values are plotted in figure 6.12 and compared to values previously obtained with XRR. We can therefore calculate a CPG of 0.043 nm/cycle.

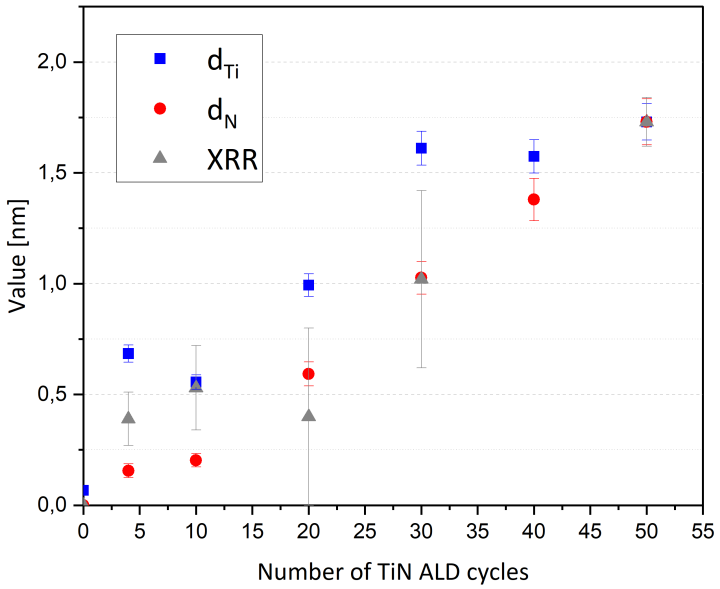

Figure 6.11: Estimation of TiN film thickness using XPS measurements

6.5.2 Chemical composition of TiN films

In order to study the chemical composition of TiN films, the Ti-2p core level spectra have been fitted using CasaXPS software [49]. We used three core level components and a Shirley type background:

- The TiN component of Ti 2p region was fitted with a line shape extracted from the Ti 2p spectrum of a clean TiN surface deposited by ALD, the corresponding Ti $2p^{3/2}$ signal is described by a major peak at 455.7 eV ± 0.5 eV and by a shake-up satellite at 457.9 specific to TiN [94].
- The TiO_2 oxide layer component which is characterized by a broad peak at 458.7 eV [94].
- The TiO_xN_Y oxynitrides component at a binding energy of 457.0 eV [95].

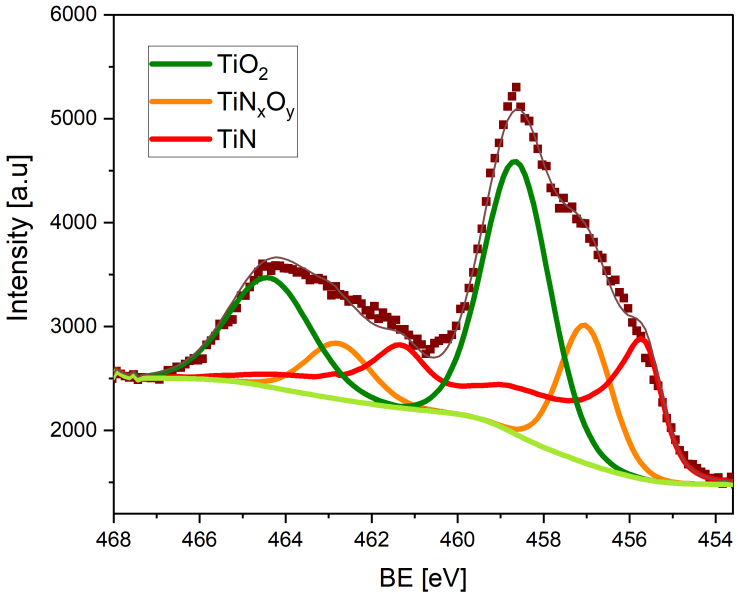

Figure 6.12: The fitted Ti-2p core level spectra of the TiN film with 50 ALD cycles

Figure 6.13 summarizes the chemical composition of TiN films as a function of the number of ALD cycles used. The chemical composition of TiN films shows significant dependence on the layer thickness i.e. the number of ALD cycles: We found that the 4 cycles film of TiN is mainly composed of TiO_2 oxides. The fitting of the Ti 2p window gives a film composition of 87.5 ±3 % of TiO_2 with 9± 1.7 % of TiN and 3.5±2.5 % of oxynitride TiO_xN_Y. When increasing the number of ALD cycles, the percentages of pure TiN in the films increases continuously until it reaches 54.25 ±0.4 % in the 230 cycles film, whereas the percentages of TiO_2 decreases to reach 26.8 ±0.5 % for the same film. The percentage of oxynitrides in the films shows an increase from 3.5±2.5 % at 4 cycles to 17.6 ±2.5 % for the 50

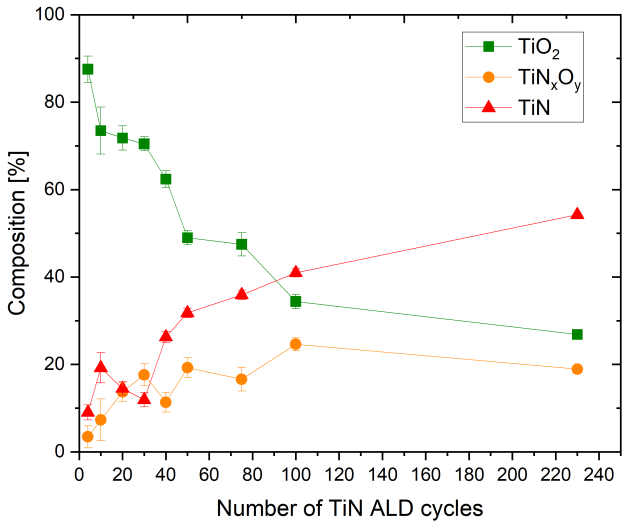

Figure 6.13: The chemical composition of the ALD-deposited TiN films as a function of the number of ALD cycles

cycles film, and then remains constants for thicker films. As postulated in section 6.4.1, ultra thin films (N<50) have a high TiO_2 concentration which explains their high resistance. Upon increasing the film thickness, the composition gets closer to pure TiN film and their resistance decreases accordingly.

6.6 Electron bombardment of thin TiN films and its effect on the SEY

As mentioned in section 6.4.1, electron bombardment of a surface with doses in the 10^{-3} mC/mm^2 have been widely reported to reduce significantly the SEY. In order to understand the origin of the SEY modification after the conditioning by electron bombardment on our sample, XPS spectra have been taken on the as deposited films without any conditioning and after different electron doses.

6.6.1 40 cycles TiN film

Figure 6.14 shows the evolution of the SEY curves on 40 cycles TiN film, we notice that the SEY_{max} decreases from 2 to 1.5 when the sample is conditioned with an electron dose of 400 mC/mm^2.

In order to understand the origin of the SEY variation after the conditioning by electron bombardment on our sample, XPS spectra have been taken on the as deposited films without any conditioning and after 400 mC/mm^2 dose.

Figure 6.15 shows the composition of the Ti 2p core-level spectrum before and after conditioning. We observe a reduction of titanium oxide TiO_2 component into oxynitride TiO_xN_Y.

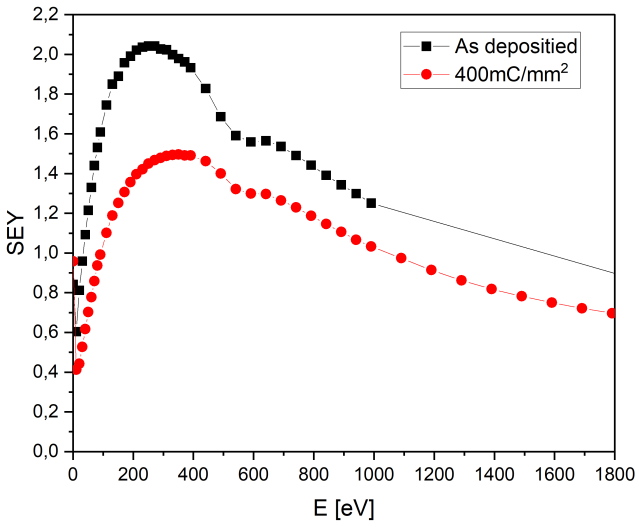

Figure 6.14: SEY of the 40 cycles - TiN film

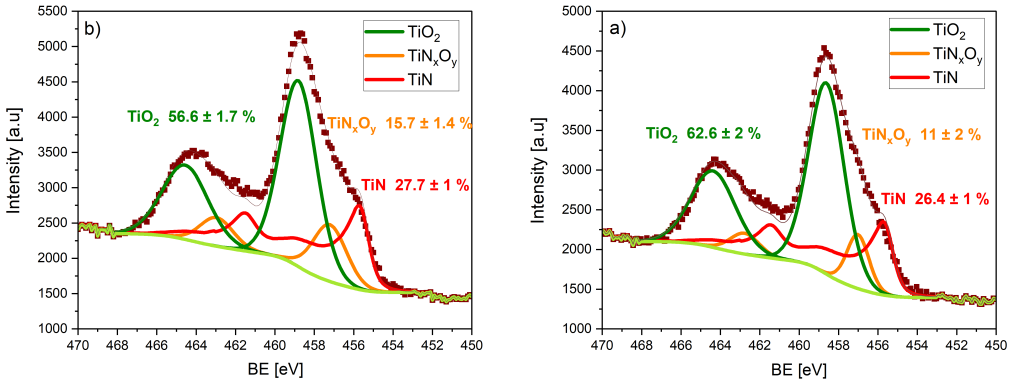

Figure 6.15: Composition of the 40 cycles TiN film: (a) as deposited (b) after conditioning with 400 mC/mm^2 dose

The effect of conditioning have been commonly explained by the fact that electron impinging on the contamination layer transform it into a graphite-like thin film of carbon which reduces the SEY thanks to its sp2 hybridization state [96]. When conditioning our 40 cycles TiN film, we did not observe this effect[4]. However, when conditioning a 50 cycles TiN samples by increasing progressively the electron dose, we did notice a transformation of the adventitious carbon [97] into a graphite-like chemical state.

6.6.2 50 cycles TiN film

For the 50 cycles TiN film, we noticed that when we increase the electron doses from 8 mC/mm^2 to 400 mC/mm^2, the SEY$_{max}$ decreases from 1.55 to 1.35 as it can be

[4]No intermediate doses have been tested on the 40 cycles sample

seen in figure 6.16.

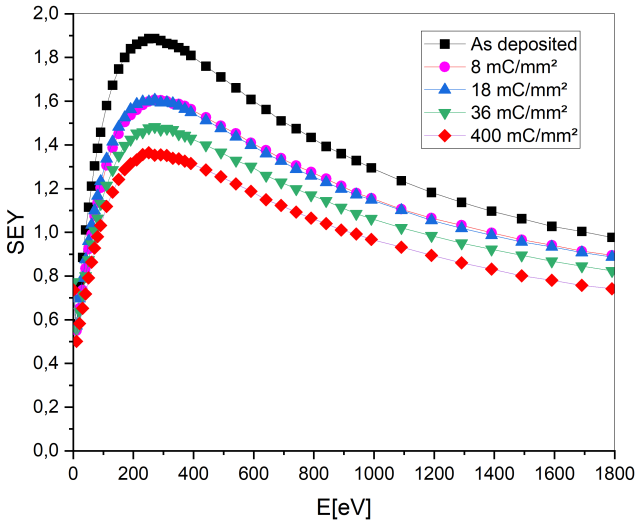

Figure 6.16: SEY of the 50 cycles - TiN film

The Ti 2p and the C 1s core level spectra have been recorded after each electron dose and fitted as shown in figure 6.17 and summarized in figure 6.18.

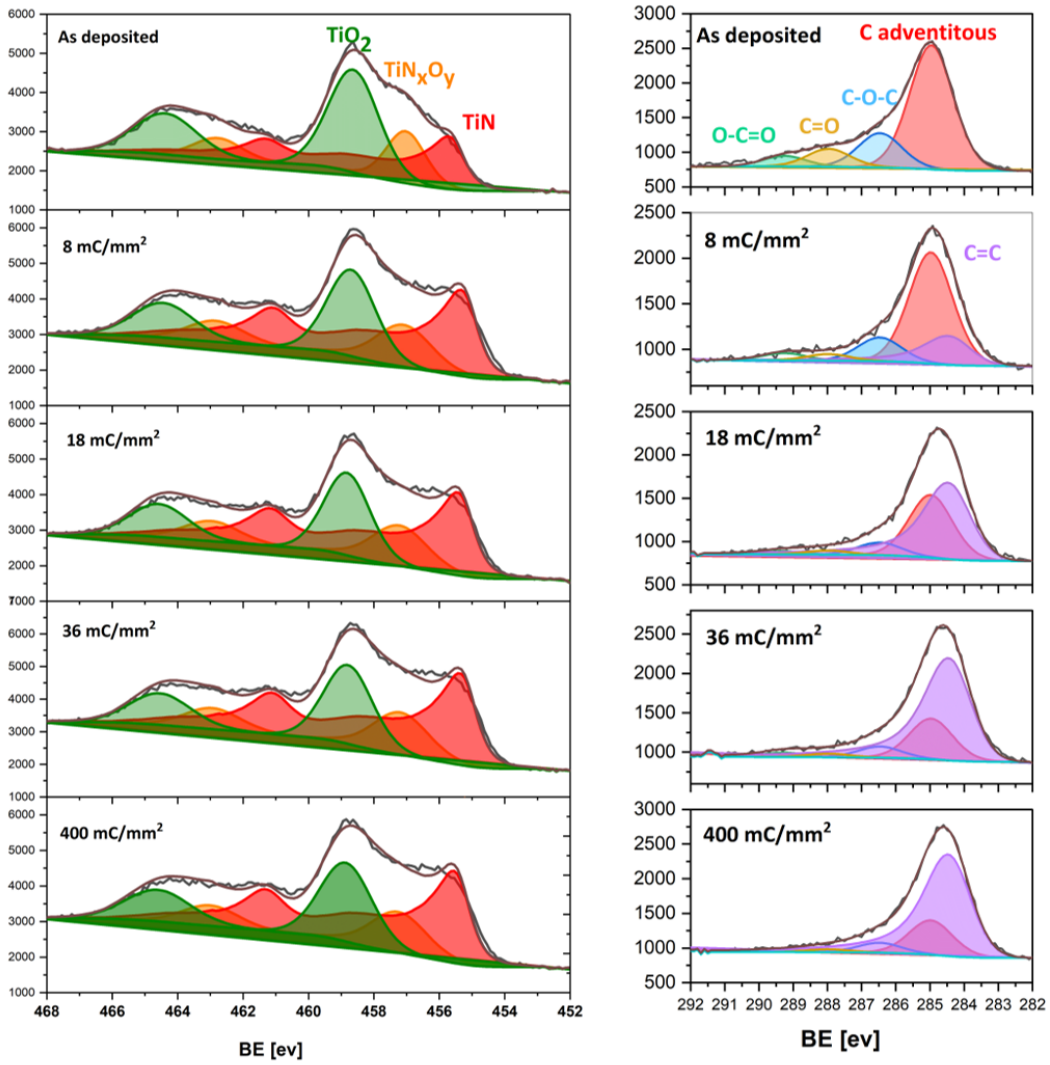

Figure 6.17: Ti 2p and C 1s core level spectra of the 50 cycles TiN film

The Carbon 1s spectra were best fitted with a shirley-type background and mixed Gaussian/Lorentzian functions. The as deposited C 1s spectrum can be decomposed into a main peak at a BE= 284.9 eV with a FWHM = 1.5 eV coming from the sp^3 hybridized C atoms in C-C and C-H bonds and three weak peaks accounting for the C-O-C, O-C=O and C=O bonds at binding energies of 286.5, 289.3 and 288 eV respectively. We noticed that when increasing the electron dose, the peaks attributed to C-O-C, O-C=O and C=O bonds decreases significantly and converts the sp^3 hybridized C atoms into a graphite-like sp^2 bonds fitted with an asymmetric peak at a BE=284.5 eV as suggested in [96].

When fitting the Ti 2p spectra, we noticed that, when increasing the electron dose, the TiO_2 component of the film decreases while the TiN increases which suggest that the electron-bombardment causes a reduction of the Ti oxides that covers the TiN film.

Based on our experiments, unlike the change in the carbon hybridisation state

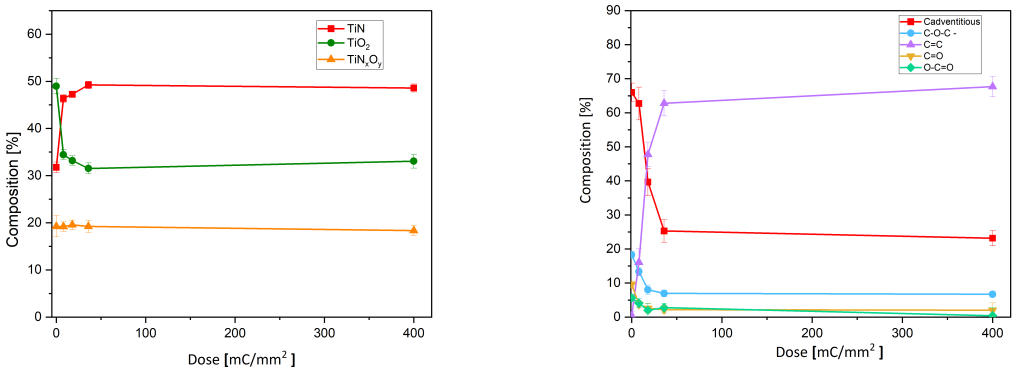

(a) C 1s

(b) Ti 2P

Figure 6.18: Summary of Ti 2p and C 1s core level spectra of the 50 cycles TiN film

that have been observed on some of our samples, the reduction of the TiO_2 after conditioning have been systematically observed.

6.7 Test on 1.3 Ghz cavity

6.7.1 Thermal stability on niobium

At this point of our research, We have managed to find a suitable range of TiN coating thickness where we have promising SEY properties and high electrical resistance. However, in order to test this approach into an Al_2O_3 coated niobium cavity, we need to assess the thermal stability[5] of (1 ∼2 nm) thin film of TiN on top of a Al_2O_3 coated niobium substrate.

To this end, we performed the deposition of 50 cycles ∼ 2 nm of TiN on a 10 nm Al_2O_3 coated niobium sample, we annealed the sample at 650°C during 10 hours under vacuum in order to examine it using XPS profiling. The depth profile is plotted in figure 6.20. The profile shows clearly two distinct layers of TiN and Al_2O_3 on top of the niobium substrate.

[5]The subsequent annealing is necessary to dissolve niobium native oxides as explained in chapter 5

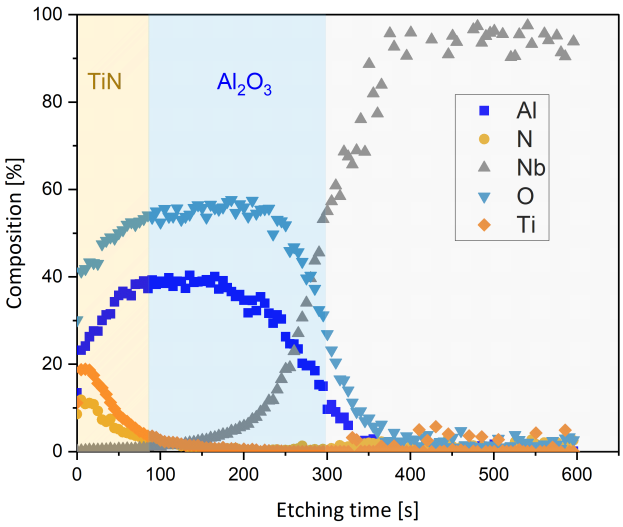

Figure 6.19: XPS depth profile of TiN-Al_2O_3-Nb sample after annealing at 650°C during 10 hours under vacuum

6.7.2 RF test on 1.3 Ghz Niobium cavity

In order to put to test our findings, we performed a Al_2O_3 coating on an electro-polished bare niobium surface and annealed it at 650°C during 10 hours in vacuum, then tested the cavity under RF fields(This RF test is already shown in section 5.20). The Al_2O_3 coating gave rise to a sharp multipacting barrier at 17 MV/m. Once we added a 40 cycle of TiN coating, the multipacting barrier vanished which clearly proves that the 40 cycles TiN coating played an effective role in suppressing multipacting. We noticed also an overall degradation of the Q_0 of the cavity that still remain acceptable Q values for operation. Possible reasons for this degradation is that the cavity have been annealed twice (before and after the TiN deposition). Further investigations are needed to explain this observation.

It is important to mention that during the RF test, the onset of multipacting was recognized around 20 MV/m, so we performed some processing by allowing multipacting to progress for few minutes while slowly increasing the RF power [98]. This was sufficient to stop the multipacting.[6]

[6]Processing RF cavities during the vertical RF test can be assimilated to the "conditioning" .

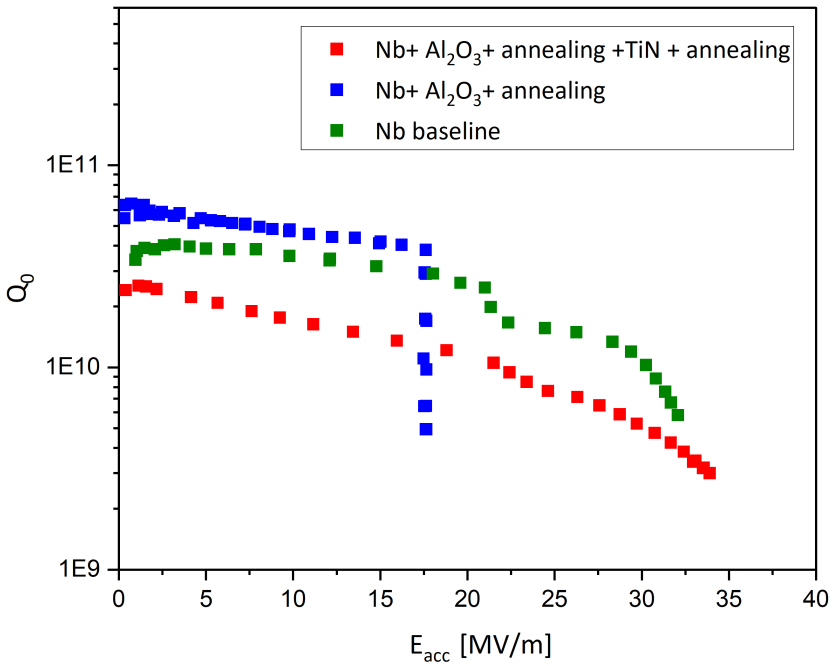

Figure 6.20: RF test of the 1.3 GHz cavity with different surface treatment

6.8 Summary

Throughout this chapter, we investigated the possibility of coating niobium cavities with TiN as a multipactor suppressor: We established that the minimum thickness of the TiN coating is around $1 \sim 1.5$ nm (30 to 50 cycles of ALD) and we studied their chemical composition using XPS and their thermal stability after annealing. A first test on an RF cavity proved indeed the effectiveness of these extremely thin films in multipacting mitigation. For our project, we focused on applying this approach into a RF cavity but it can easily be applied to several others RF devices.

Chapter 7

ALD-deposited multilayer to improve the superconducting performances of RF cavities

7.1 Introduction

For approximately five decades, niobium resonators have been the best RF accelerating cavities available for accelerators. Thanks to the huge research efforts made by the SRF community, maximum accelerating gradients with values above 40 MV/m at 2 K[1] have been reliably achieved. Such accelerating gradients induces a surface magnetic field in the cavity close to the Nb critical field H_{c1} of 176 mT , which means that we are approaching the theoretical limit for bulk niobium technology. Any further increase in the maximum accelerating gradient would inevitably need a new superconducting technology.

As introduced in section 3.3.3, in 2006, A. Gurevich proposed a multilayer approach (also referred to as SIS structure) that could outperform the bulk Nb cavity [1]. This approach consists in coating the inner surface of a Nb cavity with an alternating superconducting layers (S) and insulating layers (I) (as illustrated in figure 7.1).

This approach is based on an interesting particularity of very thin superconducting films: When the superconducting film thickness is lower than their penetration depth (d $<$ λ), it becomes thermodynamically difficult for parallel vortices to be stable. This property also manifest itself in a strong enhancement of H_{c1} for thin superconducting films. The effective $H_{c1}^{'}$ of a superconductor with a thickness d $<$ λ can be expressed as:

$$H_{c1}^{'} = \frac{2\phi_0}{\pi d^2} \ln\left(\frac{d}{1.07\xi_0}\right) \tag{7.1}$$

where ϕ_0 is the magnetic flux quantum and ξ_0 is the coherence length.

According to Gurevich theory, this multilayer would lead to a potential shielding effect toward the bulk Nb if tailored properly inside the cavity. This could push the limit of the maximum surface magnetic field that a cavity can withstand

[1] 1.3 GHz "Tesla shape" elliptical cavities at 2 K. It corresponds to $\sim$ 170 mT, i.e. very close to the theoretical limits of Nb.

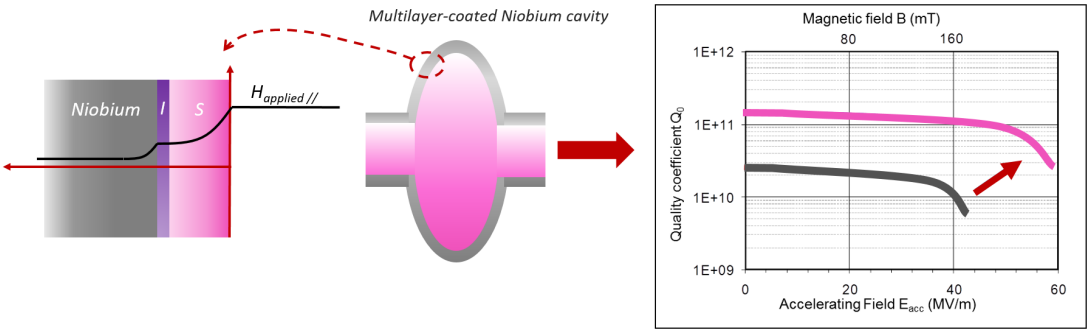

Figure 7.1: Illustration of the multilayer structure inside a Niobium cavity after [1]

and therefore further increase the maximum accelerating gradient. Another potential advantage of this approach is to benefit from the lower BCS resistance R_{BCS} of high T_c superconductors and therefore further increase the quality factor Q_0 of the resonator. The insulating layer (I) serves as a protection layer against vortex penetration avalanche. It would intercept the propagating vortex and limit their dissipations.

7.2 State of the art

The aim of this work is to test this promising, yet not enough explored, approach on an SRF cavity. Several experimental studies have been led in this direction using different combination of SIS structures: For instance, an SIS structure based on Nb films (as the superconductor) and Al_2O_3 (as the insulator) at INFN using DC and RF magnetron sputtering showed a clear improvement in the H_{c1} due to multilayer coating [99]. Another promising results have been also achieved using an SIS multilayer based on niobium natride NbN (S) and magnesium oxide MgO (I) measured at CEA saclay [100, 101] and the college William & Mary [102]. The first penetration of vortices in the multilayer appears to be postponed and the RF surface resistance of a NbN/MgO/Nb was shown to be lower than that of bulk Niobium. Another interesting SIS structure was studied at Jefferson Lab [34] using NbTiN as a superconducting layer (S) and AlN as an insulating layer (I) on niobium where the surface resistance of the multilayer was shown to be lower than the bulk for a temperature above 4 K. These preliminary results emphasize on the potential of multilayers in postponing flux penetration inside SRF cavities. Nonetheless most of these measurements were performed using SQUID magnetometery in the DC range or third harmonic measurements (described in [103]) at low frequencies which complicates any predictions for SRF cavities. Moreover, all of these studies were conducted on Nb coupons or at best on flat disks of sample cavities. To this day, no Niobium cavity have ever been successfully coated with an SIS structure and tested to prove Gurevich predictions. The main reasons behind this belatedness are the technological difficulties that comes with depositing a high quality superconducting film whose thickness is barely few hundreds of nanometers thick uniformly inside a complex shape object such as a Nb superconducting resonator. Thin film supercon-

ductors tend to have lower critical temperatures and overall degraded performances in comparison with the bulk due to lattice strain, poor crystallinity and smaller mean free path in general. Furthermore, most of the studies conducted up to now use line of sight deposition techniques such as magnetron sputtering which makes it difficult to adapt the process to an RF cavity geometry.

Throughout this chapter, we will present the development of a multilayer structure using atomic layer deposition ALD. Our multilayer is composed of a thin film of niobium titanium nitride NbTiN as the top superconducting layer (S), an aluminium nitride AlN layer as an insulating layer (I) and bulk niobium as the main superconductor. Chemical and structural properties of the NbTiN films will be discussed as well as their superconducting performances. Optimization of these performances were conducted on cavity grade Niobium substrates and led to an optimized SIS recipe with a critical temperature of 16 K.

7.3 Choice of the multilayer structure

7.3.1 Choice of the superconductor

Although other superconductors such as Nb_3Sn and MgB_2 have higher critical temperatures with T_c respectively at 18 K and 39 K, Their deposition is solely based on sputtering techniques and remains inaccessible by ALD to this date. Moreover, they are very sensitive to radiation damage and crystalline disorder. B1-compounds such as NbN and NbTiN have, on the other hand, have very attractive superconducting properties and present considerable advantages when it comes to our particular application.

- The binary niobium nitride NbN have a NaCl-like cubic structure (δ-phase) with a bulk critical temperature up to 17 K. Yet, this phase exists over a narrow window of nitrogen content. Outside this window, other non-superconducting phases can form which gives rise to films with lower critical temperatures. NbN also presents high resistivity due to presence of vacancies in the lattice. As explained in chapter 2, having a low resistivity in the normal state ρ_n is crucial to have low RF losses.

- Niobium titanium nitride NbTiN, on the other hand, presents all the advantages of NbN, in particular the high Tc of 17 K and offers a much lower resistivity in the normal state with the addition of Ti atoms in the lattice. As a matter of facts, NbTiN is the results of the miscible nature of the binary NbN and TiN compounds. TiN seems to be much less prone to nitrogen off-stoichiometry compared to NbN. Thus, adding Ti, which is a good nitrogen getter, seems to stabilize the δ-phase NbN and produce a lower resistivity compound while maintaining a high critical temperature.

Niobium titanium nitride have been deposited successfully using atomic layer deposition with good critical temperatures [36]. ALD offers the possibility to control the stoichiometry of $Nb_{1-x}Ti_xN$ films, which makes it possible to explore the potential of a wide range of $Nb_{1-x}Ti_xN$ compounds. On the ground of these reasons, our work

will be mainly focused on the study of NbTiN thin films and the optimization of their superconducting performances.

7.3.2 Choice of the insulator

Aluminum nitride (AlN) is an excellent insulator for our multilayer structure. It has a low dielectric constant of 4.8 at high frequency (implies moderate RF losses) as well as a high thermal conductivity among insulators (3 W/(m.K)). It exhibits a good chemical stability (melting point $>$ 2000°C). Its crystalline structure is compatible with the superconducting nitride films and easily deposited with ALD. AlN can be grown with a wurtzite structure with a= 3.11 Å, c= 4.98 Å or a metastable cubic lattice with a= 4.08 Å. However, when deposited using ALD, it is reported that thin films of AlN grew amorphous up to 500°C [36]. AlN is also reported to enhance superconducting properties of NbTiN thin films [104] and not to cause any contamination in the ALD-deposited NbTiN films [36] which makes it a very promising insulator for the multilayer.

7.3.3 Choice of the film thickness

According to Gurevich model, the superconducting layer must have a thickness smaller than the penetration depth of the material. In the case of NbTiN, λ is around 200 nm [34] so the superconducting layer thickness must not exceed this thickness. On the other hand, some studies [34, 36] reported that critical temperature of superconducting nitride thin films tend to increase when increasing the film thickness until it reaches a steady value around 50 nm. Moreover, given the low growth rate per cycle GPC of atomic layer deposition, a 50 nm film of NbTiN takes approximately 20 hours to be deposited, which makes it more practical to study films of 50 nm as a starting point for our research. Thicker films can be tested once we optimise the recipe for 50 nm NbTiN films. According to Kubo calculations [105] on a NbN-AlN-Nb multilayer, optimal screening can be obtained with a NbN thickness of 150 nm.

As far as the insulator layer is concerned, its thickness should be sufficient to prevent Josephson coupling between the two superconductors. Based on the theoretical calculations made by [105], a 10 nm layer of insulation between the niobium titanium nitride thin film and the bulk niobium would result in optimal vortex protection. Based on these arguments, we decided to study a layer of $\sim$ 50 nm of NbTiN on top of an AlN layer of $\sim$ 10 nm thickness deposited on bulk Niobium as a starting point for our study (see fiugre 7.2).

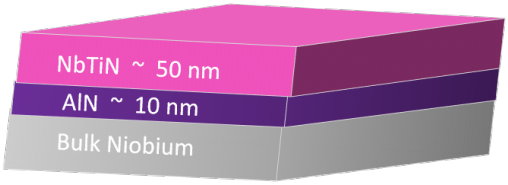

Figure 7.2: the multilayer structure studied in this project

7.4 ALD-deposition of the multilayer structure

7.4.1 ALD-deposition parameters

As a first step, NbTiN layers where grown on AlN films using our research-scale ALD system[2] at 450°C with 1 mbar of nitrogen as transport gas. Substrate used were bulk niobium coupons of (1 cm × 1 cm × 0.5 cm) size as well as witness silicon and sapphire wafers samples to benefit from their very low roughness (<1 nm) for characterizations such X-ray reflectivity. All Niobium substrates were previously electro-polished, cleaned and dried in a similar manner to that applied on cavities.

To deposit the AlN layer, we used a standard ALD recipe using $AlCl_3$ and NH_3 which resulted in an amorphous AlN film as reported in [36]. The AlN growth condition matches the ones of NbTiN, avoiding thermal cycling between the different alloy synthesis. For the deposition of NbTiN films, we used a combination of m cycles of NbN and n cycles of TiN as illustrated in figure 7.3. Each NbTiN supercycle is of the form of:

$$n(TiCl_4 + NH_3) + m(NbCl_5 + NH_3) = Nb_{1-x}Ti_xN \tag{7.2}$$

Where n is the number of TiN cycles and m is the number of NbN cycles. The n/(n+m) ratio will be referred to as the Ti/(Ti+Nb) ALD ratio.

NH_3 is pulsed for 0.5 s whereas $TiCl_4$ and $NbCl_5$ where pulsed respectively for 2.5 s and 1 s. Purge time after each pulse was maintained at 10 seconds for all cycles.

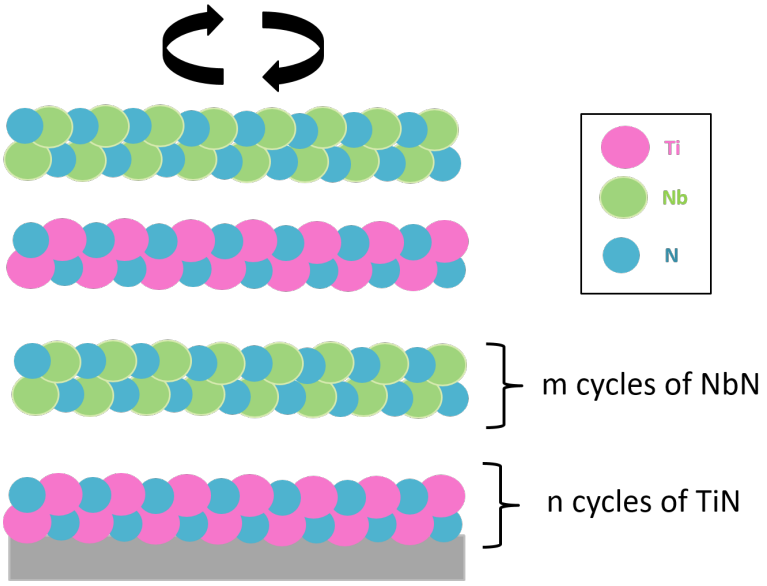

Figure 7.3: Illustration of the ALD process for NbTiN film deposition

7.4.2 X-ray reflectivity measurements

Several combinations of NbN and TiN cycles were tested to investigate the superconducting properties of different stochiometries of NbTiN films. In order to determine

[2]see chapter 4 for more details on the ALD technique and the research-scale system

the thickness, density and roughness of the deposited films, we performed X-ray reflectivity measurements in a 5-circle diffractometer (Rigaku SmartLab) with CuKα radiation from a rotating anode on the Si and sapphire witness samples (whose roughness is at the angstrom level) . The results of XRR curves are presented in figures 7.4 and 7.5:

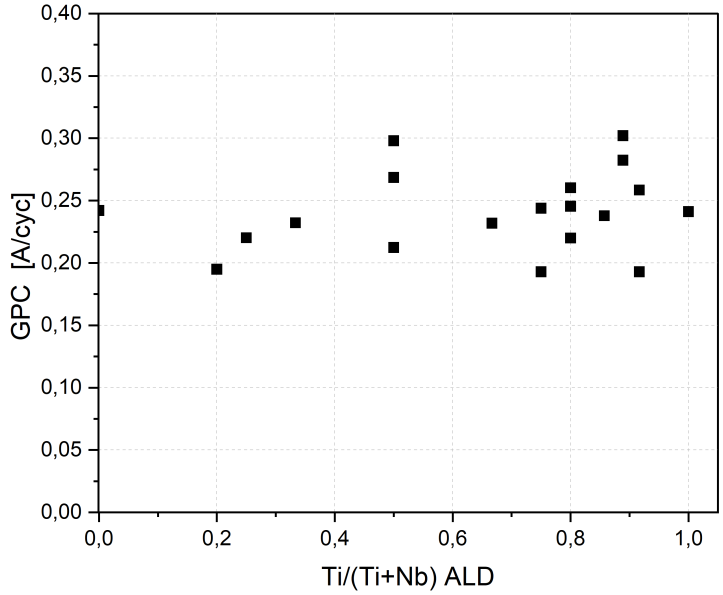

Figure 7.4: The growth rate per cycle of NbTiN films as a function of Ti/(Ti+Nb) ALD

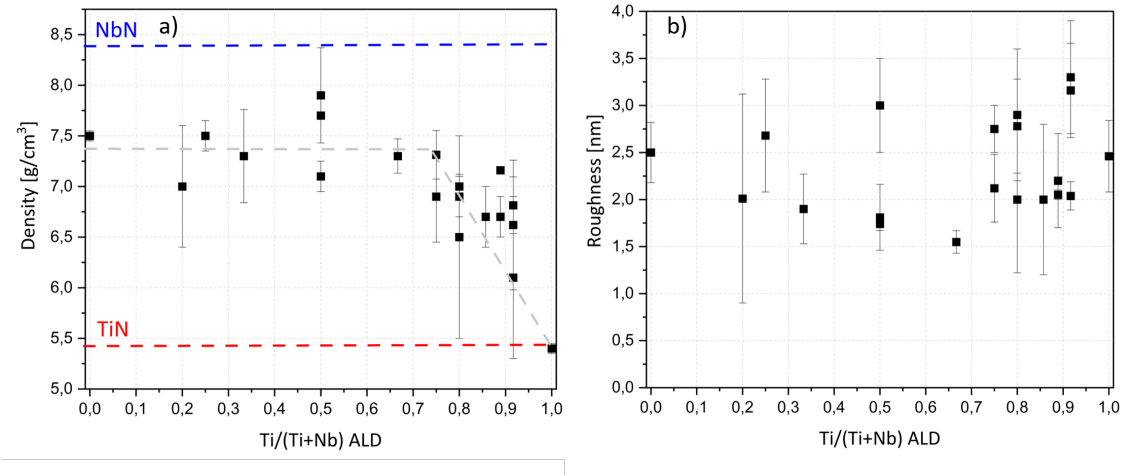

Figure 7.5: XRR measurements summary: (a) The density of NbTiN films as function of Ti/(Ti+Nb) ALD.The blue and red dashed lines represent the density of bulk TiN and NbN. (b) The roughness of the NbTiN films as a function of Ti/(Ti+Nb) ALD

Figure 7.4 shows the growth rate per cycles obtained from different ALD recipes as a function of Ti/(Ti+Nb) ALD . We can see that, regardless of the Ti/(Ti+Nb)

ALD ratio, we measured an average GPC of 0.24 Å ± 0.03 at 450°C which means that in order to deposit an NbTiN thickness of ∼ 50 nm, we need to keep a total number of cycles of n+m ≈ 2000 for all our films.

As illustrated in figure 7.5, the ratio of Ti/(Ti+Nb) ALD does not influence the roughness of the films. All films have an average roughness of 2.3 ± 0.5 nm. The density of the NbTiN films, on the other hand, has an intermediate value between the densities of pure ALD-deposited NbN films of 7.5 g/cm^3 and the density of pure ALD-deposited TiN at 5.4 g/cm^3. We can also notice that up to ratio of Ti/(Ti+Nb) ALD of 0.7, the density of the films has a constant value of 7.5 g/cm^3 (which is very close from the pure NbN density), then it starts to decrease when increasing the number of TiN cycles in the NbTiN supercycles to have a closer value from TiN pure films. Note that the Ti/(Ti+Nb) ALD ratio does not reflect the Ti content in the NbTiN film but rather the number of TiN cycles used in our deposition recipe. We will further discuss the density behaviour in section 7.4.3.

7.4.3 NbTiN films chemical composition

X-ray photoelectron spectroscopy analysis

In order to study the chemical composition of our ALD-deposited NbTiN films, we performed XPS analysis with depth profiling on NbTiN films deposited with different ratios of TiN to NbN cycles. In order to remove surface oxides and contamination layers, we used Ar^+ sputtering which is a common technique used prior to XPS analysis in order to "clean" the surface. As a matter of fact, XPS is an excellent chemical characterization technique as it enables us to assess the chemical state of atoms in addition to quantitative and qualitative elemental analysis. However, one should be aware of some technical artifacts before getting into the results analysis and interpretation:

XPS depth profiling consists in progressively etching the material with noble ion sputtering. In our analysis, we used Ar^+ ions with an incident energy of 1 Kev for all the samples. It is well-known that irradiation by ions having energies in the range of 500 eV to 4 KeV leads to a number of added artifacts including preferential etching of light element, ion implantation, atomic mixing and changes in the surface chemistry. Hence, it is important to keep in mind these potential artefacts when quantifying our thin films stochiometries. These effects are present in most of the material systems and makes the composition analysis challenging. Greczynski et al [106] performed a systematic study of the influence of Ar^+ etching prior to XPS analysis on several metal nitrides. Their findings confirmed that XPS analysis of Ar^+ etched metal nitrides is not representative of native material and leads to a decrease of the ratio N/Ti to 0.8 with respect to the 1 value obtained for native TiN by other methods such as Rutherford backscattering spectrometry (RBS). This N preferential etching have been observed even with the mildest set of sputtering conditions (500 eV). For 4 KeV Ar^+ ions etching, the N/Ti ratio obtained was 0.7. The N deficiency was found to be even more pronounced for higher mass nitrides such as ZrN, HfN and NbN [107] . For instance, when etched with 500 eV Ar^+ ions, these films exhibited a N/Metal ratio of 0.58. The N/Metal ratio was found to be 0.5 when the irradiation energy increased to 4 KeV. Based on these studies

[106, 107] and since we used for our experiments an energy of 1 Kev, we can expect intermediate N/Metal ratios to those obtained with 500 eV and 4 KeV.

Let us examine a typical XPS depth profile obtained on one of our NbTiN-AlN coated sapphire sample. Figure 7.6 shows the chemical composition of the different atoms involved Ti, Nb, N, O and Al. Through the composition evolution with the increasing etching time, we can distinguish the two layers deposited on the surface of the sapphire substrate: NbTiN film on the outermost surface with an AlN layer underneath.

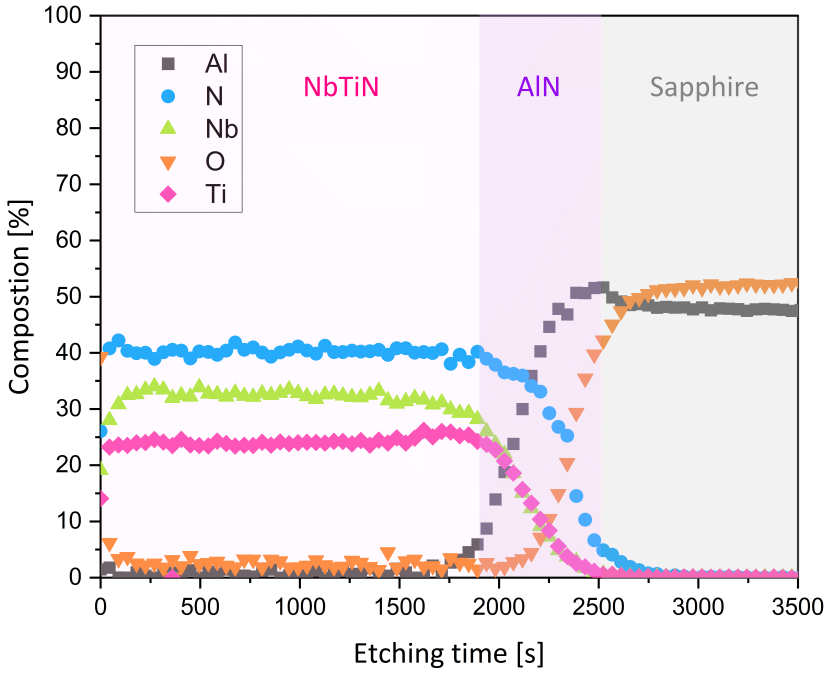

Figure 7.6: A typical XPS-depth profile of NbTiN-AlN bilayer deposited on sapphire.

The NbTiN film composition looks invariable along the film depth except at the very surface where a native oxide layer is present, which vanishes rapidly as we start etching. The different atomic compositions reach their steady state values after few minutes of etching. Since the Ar^+ etching would necessarily affect the N/metal ratio due to preferential etching of nitrogen, other techniques (such as RBS and XRD) will be used to have a more accurate idea of nitrogen content in the $Nb_{1-x}Ti_xN$ films. Let us focus first on the niobium and titanium content in the different $Nb_{1-x}Ti_xN$ films.

Titanium and niobium content in the NbTiN films

Titanium and niobium content in the NbTiN films where averaged over the depth profile[3] and plotted in figure 7.7 as a function of Ti/(Ti+Nb) ALD. Ti/(Ti+Nb)

[3]Once the native oxide is completely etched.

ALD refers to the ratio of TiN to NbN ratio in the ALD recipe whereas Ti/(Ti+Nb) XPS refers to the titanium and niobium content in the $Nb_{1-x}Ti_xN$ films as obtained from XPS analysis.

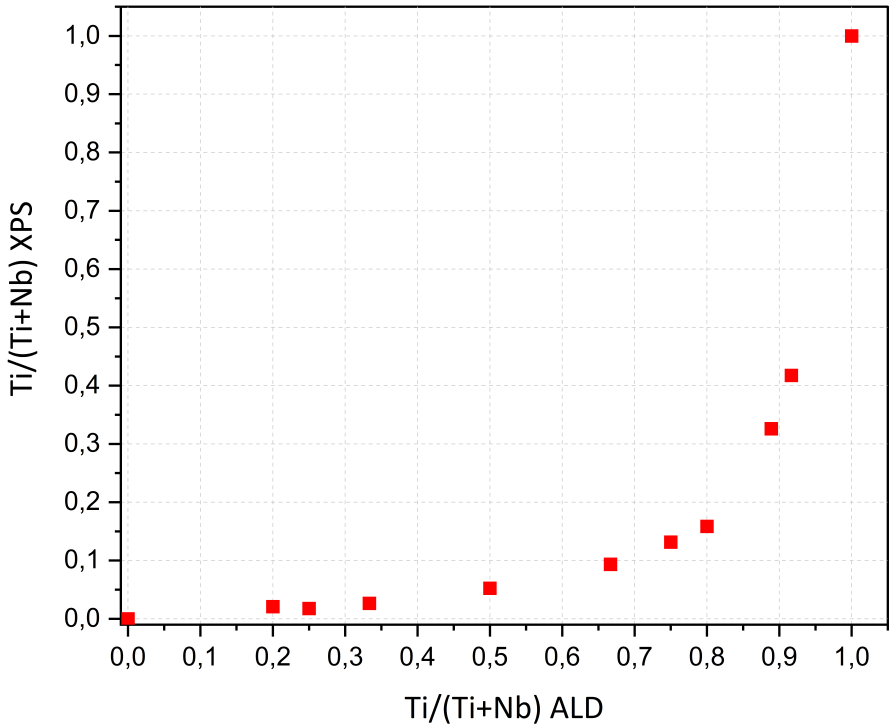

Figure 7.7: Ti/(Ti+Nb) content in NbTiN films in NbTiN-AlN layer deposited on Niobium as obtained from XPS analysis

We can see that when we increase the number of TiN cycles in the ALD recipe, the Ti/(Ti+Nb) content increases in the film. Starting from Ti/(Ti+Nb) ALD equal to 0 , which corresponds to a pure NbN film, the ratio of Ti/(Ti+Nb) XPS increases when increasing the number of TiN cycles in the recipe but following a power law instead of a linear trend. It is only with a ratio of Ti/(Ti+Nb) ALD higher than 0.7 that the ratio of Ti/(Ti+Nb) chemical composition exceeds 0.13 . This observation is in agreement with the density measurements, as it seems that for Ti/(Ti+Nb) ALD < 0.7, the NbTiN films have very low Ti content which explains the fact that their density is very close to pure ALD-deposited NbN density.

For instance, if one wants to deposit a film with a composition of Ti content of 25% , we would need a ALD recipe composed of 11 cycles of TiN followed with only 1 cycle of NbN i.e an Ti/(Ti+Nb) ALD equal to 0.92.

This trend is inherent to the choice of the chemical precursors chosen in this work. For instance, NbTiN films deposited with plasma-enhanced ALD using organometallic precursors such as TDMAT and TBTDEN does not show this power-law like increase of Ti content when increasing the TiN number of cycles in the recipe but rather a linear trend [108]. We found out that, when using Chlorides precursors, the

observed dependence suggests a Ti etching process ongoing during the ALD growth of NbTiN films.

For clarity, let us examine the residual gas analyzer RGA signal recorded during the deposition process of NbTiN film with a recipe composed of 2 TiN cycles followed by 2 NbN cycles.

$$2(TiCl_4 + NH_3) + 2(NbCl_5 + NH_3) \tag{7.3}$$

Figure 7.8 shows the RGA signal of the three observed masses: 17, 36 and 153, which corresponds respectively to the NH_3, HCl and $TiCl_3$ (which is the dominant signal for $TiCl_4$) signals. We can see that each time the valve of $TiCl_4$ is opened (in purple), we observe a peak in the signal of mass 153. The interesting observation is that we also see a small peak (encircled in red) in the signal of $TiCl_3$ when we pulse $NbCl_5$. These small peaks which have been repeatedly observed when pulsing $NbCl_5$ hints that each time we pulse $NbCl_5$, a certain amount of the Ti-N surface species previously deposited are etched away and removed from the surface in the form of $TiCl_4$. This phenomena explains the lower Ti concentration in the films as compared to what was intended.

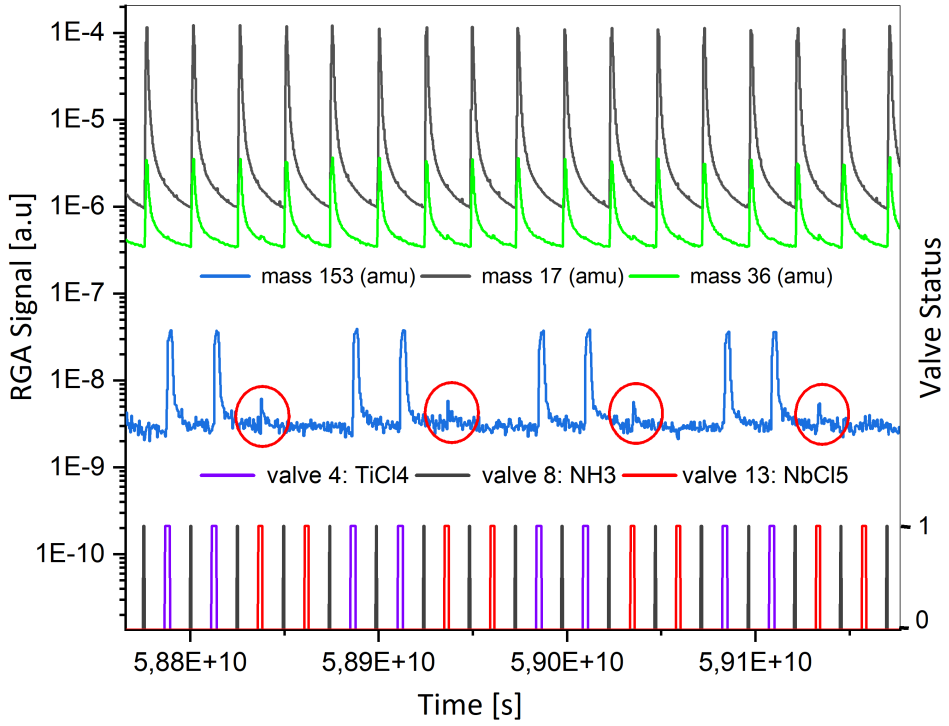

Figure 7.8: RGA signal and valve status recorded during the deposition process of a NbTiN film

In order to further investigate this etching process and quantify the amount of Ti-N surface species removed after the $NbCl_5$ pulse, we performed several depositions during which we recorded the intensity of the mass 153 signal after $NbCl_5$ pulses.

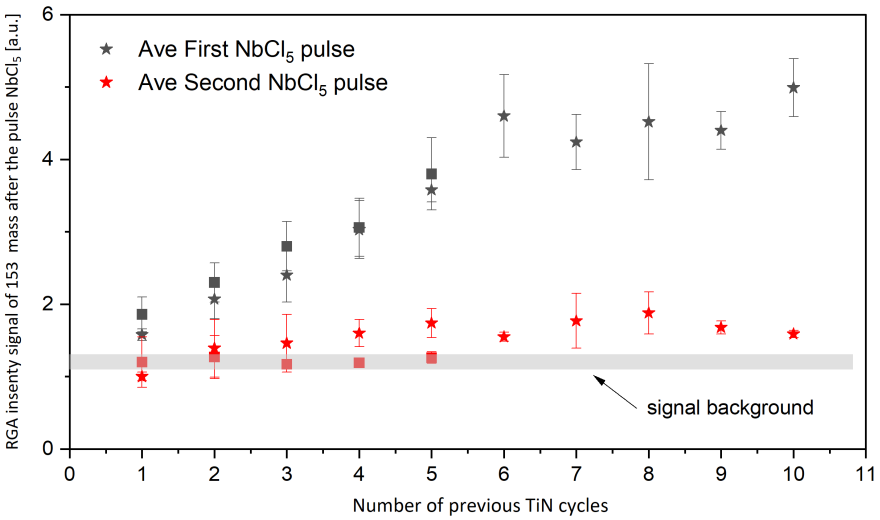

Figure 7.9: The intensity of the 153 mass as recorded by the RGA when we pulsed the $NbCl_5$ for the first time (in black) and for the second time (in red) as a function of the number of TiN cycles previously done

In our experiments, we increased progressively the number of TiN cycles from 1 to 10 and then pulsed twice the $NbCl_5$ into the system.

Figure 7.9 shows the intensity of the 153 mass as recorded by the RGA when we pulsed the $NbCl_5$ for the first time (in black) and for the second time (in red) as a function of the number of TiN cycles previously deposited.

The mass 153 intensities has been averaged over multiple cycles of TiN + $NbCl_5$ sequence and the error bars reflect the variation in intensities measured. Let us look first at the intensity of the mass 153 after the first $NbCl_5$ pulse (in black): It can be seen that there is a linear increase in the 153 mass intensity when we increase the number of previous TiN cycles up to 6 cycles . For higher number of TiN cycles, there seems to be a saturation in the 153 mass signal which indicates that the amount of Ti-N surface species etched by $NbCl_5$ pulses also saturates when the number of TiN cycles exceeds 6 cycles. As the TiN growth rate is 0.25 Å /cycle, the mass 153 saturation occur for TiN film thickness of $\sim$ 1.5 Å. This means that for a NbTiN supercycle composed of:

$$n(TiCl_4 + NH_3) + m(NbCl_5 + NH_3) \tag{7.4}$$

- Once n is higher than 6, the amount of Ti-N surface species etched by $NbCl_5$ pulses saturates and we can finally start increasing signifciantly the Ti content in the NbTiN films. We can postulate that for n$\geq$6, the surface is saturated with Ti-N-H surface species from the $TiCl_4$+ NH_3 cycles (full surface coverage) and the subsequent $NbCl_5$ pulse remove the maximum amount of Ti in the form of $TiCl_4$.

- For n lower than 6, we keep increasing the Ti-N deposited on the surface but the first pulse of $NbCl_5$ removes increasingly higher amounts of Ti-N species

from the surface which is in perfect agreement with the power law trend seen in figure 7.7.

Now, if we look at the signal of the mass 153 after the second $NbCl_5$ pulse (in red), we can see that is that it is very low and comparable with the background signal (measured without any TiN or NbN pulses) regardless of the number of TiN cycles previously performed. This indicates that with only one cycle of NbN, we are already in the "limiting regime" and we can hope for a reproducible deposition recipe in particular on large objects with complex geometries.

7.5 NbTiN film superconducting properties

Two of the most important criteria for the NbTiN film to fulfil in the multilayer structures are a low resistivity in the normal state ρ_n and a high superconducting temperature T_C. This is crucial to reduce the R_{BCS} and enhance the quality factor Q_0 of SRF cavities. In this sense, we investigated the room temperature resistivity and the transition temperature of our NbTiN films as deposited with different Ti content in order to find the best stoichiometry in terms of superconducting performances. The following measurements are done on silicon or sapphire substrate coated with AlN ($\sim$ 10 nm)- NbTiN ($\sim$ 50 nm). The film resistance was measured using the 4-probe methods and the critical temperature was determined using 4-probe transport measurement while progressively cooling the sample in a home-made setup.

7.5.1 NbTiN films resistivity

The resistivity of the different NbTiN films were measured and plotted in figure 7.10 as a function of the Ti content in the film. We can observe a linear trend in the resistivity values. The pure NbN film have a resistivity of 502 µΩ.cm which decreases linearly when we increase the Ti content in the films to eventually reach 63 µΩ.cm for the pure TiN films. The linear dependence is to be expected as the NbTiN films are in fact a solid solution of the two miscible nitrides: NbN and TiN. We noticed that the NbTiN film resistivity values are 5 times lower than values obtained with plasma-enhanced ALD [108]. However, the resistivity seems to be higher than what is measured for NbTiN films with superconducting temperature above 15 K: 90 µΩ.cm to 150 µΩ.cm (depending on the film stochiometries [108, 109]).

7.5.2 NbTiN films critical temperature

The critical temperatures of our NbTiN films are summarized in figure 7.11. Unlike the resistivity measurements, the critical temperatures of the NbTiN films showed no obvious trend when increasing the Ti content in the films. The films exhibited superconducting transitions at temperatures around 7 and 8 K, which are much lower than the reported values for NbTiN at 17 K.

To elucidate the origins behind these low superconducting performances, it is crucial to study the crystalline structure of the NbTiN films. It is acknowledged

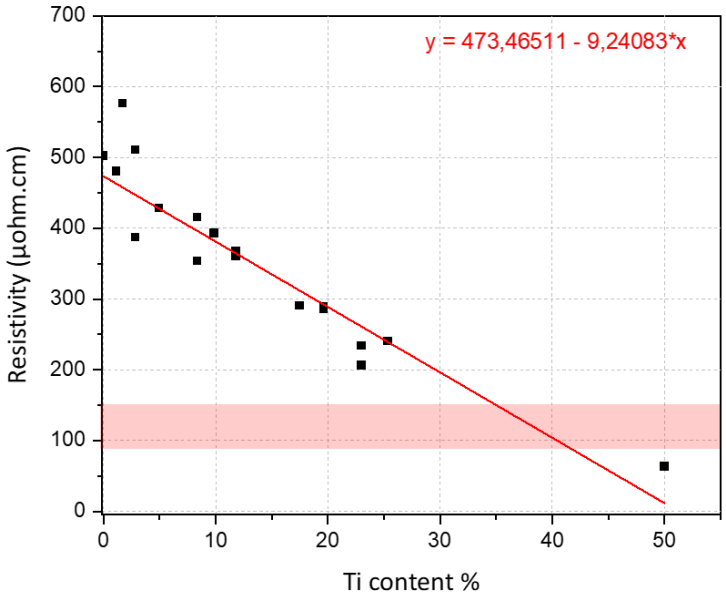

Figure 7.10: NbTiN film resistivity as a function of the Ti content in the film. The red bar represents the range of resistivity measured for NbTiN films with critical temperatures above 15 K from [108, 109]

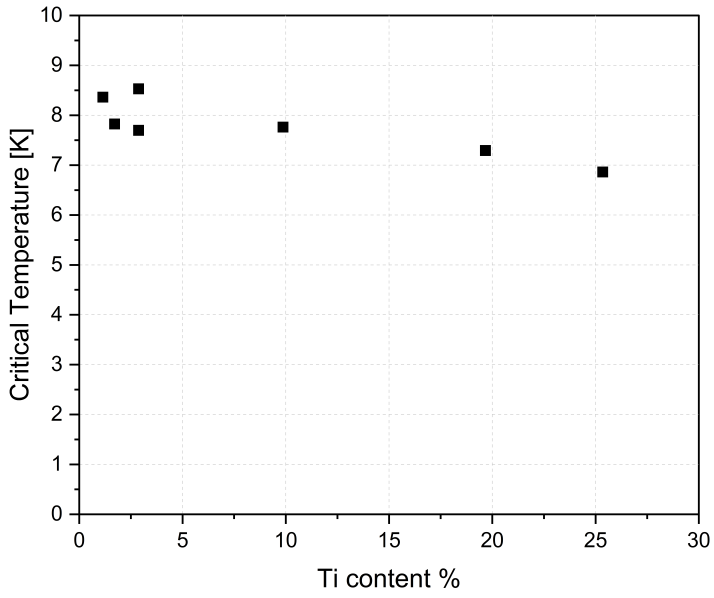

Figure 7.11: Critical temperature of the NbTiN films as a function of the Ti content

that the superconducting properties of the NbTiN films are strongly dependent on the formation of the particular crystallographic cubic phase. In this perspective, we will examine the crystalline structure of the NbTiN with different Ti content.

7.5.3 NbTiN film structural analysis

We performed X-ray diffraction using a 5-circle diffractometer (Rigaku SmartLab) with CuKα radiation from a rotating anode on the NbTiN-AlN bilayer deposited on Si wafers. It is necessary to use grazing incidence configuration in our measurements otherwise we will collect signal mainly from the substrate. Figure 7.12 shows the GIXRD patterns of the NbTiN films deposited with different TiN to NbN ratios. At first glance, all the films shows five main peaks corresponding to different orientation of the face-centered cubic structure of the space group Fm-3m as expected for NbTiN film. Nonetheless, all the peaks are shifted to higher angles compared to the values reported for the cubic NbTiN phase.

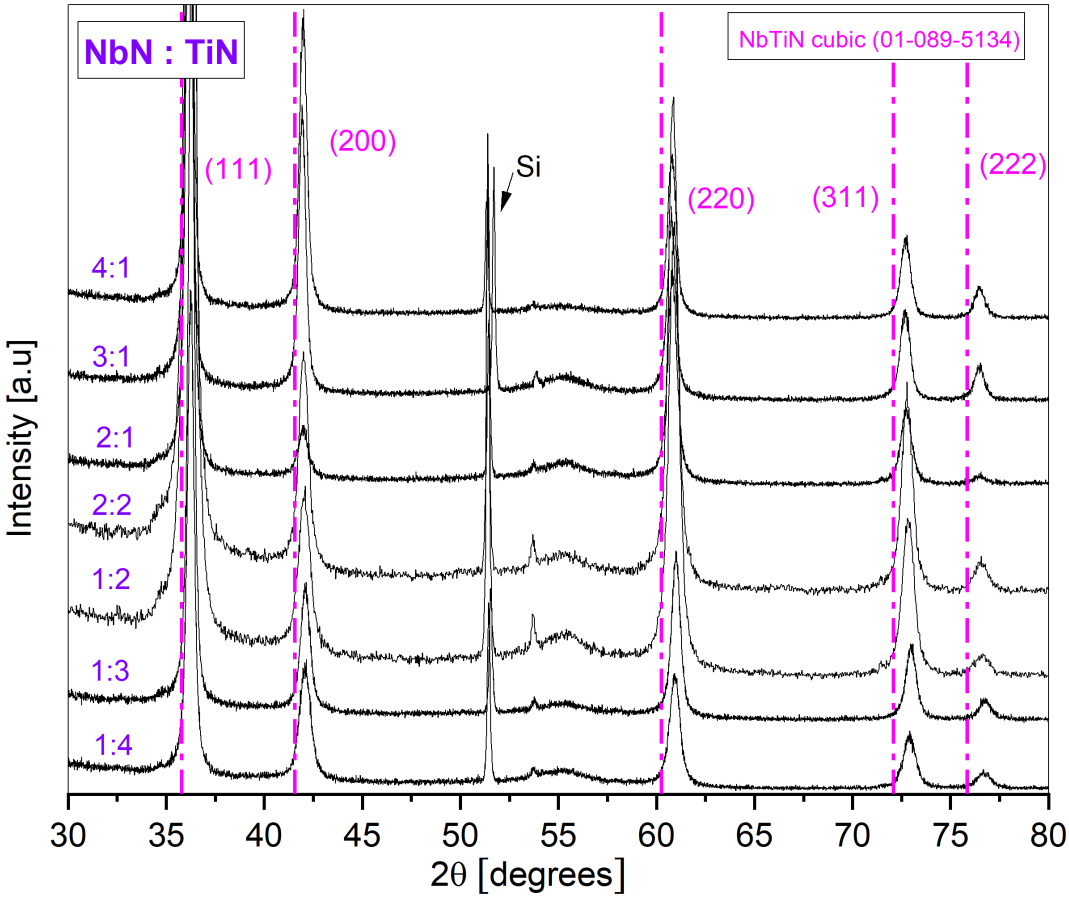

Figure 7.12: GIXRD pattern of NbTiN films with different ALD recipes deposited on ALN (10 nm) - silicon

The Calculation of the lattice parameter from these GIXRD patterns revealed that the lattice parameters of our NbTiN films are much lower than reported. As plotted in figure 7.13, the lattice follows a linear dependence with the Ti content in the films: The lattice constant decreases when increasing the titanium content in the NbTiN film. This is consistent with the fact that the TiN cubic phase have a smaller lattice constant (4.24 Å) than the pure NbN phase (4.37 Å). However,

comparing the lattice parameter of 4.26 Å measured on our ALD-deposited NbTiN with 25% of Ti to the reported value of 4.34 Å, there is a deviation of 2% which explains the lower critical temperatures measured on our films. Similar results have been observed with NbTiN films deposited by DC magnetron sputtering where films with small lattice parameters 4.305 Å where associated with T_C below 8 K [109].

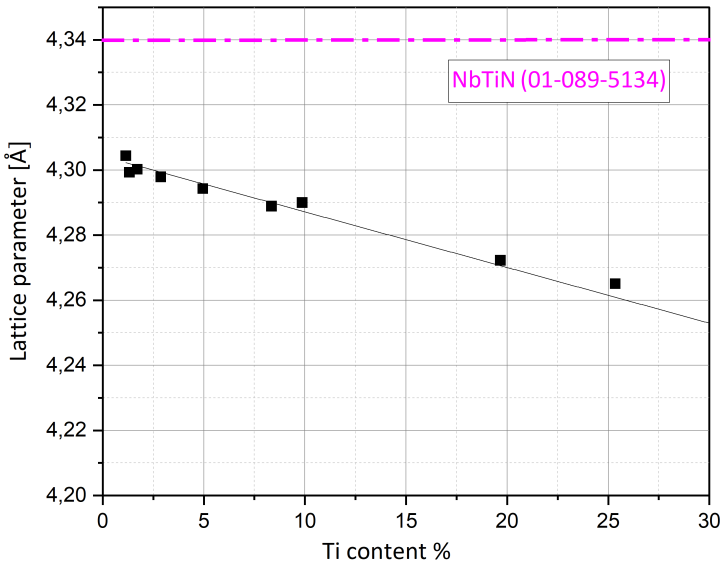

Figure 7.13: Lattice parameter of the NbTiN films as a function of their Ti content

Why is the lattice parameter of our NbTiN films lower than expected?

This has been a crucial question in our work and the answer is not yet trivial at this point. It is acknowledged that the shift in a diffraction pattern is the result of uniform macrostrain along the film [110]. A shift to higher angles is synonym of lower d-spacing in the lattice, which implies that the film is under uniform compressive strain. Nonetheless, a deviation of 2% in the lattice constant seems to be too high to be only the results of uniform strain.

Let us examine more closely our GIXRD patterns. In figure 7.14, we plot the GIXRD patterns obtained from our NbTiN film with 25 % of Ti, pure TiN and pure NbN film as deposited by ALD and compare their peak positions with the reported peak positions in the literature:

- Pure ALD-deposited TiN film shows diffraction peaks with positions close to the reported cubic TiN phase. The measured lattice parameter is 4.215 Å for a TiN film thickness of 48 nm, which represent a deviation of 0.5% as compared to the value of 4.24 Å reported from the literature for bulk TiN (00-038-1420) .

- Pure ALD-deposited NbN film shows five peaks similar to the cubic NbN phase but their positions does not match the reported values for the cubic NbN (03-065-9399). When compared to other NbNx phases, the peak positions of our

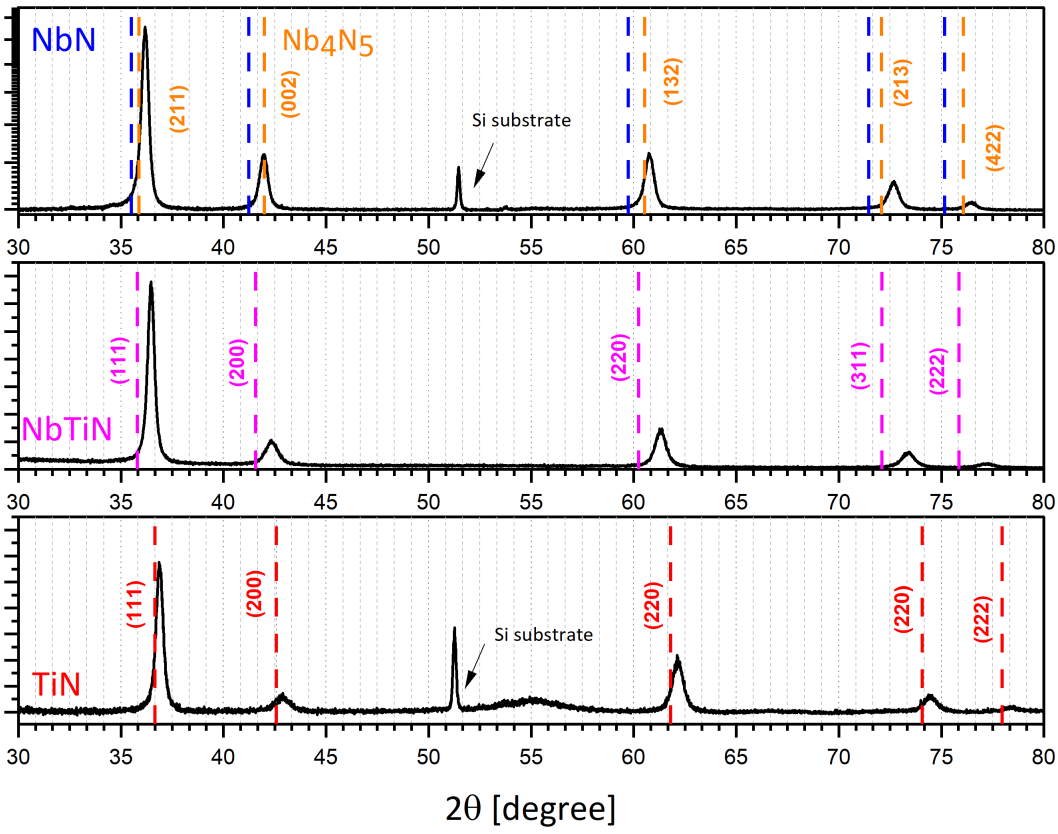

Figure 7.14: GIXRD patterns of pure NbN and TiN films, NbtiN film with 25 % of Ti as deposited by ALD and compared to the literature XRD patterns

sample matches more accurately with the nitrogen Nb_4N_5 phase. Nb_4N_5 phase belongs to the tetragonal I4/m space group (96-153-9324) and is a defective NaCl-type structure with niobium vacancies [111].

Rutherford backscattering spectrometry (RBS) measurement done on pure TiN showed a N/Ti ratio of 1 ± 0.1 whereas it showed a ratio of N/Nb between 1.2± 0.1 and 1.25± 0.1 for pure NbN films. These measurements are also consistent with the density measurements obtained on pure ALD-deposited NbN films (see figure 7.5). We realized that the density measured of pure ALD-deposited NbN films at 7.3 g/cm^3 is characteristic of Nb_4N_5 phase.

Previous studies of the reaction of $NbCl_5$ with NH_3 in temperatures around 450°C also confirms that the niobium nitride obtained could be the Nb_4N_5 phase [112, 113].

In the light of these findings, and since our NbTiN films are a combination of $TiCl_4$ and $NbCl_5$ reactions with NH_3, we came to the conclusion that our NbTiN films are also nitrogen rich. The excess nitrogen in the film give rise to a deformed lattice, which translates into smaller lattice constants as it have been measured. Despite the prevailing belief that Ti stabilizes the NbN into the cubic phase with

the highest superconducting temperature, this does not seem to be the case for our ALD-grown films. NbTiN films with Ti content up to 25 % still exhibited a small lattice constant and a low critical temperature.

7.6 Enhancing NbTiN films superconducting properties

Given the low superconducting temperatures of the NbTiN films as deposited, we decided to test post-deposition thermal treatments in order to enhance their performances. Annealing treatments were already proven to improve the crystallinity of thin films and improve their performances, in particular superconducting nitrides [114, 115]. However, the previous studies were made on NbTiN films deposited on MgO [115] or Si wafer substrates [114]. Our main concern when exploring this route was the thermal stability of the NbTiN-AlN bilayer on niobium substrates. Heating the nitrides layer deposited on Niobium to high temperatures around 800°C-900°C might cause their degradation and diffusion of nitrogen or other elements into bulk Niobium. Accordingly, we performed post-thermal treatments on both niobium and sapphire coated samples. For each experiment, Nb and sapphire substrates were coated and annealed simultaneously.

7.6.1 Testing the vacuum annealing on NbTiN-AlN bilayers

Given the suspicion of an excess of nitrogen present in our NbTiN films, we opted for annealing our samples under vacuum hoping to get rid of the excess nitrogen and to improve the superconducting properties of the NbTiN films.

Vacuum annealing conditions

As a start, we tested two different annealing treatments on NbTiN films with three different Ti content (2%, 8% and 25%) :

- Vacuum annealing at 850°C during 10 minutes, where we heat the samples with a ramp of 6°C per minute up to 850°C, maintain them at 850°C during 10 minutes and then cool them down.
- Vacuum annealing at 900°C during 10 minutes. We used the same annealing conditions as the previous one.
- The vacuum level was maintained in the 10^{-6} mbar range during annealing in a custom made resistive-walls vacuum oven with passive cooling.

Effect of the vacuum annealing on the superconducting properties of NbTiN films

The resistivity and critical temperatures of the annealed NbTiN-AlN layers are summarized in figure 7.15 and 7.16. We can see that the post-deposition thermal treatments turned out to be very effective: The critical temperatures were greatly

enhanced from 8 K at best to 15.5 K. The resistivity of the films were also significantly lowered. The NbTiN stoichiometry that showed the highest critical temperature among the ones tested was the one with 25% of Ti. This stoichiometry is obtained with an ALD recipe composed of 11 cycles of TiN with 1 cycle of NbN. For clarity, we plot, in figure 7.17, the superconducting transition of this film. The samples showed very sharp superconducting transitions, which indicates a high film quality.

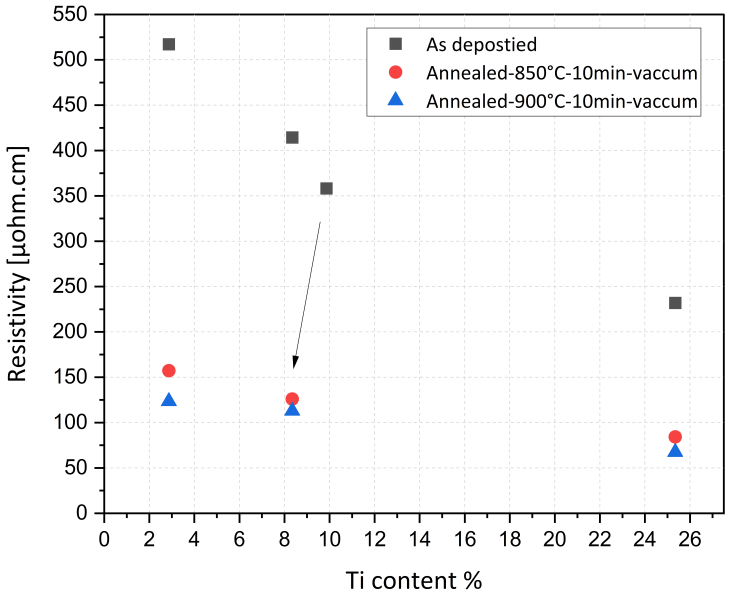

Figure 7.15: The resistivity of the NbTiN films after different annealing treatments measured on sapphire substrates

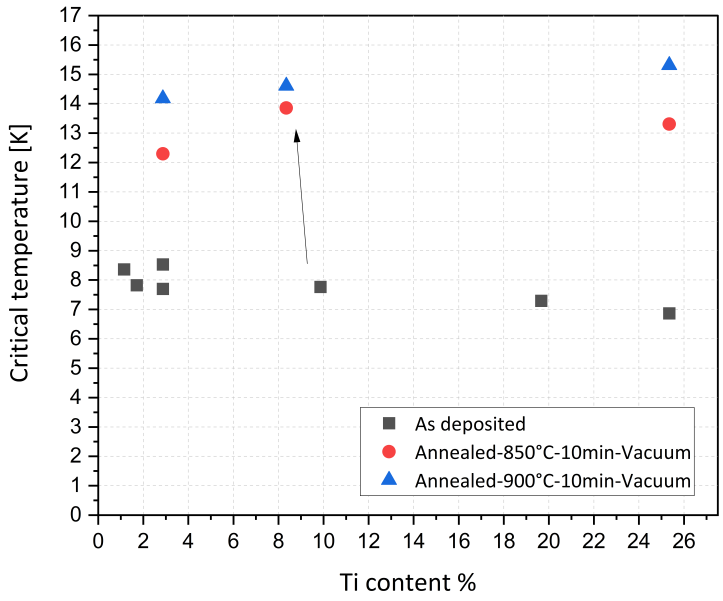

Figure 7.16: The critical temperature of the NbTiN films after different annealing treatments measured on sapphire substrates

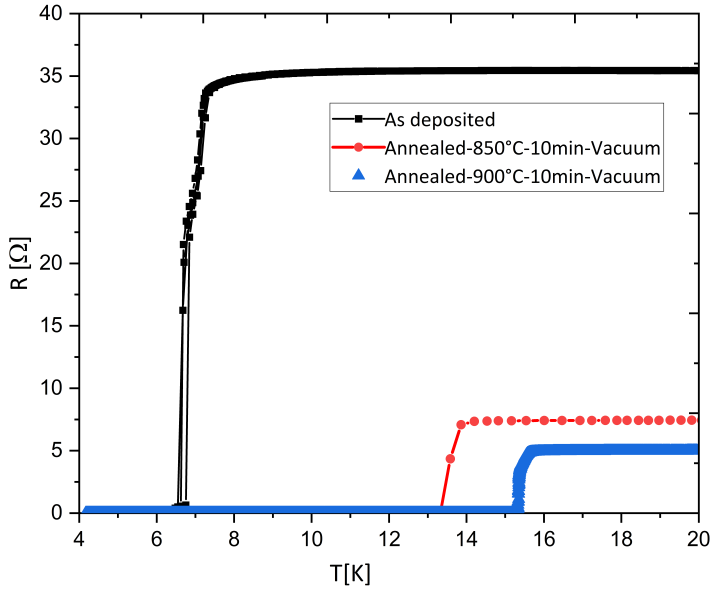

Figure 7.17: Resistance as a function of the temperature for the NbTiN film with 25 % of Ti

7.6.2 Effect of the vacuum annealing on the crystalline structure of NbTiN films

To understand the origin of this improvement in the superconducting properties of the post-annealed NbTiN films, we performed GIXRD measurements on the annealed samples and compared the structure obtained on different substrate (niobium and sapphire). The GIXRD measurements revealed a peak shifting to lower angles on all the peaks on the sapphire substrates regardless of the Ti content in the films. For clarity, we will now focus on the film stoichiometry with the highest critical temperature. i.e. the NbTiN film with 25 % of Ti.

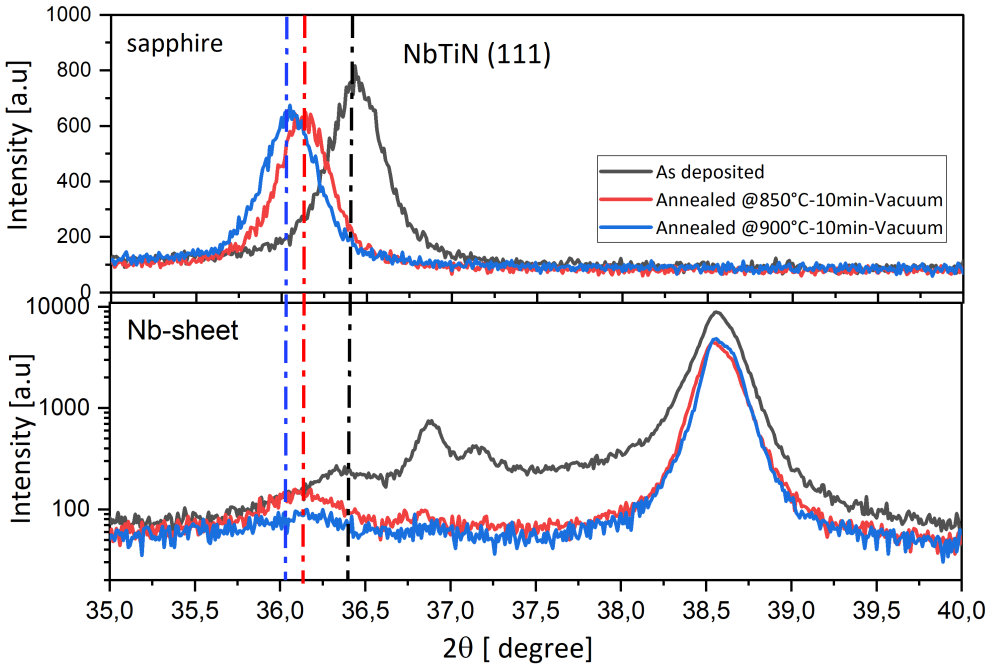

Figure 7.18: Comparison between the GIXRD pattern on Niobium and sapphire substrate coated with the NbTiN film with 25 % of Ti

Figure 7.18 shows the clear shift between the as deposited films and the annealed films:

- The sapphire and the niobium samples shows similar peak positions for the as deposited film (in black) and after annealing at 850°C (in red) but this no longer holds true for the film annealed at 900°C for 10 minutes (in blue).
- On sapphire substrate, the higher the annealing temperature is, the higher the shift in the position of the diffraction peaks is.
- On Niobium substrate, the (111) peak is shifted to lower angles after annealing at 850°C (in red). When increasing the annealing temperature from 850°C to

900°C, the peak doesn't show a bigger shift as it is the case for the sapphire substrate.

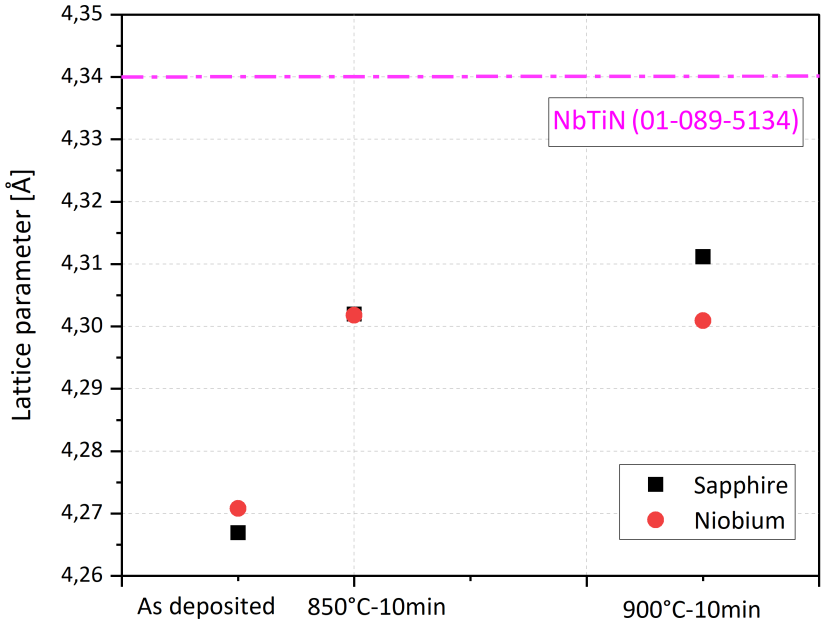

Figure 7.19: Evolution of the lattice parameter of the NbTiN film with 25% of Ti with different thermal treatment on Nb and sapphire substrates

As a matter of fact, the shift of the diffraction peaks towards lower angles translates into an increase in the lattice parameters. We calculated the lattice parameters of the previous samples with the different thermal treatments, which are presented in figure 7.19.

We can see that the significant increase in the lattice parameters is consistent with the improvement of the superconducting properties obtained on sapphire substrates: The higher the annealing temperature is, the closer the lattice parameters gets from the literature values. Nonetheless, the discrepancy between the sapphire and niobium coated samples after annealing at 900°C for 10 min is quite intriguing. This could be a sign of inter-diffusion between the NbTiN-AlN layers and the Niobium substrate. Since niobium is a getter material, inter-diffusion is more likely to occur on niobium substrate than on sapphire substrate. Hence, we will examine the thermal stability of our NbTiN-AlN bilyar on niobium in the following section.

7.6.3 Thermal stability of the NbTiN-AlN bilayer on niobium substrates

In order to assess the thermal stability of the NbTiN-AlN bilayer on Niobium and understand the origin of the increase in the lattice parameter, we performed XPS profiling on the same samples shown in 7.6.2. The results are plotted in figure 7.20 and reveals several interesting points. First, the three samples showed two distinct layer: the NbTiN film on the topmost surface and the AlN layer underneath it.

The major difference between the three samples lies mainly in the nitrogen and the oxygen profiles:

- We can see that the nitrogen concentration in the NbTiN films decreases from 38 % in the as deposited sample to 36 % after the 850°C-10 min annealing and reaches 27 % after the annealing at 900°C-10 min. This confirms that the vacuum annealing decrease the amount of the excess nitrogen in the films, which results in an increase in the crystalline lattice constant and also an increase in the critical temperature. Comparing the nitrogen profiles at the interface between the AlN and the niobium for each sample, it seems that the nitrogen diffuses into bulk niobium. This issue will be discussed more thoroughly in the following chapter.

- Unlike the two first samples, the sample annealed at 900°C during 10 min showed the presence of about 5 % of oxygen in the NbTiN films and up to 15 % in the AlN film. The presence of oxygen in superconducting nitride is known to affect their performances. This is consistent with our previous observations as the film annealed 900°C during 10 min on niobium showed lower lattice constant (see figure 7.19) and less pronounced diffraction peak (see figure 7.18). In addition, the increased concentration of O within the AlN layer, at the interface with the Nb, after the thermal treatment under vacuum have been systematically observed on all annealed sample. It strongly suggests a gathering effect of the O from the native Nb oxide layer to the AlN one upon annealing. This effect should not change the insulating property of the AlN layer.

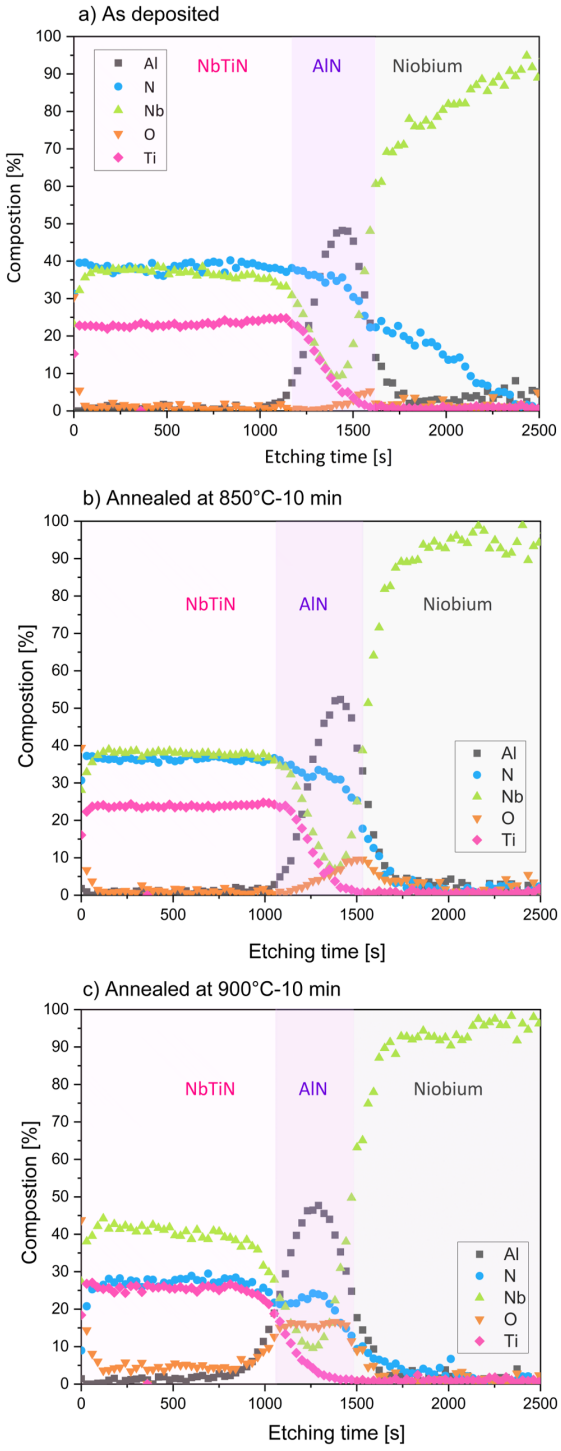

Figure 7.20: XPS profiles of the NbTiN layer deposited on Niobium substrate with different thermal treatments

7.6.4 SEM analysis

The SEM analysis were performed using a "ZEISS Sigma 300" microscope on the the NbTiN-ALN bilayer deposited on both sapphire and niobium samples and annealed at 900°C for 10 minutes. Unlike coated- sapphire samples that showed no defects, coated-niobium samples showed the presence of cracks on the NbTiN films. The cracks occurred at the grain boundaries of the niobium as it can be seen in figure 7.21 for the NbTiN film with 25% of Ti but it has also been observed outside the grain boundaries for other NbTiN stochiometries (see figure 7.22).

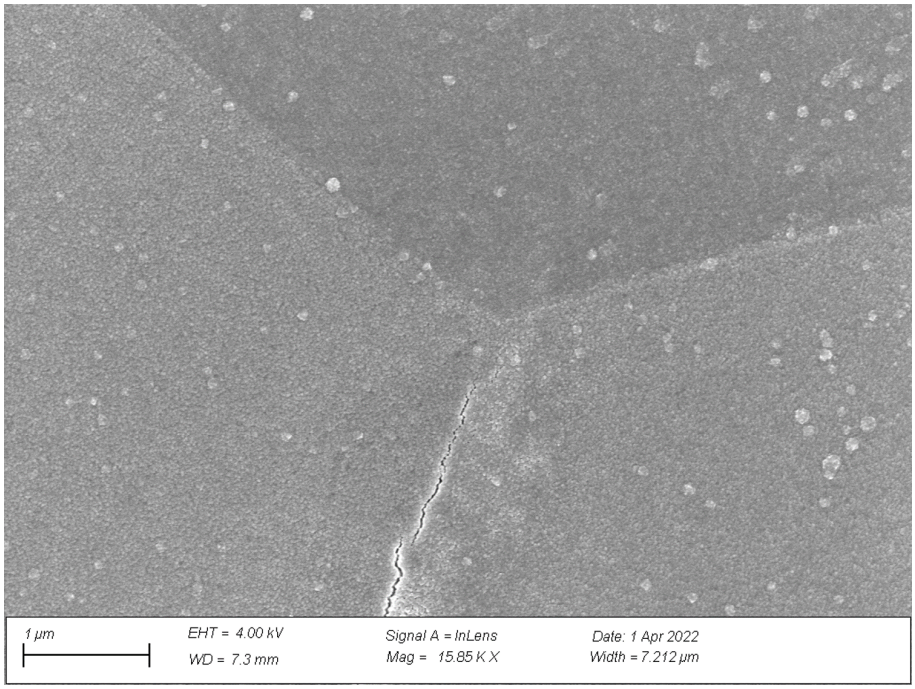

Figure 7.21: SEM image on the NbTiN-AlN-Niobium samples annealed at 900°C-10min with 25% of Ti in the NbTiN films

The presence of these cracks can explain the presence of oxygen in the NbTiN films. This implies that the annealing step at 900°C during 10 minutes cannot be implemented on niobium substrate despite the encouraging critical temperatures obtained on sapphire: Based on our XPS and SEM analysis, it seems that when annealing NbTiN-AlN layer on niobium substrate at 900°C during 10 min, the NbTiN layers (initially nitrogen rich) ends up by loosing too much nitrogen probably through diffusion into bulk niobium. This worsens the NbTiN film quality and causes cracks and thus a great deal of oxygen contamination.

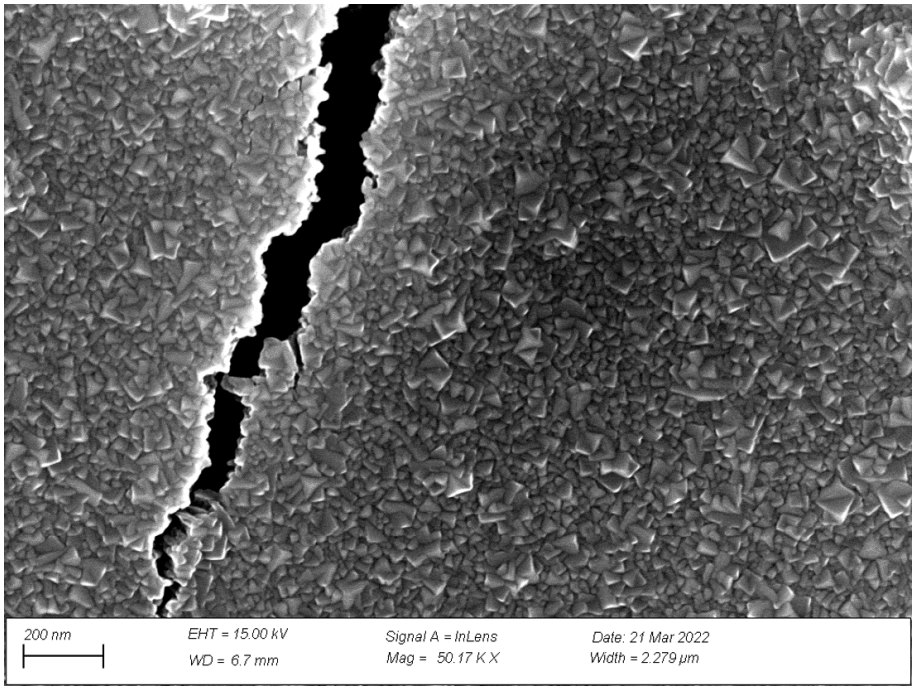

Figure 7.22: SEM image on the NbTiN-AlN-Niobium samples annealed at 900°C-10min with 8% of Ti in the NbTiN films

7.7 Optimizing the thermal treatment on niobium substrate

Based on our previous experiments, our annealing step needs optimization to guarante the enhancement of the NbTiN films performances not only on sapphire samples but also on niobium substrate. We thought of testing an intermediate annealing step where we anneal the samples up to 900°C and immediately ramp down without maintaining the temperatures at 900°C for few minutes. In the following, we will present results of two different intermediate annealing treatment. The two treatments are presented in figure 7.23 along with the vacuum level measured in our oven (in blue).

- Annealing-900°C-SP-1R: This annealing step consists in heating the samples up to a set point of 900°C with a ramp of 6°C per minute under vacuum. The same ramp is used in the cooling process.
- Annealing-900°C-SP-2R: This annealing is more sophisticated than the 900°C-SP-1R. It consists in heating the samples up to 800°C with a fist ramp of 6°C per minute, then heating up to the set point of 900°C with a ramp of 18°C/min. The same ramps are used in the cooling process.

The main difference between the two thermal treatments tested is that by using a ramp of 18 °C instead of 6°C in the temperature region of 800°C-900°C, the NbTiN films will spend less time in this critical range of temperature. For instance, when using the 2 ramps, the samples spend $\sim$ 5 min at temperatures higher than 850°C (for Annealing-900°C-SP-2R) instead of 18 min when using only one ramp

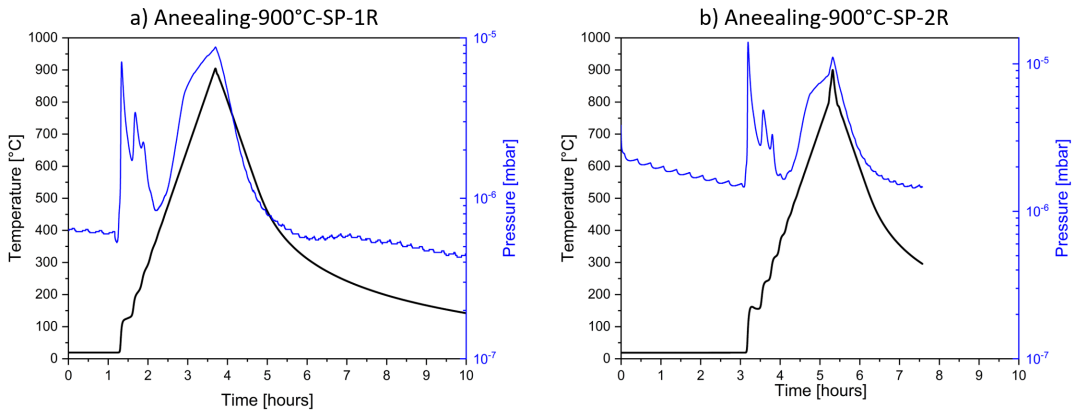

Figure 7.23: a) Annealing-900°C-SP-1R b) Annealing-900°C-SP-2R

(for Annealing-900°C-SP-1R). By tuning the time that the bilayer-coated niobium spend at temperatures higher than 850°C, we can perhaps find an optimal annealing conditions where we improve the crystalline structure (by loosing the right amount of nitrogen) without impacting the thermal stability of the bilayer.

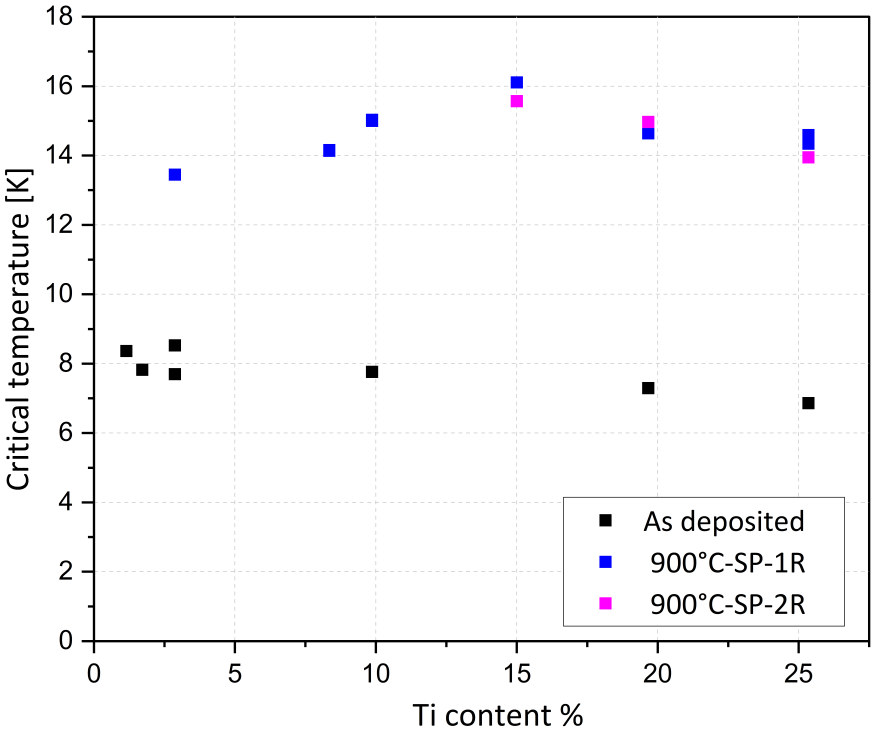

Figure 7.24: Critical temperature measured on 50 nm NbTiN films deposited on 10 nm AlN on sapphire substrates after annealing in vacuum

We can see from figure 7.24 that after the annealing step at 900°C , all the films

see their critical temperature greatly enhanced regardless of the Ti content in the NbTiN film or the ramping parameters in the thermal treatments. Nonetheless, we seem to have a maximum of the critical temperatures for films deposited with Ti content of 15 % . The highest Tc measured is 16.1 K on a film of 50 nm of NbTiN annealed with the 900°C-SP-1R thermal treatments and deposited with Ti content of 15%. This corresponds to an ALD supercycle composed of 6 cycles of TiN followed with 1 cycles of NbN.

When examining this samples with GIXRD and XRR, we noticed an increase in the lattice parameters of the films after the thermal treatments (see figure 7.25) and also an increase in the density of the films (see figure 7.26).

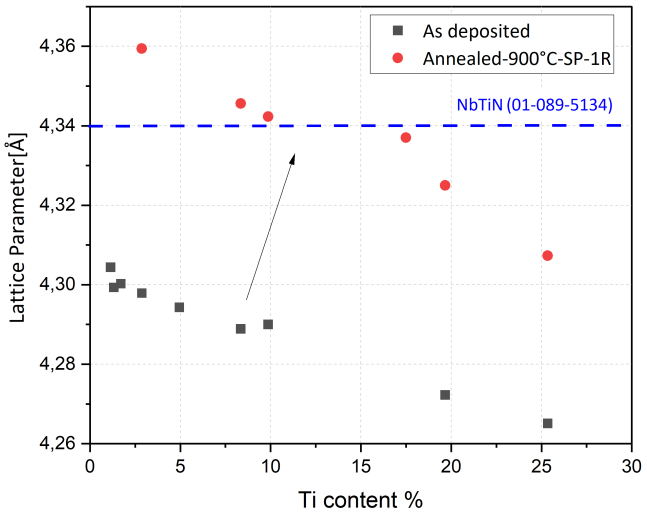

Figure 7.25: Evolution of the lattice parameters of NbTiN films after the thermal treatment 900°C-SP-1R measured on sapphire substrate

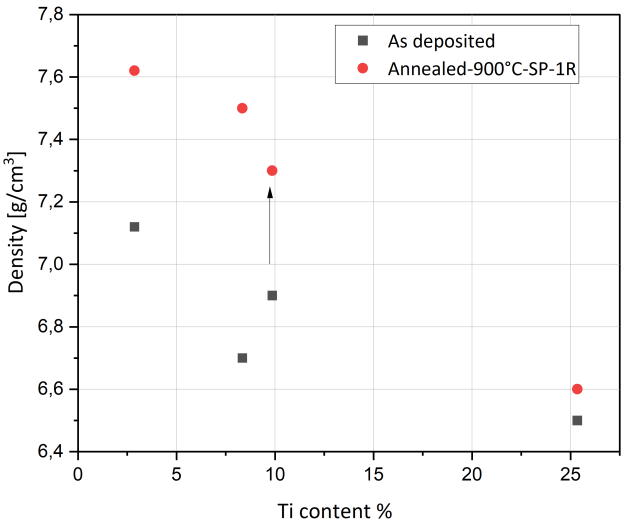

Figure 7.26: Evolution of the lattice parameters of NbTiN films after the thermal treatment 900°C-SP-1R measured on sapphire substrate

7.7.1 Comparison of the NbTiN crystalline structure on niobium and sapphire substrates

At this point, we will mainly focus on studying NbTiN films with the highest critical temperature after annealing. In order to assess the crystalline structure on niobium samples in comparison with the sapphire samples on which we measured the highest T_C, we will examine closely two NbTiN films deposited respectively with two different ALD recipes (NbN cycles:TiN cycles): (1:6) and (1:8) deposited on three different substrates : sapphire wafers, cavity-grade niobium coupons and Nb-sheets coupons. Cavity-grade niobium coupons have much larder grains ($\sim$ 100 µm) than Nb-sheets coupons and are thicker (4 mm compared to 1 mm).

Figure 7.27 and 7.28 shows GIXRD patterns along with the lattice parameters of respectively NbTiN (6:1) and NbTiN (8:1) films after the thermal treatments at 900°C in vacuum.

- For both NbTiN films (6:1) and (8:1), the thermal treatments 900°C-SP-1R results in higher lattice parameters on sapphire samples but lower lattice parameters on the two different Nb substrates. This indicates that this annealing is not well suited for enhancing the NbTiN film properties on niobium substrate.

- With the thermal treatment 900°C-SP-2R, we obtain higher lattice parameters on Nb samples than obtained with the thermal treatment 900°C-SP-1R with values almost identical to the ones measured on sapphire. This indicates that the annealing 900°C-SP-2R does not impact negatively the NbTiN-AlN stability on niobium.

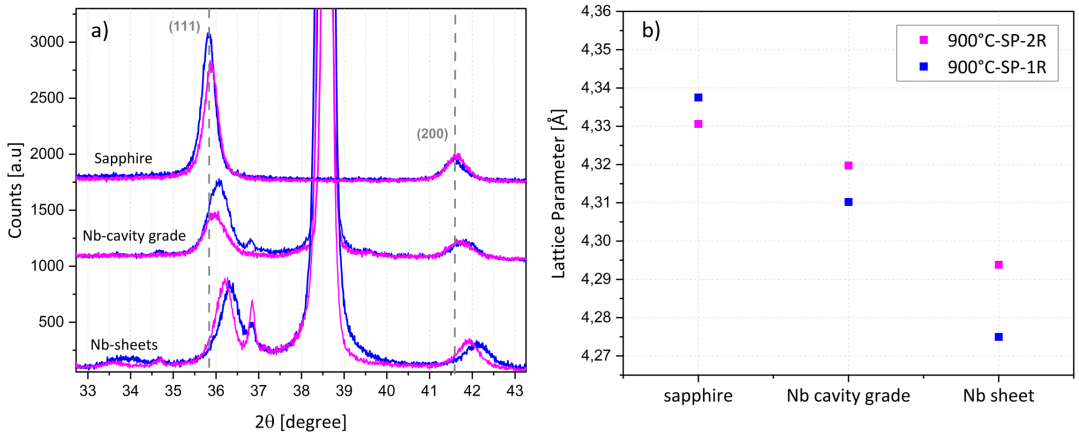

Figure 7.27: GIXRD measurements on NbTiN films deposited with an ALD recipe of 6 TiN :1 NbN cycles

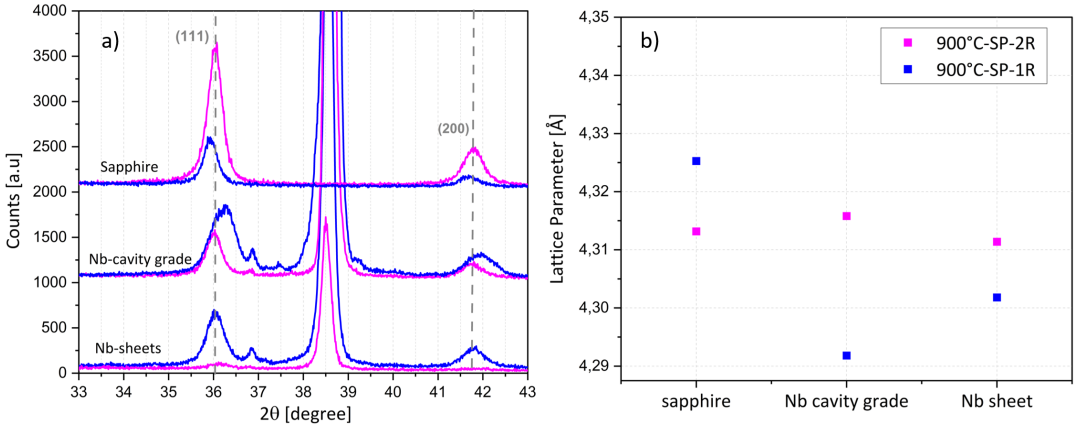

Figure 7.28: GIXRD measurements on NbTiN films deposited with an ALD recipe of 8 TiN :1 NbN cycles

- The NbTiN films (6:1) have a higher lattice parameter than the (8:1) NbTiN film, which is consistent with the fact that NbTiN films with higher Nb content have higher lattice parameters.

- Regardless of the thermal treatments, cavity grade niobium samples shows higher lattice parameters than niobium sheets. This could be explained by the fact that cavity grade niobium have bigger grains size $\sim$ 100 microns than the Nb sheets which could result in lower nitrogen diffusion than that found on Nb sheets, for instance at grain boundaries. This could lead to a better thermal stability of the multilayer on cavity grade coupons than on niobium sheets.

Based on these observations, one could expect that NbTiN films on niobium annealed with the thermal treatments 900°C-SP-2R would show close critical temperatures to those measured on sapphire as they show overall close lattice constants.

7.7.2 Comparison of the NbTiN critical temperature measured on niobium and sapphire substrates

In order to measure the critical temperature of the previous NbTiN films deposited on niobium samples, we performed magnetometry measurements[4] on the Nb sheet samples. The cavity-grade niobium (being 4 mm thick) are difficult to use in magnetometry measurements.

Before getting into the analysis of magnetometry measurements, we would like to draw the attention of the reader to two important points:

- Unlike the transport measurements done on sapphire substrate where we used the 4-probe method to measure locally the resistance of the superconducting film on the upper-face of the sample as a function of the temperature, magnetometry is a measurement of the total magnetic moment of the sample which means that we not only observe the response of the NbTiN film deposited on the upper face of the substrate but also the response of both the substrate and the film deposited on lower face of the sample (the face in contact with the sample holder in the deposition chamber). The film deposited on this hidden face has a lower critical temperature and based on our experience, needs to be mechanically removed in order to only measure the magnetic response of the NbTiN film on the upper face of the substrate and the one of the niobium substrate.

- Even after mechanically removing the NbTiN film deposited on the hidden face of the sample, we noticed that in the temperature range of 9.5 K to 14 K ie the temperature range where the niobium substrate is normal whereas the NbTiN film is superconducting, the paramagnetic signal of the substrate and the diamagnetic signal of the superconducting NbTiN film are of the same level (as shown in figure 7.29) . Their superposition results in less sharp superconducting transitions than what it could be observed on sapphire substrate. For clarity, we present in figure 7.29 an example of measurement performed on a NbTiN-AlN-niobium sample where the SQUID signal was fitted with two magnetic dipoles model to distinguish the NbTiN film diamagnetic signal (in red) from the substrate signal (in blue). However, this fitting procedure can only be performed on SQUID signal[5].

At this point, let us compare the superconducting transitions of NbTiN films on sapphire (as obtained from transport measurements) and on niobium (as obtained from magnetometry) in order to determine the best NbTiN recipe and the most suited thermal treatment to implement on a niobium cavity.

As plotted in figures 7.30 and 7.31, Nb samples annealed with the 900°C-SP-2R annealing showed sharper superconducting transition than those annealed at 900°C-SP-1R for both NbTiN films. This is perfect agreement with the lattice parameter

[4]The magnetometry measurements were performed at the "Plateforme Mesures Physiques à Basses Températures, Sorbonne Université, 75005 Paris, France" using a vibrating sample magnetometer (VSM) "Quantum Design PPMS 9T" and a superconducting quantum interference device SQUID (Quantum Design MPMS XL 5T).

[5]The author recognizes the help of David Hrabovsky at Sorbonne university with this fitting procedure.

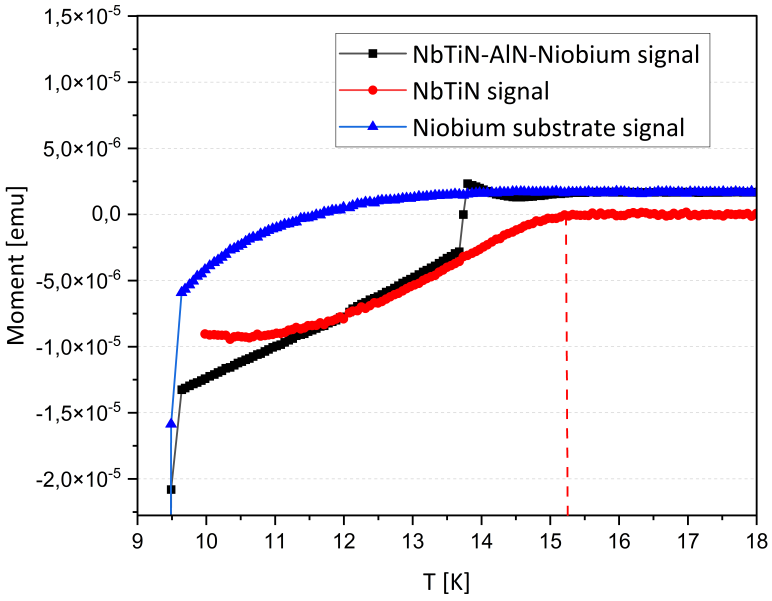

Figure 7.29: An example of SQUID measurement on a NbTiN-AlN-Nb sample fitted with two magnetic dipoles model (a first one for the NbTiN film (in red) and a second one for the niobium substrate (in blue)

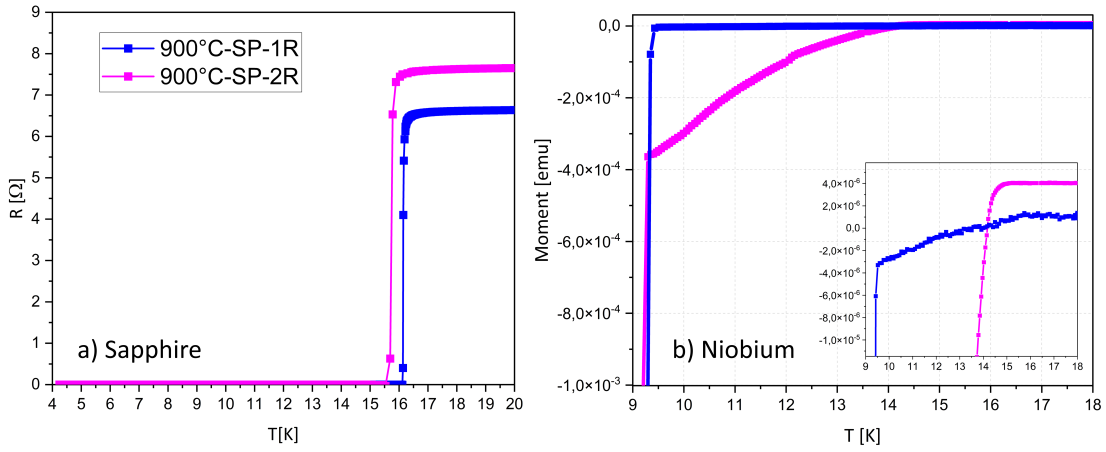

Figure 7.30: Critical temperature measurements on the NbTiN film (6:1)

measurements presented in the section 7.7.2 and indicates a higher quality of the superconducting films.

We can conclude that the thermal treatment of 900°C-SP-2R is the most promising for NbTiN-AlN films deposited on niobium substrate. One could also expect that films deposited on cavity grade niobium would show better performances than the Nb sheet as they exhibited higher lattice parameters than those obtained on Nb sheet coupons. As far as the NbTiN film composition is concerned, the film with the ALD recipe of 6 TiN :1 NbN showed slightly higher T_c on both sapphire and niobium samples. This film recipe will be the one used for trial on 1.3 GHz cavity

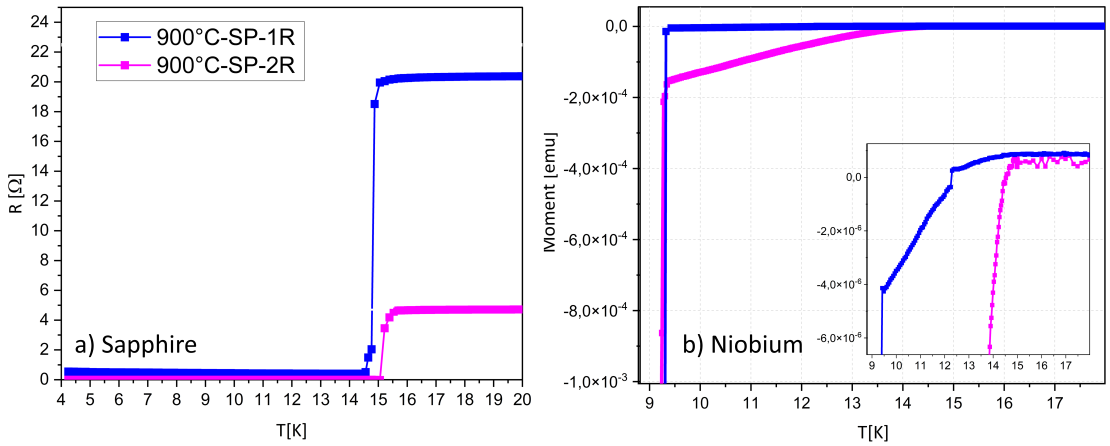

Figure 7.31: Critical temperature measurements on the NbTiN film (8:1)

presented in the following chapter.

Colour change observed with the annealing 900°C-SP-1R

Another worth-noting result is the colour change noticed on Nb samples annealed with 900°C-SP-1R. Unlike samples annealed with 900°C-SP-2R which showed no discoloration after the annealing, samples annealed with 900°C-SP-1R showed some changes in color. We witnessed the emergence of gray metallic spots after the thermal treatment (as it can be seen in figure 8.1). In order to understand the origin of this discoloration, we performed both SEM analysis and XPS profiling on two areas with different colors:

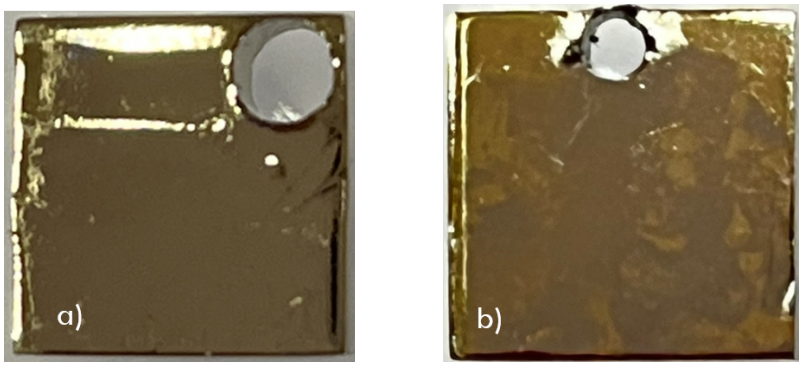

Figure 7.32: Picture of the cavity grade coupons after annealing (a) 900°C-SP-2R (b) 900°C-SP-1R

XPS profiling performed on one gray region and one golden region showed that NbTiN films in the grey region have a lower nitrogen content (as it can be seen in figure 7.33): The gold areas have a 35 % of nitrogen whereas the grey areas showed 33 % of nitrogen content. It is important to recall that the nitrogen concentration in the films are highly underestimated because of the preferential etching of nitrogen. Nonetheless, since we kept the same etching parameters, this indicates that there is a chemical origin to this discoloration, most probably due to difference in nitrogen

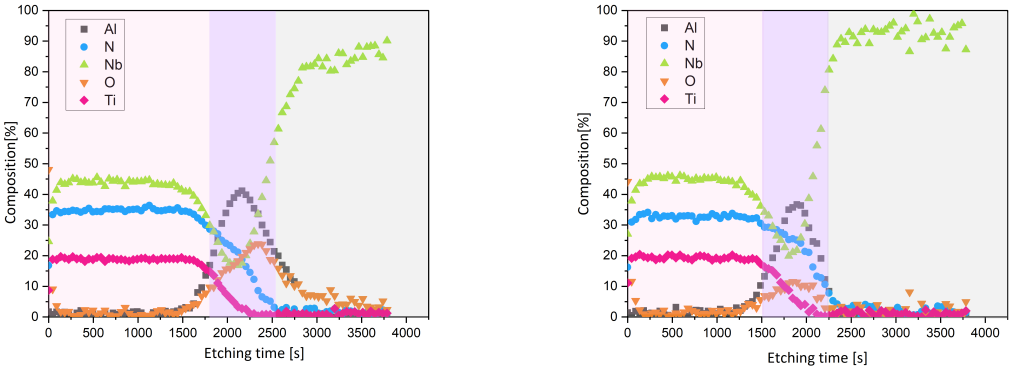

(a) Gold coloured area

(b) Grey coloured area

Figure 7.33: Exploration of the post-annealing chemical aspect of a cavity-grade Niobium samples coated with NbTiN (8:1)- AlN bilayer after the annealing 900°C-SP-1R

content. The XPS depth profile also shows a higher concentration of oxygen within the AlN, at the interface with the Nb, on the gold colored areas. Together with the N difference, one possible explanation is that, for some reason, the native oxide of Nb could be thicker locally and hence slow down N diffusion in some regions. Niobium oxide thickness is known to depend on the crystallographic orientation of the Nb [116]. If some golden area could be clearly limited to some underneath Nb grains, other areas does not seem to follow clear crystallographic structure of the Nb substrate. The origin of these color patches is therefore unclear at the present moment and more detailed investigation of the oxide thickness are required. Nonetheless, it is worth noting that no oxygen have been observed in the NbTiN layer after annealing which indicates a good stability of the NbTiN layer. The two

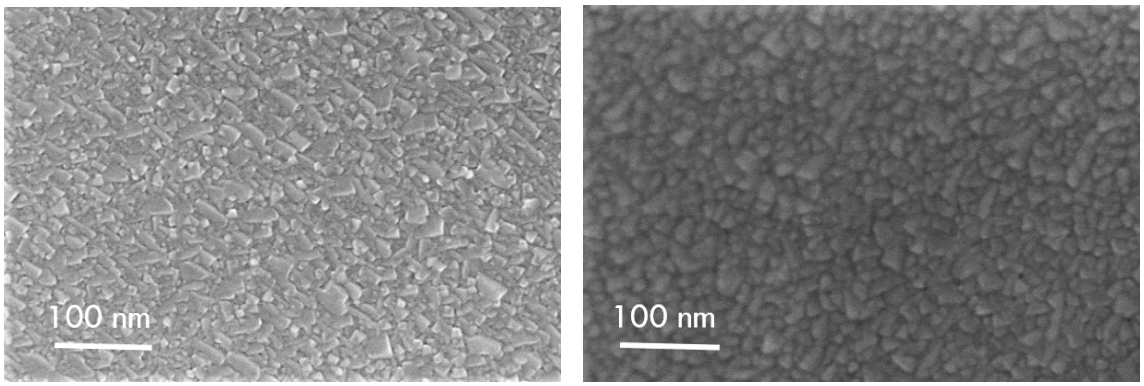

(a) Gold coloured area

(b) Grey coloured area

Figure 7.34: Exploration of the post-annealing morphological aspect of a cavity-grade Niobium samples coated with NbTiN (8:1)- AlN bilayer after the annealing 900°C-SP-1R

differently colored areas showed also some changes in their micro-structure as it can be seen in figure 7.34. The grey-coloured area showed crystallites which rounder edges than the ones observed in the gold-coloured area.

7.8 Conclusion

Throughout this chapter, we studied the atomic layer deposition of the NbTiN-AlN layers and examined their chemical, crystalline and superconducting properties. We tested several thermal treatments to improve their performances and we optimized these treatments in order to have the best performances on cavity-grade niobium samples. The following chapter will be dedicated to testing this optimized recipe in a 1.3 GHz niobium cavity.

Chapter 8

Towards high-performance multilayer-coated niobium cavities

8.1 Introdcution

In the previous chapter, we demonstrated that good quality NbTiN and AlN layers can be deposited with atomic layer deposition on cavity grade niobium coupons. We discussed the deposition parameters, the chemical composition and crystalline structure of the NbTiN films and we have optimized a post-deposition thermal annealing to enhance the critical temperature of our 50 nm NbTiN films up to 16 K. However, several other criteria should be met in order to successively implement this technology into an SRF cavity. Throughout this chapter, we will discuss the applicability of this multilayer structure into a 1.3 GHz niobium cavity.

8.2 Critical field enhancement on Niobium sample

The S-I-S structure proposed by Gurevich [1] promised to delay flux penetration and lower RF losses for SRF cavities. A good way to investigate the enhancement of critical filed on niobium samples is DC magnetometry. In this section, we will test whether coating a niobium surface with our bilayer of AlN-NbTiN film can increase the first critical magnetic field. At this point of our research, we will focus of the NbTiN film showing the highest critical temperature with the optimized post-annealing at 900°C-SP-2R[1].

8.2.1 Preparation of the ellipsoid sample

Fabrication and surface preparation

It is widely known that sharp edges on a superconducting sample can induce early field penetration. To avoid this effect, we used a niobium ellipsoidal sample for our experiment. In an ellipsoid sample, the magnetic field distribution can be calculated and in particular the demagnetization factor at the smaller diameter [117]. In our

[1] discussed in the previous chapter

case, the demagnetization factor N is 0.13, leading to an effective magnetic field at the equator of:

$$H_{equator} = \frac{H_{applied}}{(1 - N)} \tag{8.1}$$

The bare ellipsoid weights 768.4 mg and was made to be 10 mm from tip to tip and to have a 4 mm diameter at the equator. Junginger Tobias prepared the bare ellipsoid sample in the department of physics, university of Victoria, Victoria, Canada. The sample was machined and hand polished followed by a buffer chemical polishing (BCP) to remove any damaged layer. Then, the sample was annealed for 5h at 1400°C to remove any stress within the Niobium. Finally, the ellipsoid had again a second round of BCP (10 µm) to remove any contamination from the annealing oven [117].

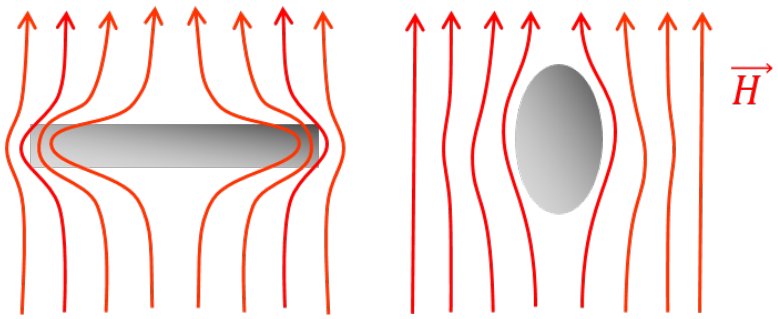

Figure 8.1: Illustration of the early field penetration in samples with sharp edges

ALD-coating of the ellipsoid sample

Once we received the bare niobium ellipsoid sample, we performed a cleaning step in ultra-sound (alcohol + acetone) for 20 min. The sample was then inserted into the ALD system with other witness sapphire and cavity grade niobium samples. As you can see in figure 8.2, we specially designed a small holder to maintain the ellipsoid sample suspended during the deposition and to limit any contact with the deposition system walls. This would maintain a uniform gas flow around the ellipsoid, which will grant a uniform thickness all over the ellipsoid. As far as the NbTiN film is concerned, we used the same deposition parameters for the NbTiN (6:1) film discussed in the previous chapter followed by an annealing step at 900°C in vacuum using the recipe with 2 ramps (900°C-SP-2R).[2]

NbTiN film characterization

In order to make sure that the ellipsoid have been coated properly, we performed XRR and GIXRD measurement on the witness sapphire and niobium samples that were coated and annealed simultaneously with the ellipsoid. The XRR measurement revealed a bilayer thickness of 10 nm of AlN and 43 nm of NbTiN.

[2]These deposition parameters followed with the thermal treatment 900°C-SP-2R resulted in the highest critical temperature we measured on sapphire 16.1 K. See chapter 7 for more details.

Figure 8.2: Picture of the niobium ellipsoid sample before and after the coating with AlN-NbTiN (6:1) films. The golden coloration is a typical sign of the presence of nitrides

The GIXRD patterns are presented in figure 8.3 and compared to the GIXRD patterns of the reference sample[3]. We can see that the witness sample have the same peak position and intensity as the references sample. This indicates that we have the same bilayer properties on the ellipsoid and demonstrates that the process is reproducible.

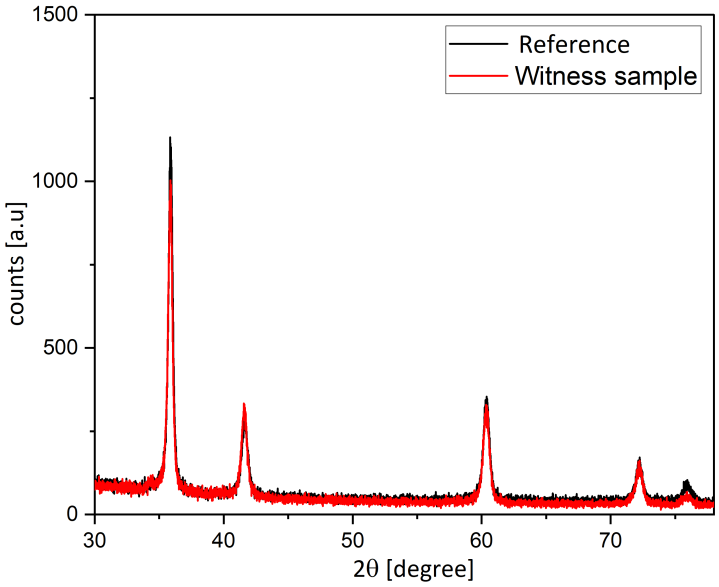

Figure 8.3: GIXRD pattern of the sapphire sample coated and annealed with the ellipsoid

8.2.2 Critical temperature measurement

Before the coating, we tested the ellipsoid sample using a vibrating sample magnetometer in order to have a baseline measurement for comparison. Then, once the

[3]The reference sample is the sample presented in the previous chapter and exhibited the highest critical temperature

ellipsoid was coated with the NbTiN-AlN bilayer and annealed, we measured the magnetic moment as function of the temperature to look for the superconducting transition of the NbTiN film.

Figure 8.4 presents the magnetic moment measurements as a function of the sample temperature performed on the ellipsoid sample.

The bare ellipsoid sample showed a sharp superconducting transition at 9.3 K corresponding to the bulk Niobium critical temperature. After the coating, we can observe a first superconducting transition at 15 K followed with a second one at 9.3 K.

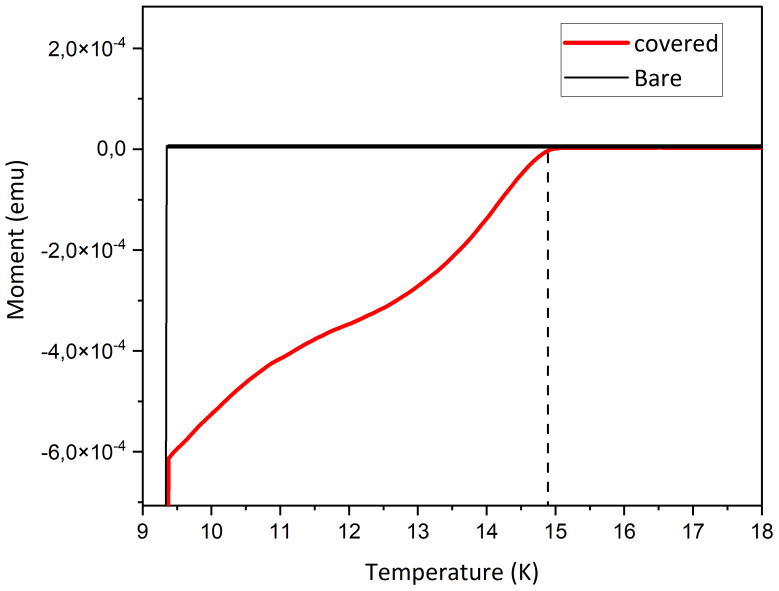

Figure 8.4: SQUID measurement on the coated Nb ellipsoid sample after the annealing treatment

8.2.3 Hysteresis loop analysis

The sample were zero field cooled (ZFC) to 2 K. Then, the magnetic moment was measured as a function of the magnetic field applied parallel to the sample. Figure 8.6 presents the magnetization curve of the ellipsoid sample before the coating (bare) and after the coating with the multilayer (covered).

Before looking into the hysteresis loop of the ellipsoid after the coating with AlN-NbTiN layers, let us focus on the magnetization curve of the bare ellipsoid sample (plotted in black in figure 8.5). After the zero field cooling, the applied field is slowly increased which results in a perfect diamagnet response as expected for a superconductor. The magnetic moment response is linear at first up to first critical field H_{vp} where flux start entering the superconductor. This divides the ellipsoid into normal and superconducting regions. Once the flux have entered the sample, the superconductor transits from the Meissner to the mixed state. As the applied

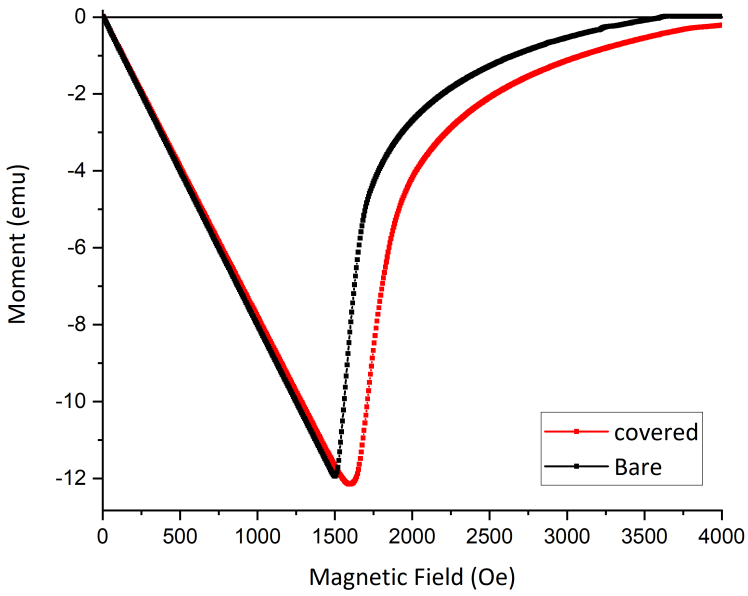

Figure 8.5: Determination of the first vortex penetration field using the virgin curve.

field is increased above H_{vp}, the absolute value of the moment decreases due to vortex penetration. This first evolution of the moment as function of the applied field is called the virgin curve.

Using this virgin curve, we can determine the field of the first flux penetration H_{vp} in the sample (bare and covered). For more accuracy, we used the standardization method described in [117]. As it can be seen in figure 8.5, The bare ellipsoid shows a first flux penetration field H_{vp} of 1482.98 Oe. The H_{vp} is enhanced after the coating to a value of 1596 Oe.

This means that the true flux penetration field H_{vp} of the bare ellipsoid is 1704 Oe which increased to 1835.5 Oe after the multilayer coating so an increase of the critical penetration field H_{vp} of 13.4 mT, which should correspond, in a Tesla shape cavity, to an increase of the accelerating gradient of about 5 MV/m. This is in good agreement with the multilayer theory. The next step to further increase the flux penetration field H_{vp} would be to test thicker NbTiN films as suggested by [105].

Let us look now at the full magnetization curve shown in figure 8.6. When H_{c2} is reached, the moment becomes slightly positive, as the sample has completely turned normal. When we decrease the applied magnetic field, the flux are progressively expelled from the superconductor and the magnetic moment become negative again. For a perfect superconductor, the magnetic moment would follow the virgin curve. However, this is not the case for our sample. It can be seen in figure 8.6 that the absolute value of the magnetic moment is lower than the virgin curve. This is due to the trapped magnetic flux inside the sample that give rise to a hysteresis shape. After decreasing the applied field to zero, the field is ramped again with a reverse polarity.

After the coating, we noticed an increase in the surface of the hysteresis loop

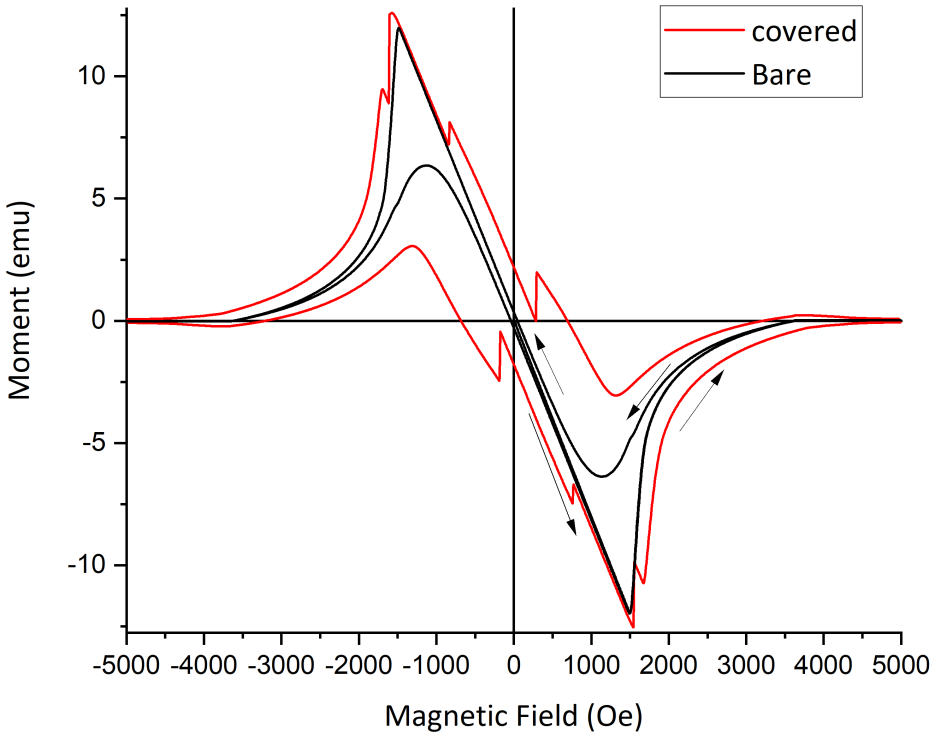

Figure 8.6: Magnetization curve of the ellipsoid sample before and after the NbTiN-AlN coating after the post-annealing treatment

plotted in figure 8.6, which indicate a stronger pinning force. We witnessed also the appearance of sharp transitions in the magnetization curve of the coated ellipsoid, which is a synonym of sudden flux penetration within the sample.

8.3 High pressure rinsing test

High pressure rinsing (HPR) is an inevitable step in cavity preparation. It allows to get rid of small dust particles that would not be carried by a simple water flow [26]. For this reason, it is of great importance to investigate the HPR effect on our deposited multilayer. This would allow us to test the adhesion of the multilayer to the bulk niobium and to see whether the film would suffer any degradation after the HPR. To do so, we tested the HPR on two cavity-grade niobium coated samples. Two samples were coated with a bilayer of AlN (10 nm) - NbTiN (50 nm) using the same deposition conditions explained in the previous chapter. One of the sample underwent the post-deposition thermal treatment whereas the second one was kept as deposited . The two samples where fixed into a specially designed sample holder and inserted into the high pressure rinsing system. We tested an hour long HPR program with the same parameters to that applied on our 1.3 GHz cavity so that the sample surface would undergo the same treatment that a cavity surface would

see. In order to examine the chemical composition of the films after the HPR, we performed XPS profiling on the two samples. The XPS profiles are shown in figure 8.7.

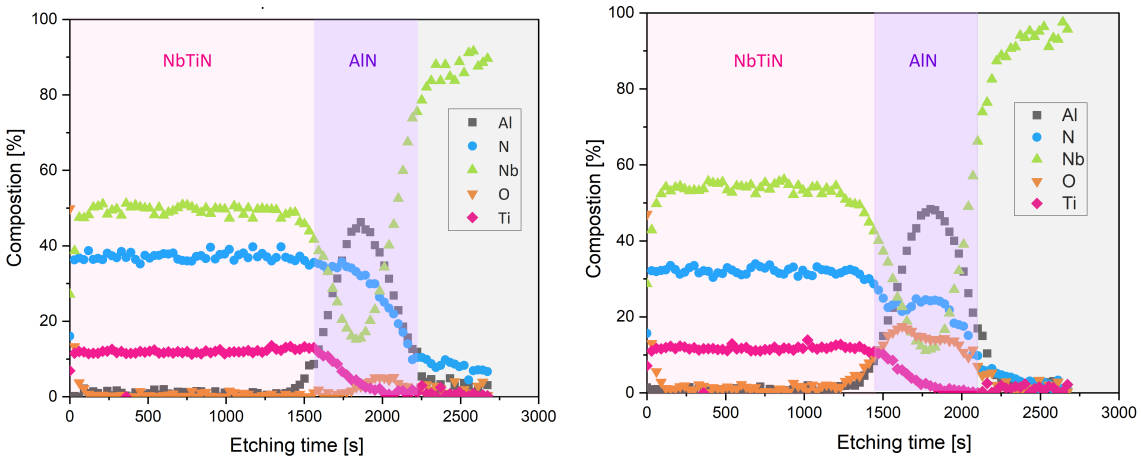

(a) As deposited + HPR

(b) Annealed + HPR

Figure 8.7: XPS profile of the Nb coated sample after the HPR treatment

The XPS profiles shows that the bilayer is still present on the surface with no noticeable oxidation in the NbTiN or change of the composition. The difference between the two samples are seen mainly at the interface between the AlN layer and the bulk Niobium and results from the annealing step (as discussed in the previous chapter). We performed also SEM examination of the two samples. No degradation was seen on the two samples due to the HPR. The film showed good adhesion to the niobium substrate. We paid close attention to the bilayer structure at the grain boundaries of the niobium substrate. No defects where noticed as it can be seen in figure 8.8 and 8.9.

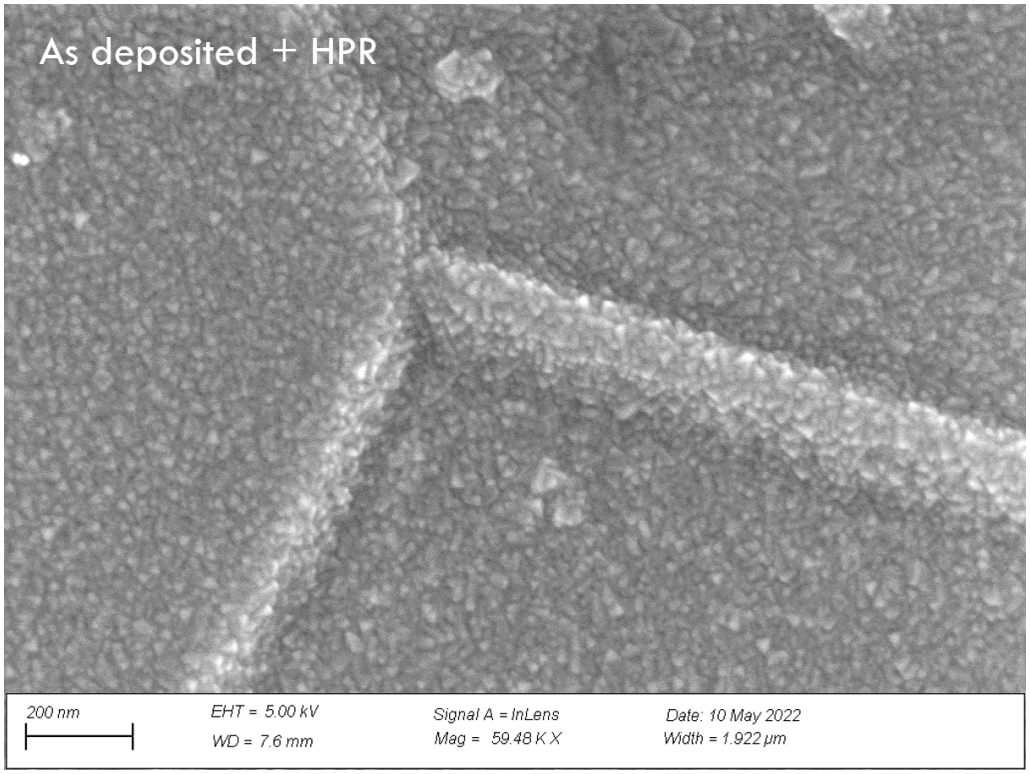

Figure 8.8: SEM image of a coated Nb sample after the HPR (as deposited)

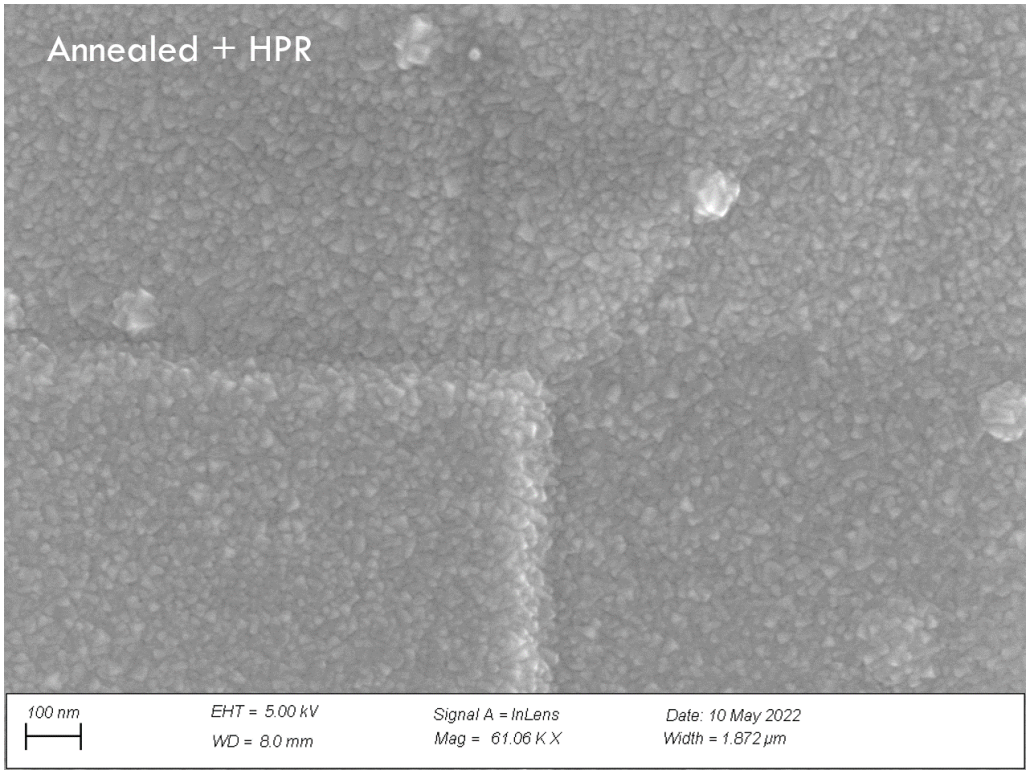

Figure 8.9: SEM image of a coated Nb sample after the HPR (annealed)

8.4 Nitrogen diffusion at the interface between the multilayer and bulk niobium

When addressing the thermal stability of the NbTiN-AlN bilayer on niobium substrate in section 7.6.3, we noticed the diffusion of nitrogen into bulk niobium even prior to any post-deposition thermal treatment (see figure 8.11). The diffusion of N has been observed on all the as deposited Nb samples prior to any annealing. This nitrogen diffusion have two potential origins:

- During the ALD process, we used N_2 as a transport gas for the chemical precursors. This involves exposing the niobium substrate to $\sim$ 1 mbar of nitrogen flow at 450°C during 20 hours[4]. It is important to recall that prior to the deposition, we keep the bare niobium at 450°C during $\sim$ 1 hour in order to make sure that the temperature of the deposition chamber is uniform. This could potentially explain the nitrogen diffusion.
- Ammoniac NH_3 used during the mutlilayer growth can also be a source of nitrogen.

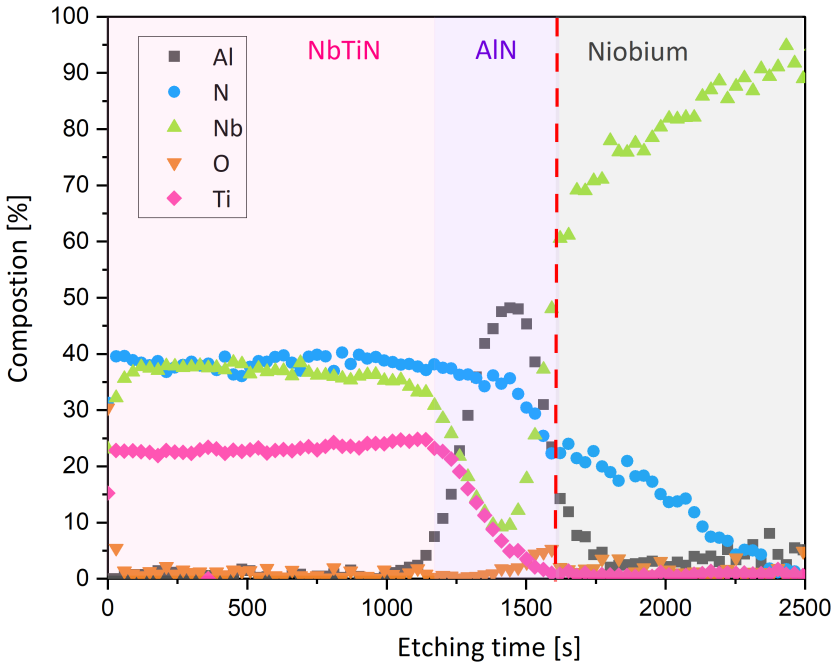

Figure 8.10: XPS profile of the NbTiN-AlN bilayer deposited on niobium using N_2 as a transport gas for the ALD deposition

To investigate this matter, we performed a bilayar deposition using argon as a transport gas instead of nitrogen. When we performed XPS profiling on this sample,

[4]The duration of the AlN-NbTiN deposition process

we noticed that the nitrogen diffusion tail (previously seen at the interface of into the bulk niobium in figure 8.11) vanished. Based on these results, we can conclude that nitrogen originates mainly from the interaction of the transport gas with the bare niobium substrate during the deposition.

Nonetheless, since we need to further anneal the bilayer at 900°C to enhance the superconducting performances of the NbTiN film, it is crucial to further protect bulk niobium from N diffusion by depositing first a diffusion barrier. This issue have been the main subject of chapter 5. We tested three potential diffusion barriers (Al_2O_3, Y_2O_3 and MgO) and we witnessed that Al_2O_3 is the best suited layer among the one tested. As a proof of concept, we deposited a 10 nm thick Al_2O_3 at the interface between a bulk niobium sample and a multilayer structure composed of NbN-AlN bilayer. It can be seen on the XPS profile (see figure 8.12) that the Al_2O_3 layer can indeed block nitrogen diffusion even when using N_2 as a transport gas. A key element behind this protection is that the Al_2O_3 layer is deposited at a lower temperature of 250°C. This enables us to protect the bulk niobium before ramping up the temperature to 450°C for the nitride deposition. Further investigations needs to be done on the thermal stability of the Al_2O_3 layer after the annealing step at 900°C.

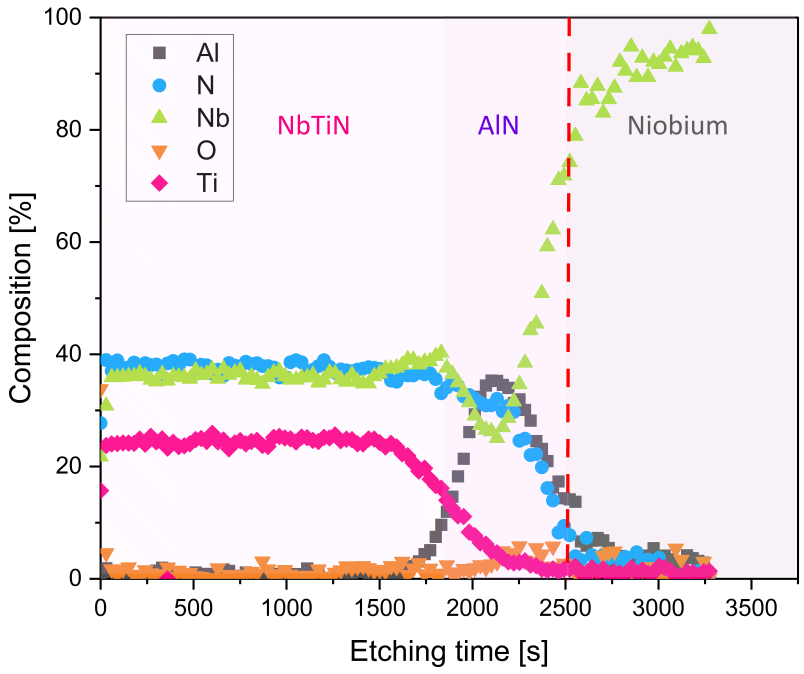

Figure 8.11: XPS profile of the NbTiN-AlN bilayer deposited on niobium using Ar as a transport gas for the ALD deposition

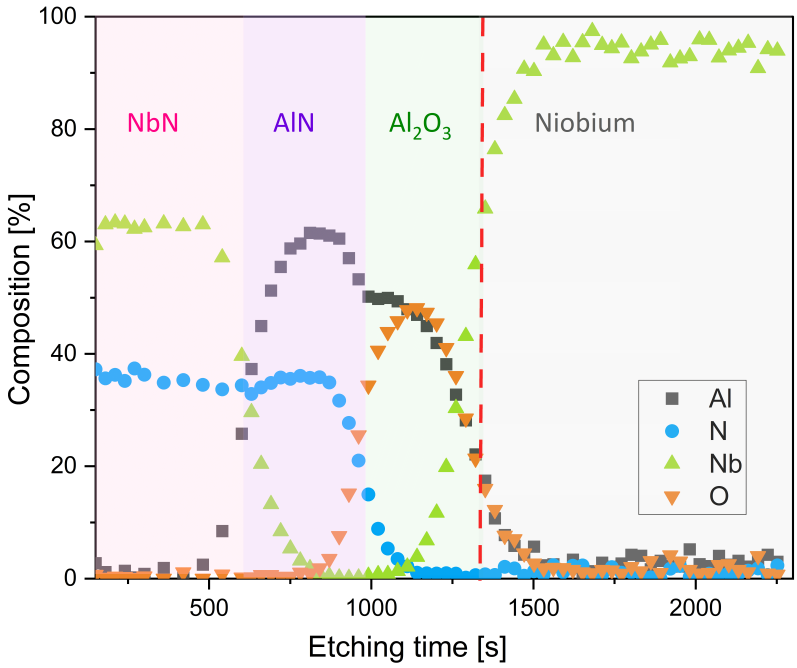

Figure 8.12: XPS profile of the NbN-AlN-Al_2O_3 bilayer deposited on niobium using N_2 as a transport gas for the ALD deposition

8.5 Topography and roughness considerations of the NbTiN films

It widely recognized that the SRF performance of an accelerator cavity are strongly dependent of its interior surface morphology. To achieve high performances, it is crucial to have an inner surface without particulate contamination, sharp irregularities or scratches. Systematic studies have been made on Nb cavities to inspect its surface roughness and understand how it affects its performances. It has been found that roughness lower than 2 µm is necessary if one want to prevent local magnetic field enhancement and avoid lowering the quench field of the cavity [118, 119, 120, 121, 122]. Being aware of this matter, we kept a close eye on the surface morphology and nano-roughness of our NbTiN-AlN layers. During our use of the SEM technique to assess the quality of our films, we observed regularly and mainly on niobium samples some round structures with sharp features. They have been observed regardless of the stoichiometry of the film and whether or not the samples have been annealed. In order to characterize their height and find out their origin, we performed atomic force microscopy (AFM)[5] and secondary electron microscopy (SEM) analysis on both bare electro-polished EP and coated niobium samples. When comparing the surface morphology of the bare and coated Niobium samples with SEM, we found

[5]The AFM analysis were perfomed using a Bruker diinnova AFM at "Plateforme ICMMO",91400 Orsay France

that they have similar aspects with the presence of some round features (see figure 8.13). The close up SEM images on these particles shows a lateral size ranging from several tens of nanometer to $\sim$ 200 nm.

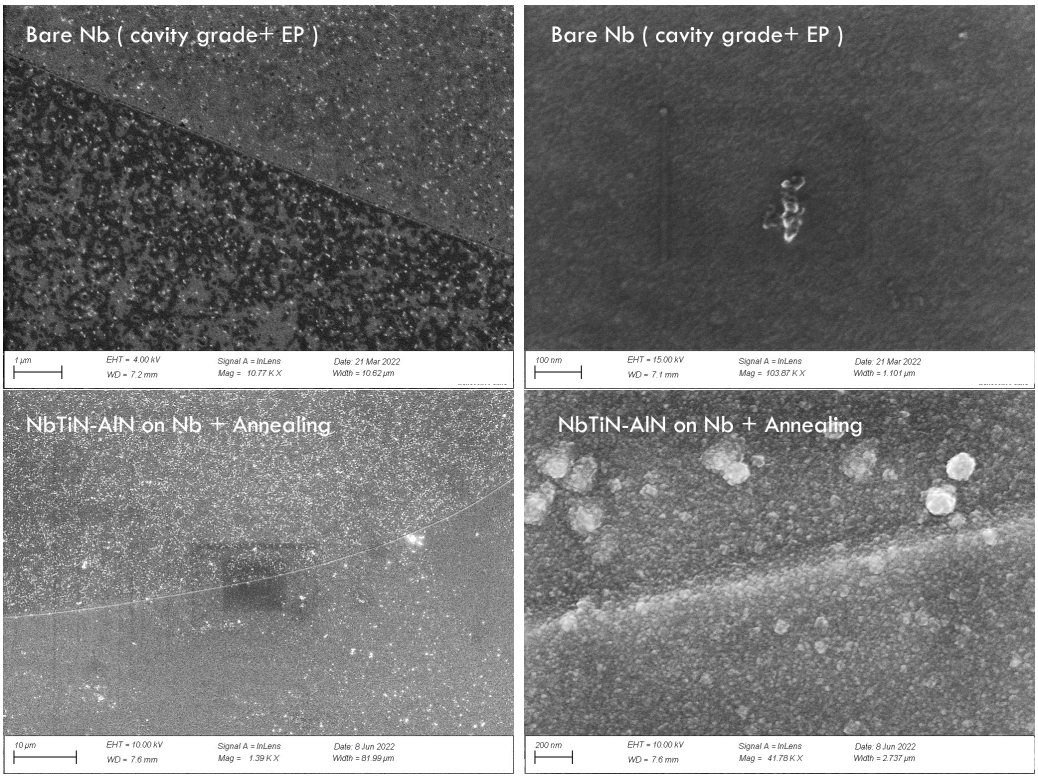

Figure 8.13: SEM images comparing a bare niobium sample with a coated sample after annealing (see text for comments)

Our tapping-mode AFM characterization are presented in figure 8.14 and 8.15. Surface analysis on both samples showed that these features are $\sim$ 50 nm height and have a lateral size of $\sim$ 100 nm. Despite the presence of these features, the coated Nb films showed an average roughness $\sim$ 5 nm for a scanned area of 5×5 µm.

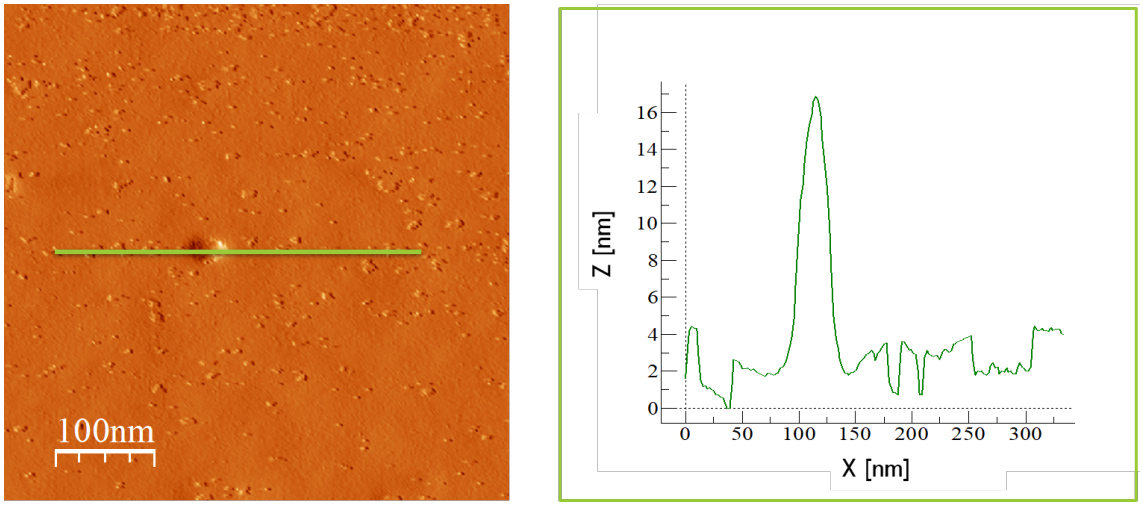

Figure 8.14: AFM scan on the bare niobium sample

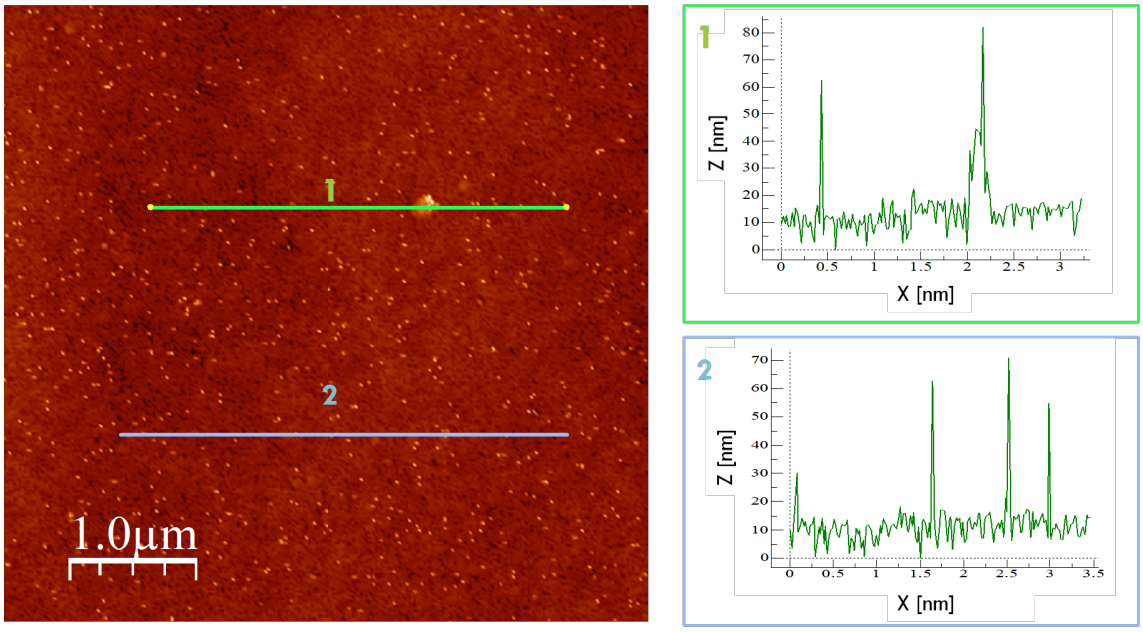

Figure 8.15: AFM scan on a the coated Nb sample after annealing

These observations indicates that these particles are substrate-related and are not inherent to the growth mechanism. These particles might originate from the EP process as it have been observed in [123], the rinsing water or simply the atmosphere. Because ALD is highly conformal, these round contaminants are also coated which gives them sharp edges.

To further emphasize these findings, it can be seen on figure 8.16 two SEM scans on the same coated Nb sample where we can observe a bumpy structure that looks like a contaminant particle that have been coated with the NbTiN-AlN layer on 8.16 (a) whereas elsewhere on the sample (where the niobium substrate was sufficiently clean) we see a very flat NbTiN film over an area of $\sim 3{\times}2.5$ µm. (see figure 8.16 (b))

Unlike niobium coupons, that were simply cleaned with deionized water, niobium cavities are systematically high pressure rinsed before any ALD-coating so these particulates shouldn't be a problem in a cavity.

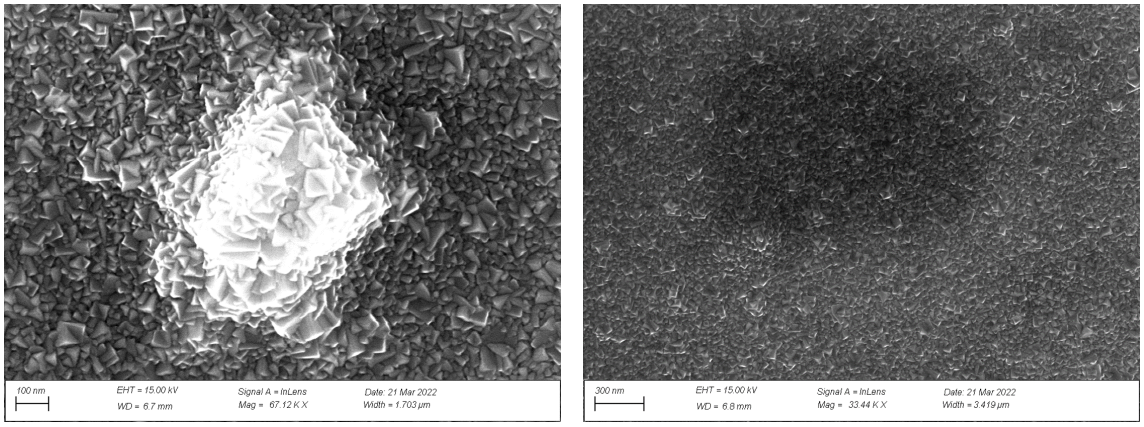

(a) (b)

Figure 8.16: SEM images on various area of the same coated Nb sample after annealing

8.6 NbTiN-AlN uniformity test on 1.3 GHz cavity geometry

8.6.1 Experiment preparation

The uniformity of the NbTiN-ALN bilayer coating on the SRF cavity geometry is crucial for their performances. Atomic layer deposition technique is inherently the best-suited deposition technique in terms of layer uniformity. Nonetheless, the deposition parameters, in particular, the pulse and purge time have a huge impact on this aspect. In order to find out the best deposition recipe for the 1.3 GHz cavity geometry, we performed two tests on a 1.3 GHz copper cavity. Prior the deposition, we inserted a sample holder that follows the cavity shape and loaded with 15 clean Si samples. The cavity tests were performed on the research-scale ALD system where we replaced the deposition chamber with the cavity itself. Figure 8.17 shows a picture of the copper cavity installed into the deposition system. K-type thermocouples where fixed on the cavity to control its temperature during the process and maintain a uniform temperature of 450°C. The cavity was then covered with resistive heaters and thermal isolation. For the first deposition test, we choose to use the same purge and pulse time used for coating samples[6]. We deposited 110 cycles of AlN using the following recipe ($AlCl_3$ 1.5 s/ 15 s - NH_3 0.5 s/ 15 s) followed with 550 cycles of NbTiN supercycles. We used the following combination for the NbTiN supercycles:

$$2(TiCl_4 + NH_3) + 2(NbCl_5 + NH_3) \tag{8.2}$$

[6]same paramters used in the previous chapter

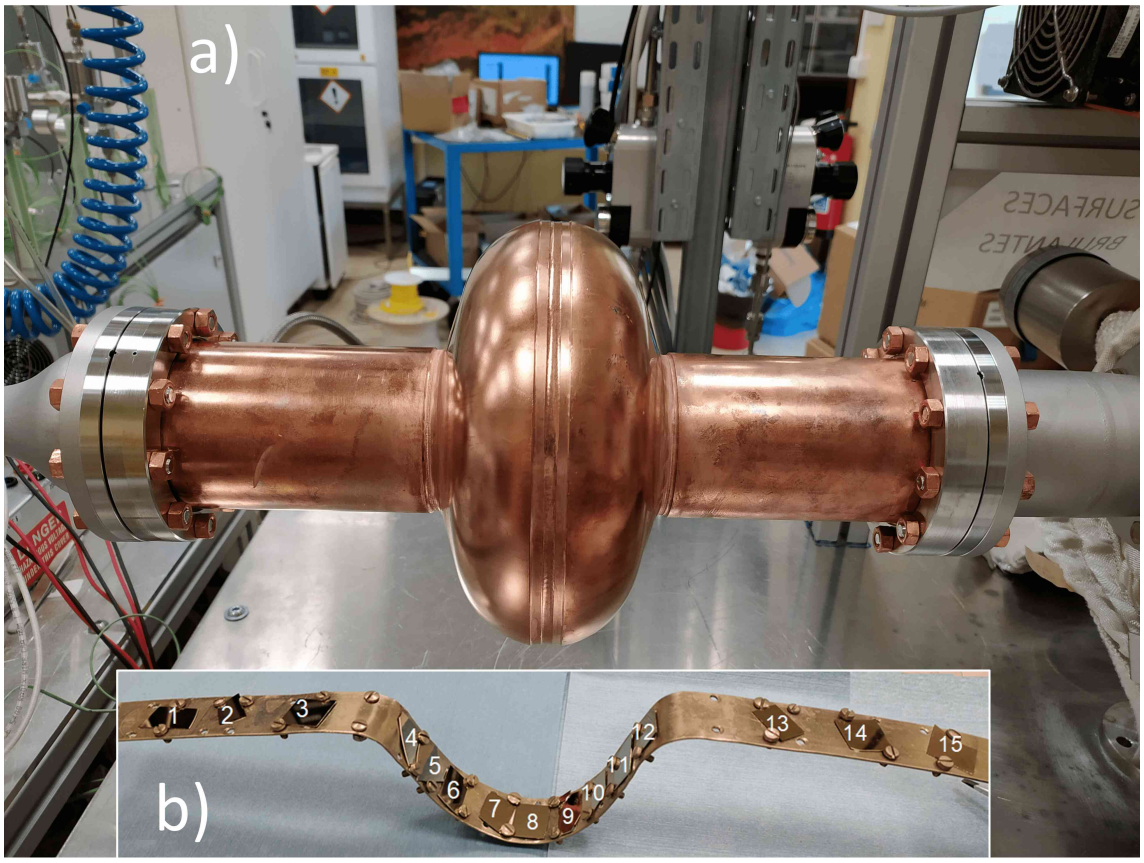

Figure 8.17: a) Picture of the copper cavity installed on the research-scale ALD system. b) Picture of the sample holder loaded with 15 Si samples

The pulse time where 2.5 s, 2 s and 0.5 s respectively for $TiCl_4$, $NbCl_5$ and NH_3 and the purge time was fixed at 10 s for all the three precursors. As it is can be observed in the figure 8.18, the cavity coating showed a golden and uniform color typical of nitrides all over the cavity walls and on the sample holder.

8.6.2 Optimizing the deposition parameters on the 1.3 GHz cavity

In order to have a precise idea of the thickness profile along the cavity, we performed XRR measurement on the 15 Si samples. We measured also the room temperature resistance of the different samples. The thickness measurements as well as the resistivity profile of the first deposition test are summarized in figure 8.19. Unlike the AlN layer, which was uniform along the cavity profile, the NbTiN layer showed a uniform thickness of $\sim$ 50 nm up to the iris of the outer beam tube. The three samples placed at the outer beam tube showed an NbTiN thickness of 80 nm which is 60% higher than what is expected. This is a typical sign of a CVD growth component that took place in the outer beam tube of the cavity. A trivial explanation to this observation is that the purge time is not sufficient to enable the evacuation of excess precursors. This causes an accumulation of the NbTiN precursors in the outer beam

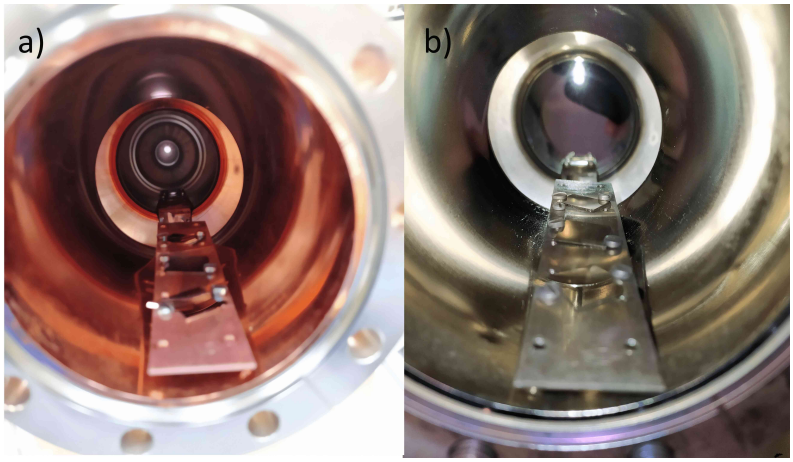

Figure 8.18: Picture of the inside of the copper cavity with the sample holder before (a) and after (b) the deposition

tube and give rise to a CVD regime, which explains the much thicker film in this area.

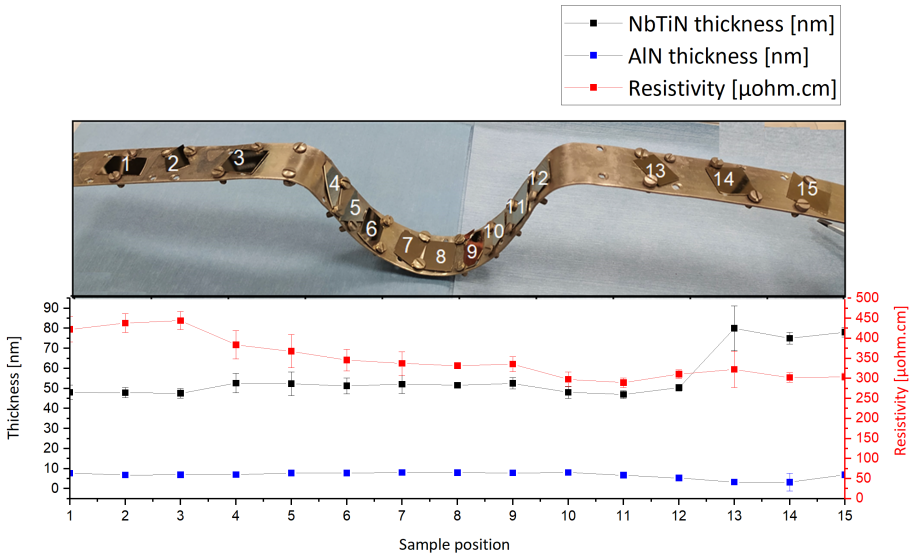

Figure 8.19: Results of the first test with 10 s purge for NbTiN film

To cure this problem, we performed a second deposition test in the same deposition conditions and we only altered the purging time from 10 seconds to 20 seconds for the NbTiN film recipe. Then, we preformed XRR measurement on the Si samples (summarized in figure 8.20). We can see that the thickness profile is now uniform and compatible with an ALD growth regime.

To successfully coat an Nb coating, not only should the thickness of the bilayer be uniform all over the cavity but also the crystalline structure and the chemical composition. To test this aspect, we performed GIXRD measurement on three Si samples (one from the equator and two others from the two beam tubes). The GIXRD patterns of the figure 8.21 proves that crystalline structure of the films is identical in the cavity, which is in itself a sign of uniform chemical composition of the NbTiN layers.

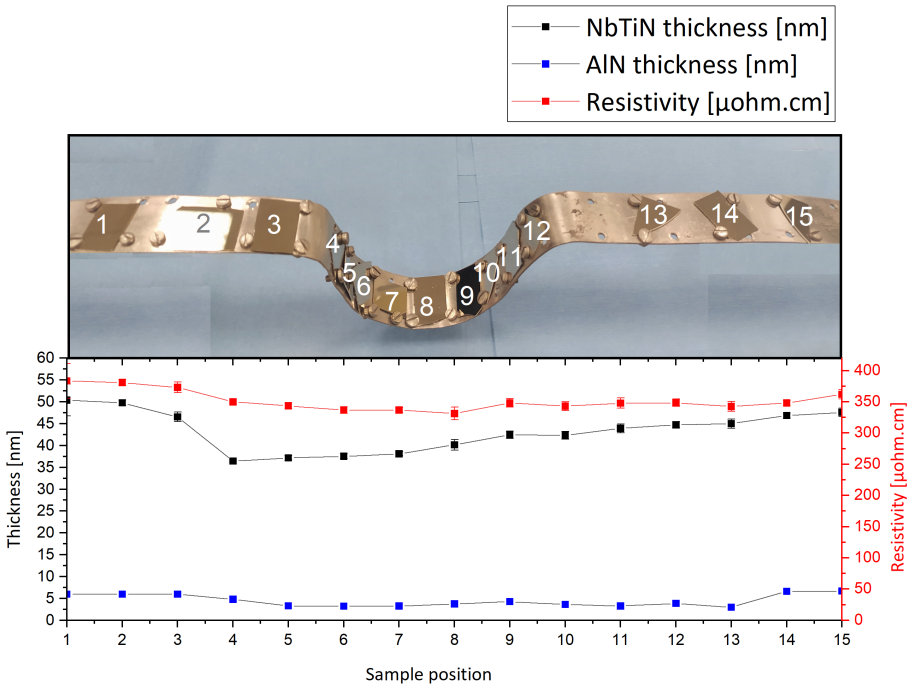

Figure 8.20: Results of the second test with 20 s purge for NbTiN film

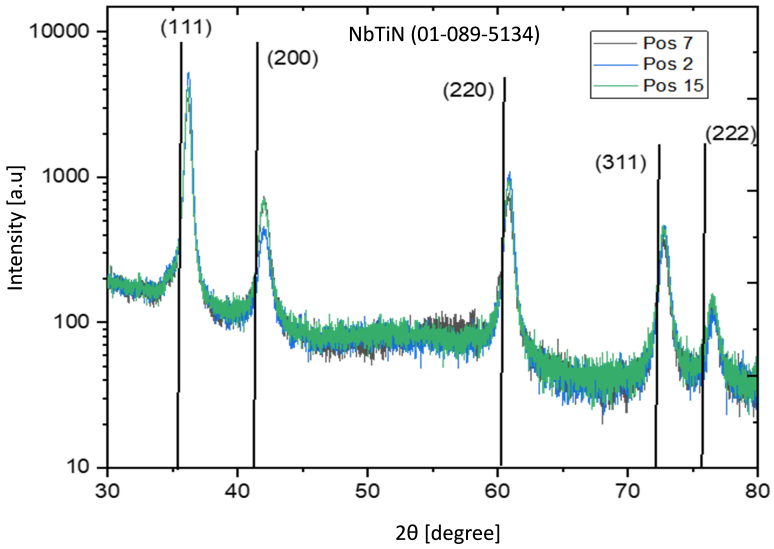

Figure 8.21: GIXRD patterns from Si samples of the second deposition test

8.7 Testing the NbTiN-ALN layer on 1.3 GHz Niobium cavity

8.7.1 Cavity Preparation

By the time we reached this point of our research, we were able to construct the new ALD system for cavity coating and we were finally able to coat properly niobium cavities at temperature higher than 250°C. In order to coat the niobium cavity with the multilayer structure, we prepared the cavity in the clean room. First, we performed a HPR treatement on the cavity to avoid any contamination or EP residues on the surface. The ALD-system connectors were then mounted onto the cavity. The cavity was then sealed and transferred to the ALD lab to be installed onto the deposition system. Figure 8.22 (a) shows a picture of the cavity installed into the oven with five thermocouples connected on the equator and the beam tubes to monitor the cavity temperature during the process and maintain it at 450°C.

Once the cavity were ready for coating, we performed the deposition of our optimized AlN-NbTiN recipe. We waited for the cavity to cool down to room temperature. Then, we disconnected it from the ALD system and transferred it to the clean room. After the coating, as it can be seen in figure 8.23, the cavity had a bright golden and uniform colour. The inner surface were mirror-like with no sign of defects.

After the optical inspection, we transferred the cavity to our annealing oven were we put niobium caps on the beam tubes (see figure 8.22 (b)) and performed the optimized annealing recipe at 900°C-SP-2R with an additional step at 650°C for 5 hours. This step at 650°C during 5 hours was intended to lower the hydrogen concentration in a similar manner to that explained in section 3.2.1. During the annealing, we witnessed some vacuum degradation (there were not observed for niobium coupons) probably because of the relatively small volume of the annealing

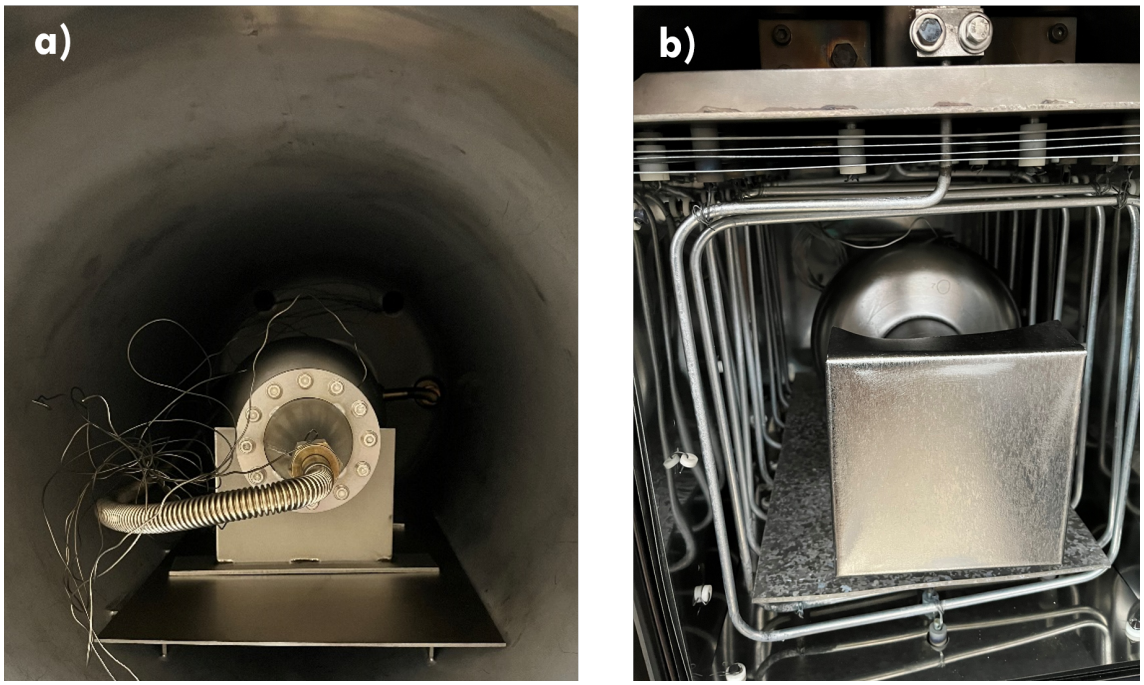

Figure 8.22: Pictures of the cavity preparation steps. (a) the cavity installed onto the ALD system. (b) the cavity inserted into the oven for post-annealing

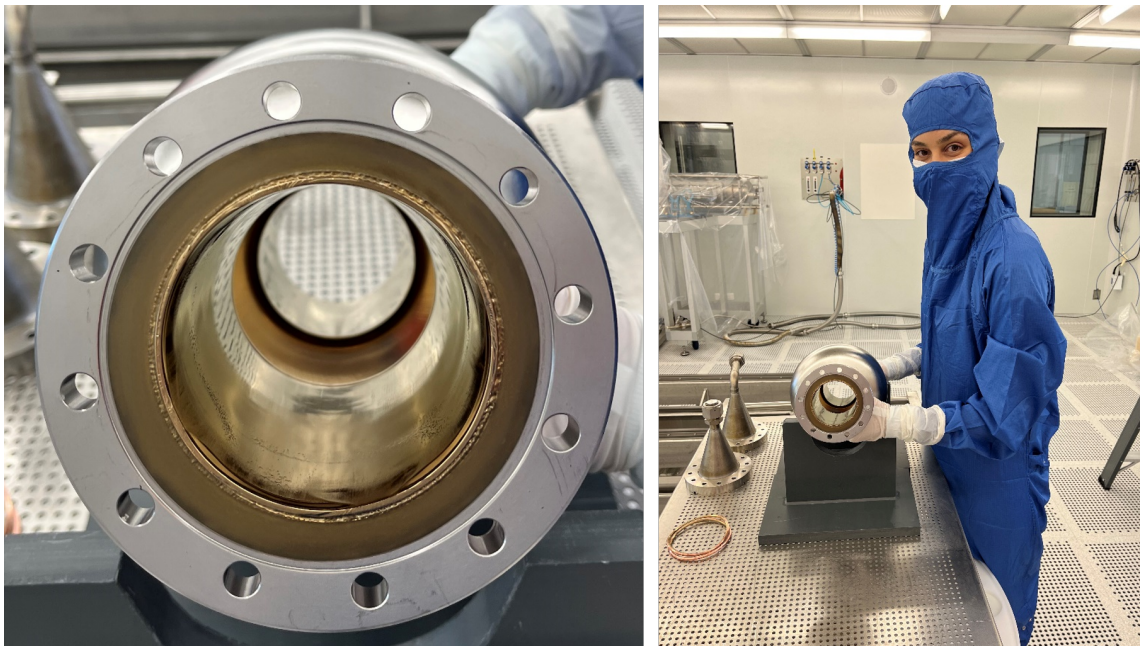

Figure 8.23: Picture of the cavity after the multilayer coating

oven as compared to the cavity volume. After the annealing, we observed some film delamination especially at the beam tube. The cavity looked overall more metallic with some golden areas as it is shown in figure 8.24.

Figure 8.24: Picture of the cavity cell after the annealing

8.7.2 RF test results

Despite the unexpected film delamination on parts of the cavity, we tested the coated cavity under RF. We measured the quality factor as a function of the accelerating gradient. We also recorded the evolution of the surface resistance as a function of the cavity temperature. The results of the RF test are illustrated in figure 8.25 and 8.26. The cavity showed overall degraded performances compared to the baseline. The quality factor showed a high Q-slope in low fields: it decreased sharply from 2.10^{10} at 1 MV/m accelerating gradient to 5.10^{9} at 1.5 MV/m. This high Q-slope is somehow similar to one observed on the NbTiN coated cooper cavities reported by [124]. Surprisingly, the cavity exhibited an anti-Q slope where the quality factor started increasing again from 7 MV/m to 20 MV/m, field at which the cavity quenched. This anti-Q slope behaviour have been widely reported for N-doped Niobium cavities [31]. Since we used N_2 as a transport gas during the cavity coating without using a diffusion barrier, a certain amount of nitrogen would have necessarily diffused into bulk niobium , which could explain this anti Q-slope observed. The surface resistance of the coated cavity showed very close values to the baseline measurement at 4 K. Nonetheless, the residual resistance turned out to be much higher at 2 K (30 nΩ while the bare niobium cavity had a surface resistance of $\sim$ 5 nΩ at the same temperature).

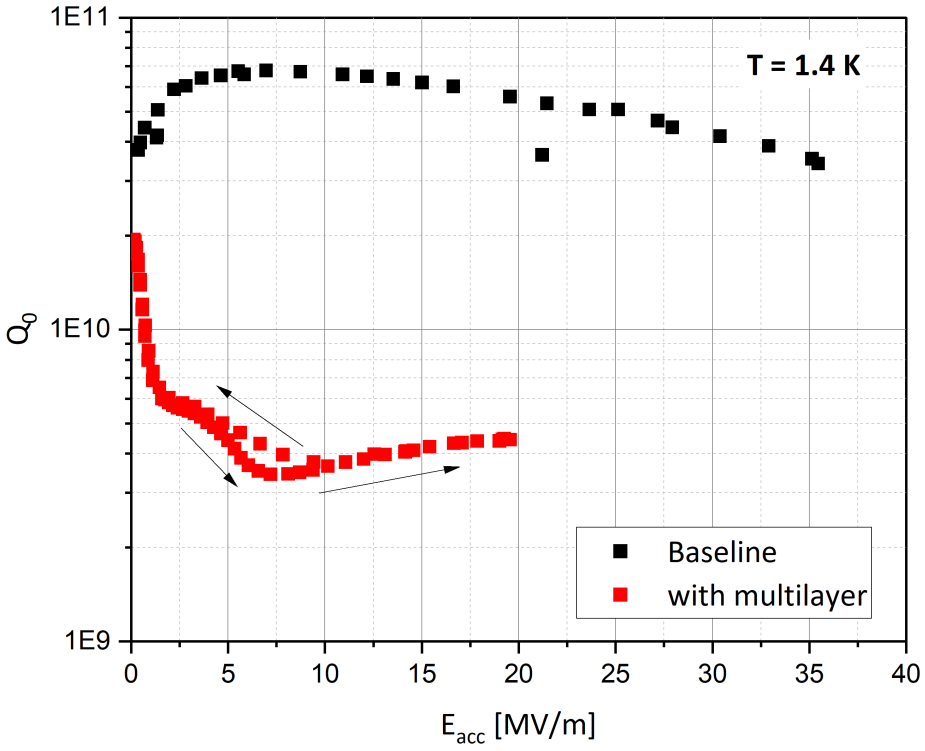

Figure 8.25: Quality factor of the coated cavity as a function of the accelerating gradient at 1.4 K

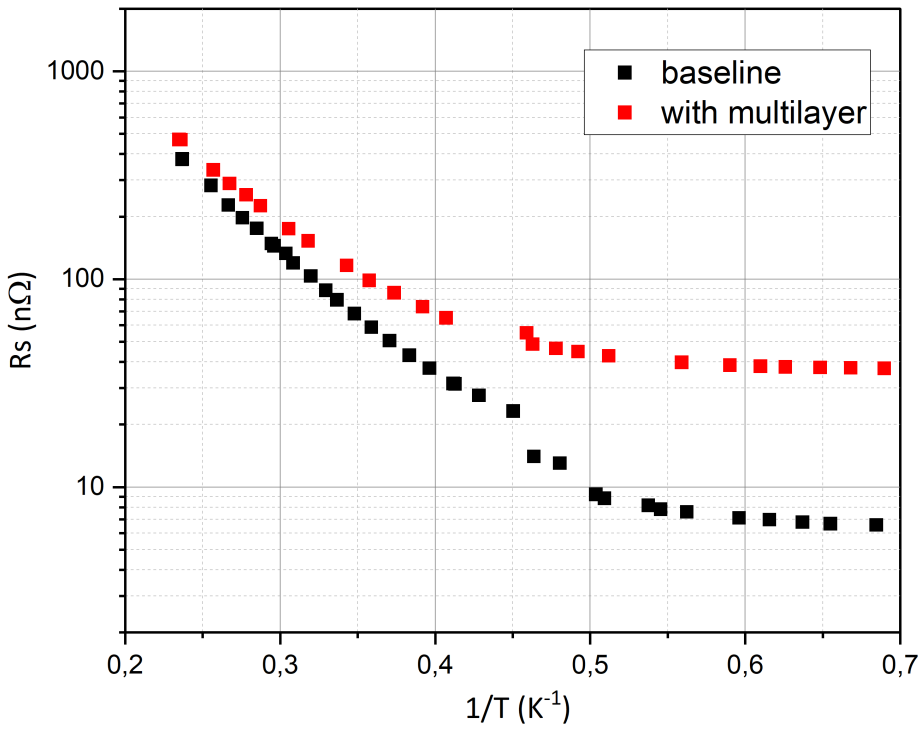

Figure 8.26: Surface resistance as a function of 1/K of the coated cavity at 1 MV/m

8.8 Perspectives

Despite the low performances of the first multilayer-coated niobium cavity, the reported results are encouraging on many levels. It is noteworthy that these are the results of the very first multilayer-coated Nb cavity. Finally, after 15 years of R&D effort in the SRF community, we managed to coat and test a cavity with the promising multilayer structure [1]. We are planning to perform more coating tests in the future in order to understand better the origin of these interesting results. We suspect that the film delamination is a result of inappropriate annealing condition where the vacuum was poorly controlled. The fact that the cavity-deposition system is freshly built may have somehow played a role in this film delamination that have never been observed before on any of our samples deposited with the research-scale ALD system.

Chapter 9

New route for doping SRF cavities using atomic layer deposition

9.1 Introduction

Great R&D efforts over the last four decades in the SRF community allowed reaching accelerating gradients of ~ 40 MV/m, which corresponds to a surface magnetic field close to the critical field of Niobium. However, the quality factor of the cavity decreases when increasing the accelerating gradient as the dissipation are proportional to the surface resistance times the square of the local magnetic field. Few years ago, a unexpected phenomenon of increase in the quality factor with the magnetic field have been observed in so-called doped-niobium cavities [31](see figure 9.1).

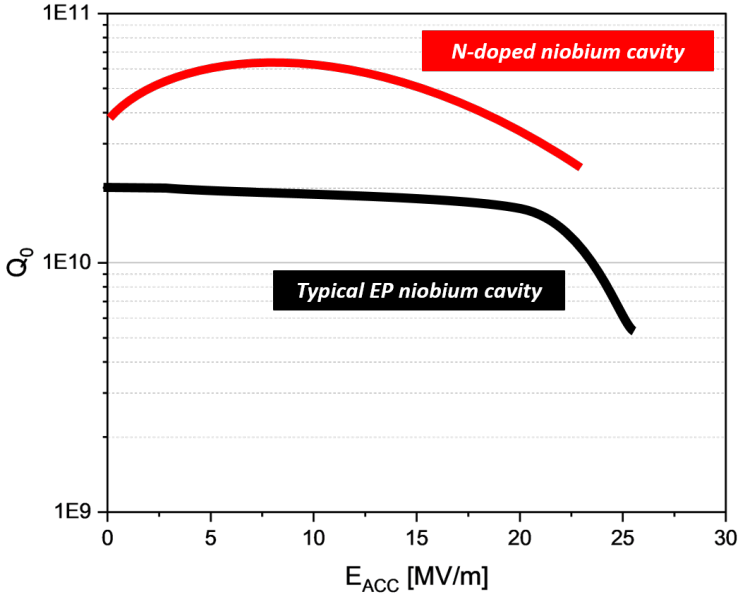

Figure 9.1: Comparison between typical electropolished niobium cavities and N-doped niobium cavities performances (figure after [31])

Introducing some non-magnetic impurities, in particular nitrogen, have been proven very beneficial in terms of surface resistance but at the detriment of accelerating field. For several application were cryogenic losses are prevailing on the costs, this doping treatment has become mandatory. Ever since this discovery, several studies have been performed to understand the origin of this effect and optimize this surface treatment [31, 32, 125].

In this chapter, we will present a new approach for doping niobium cavities using atomic layer deposition. We will introduce its potential advantages and we will discuss the first set of measurements performed on both niobium coupons and 1.3 GHz cavity.

9.2 Conventional approach for N-doping

The N-doping was fortuitously discovered by Fermilab in 2013 [126] after electropolishing some niobium cavities treated with nitrogen. The initial aim of their study was to form a surface niobium nitride layer by reacting bulk niobium cavity with nitrogen in high temperature UHV furnace. They wanted to investigate whether they can lower the niobium cavity surface resistance by creating an RF layer with a higher critical temperature than niobium. Directly after the nitrogen treatments at temperature in 800°C- 1000°C, all their cavities exhibited very poor quality factor $\sim 10^7$ at 2 K. They attributed this poor behavior to the possible formation of unwanted poorly superconducting Nb_2N phases at the surface. Surprisingly, as soon as they removed a certain amount of material (5 µm) via electro-polishing, the performances of cavities were drastically enhanced: The Nitrogen-treated + EP cavities showcased not only significantly higher quality factors at 2 K but they also exhibited an "anti-Q slope". Contrary to the usual decrease of the quality factor when increasing the accelerating gradient, the quality factor of these cavities showed an unexpected reversed field dependence (as schematised in figure 9.1).

Ever since this observation, in-depth investigations were carried out on this promising surface treatment to understand its origin. The hypothesis of the formation of higher T_c nitrides were ruled out by chemical and optical characterizations and the role of nitrogen in the enhancement of niobium SRF cavities performances was confirmed. Further investigations revealed that this unusual and extended anti Q-slope stems from an inverted field dependence of the BCS resistance possibly resulting from a reduction of inelastic scattering [127].

It is important to mention that a similar anti-Q slope result was previously reported on a 1400°C-treated cavity with argon injection during the cool down [128]. The witness samples showed significant contamination of other impurities such as titanium, which hints that doping niobium with some impurities (nitrogen, titanium...) could be the common origin of the anti Q-slope behavior.

Soon after this discovery, extensive research effort have been made into understanding the parameters in play leading for the enhanced performances and optimizing the recipe in order to be implemented in LCLS-2. Grassellino et al [126] reported that the best performing cavities had a nitrogen concentration in the range 50-200 ppm with the doping recipe as illustrated in figure 9.2. First, the cavity is annealed at 800°C for 3 hours in UHV for degassing. Nitrogen is injected at the

end of the degassing step at $\sim 3.10^{-2}$ mbar and held for few minutes, then the furnace is evacuated and the cavity is annealed for few minutes before cool down to room temperature. Thereafter, 5 µm to 10 µm of material removal is performed via electro-polishing to get rid of the low Tc Nb_2N contaminated inner surface layer. Note that the surface oxide is reconstituted after electropolishing, and a little hydrogen is reintroduced by the wet treatment.

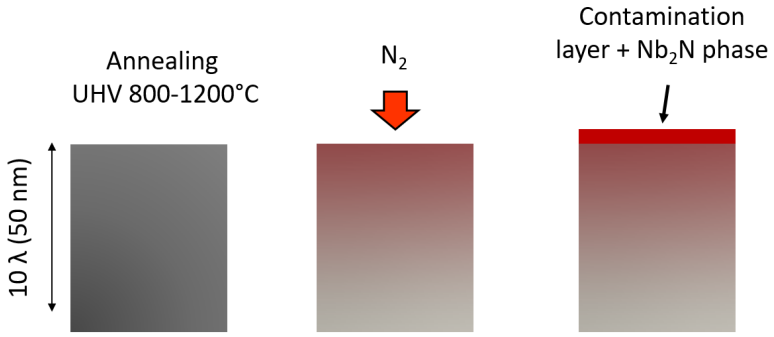

Figure 9.2: Illustration of the N-doping approach proposed by Fermilab

An alternative to Nitrogen-doping at high temperature followed by the electro-polishing step was suggested by adding nitrogen to the low-temperature baking previously used to attenuate the high-field Q-slope [32]. In this so-called nitrogen-"infusion" treatment, the cavities are heated at 800°C for 3 hours. This step is meant not only for hydrogen degassing but also to dissolve niobium native oxide into the bulk. The oven is then cooled down to 120 -300°C and the nitrogen is introduced to the system during 24 to 96 hours at a partial pressure of $\sim 3.10^{-2}$ mbar. This method has shown great improvement of the quality factor and the quench fields of the SRF cavities without the need for post-furnace electro-polishing [32] but does not present an anti Q-slope. The difference of behavior suggests that superconducting properties of the near surface are not affected in the same way.

9.3 ALD-approach

The previously reported results suggests that introducing a small amount of impurities in the surface might need to become a standard process in cavity preparation to reach the full potential of SRF niobium cavities. Although the greatest part of R&D effort have been focused on nitrogen doping, other potential dopant such as titanium [128] and oxygen [129] have been pointed out to be beneficial to niobium SRF performances. In this chapter, we introduce a new approach for SRF cavities doping using atomic layer deposition followed by a subsequent annealing step at high temperature. Our approach consists in coating the SRF cavity with an ultra-thin film of metal nitrides or oxides (depending on the dopant desired) as a finite well-controlled source of nitrogen or oxygen. Then, the cavity is annealed

at high temperature to allow the diffusion of the dopant atoms into the RF penetration depth layer. Unlike the oxygen or nitrogen, the metal atoms (because they have a much lower diffusion coefficient than N and O) would stay at the surface and would give rise to a new passivating oxide post-exposition to ambient air without the use of post-doping electro-polishing treatment. The use of atomic layer deposition would grant a uniform and well-controlled amount dopant thanks to its inherent sub-nanometric thickness control. We would also benefit from the great variety of possible coating layers that offers ALD. This can result in not only an alternative to "conventional" nitrogen doping techniques but would also allow experimenting with other type of dopants and overall improve our understanding of the physics that governs the first tens of nanometers of a niobium cavity surface.

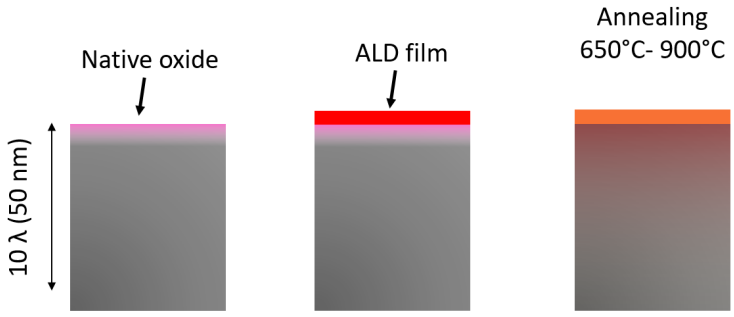

Figure 9.3: Illustration of the N-doping approach using ALD

9.4 Preliminary results on Nb coupons

As a first step in our exploration of this approach, we mainly focused on doping niobium with nitrogen in the quest of achieving similar levels of doping obtained with the "conventional approach". To do so, we tested the deposition of four different layers of metal nitrides TiN, AlN, NbN and ZrN as our nitrogen source on niobium. The coated samples were then annealed at 900°C during 3 hours in UHV to allow the nitrogen diffusion into the niobium. For each film, we performed X-ray photoelectron spectrometry XPS and time-of-flight secondary ion mass spectrometry TOF-SIMS[1] analysis to track the doping levels and examine the surface composition of the samples after their re-exposition to ambient air. The nitride films where deposited using standard ALD recipes involving the reaction of metal chlorides with ammonia NH_3 at 450°C in our research-scale ALD system. More details on the ALD deposition can be can be found in chapter 4.

[1]TOF-SIMS analysis were performed by TESCAN ANALYTICS

9.4.1 Niobium nitride

As a start, we coated niobium samples with two niobium nitride film thicknesses, 10 nm and 5 nm. The samples were then annealed at 900°C during 3 hours in UHV. After the annealing, XPS analysis with depth profiling was performed on the sample to probe the remaining nitrogen concentration at the surface. The results of XPS analysis on these NbN coated Niobium samples are showcased in figure 9.4.

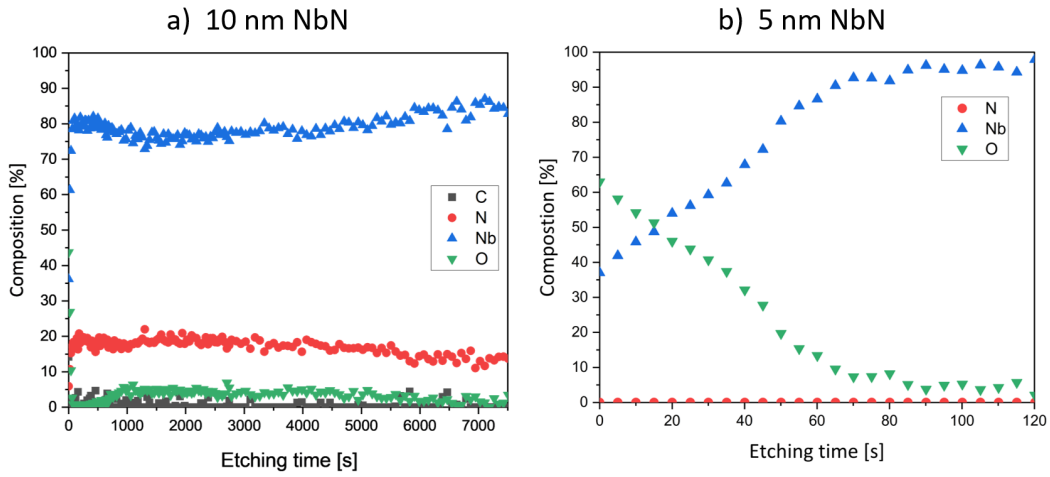

Figure 9.4: XPS profile on the NbN coated Nb sample after annealing at 900°C - 3 hours and re-exposition to air. (a) 10 nm of NbN, (b) 5 nm of NbN

It can be seen on the XPS profiles that with 10 nm of NbN, we measure $\sim$ 10 % of nitrogen at the very surface of the niobium sample. This concentration is very high compared to the doping levels obtained with the "conventional approach". On the other hand, when we annealed the 5 nm of NbN, no nitrogen have been detected in the surface of the NbN coated sample (see figure 9.4-b). Instead, we witnessed the formation of a niobium native oxide layer, which is confirmed by the analysis of the Nb 3d core level spectra (see figure 9.5).

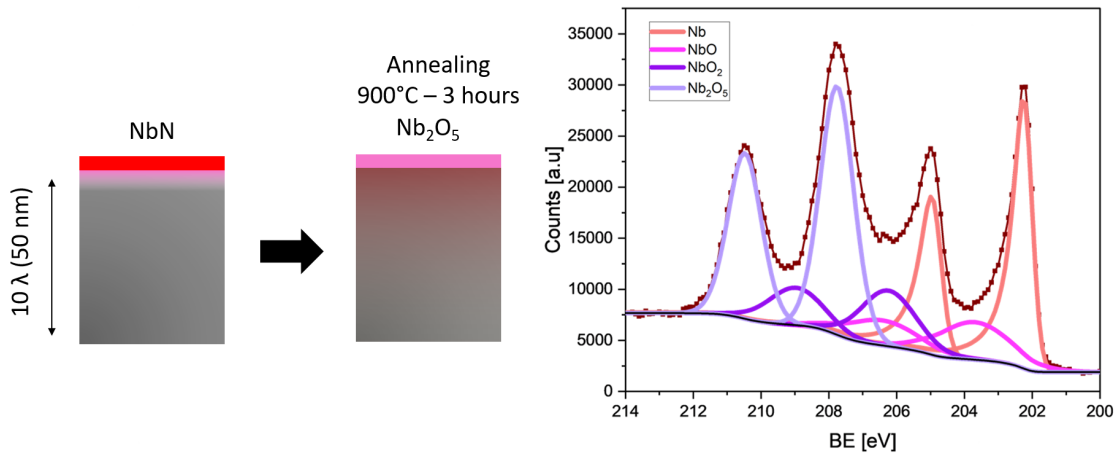

Figure 9.5: The Nb 3d core level spectrum showing the formation of a native oxide layer after the annealing of the 5 nm NbN film and its re-exposition to air. The fitting procedure of the Nb 3d core-level spectrum is the same described in table 5.1.

At this point, we performed TOF-SIMS analysis on the sample coated with 5 nm in order to have a measurement with a much better sensitivity for trace elements than XPS. Figure 9.6 shows the profile of NbN-/Nb- as a function of the sputtering time on the NbN coated sample after the annealing. It is important to recall that using the "conventional" doping approach, a flat NbN-/Nb- profile is obtained around 0.1 value [130]. In that sense, the sample coated with the 5 nm of NbN film appears to have similar doping level to that reported for N-doped cavities as it can be seen in figure 9.6.

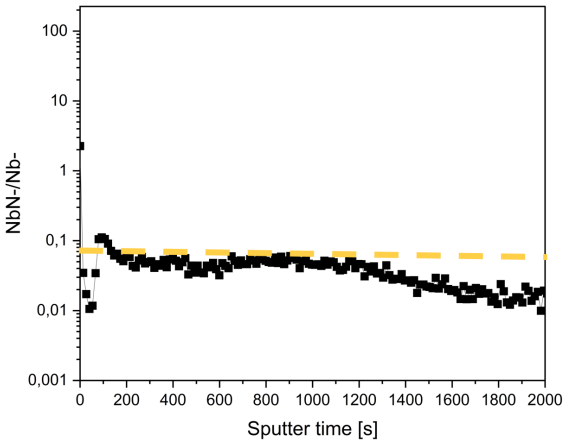

Figure 9.6: TOF-SIMS analysis on NbN coated Nb sample after ALD coating + annealing. The dashed line in yellow represents the NbN-/Nb- obtained with the conventional doping approach (after [130])

9.4.2 Titanium nitride

From the N doping level stand point, our doping approach using ALD-depositied NbN presented earlier seems promising. We wanted to explore one step further and not only dope Nb with N but also replace the NbO_x with another dielectric layer that could also be beneficial to RF performances (as discussed in chapter 5). To that end, we started exploring TiN. A 5 nm thick titanium nitride was deposited on a niobium sample. After the deposition, the sample was annealed at 900°C during 3 hours in UHV. After the annealing, XPS analysis with depth profiling was performed on the sample. The XPS profile is presented in figure 9.7. It can be seen in figure 9.7 that the nitrogen diffuses into the bulk as only about $\sim$ 5 % of N remain in the Ti rich overlayer as seen on depth profile. On the other hand, we observe the formation of a TiO_2 oxide on the surface.

The Ti 2p core level and the Nb 3d spectra are shown in figure 9.8. As observed on the XPS profile, the Ti 2p core level spectrum exhibit an important contribution of TiO_2 component and the presence of smaller contributions of TiN and TiN_xO_y components. The Nb 3d core level spectra reveals also the presence of Nb_2O_5 native oxides.

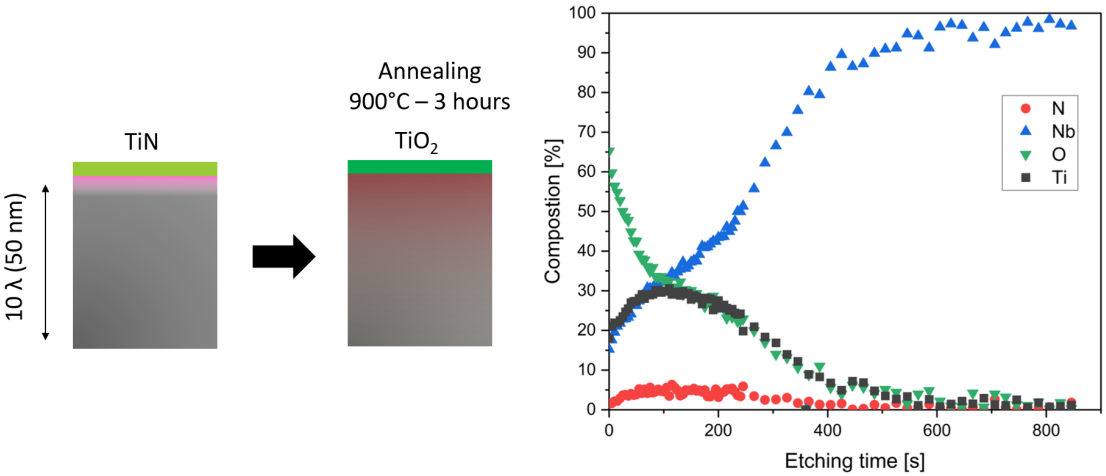

Figure 9.7: XPS analysis on the TiN coated sample after annealing at 900°C-3 hours

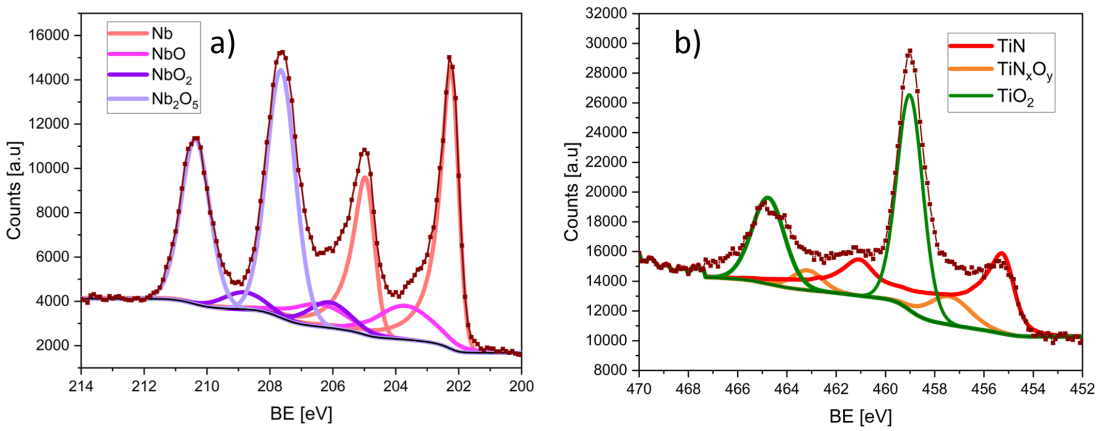

Figure 9.8: XPS analysis on the TiN coated sample after annealing at 900°C-3 hours: a) the Nb 3d core level spectra. b) the Ti 2p core level spectra fitted with the same procedure described in 6.5.2

Figure 9.9 shows the TOF-SIMS measurement on the TiN coated Nb sample after annealing. It can be seen that the NbN-/Nb- level is higher to that obtained with NbN which is consistent with the $\sim$ 5 % of N seen on the XPS depth profile.

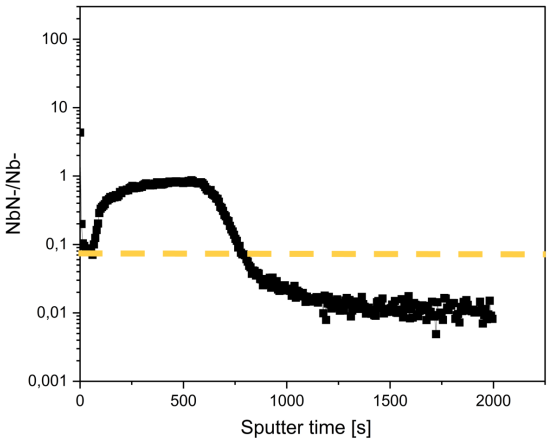

Figure 9.9: TOF-SIMS analysis on TiN coated Nb sample after ALD coating + annealing. The dashed line in yellow represents the NbN-/Nb- obtained with the conventional doping approach (after [130])

9.4.3 Zirconium nitride

Pursuing our approach tested with TiN, we explored ZrN as a dopant source and a protecive surface. Figure 9.10 represents the XPS analysis of a similar experiment done on 5 nm- ZrN coated Niobium sample. The XPS profile shows no nitrogen in the surface of the niobium sample. It seems that the ZrN layer lost its nitrogen through diffusion toward bulk Niobium. Upon re-exposure to air, the metallic Zirconium layers is transformed into a ZrO_2 layer as it can be also seen from the Zr 3d core level spectrum (see figure 9.11). Interestingly, the Nb showed no presence of niobium native oxides and showed only a pure metallic contribution on the Nb 3d core level spectrum. This results is particularly interesting as ZrO_2 is a relatively stable dielectric with potentially low losses under RF fields. It is definitely worth testing as a diffusion barrier in the same way described in chapter 5.

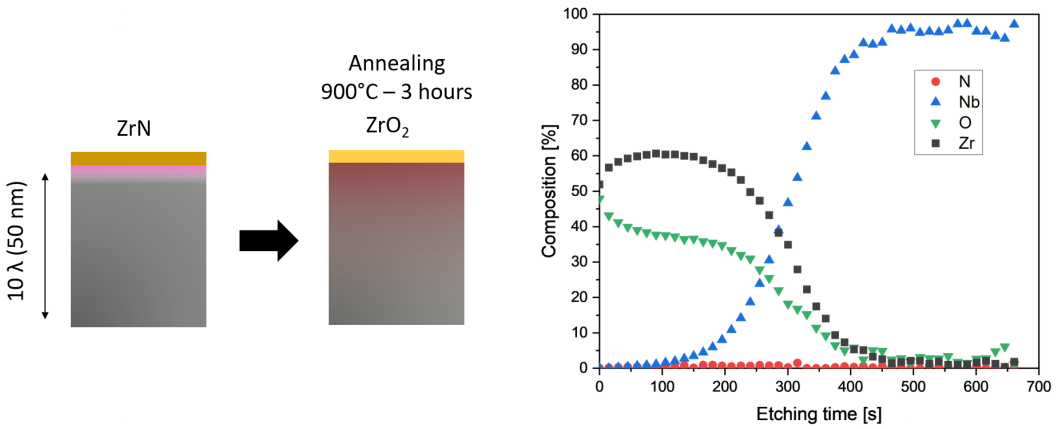

Figure 9.10: XPS analysis on ZrN coated Nb sample after ALD coating + annealing

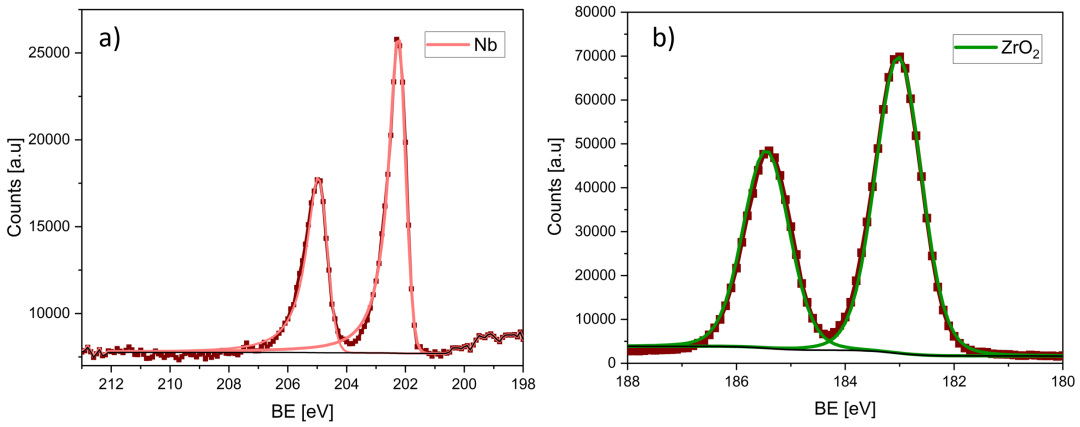

Figure 9.11: a)The Nb 3d core level spectra on the ZrN coated sample after annealing at 900°C-3 hours. b) The Zr 3d core level showing ZrO_2 contribution at BE =183 eV

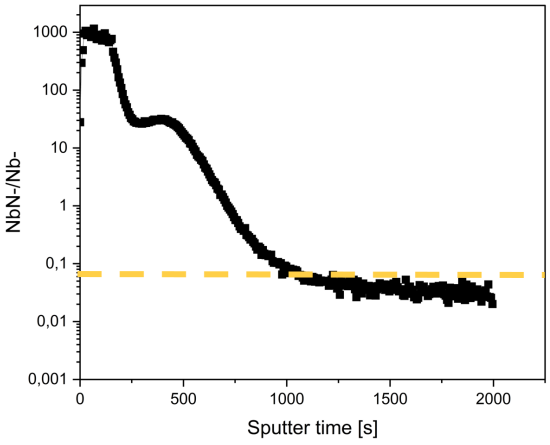

Figure 9.12: TOF-SIMS analysis on ZrN coated Nb sample after ALD coating + annealing. The dashed line in yellow represents the NbN-/Nb- obtained with the conventional doping approach (after [130])

TOF-SIMS measurement on the ZrN showed (see figure 9.12) a NbN-/Nb- peak at the very surface despite the absence of N signal on XPS analysis.

9.4.4 Aluminium nitride

In a similar manner to the previously presented experiments, we deposited 5 nm of AlN on a niobium substrate and annealed it at 900°C during 3 hours. After the annealing, we detected no nitrogen nor aluminum on the sample as it can be seen in the XPS results in figure 9.13. Only a layer of niobium native oxide covered the surface of the sample (see figure 9.14). This observation is similar to the one we reported in chapter 4 where the Al vanished after heating an Al_2O_3 layer at 800°C during 4 hours. A plausible explanation is that the AlN is depleted from nitrogen which leaves a thin layer of Al at the surface. The thin Al layer is then evaporated from the surface.

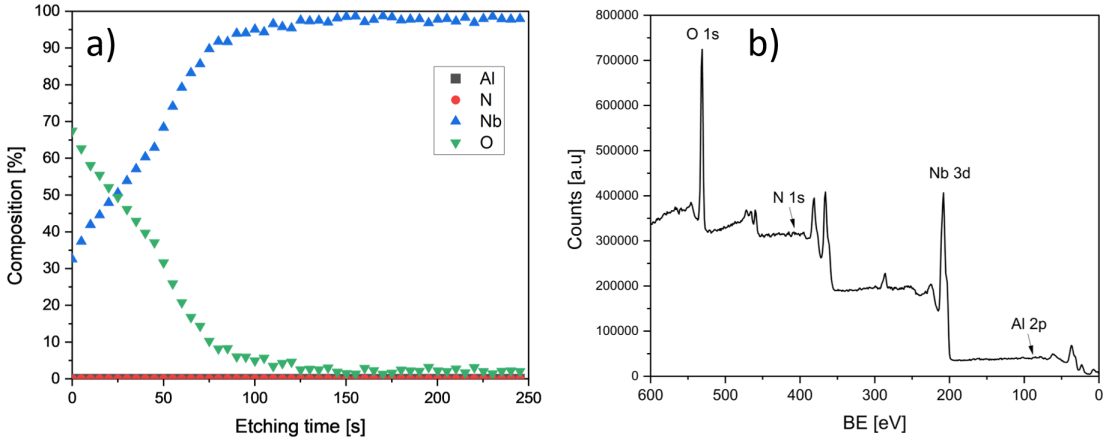

Figure 9.13: XPS analysis on AlN coated Nb sample after ALD coating + annealing: a) The XPS depth profile. b) The survey showing the absence of N and Al signals.

Figure 9.15 shows the TOF-SIMS measurement on the AlN coated Nb sample after annealing. It can be seen that the NbN-/Nb- level is lower than the level reported for N-doped cavities.

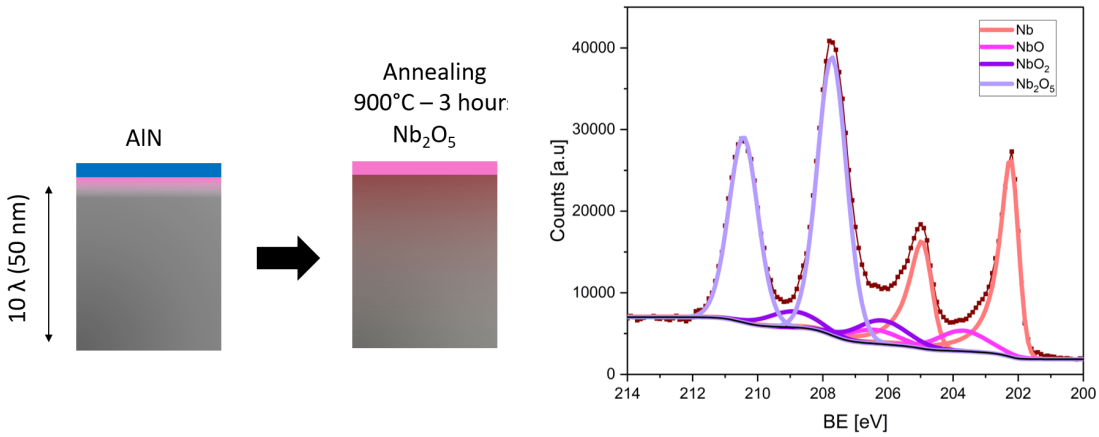

Figure 9.14: The Nb 3d core level spectra on the AlN coated sample after annealing at 900°C-3 hours

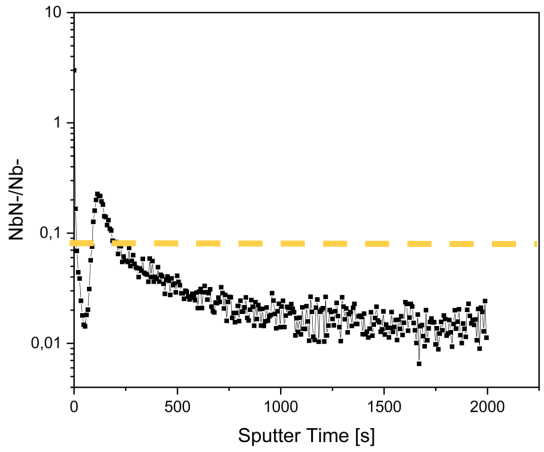

Figure 9.15: TOF-SIMS analysis on AlN coated Nb sample after ALD coating + annealing. The dashed line in yellow represents the NbN-/Nb- obtained with the conventional doping approach (after [130])

9.5 Test on SRF cavity

As a start, we chose to test this doping approach on a Niobium 1.3 Ghz cavity using the niobium nitride film. The cavity was coated with a 5 nm thick niobium nitride film using our cavity-coating ALD system. The cavity have been then annealed at 900°C during 3 hours in UHV and then sent to the clean room for HPR rinsing and assembly for the RF test. It is important to emphasize that no electro-polishing was performed on the cavity after its ALD + annealing treatment. The RF test of the N-doped cavity is presented in figure 9.16 (in green) and compared to the RF performance of the cavity prior to the N-doping (in black). We can see the surface resistance showed improved values compared to the baseline for temperature higher than 2 K but a two times higher residual resistance. This resulted in a two times

higher Q_0 at 4 K but lower performances at 2 K. As it can be seen in figure 9.16, the cavity showed an overall degraded performances compared to the baseline. Anti Q-slope was not observed on this cavity's RF tests.

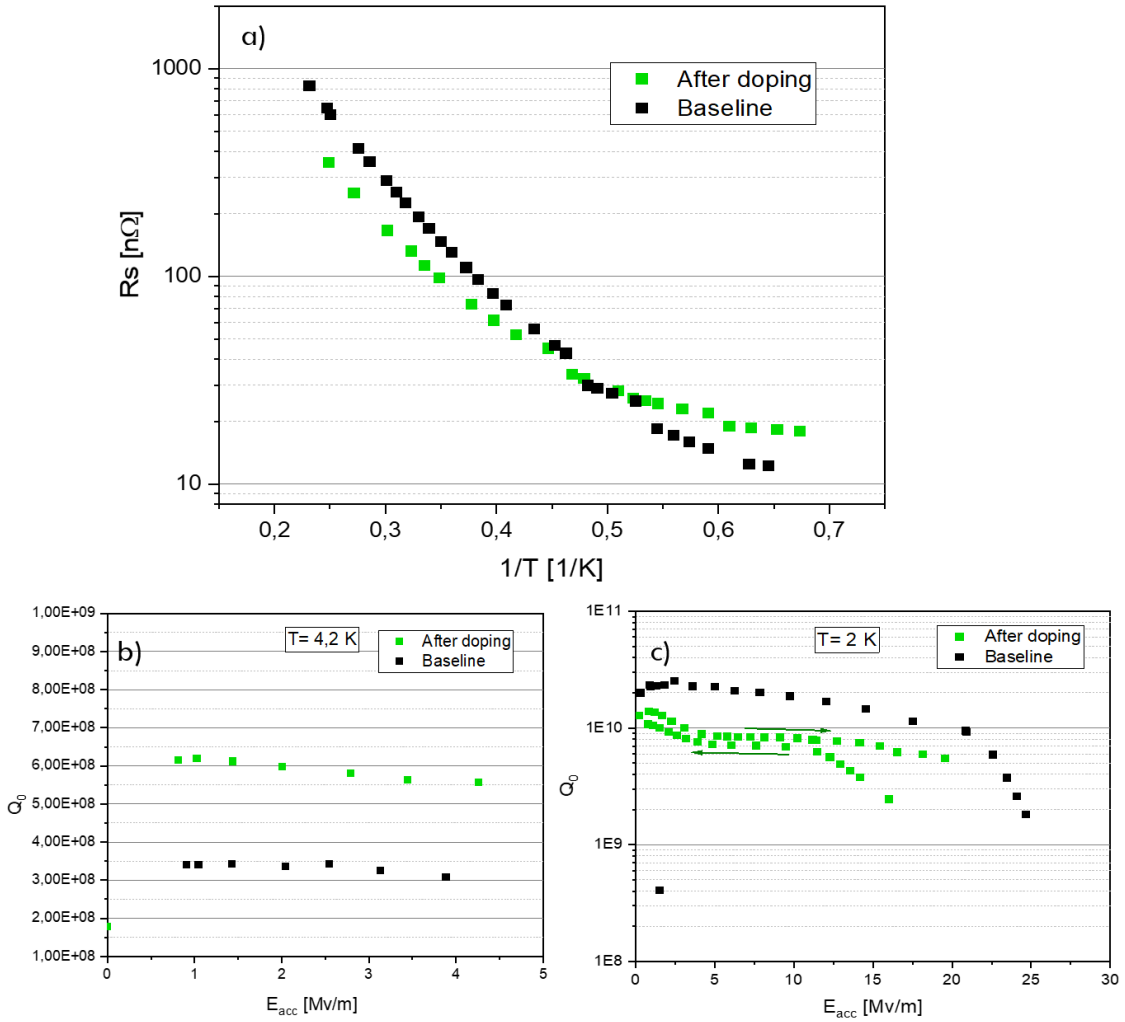

Figure 9.16: RF test of the N-doped Niobium cavity. a) The surface resistance as a function n of the temperature at 1 MV/m. b) The quality factor of the cavity at 4.K. c) The quality factor as a function of the accelerating gradient at 2 K.

9.6 Perspectives

Despite the modest performances of our "N-doped" niobium cavity, we think that these results are interesting on many levels. The fact that the BCS resistance is improved at 4.2 K compared to the baseline is definitely worth-investigating. We also noticed that these results are much higher than the performances of the "N-doped" cavities prior to the electro-polishing step, this hints that maybe we introduced a contamination layer that needs to be removed. We removed 5 µm of material via electro-polishing and we are currently waiting for helium supply to test again the cavity. These preliminary results deserve further exploration. We have seen that depending on the nitride layer (nature and thickness) used as a nitrogen source, we can achieve different levels of doping and end up with different passivating layers after the annealing. Exploring further the different post annealing conditions such as temperature and time is also a future prospect. Testing other layers on niobium cavities would help us further understand the physics behind nitrogen doping while using a relatively simple approach.

Conclusions and perspectives

The main purpose of this work have been to suggest and explore new routes to functionalize the inner surface of niobium RF cavities in quest of improving their performances. Through the use of atomic layer deposition as a coating technique, we were able to explore the potential of several original solutions to mitigate some of the most detrimental effects to RF cavities operation. Through the use of ALD-deposited oxide layers, we managed to compare their thermal stability with niobium native oxides and we were able to test their effect on niobium cavities performances. The Al_2O_3-coated niobium cavities showed enhanced quality factors in particular in the low field regime which is of huge interest to the Qubits community.

In order to mitigate multipacting in SRF cavities, we investigated the possibility of coating cavities with titanium nitride thin films. We established that with a 1 $\sim$1.5 nm thick TiN film, we were able to suppress multipacting in RF cavities while maintaining reasonable RF performances. In our study, we focused on testing this route into an RF cavity but it can easily be applied to several others RF devices.

One of our main goals through this research project was to explore the multilayered SIS (superconductor-insulator-superconductor) structure suggested in [1]. To that end, we developed a ALD-deposited bilayer based on aluminium nitride as an insulator and niobium titanium nitride NbTiN as a superconductor with critical temperatures up to 16 K. This multilayer have been optimised to meet with niobium cavities requirements and was implemented for the very first time in a niobium 1.3 GHz cavity.

Moreover, we tested a novel route to dope niobium cavities using ALD-deposited thin films as a dopant source followed by a subsequent annealing. We discussed our first set of measurement performed on both niobium coupons and 1.3 GHz cavity which showed encouraging results in particular at 4.2 K.

We believe that the results obtained through this project are promising in many aspects and are definitely worth pursuing. SRF is fundamentally a surface phenomenon. In that sense, the use of atomic layer deposition to alter the uppermost surface of RF cavities allows us to explore a great variety of possible coating layers. This would eventually help us understand further the physics that governs the first tens of nanometers of a niobium cavity and hopefully enables a real breakthrough in their performances.

Acknowledgments

I am very grateful for these last three years. Despite the challenges, these have been the best years of my life so far. I have been very fortunate to work with amazing people that have welcomed me, encouraged me and provided their help whenever needed.

First of all, i would like to to express my deepest appreciation to the jury members of my PhD thesis: Mohamed Belhaj, Nathanaelle Schneider, Anne Marie Valente Feliciano, Sergio Calatroni and Jens knobloch for taking the time to review my work.

I have been very fortunate to learn from an outstanding scientist and a great person, Thomas Proslier. I am deeply indebted to him for the time and patience he invested in teaching me first and then for believing in me and always giving me the opportunity to grow as a scientist. Thank you for the amazing journey that have opened so many doors for me.

I am also very grateful to my PhD director Claire Antoine for her support, encouragement and guidance throughout the PhD journey.

It was a great pleasure for me to work in the LiDC2 laboratory and i would like to express here my gratitude to the lab head Arnaud Madur and the department head Pierre Vedrine for their continuous support and all of my colleagues, especially Baptiste Delatte, Aurélien Four, Thomas Plaisant, Gregoire Julien, Christophe Servouin, Thierry Vachet, Jerome Sobre, Quentin Bertrand, Patrick Sahuquet, Mathieu Baudier, Claude Marchand, Bertrand baudouy, Pierre Bosland, Luc Maurice, Carlos Manuel Oliveira Faria, Sabrina Boudjerida, Gilles Monnereau, Cyril Blouch, Enrico Cenni, Catherine Madec, Juliette Poulin, Sylvie Regnaud, Guillaume Ferrand, Hassen Jenhani, Nicolas Bazin and Stephane Berry.

Several characterization measurements have been made possible thanks to several external collaborations. I would like to extend my sincere thanks to Diana Dragoe, Frederic Miserque, Jocelyne Leroy, Sandrine Tusseau-Nenez, Yunlin Zheng, David Hrabovsky, Mohamed Belhaj, Tobias Junginger, Guillaume Dubourdieu and Nicolas Lochet. You have been very nice and helpful.

I also want to commemorate here my first physics teacher at the preparatory institute for scientific and technical studies IPEST in Tunis, Elyes Dhaoudi, with whom i shared my first research experience. Thank you for sharing with me your outstanding understanding and passion for physics. You were also present for me whenever i needed moral support.

Finally, i thank my friends Renato, Zeineb, Oussema, Hiba and Souhail for their great support and continuous encouragement. You were so patient and you always provided good advice.

My family is the foundation of this work, and all of my work. I could not

have undertaken this journey without the love, understanding and moral support i received from my parents Moncef and Sabah, my sisters Rania and Abir and my life partner Hamza. You gave me the courage i needed at time of doubts. I hope this work made you proud.

Bibliography

[1] A. Gurevich. Enhancement of rf breakdown field of superconductors by multilayer coating. *Applied Physics Letters*, 88(1):012511, January 2006.

[2] Klaus Wille (prof.). *The Physics of Particle Accelerators: An Introduction*. Oxford University Press, 2000.

[3] R. J. Van de Graaff, K. T. Compton, and L. C. Van Atta. The Electrostatic Production of High Voltage for Nuclear Investigations. *Physical Review*, 43(3):149–157, February 1933.

[4] A. P. Grinberg. History of the invention and development of accelerators (1922-1932). *Soviet Physics Uspekhi*, 18(10):815, October 1975. Publisher: IOP Publishing.

[5] Rolf Widerøe and Pedro Waloschek. *The infancy of particle accelerators: life and work of Rolf Wideröe*. Vieweg, Braunschweig, 1994.

[6] Shyh-yuan Lee. *Accelerator Physics (Fourth Edition)*. World Scientific Publishing Company, 2018. Accepted: 2021-08-20T11:39:51Z.

[7] C Pira, E Chyhyrynets, G Caldarola, V Palmieri, F Stivanello, and R Vaglio. Nb thick films in 6 ghz superconducting resonant cavities. *Condens. Matter*, 197(1):72–83, 1994.

[8] Hasan Padamsee. The science and technology of superconducting cavities for accelerators. *Superconductor Science and Technology*, 14(4):R28–R51, April 2001.

[9] Martina Martinello. *The path to high Q-factors in superconducting accelerating cavities: Flux expulsion and surface resistance optimization, PhD thesis*. Illinois Institute of Technology, 2016.

[10] Rod V Latham. *High voltage vacuum insulation: Basic concepts and technological practice*. Elsevier, 1995.

[11] Hasan Padamsee. *RF Superconductivity: Science, Technology, and Applications*. Wiley-VCH, Weinheim, 1st edition edition, April 2009.

[12] R.G. Sharma. *Superconductivity: Basics and Applications to Magnets*, volume 214 of *Springer Series in Materials Science*. Springer International Publishing, Cham, 2015.

[13] Pascal Tixador and Yves Brunet. Supraconducteurs - Bases théoriques. *Conversion de l'énergie électrique*, November 2003.

[14] W.D Gregory, W.N Mathews Jr, and E.A Edelsack. *The Science and technology of superconductivity*, volume 1.

[15] Peter Schmüser. Basic principles of rf superconductivity and superconducting cavities. 2006.

[16] Di Giorgio et al. Superconducting vortex-antivortex pairs: Nucleation and confinement in magnetically coupled superconductor-ferromagnet hybrids. In *Vortex Dynamics and Optical Vortices*. IntechOpen, 2017.

[17] Daniel C Mattis and John Bardeen. Theory of the anomalous skin effect in normal and superconducting metals. *Physical Review*, 111(2):412, 1958.

[18] CP Bean and JD Livingston. Surface barrier in type-ii superconductors. *Physical Review Letters*, 12(1):14, 1964.

[19] Claire Antoine. Materials and surface aspects in the development of srf niobium cavities (no. eucard-boo-2012-001). Technical report, 2012.

[20] Hasan Padamsee. History of gradient advances in srf. *arXiv preprint arXiv:2004.06720*, 2020.

[21] J. Knobloch. The "Q disease" in Superconducting Niobium RF Cavities. *AIP Conference Proceedings*, 671(1):133–150, July 2003. Publisher: American Institute of Physics.

[22] Padamsee Hasan, Knobloch Jens, and Hays Tom. Rf superconductivity for accelerators. *John403 Wiley Sons Inc*, 1998.

[23] Ralph Howard Fowler and Lothar Nordheim. Electron emission in intense electric fields. *Proceedings of the Royal Society of London. Series A, Containing Papers of a Mathematical and Physical Character*, 119(781):173–181, 1928.

[24] Gregory Richard Werner. *Probing and modeling voltage breakdown in vacuum*. Cornell University, 2004.

[25] K Saito, S Noguchi, M Ono, H Miwa, E Kako, P Kneisel, T Suzuki, T Shishido, and K Kurosawa. Study of ultra-clean surface for niobium sc cavities. Technical report, P00024607, 1994.

[26] Kenji Saito, S Noguchi, M Ono, H Inoue, T Fujino, E Kako, and Toshio Shishido. Superiority of electropolishing over chemical polishing on high gradients. *Part. Accel.*, 60(KEK-98-4):193–217, 1998.

[27] Hasan Padamsee. *RF superconductivity: science, technology, and applications*. John Wiley & Sons, 2009.

[28] Marco Arzeo, F Avino, S Pfeiffer, G Rosaz, M Taborelli, L Vega-Cid, and W Venturini-Delsolaro. Enhanced radio-frequency performance of niobium films on copper substrates deposited by high power impulse magnetron sputtering. *Superconductor Science and Technology*, 35(5):054008, 2022.

[29] Y Trenikhina, S Posen, A Romanenko, M Sardela, JM Zuo, DL Hall, and M Liepe. Performance-defining properties of nb3sn coating in srf cavities. *Superconductor Science and Technology*, 31(1):015004, 2018.

[30] P Kneisel, R Roeth, H Piel, D Mansen, J Pouryamout, and G Müller. Nb _{3} sn layers on high-purity nb cavities with very high quality factors and accelerating gradients. 1996.

[31] A. Grassellino, A. Romanenko, D. Sergatskov, O. Melnychuk, Y. Trenikhina, A. Crawford, A. Rowe, M. Wong, T. Khabiboulline, and F. Barkov. Nitrogen and argon doping of niobium for superconducting radio frequency cavities: a pathway to highly efficient accelerating structures. *Superconductor Science and Technology*, 26(10):102001, August 2013. Publisher: IOP Publishing.

[32] A. Grassellino, A. Romanenko, Y. Trenikhina, M. Checchin, M. Martinello, O. S. Melnychuk, S. Chandrasekaran, D. A. Sergatskov, S. Posen, A. C. Crawford, S. Aderhold, and D. Bice. Unprecedented quality factors at accelerating gradients up to 45 MVm1 in niobium superconducting resonators via low temperature nitrogen infusion. *Superconductor Science and Technology*, 30(9):094004, August 2017. Publisher: IOP Publishing.

[33] Claire Z Antoine, M Aburas, A Four, F Weiss, Y Iwashita, H Hayano, S Kato, Takayuki Kubo, and T Saeki. Optimization of tailored multilayer superconductors for rf application and protection against premature vortex penetration. *Superconductor Science and Technology*, 32(8):085005, 2019.

[34] Anne-Marie Valente-Feliciano. *Development of SRF monolayer/multilayer thin film materials to increase the performance of SRF accelerating structures beyond bulk Nb*. PhD thesis, Université Paris Sud-Paris XI, 2014.

[35] T. Proslier, J. Zasadzinski, J. Moore, M. Pellin, J. Elam, L. Cooley, C. Antoine, J. Norem, and K. E. Gray. Improvement and protection of niobium surface superconductivity by atomic layer deposition and heat treatment. *Applied Physics Letters*, 93(19):192504, November 2008.

[36] Thomas Proslier, Jeffrey Klug, Nicholas Becker, Jeffrey Elam, and Michael Pellin. Atomic Layer Deposition of Superconductors. *Journal of The Electrochemical Society*, 41, March 2011.

[37] Thomas Proslier. 3.5 atomic layer deposition. In *Ametis*, pages 285–289. EDP Sciences, 2021.

[38] Ville Miikkulainen, Markku Leskelä, Mikko Ritala, and Riikka L. Puurunen. Crystallinity of inorganic films grown by atomic layer deposition: Overview and general trends. *Journal of Applied Physics*, 113(2):021301, January 2013.

[39] Riikka L. Puurunen. Surface chemistry of atomic layer deposition: A case study for the trimethylaluminum/water process. *Journal of Applied Physics*, 97(12):121301, June 2005.

[40] Tuomo Suntola and Jorma Antson. Method for producing compound thin films, November 15 1977. US Patent 4,058,430.

[41] Database of ALD processes. Publisher: Eindhoven University of Technology https://www.atomiclimits.com/alddatabase/.

[42] Riikka L Puurunen. Surface chemistry of atomic layer deposition: A case study for the trimethylaluminum/water process. *Journal of applied physics*, 97(12):9, 2005.

[43] Miho Yasaka et al. X-ray thin-film measurement techniques. *The Rigaku Journal*, 26(2):1–9, 2010.

[44] Andrei A Bunaciu, Elena Gabriela UdriŞTioiu, and Hassan Y Aboul-Enein. X-ray diffraction: instrumentation and applications. *Critical reviews in analytical chemistry*, 45(4):289–299, 2015.

[45] David Simeone, Gianguido Baldinozzi, Dominique Gosset, Sophie Le Caer, and Jean-François Bérar. Grazing incidence x-ray diffraction for the study of polycrystalline layers. *Thin Solid Films*, 530:9–13, 2013.

[46] Alfred Benninghoven. Chemical analysis of inorganic and organic surfaces and thin films by static time-of-flight secondary ion mass spectrometry (tof-sims). *Angewandte Chemie International Edition in English*, 33(10):1023–1043, 1994.

[47] WK Chu and JR Liu. Rutherford backscattering spectrometry: reminiscences and progresses. *Materials chemistry and physics*, 46(2-3):183–188, 1996.

[48] Fred A Stevie and Carrie L Donley. Introduction to x-ray photoelectron spectroscopy. *Journal of Vacuum Science & Technology A: Vacuum, Surfaces, and Films*, 38(6):063204, 2020.

[49] Neal Fairley, Vincent Fernandez, Mireille Richard-Plouet, Catherine Guillot-Deudon, John Walton, Emily Smith, Delphine Flahaut, Mark Greiner, Mark Biesinger, Sven Tougaard, David Morgan, and Jonas Baltrusaitis. Systematic and collaborative approach to problem solving using X-ray photoelectron spectroscopy. *Applied Surface Science Advances*, 5:100112, September 2021.

[50] J. Halbritter. On the oxidation and on the superconductivity of niobium. *Applied Physics A*, 43(1):1–28, May 1987.

[51] J Norem, Th Proslier, MJ Pellin, JW Elam, J Zasadzinski, CZ Antoine, JF Moore, and L Cooley. Results from atomic layer deposition and tunneling spectroscopy for superconducting rf cavities. Technical report, 2008.

[52] R. P. Elliott. COLUMBIUM-OXYGEN SYSTEM. *Trans. Am. Soc. Metals*, Vol: 52, January 1960. Institution: Armour Research Foundation, Illinois Inst. of Tech., Chicago.

[53] Thaddeus B Massalski, Hiroaki Okamoto, PRnbsp Subramanian, Linda Kacprzak, and William W Scott. *Binary alloy phase diagrams*, volume 1. American society for metals Metals Park, OH, 1986.

[54] I. Lindau and W. E. Spicer. Oxidation of Nb as studied by the uv-photoemission technique. *Journal of Applied Physics*, 45(9):3720–3725, September 1974.

[55] J. K. Hulm, C. K. Jones, R. A. Hein, and J. W. Gibson. Superconductivity in the TiO and NbO systems. *Journal of Low Temperature Physics*, 7(3):291–307, May 1972.

[56] Mélissa Delheusy, Université de Paris-Sud Faculté des sciences d'Orsay (Essonne), and stuttgart university. *X-ray Investigation of Nb/O Interfaces-PhD thesis*. 2008. ,.

[57] D. S. Rimai and R. J. Sladek. Pressure dependences of the elastic constants of semiconducting Nb O 2 at 296 K. *Physical Review B*, 18(6):2807–2811, September 1978.

[58] Marc Wenskat, Jakub Čižek, Maciej Oskar Liedke, Maik Butterling, Martin Stiehl, Guilherme Dalla Lana Semione, Constanze Backes, Christopher Bate, Oksana Melikhova, Eric Hirschmann, et al. Vacancy dynamics in niobium and its native oxides and their potential implications for quantum computing and superconducting accelerators. *Physical Review B*, 106(9):094516, 2022.

[59] R Franchy, T. U Bartke, and P Gassmann. The interaction of oxygen with Nb(110) at 300, 80 and 20 K. *Surface Science*, 366(1):60–70, October 1996.

[60] R.J.Cava; B.Batlogg, J.J. Krajewski, H.F. Poulsen, P. Gammel, W.F. Peck, L.W. Rupp Phys.Rev.B 44, 697 (1991).

[61] A. J. Bosman and E. E. Havinga. Temperature Dependence of Dielectric Constants of Cubic Ionic Compounds. *Physical Review*, 129(4):1593–1600, February 1963. Publisher: American Physical Society.

[62] Claude Chappert, Albert Fert, and Frédéric Nguyen Van Dau. The emergence of spin electronics in data storage. *Nature Materials*, 6(11):813–823, November 2007. Number: 11 Publisher: Nature Publishing Group.

[63] Jeong-Gyu Song, Jusang Park, Jaehong Yoon, Hwangje Woo, Kyungyong Ko, Taeyoon Lee, Sung-Hwan Hwang, Jae-Min Myoung, Keewon Kim, Youngman Jang, et al. Plasma enhanced atomic layer deposition of magnesium oxide as a passivation layer for enhanced photoluminescence of zno nanowires. *Journal of luminescence*, 145:307–311, 2014.

[64] L. Yan, C. M. Lopez, R. P. Shrestha, E. A. Irene, A. A. Suvorova, and M. Saunders. Magnesium oxide as a candidate high- gate dielectric. *Applied Physics Letters*, 88(14):142901, April 2006. Publisher: American Institute of Physics.

[65] Ceramic-Matrix Composites Deborah D.L. Chung, in Carbon Composites (Second Edition), 2017. Publisher: ELSEVIER.

[66] L Manchanda and M Gurvitch. Yttrium oxide/silicon dioxide: A new dielectric structure for vlsi/ulsi circuits. *IEEE electron device letters*, 9(4):180–182, 1988.

[67] K Bundschuh, M Schüze, C Müller, P Greil, and W Heider. Selection of materials for use at temperatures above 1500 c in oxidizing atmospheres. *Journal of the European Ceramic Society*, 18(16):2389–2391, 1998.

[68] Nagaraj A, Anupama P, Jaya Mukherjee, Sreekumar K. P, R. U. Satpute, P. V. A. Padmanabhan, and L. M. Gantayet. Thermal stability studies of plasma sprayed yttrium oxide coatings deposited on pure tantalum substrate. *Journal of Physics: Conference Series*, 208(1):012124, February 2010.

[69] Alumina - Aluminium Oxide - Al2O3 - A Refractory Ceramic Oxide, February 2001. Section: Materials Article.

[70] H. A. Huggins and M. Gurvitch. Preparation and characteristics of Nb/Al-oxide-Nb tunnel junctions. *Journal of Applied Physics*, 57(6):2103–2109, March 1985.

[71] Sarra Bira. *Conception d'un résonateur quadripolaire pour la caractérisation des propriétés de couches minces supraconductrices en régime radiofréquence pour les cavités accélératrices.* PhD thesis, Université Paris-Saclay, 2021.

[72] A Romanenko and DI Schuster. Understanding quality factor degradation in superconducting niobium cavities at low microwave field amplitudes. *Physical Review Letters*, 119(26):264801, 2017.

[73] SE De Graaf, L Faoro, J Burnett, AA Adamyan, A Ya Tzalenchuk, SE Kubatkin, T Lindström, and AV Danilov. Suppression of low-frequency charge noise in superconducting resonators by surface spin desorption. *Nature communications*, 9(1):1–6, 2018.

[74] Ram Prakash, Arup Ratan Jana, and Vinit Kumar. Multipacting studies in elliptic SRF cavities. *Nuclear Instruments and Methods in Physics Research Section A: Accelerators, Spectrometers, Detectors and Associated Equipment*, 867:128–138, September 2017.

[75] J Knobloch, W Hartung, H Padamsee, and F Newman. Multipacting in 1.5-ghz superconducting niobium cavities of the cebaf shape. In *Proceedings of the 8th Workshop on RF Superconductivity, Padua, Italy*, 1997.

[76] J P Gunn. Evidence for strong secondary electron emission in the tokamak scrape-off layer. *Plasma Physics and Controlled Fusion*, 54(8):085007, August 2012.

[77] A. V. Streltsov, J.-J. Berthelier, A. A. Chernyshov, V. L. Frolov, F. Honary, M. J. Kosch, R. P. McCoy, E. V. Mishin, and M. T. Rietveld. Past, Present and Future of Active Radio Frequency Experiments in Space. *Space Science Reviews*, 214(8):118, December 2018.

[78] Jerzy Lorkiewicz, Bernhard Dwersteg, Wolf-Dietrich Möller, D Kostin, M Layalan, and Arne Brinkmann. Anti-multipactor tin coating of rf power coupler components for tesla at desy. Technical report, CM-P00047838, 2004.

[79] John Michael Golio, editor. *The RF and microwave handbook*. The electrical engineering handbook series. CRC Press, Boca Raton, FL, 2001.

[80] V Lagomarsino, G Manuzio, R Parodi, and R Vaccarone. Measurements on niobium superconductings c band cavities for linear accelerators applications. *IEEE Transactions on Magnetics*, 15(1):25–26, 1979.

[81] U Klein and D Proch. Multipacting in superconducting rf structures. In *Proceedings of the Conference of Future Possibilities for Electron Accelerators, Charlottesville, WU B*, pages 78–34, 1979.

[82] Walid Kaabi, Alessandro Variola, Giorgio Keppel, Vincenzo Palmieri, Arne Brinkmann, and Isabel Montero. Titanium nitride coating as a multipactor suppressor. In *1st International Particle Accelerator Conference (IPAC 2010)*, pages 2887–2889. Joint Accelerator Conferences Website, 2010.

[83] Alessandro Variola, Walid Kaabi, Hassen Jenhani, Pierre Lepercq, Giorgio Keppel, Vincenzo Palmieri, and Fabio Strada. Titanium nitride coating of rf ceramic windows by reactive dc magnetron sputtering. In *11th European Particle Accelerator Conference (EPAC'08)*, pages 931–933. Joint Accelerator Conferences Website, 2008.

[84] Guibai Xie, Hongwu Bai, Guanghui Miao, Guobao Feng, Jing Yang, Yun He, Xiaojun Li, and Yun Li. The Applications of Ultra-Thin Nanofilm for Aerospace Advanced Manufacturing Technology. *Nanomaterials*, 11(12):3282, December 2021.

[85] M. Angelucci, A. Novelli, L. Spallino, A. Liedl, R. Larciprete, and R. Cimino. Minimum thickness of carbon coating for multipacting suppression. *Physical Review Research*, 2(3):032030, August 2020.

[86] DD Armstrong, WD Cornelius, FO Purser, RA Jameson, and TP Wangler. Rfq development at los alamos. Technical report, Los Alamos National Lab.(LANL), Los Alamos, NM (United States), 1984.

[87] M. Kuchnir and E. Hahn. Coating power RF components with TiN. Technical Report FNAL-TM–1928, 61161, March 1995.

[88] T. Gineste, M. Belhaj, G. Teyssedre, J. Puech, and N. Balcon. Investigation of the electron emission properties of Silver: from technical Ag surface to ion-cleaned Ag surface. In *International Workshop on Multipactor, Corona and*

Passive Intermodulation (MULCOPIM'14), pages pp. 1–8, VALENCE, Spain, September 2014.

[89] E Donoghue, J Mammosser, L Phillips, R Rimmer, M Stirbet, H Wang, and G Wu. Studies of Electron Activities in SNS-Type Superconducting RF Cavities. *New York*, page 4.

[90] K Halbach. SUPERFISH-A COMPUTER PROGRAM FOR EVALUATION OF RF CAVITIES WITH CYLINDRICAL SYMMETRY. page 10.

[91] M Taborelli. Secondary electron yield of surfaces: what we know and what we still need to know. In *CERN Yellow Reports: Conference Proceedings*, volume 7, pages 97–97, 2020.

[92] Qing Ma, Dean R Walters, and Richard A Rosenberg. Electron-induced surface chemistry on TiN in ultrahigh vacuum. *Applied Surface Science*, page 9, 2002.

[93] Valentine Petit. *Conditioning of surfaces in particle accelerators*. PhD thesis, Institut Supérieur de l'Aéronautique et de l'Espace, 2020.

[94] Dominik Jaeger and Jörg Patscheider. A complete and self-consistent evaluation of XPS spectra of TiN. *Journal of Electron Spectroscopy and Related Phenomena*, 185(11):523–534, November 2012.

[95] A. Glaser, S. Surnev, F.P. Netzer, N. Fateh, G.A. Fontalvo, and C. Mitterer. Oxidation of vanadium nitride and titanium nitride coatings. *Surface Science*, 601(4):1153–1159, February 2007.

[96] R. Cimino, M. Commisso, D. R. Grosso, T. Demma, V. Baglin, R. Flammini, and R. Larciprete. Nature of the Decrease of the Secondary-Electron Yield by Electron Bombardment and its Energy Dependence. *Physical Review Letters*, 109(6):064801, August 2012.

[97] Tery L Barr and Sudipta Seal. Nature of the use of adventitious carbon as a binding energy standard. *Journal of Vacuum Science & Technology A: Vacuum, Surfaces, and Films*, 13(3):1239–1246, 1995.

[98] J Knobloch, W Hartung, H Padamsee, and Cornell University. Multipacting in 1.5-GHz Superconducting Niobium Cavities of the CEBAF Shape. page 11, 1997.

[99] Roberto Russo, Luciano Catani, Alessandro Cianchi, Domenico DiGiovenale, J. Lorkiewicz, Sergio Tazzari, Carmine Granata, Pierluigi Ventrella, Gianrico Lamura, and Antonello Andreone. Niobium Coating of Cavities Using Cathodic Arc. *IEEE Transactions on Applied Superconductivity*, 19(3):1394–1398, June 2009. Conference Name: IEEE Transactions on Applied Superconductivity.

[100] C. Z. Antoine, S. Berry, M. Aurino, J.-F. Jacquot, J.-C. Villegier, G. Lamura, and A. Andreone. Characterization of Field Penetration in Superconducting Multilayers Samples. *IEEE Transactions on Applied Superconductivity*, 21(3):2601–2604, June 2011. Conference Name: IEEE Transactions on Applied Superconductivity.

[101] C. Z. Antoine, J.-C. Villegier, and G. Martinet. Study of nanometric superconducting multilayers for RF field screening applications. *Applied Physics Letters*, 102(10):102603, March 2013. Publisher: American Institute of Physics.

[102] W. M. Roach, D. B. Beringer, Z. Li, C. Clavero, and R. A. Lukaszew. Magnetic Shielding Larger Than the Lower Critical Field of Niobium in Multilayers. *IEEE Transactions on Applied Superconductivity*, 23(3):8600203–8600203, June 2013. Conference Name: IEEE Transactions on Applied Superconductivity.

[103] M. Aurino, E. Di Gennaro, F. Di Iorio, A. Gauzzi, G. Lamura, and A. Andreone. Discrete model analysis of the critical current-density measurements in superconducting thin films by a single-coil inductive method. *Journal of Applied Physics*, 98(12):123901, December 2005. Publisher: American Institute of Physics.

[104] Tatsuya Shiino, Shoichi Shiba, Nami Sakai, Tetsuya Yamakura, Ling Jiang, Yoshinori Uzawa, Hiroyuki Maezawa, and Satoshi Yamamoto. Improvement of the critical temperature of superconducting NbTiN and NbN thin films using the AlN buffer layer. *Superconductor Science and Technology*, 23(4):045004, March 2010. Publisher: IOP Publishing.

[105] Takayuki Kubo, Yoshihisa Iwashita, and Takayuki Saeki. Radio-frequency electromagnetic field and vortex penetration in multilayered superconductors. *Applied Physics Letters*, 104(3):032603, January 2014.

[106] G. Greczynski and L. Hultman. Towards reliable X-ray photoelectron spectroscopy: Sputter-damage effects in transition metal borides, carbides, nitrides, and oxides. *Applied Surface Science*, 542:148599, March 2021.

[107] G. Greczynski, D. Primetzhofer, J. Lu, and L. Hultman. Core-level spectra and binding energies of transition metal nitrides by non-destructive x-ray photoelectron spectroscopy through capping layers. *Applied Surface Science*, 396:347–358, February 2017.

[108] I González Díaz-Palacio, Wolfgang Hillert, Marc Wenskat, Robert H Blick, and Robert Zierold. Ald-based nbtin studies for sis r&d. *Tc*, 5:6–0, 2021.

[109] Matthew C. Burton, Melissa R. Beebe, Kaida Yang, Rosa A. Lukaszew, Anne-Marie Valente-Feliciano, and Charles Reece. Superconducting NbTiN thin films for superconducting radio frequency accelerator cavity applications. *Journal of Vacuum Science & Technology A: Vacuum, Surfaces, and Films*, 34(2):021518, March 2016.

[110] Peter Baláž. Mechanochemistry in minerals engineering. In *Mechanochemistry in nanoscience and minerals engineering*, pages 257–296. Springer, 2008.

[111] Houlei Cui, Guilian Zhu, Xiangye Liu, Fengxin Liu, Yian Xie, Chongyin Yang, Tianquan Lin, Hui Gu, and Fuqiang Huang. Niobium Nitride Nb4N5 as a New High-Performance Electrode Material for Supercapacitors. *Advanced Science*, 2, July 2015.

[112] Moo-Sung Kim, Se-Won Lee, and Sergei Ivanov. Atomic layer deposition of niobium nitride thin film with NbCl5 and NH3. page 13, 2020.

[113] Akimasa Yajima, Takashi Arai, Ryoko Matsuzaki, and Yuzo Saeki. Formation Process of Niobium Nitride by the Reaction of Niobium Pentachloride with Ammonia in the Vapor Phase and Properties of the Niobium Nitride Formed. *Bulletin of the Chemical Society of Japan*, 57(6):1582–1585, June 1984. Publisher: The Chemical Society of Japan.

[114] Isabel González Díaz-Palacio, Wolfgang Hillert, Marc Wenskat, Robert H Blick, and Robert Zierold. ALD-Based NbTiN studies for SIS R&D. page 1.

[115] Y. M. Shy, L. E. Toth, and R. Somasundaram. Superconducting properties, electrical resistivities, and structure of NbN thin films. *Journal of Applied Physics*, 44(12):5539–5545, December 1973.

[116] AD Batchelor, DN Leonard, PE Russell, FA Stevie, DP Griffis, and GR Myneni. Tem and sims analysis of (100),(110), and (111) single crystal niobium. In *AIP Conference Proceedings*, volume 927, pages 72–83. American Institute of Physics, 2007.

[117] Daniel Andrew Turner, Graeme Burt, and Tobias Junginger. No interface energy barrier and increased surface pinning in low temperature baked niobium. *Scientific Reports*, 12(1):5522, April 2022. Number: 1 Publisher: Nature Publishing Group.

[118] Kenji Saito et al. Surface smoothness for high gradient niobium sc rf cavities. In *Proceeding of the XI workshop on RF Superconductivity, Lubeck*, volume 516, 2003.

[119] J Knobloch, RL Geng, M Liepe, H Padamsee, et al. High-field q slope in superconducting cavities due to magnetic field enhancement at grain boundaries. *Krawcyk [21]*, pages 77–91, 1999.

[120] Valery Shemelin and Hasan Padamsee. Magnetic field enhancement at pits and bumps on the surface of superconducting cavities. *TTC-Report*, 7:2008, 2008.

[121] Zeke Insepov and Jim Norem. Can surface cracks and unipolar arcs explain breakdown and gradient limits? *Journal of Vacuum Science & Technology A: Vacuum, Surfaces, and Films*, 31(1):011302, 2013.

[122] Sadio Sy Savane Guillaume Ferrand†, Claire Z. Antoine. Rf simulation of niobium grains and peak magnetic field enhancement.

[123] Vijay Chouhan, Shigeki Kato, Yoshiaki Ida, Keisuke Nii, Takanori Yamaguchi, and Hitoshi Hayano. Chemical analysis and field emission study of electropolished niobium surface containing synthesized niobium oxide particles. *Materials Chemistry and Physics*, 259:124044, 2021.

[124] Cristoforo Benvenuti, M Minestrini, M Hauer, Sergio Calatroni, G Orlandi, and Wolfgang Weingarten. (nbti) n and nbti coatings for superconducting accelerating cavities. Technical report, P00000818, 1991.

[125] Pashupati Dhakal. Nitrogen doping and infusion in SRF cavities: A review. *Physics Open*, 5:100034, December 2020.

[126] A. Grassellino, A. Romanenko, A. Crawford, O. Melnychuk, A. Rowe, M. Wong, C. Cooper, D. Sergatskov, D. Bice, Y. Trenikhina, L. D. Cooley, C. Ginsburg, and R. D. Kephart. Fermilab experience of post-annealing losses in SRF niobium cavities due to furnace contamination and the ways to its mitigation: a pathway to processing simplification and quality factor improvement, May 2013. arXiv:1305.2182 [physics].

[127] Alexander Gurevich. Reduction of dissipative nonlinear conductivity of superconductors by static and microwave magnetic fields. *Physical review letters*, 113(8):087001, 2014.

[128] P. Dhakal, G. Ciovati, G. R. Myneni, K. E. Gray, N. Groll, P. Maheshwari, D. M. McRae, R. Pike, T. Proslier, F. Stevie, R. P. Walsh, Q. Yang, and J. Zasadzinzki. Effect of high temperature heat treatments on the quality factor of a large-grain superconducting radio-frequency niobium cavity. *Physical Review Special Topics - Accelerators and Beams*, 16(4):042001, April 2013.

[129] H Ito, H Araki, K Takahashi, and K Umemori. Influence of furnace baking on q–e behavior of superconducting accelerating cavities. *Progress of Theoretical and Experimental Physics*, 2021(7):071G01, 2021.

[130] Alexander Romanenko. Cavity performance limitations understanding via sims studies of cavity cutouts. *Progress of Theoretical and Experimental Physics*, Presentation-SRF2021, 2021.